BISMUTH-BASED ERBIUM-DOPED FIBER FOR MODE-LOCKING AND NONLINEAR APPLICATIONS

MOHAMMADREZA ABDOLHOSSEINI
MOGHADDAM

THESIS SUBMITTED IN FULFILLMENT OF THE
REQUIERMENT FOR THE DEGREE OF
DOCTOR OF PHILOSOPHY

DEPARTEMENT OF PHYSICS
FACULTY OF SCIENCE
UNIVERSITY OF MALAYA
KUALA LUMPUR

2012

UNIVERSITI MALAYA

ORIGINAL LITERARY WORK DECLARATION

Name of Candidate: **MOHAMMAD REZA ABDOLHOSSEINI MOGHADDAM**

I.C/Passport No: **L95235152**

Registration/Matric No: **SHC070067**

Name of Degree: **DOCTOR OF PHILOSOPHY**

Title of Project Paper/Research Report/Dissertation/Thesis (“this Work”):

BISMUTH-BASED ERBIUM-DOPED FIBER FOR MODE-LOCKING AND NONLINEAR APPLICATIONS

Field of Study: **PHOTONICS**

I do solemnly and sincerely declare that:
(1) I am the sole author/writer of this Work;
(2) This Work is original;
(3) Any use of any work in which copyright exists was done by way of fair dealing and for permitted purposes and any excerpt or extract from, or reference to or reproduction of any copyright work has been disclosed expressly and sufficiently and the title of the Work and its authorship have been acknowledged in this Work;
(4) I do not have any actual knowledge nor do I ought reasonably to know that the making of this work constitutes an infringement of any copyright work;
(5) I hereby assign all and every rights in the copyright to this Work to the University of Malaya (“UM”), who henceforth shall be owner of the copyright in this Work and that any reproduction or use in any form or by any means whatsoever is prohibited without the written consent of UM having been first had and obtained;
(6) I am fully aware that if in the course of making this Work I have infringed any copyright whether intentionally or otherwise, I may be subject to legal action or any other action as may be determined by UM.

Candidate’s Signature Date

Mohammad Reza Abdolhosseini Moghaddam **1 November 2012**

Subscribed and solemnly declared before,

Witness’s Signature Date

Name:
Designation:

ABSTRACT

Nature of Bi-related emission centers is not yet clear. Further research must be conducted to have a broadband low noise amplification and to raise efficiencies to level exhibited by silica-EDF systems. The pulse duration in generated train of pulses is one order of magnitude lower than that of a typical EDFA.This thesis describes laser generation process based on nonlinear effects, utilizing highly nonlinear fibers or/and Bismuth-based Erbium Doped Fiber (Bi-EDF). Various configurations were demonstrated using the Bi-EDF to generate various seed signals for optical amplifiers and nonlinear applications. Nonlinear effects both through stimulated Brillouin Scattering and slicing of spectrum were used to generate ultra wide multiwavelength comb lines or tunable narrow linewidth signals. A high-power double-clad amplifier was theoretically analyzed and experimentally used for both ultra-narrow linewidth and ultra short pulsed signals to provide the highest and flattest possible gain in the 1545-1566 nm wavelength regions.

A maximum output power of 400 mW with a laser linewidth of less than 1 KHz was obtained in narrow linewidth operation. The construction of a low threshold mode-locked laser with an energy fluctuation of less than 2.5%. was successfully accomplished and supercontinuum (SC) in different types of fibers, was also studied. Although Bi-EDF devices have previously been used to amplify and generate pulses of light in the picosecond domain, this is the first time ultrashort pulses have been achieved in the femtosecond domain without using any intra-cavity or extra cavity compressors. The pulse width can continuously vary from 1.2 ps to 131 fs. In addition, the variations of the spectral width, time-bandwidth products, pulse duration, amplitude and timing jitters as a function of the pump power were also investigated for various output ports at various regimes.

The pulses were then amplified at different power and injected into fibers with various dispersion profiles. The results show a considerably flat spectrum covering 500 nm to about 2.2 μm in dispersion flattened highly nonlinear fiber. A temperature sensitive loop mirror (TSLM) was proposed for slicing of spectra. Compared to conventional schemes, experimental results show that by using our proposed TSLM, one can potentially achieve a substantial improvement (6.6 times more) in increasing spectral spacing variation range and a considerable increment (337.6%) in temperature sensitivity.

ABSTRAK

Sifat dasar pusat-pusat pancaran yang berkaitan dengan Bismuth tidak begitu jelas lagi. Penyelidikan lanjutan mesti dijalankan untuk mengadakan suatu amplifikasi hingar rendah berjalur lebar dan meningkatkan kecekapan ke tahap yang ditunjukkan oleh sistem serabut optik didopkan erbium silica. Kepanjangan masa denyutan dalam bentuk denyutan rangkaian terjana adalah satu tertib magnitud lebih rendah daripada suatu amplifier serabut optik didopkan erbium khusus.

Tesis ini menghuraikan proses penjanaan laser berdasarkan kesan-kesan tak linear dengan menggunakan serabut tak linear tinggi atau/dan serabut didopkan Erbium dengan Bismuth (Bi-EDF) sebagai dasar. Pelbagai bentuk susunan telah ditunjukkan dengan menggunakan Bi-EDF untuk menjanakan isyarat sumber untuk kegunaan amplifier optik dan tak linear. Kedua-dua kesan tak linear yakni melalui Penyerakan Brillouin dan hirisan spektrum telah digunakan untuk menjanakan garis-garis sikat yang berpanjang gelombang kepelbagaian yang teramat lebar atau isyarat-isyarat lebar garis tipis yang boleh ditalakan. Satu amplifier dwilapisan kuasa tinggi telah dianalisis secara teori dan digunakan dalam experimen untuk kedua-dua lebar garis tipis dan isyarat-isyarat denyutan teramat pendek untuk membekalkan perolehan yang setinggi dan sedatar mungkin dalam bahagian gelombang 1545 hingga 1566 nm.

Satu kuasa output 400 mW dengan lebar garis laser yang kurang daripada 1 kHz telah diperolehi dalam operasi lebar garis tipis. Pembuatan satu laser penguncian mod dengan turun-naik tenaga kurang daripada 2.5% telah berjaya dicapai dan rangkain kesatuan terlampau dalam berbagai jenis serabut yang dipamkan oleh laser ini juga dikaji. Walaupun peranti-peranti Bismuth-Amplifier Serabut Optik Didopkan Erbium telah digunakan untuk menguatkan dan menjanakan denyutan-denyutan cahaya dalam domain piko-saat sebelum ini, ini adalah kali pertama denyutan-denyutan yang teramat sangat pendek tercapai dalam domain femto-saat tanpa menggunakan sebarang rongga intra ataupun pemampat-pemampat rongga tambahan.

Kita telah menunjukkan satu laser ambang rendah di mana lebar denyutannya boleh berubah dari 1.2 ps ke 131 fs secara berterusan. Tambahan pula, perubahan lebar spektrum, produk masa-lebar jalur, kepanjangan masa denyutan, amplitude dan ketaran pengaturan masa sebagai fungsi kuasa pam juga dikaji siasat untuk pelbagai gerbang output pada rejim yang berlainan. Denyutan-denyutan ini diperkuatkan pada peringkat kuasa yang berlainan dan disuntik ke dalam serabut dengan profil penyebaran yang berlainan. Keputusannya menunjukkan spectrum hingar yang agak rata dan rendah, meliputi julat gelombang daripada 500 nm ke lebih kurang 2.2 μm dalam serabut tak linear yang diratakan penyebarannya. Satu cermin gelung yang peka terhadap suhu (TSLM) telah ditawarkan untuk penghirisan spectra. Berbanding dengan skim lazim, keputusan-keputusan experiment menunjukkan bahawa kita berpotensi mencapai suatu kemajuan yang kukuh dalam meninggikan julat berbezaan ruangan spectra (6.6 kali lebih) dan kepekaan suhu (337.6%) dengan menggunakan TSLM yang dicadangkan.

ACKNOWLEDGMENTS

In the name of Allah, most merciful most gracious. First and foremost, I am so thankful to Allah for his guidance and for letting me complete this project successfully. Thence I thank my supervisor, Prof. Dr. Harith B. Ahmad, for his patience and his amazing insight throughout the duration of this thesis. Not to forget his encouragement that has helped me in this research at all times. The same appreciation goes to my co-supervisor. I am deeply indebted to him for their help. To Prof. Dr. Sulaiman Wadi Harun, thanks a lot for your effort and support in giving me the guidance to finish both the experimental work and the thesis writing.

To them I dedicate this thesis. Special gratitude is to my parents for their inordinate sacrifice and emotional support will not be forgotten forever. To them, those, raised me, supported me, taught me, and loved me. My full-hearted thanks should go to my family members particularly to my wife Zahra Kiyarad, my brothers, and my son Ali for helping me get through the difficult times. Without their help, I was not able to do my research in Malaysia.

I wish to express my gratitude to Prof. Dr. Shaif-ul Alam for their endless guidance, through the duration of my studies.

Also, my special thanks should go with the member of photonics research center, N. Shahrizan, Dr. S. Shahi, Dr. P. Parvizi and Dr. N. Tamchek for their assistance during the experiments as well as the living in Malaysia.

M. R. A. Moghaddam

Department of Physics, Faculty of Science,

University of Malaya.

October, 2012

TABLE OF CONTENTS

ORIGINAL LITERARY WORK DECLARATION ii
ABSTRACT iii
ABSTRAK v
ACKNOWLEDGMENTS vii
TABLE OF CONTENTS viii
LIST OF FIGURES xi
LIST OF TABLE xvi
APPENDIX xvii
ACRONYMS xviii

CHAPTER 1: INTRODUCTION

1.1 IMPORTANT NONLINEAR EFFECTS IN OPTICAL FIBERS 1
1.2 MODE LOCKED LASER AND SUPERCONTINUUM 3
1.3 MULTIPLE WAVELENGTH GENERATION 5
1.4 SCOPE AND OBJECTIVE 6
1.5 METHODOLOGY OF RESEARCH 9
1.6 THESIS OVERVIEW 11

CHAPTER 2: LITERATURE REVIEW

2.1 DISPERSION 13
    2.1.1 Normal and Anomalous Dispersion Regions 15
    2.1.2 Temporal Broadening Imposed by Dispersion 15
2.2 NONLINEAR EFFECTS 16
    2.2.1 Longitudinal and Transverse Optical Kerr Effect 18
        2.2.1.1 Self Phase Modulation (SPM) 21
        2.2.1.2 Cross Phase Modulation (XPM) 23
    2.2.2 Four-Wave Mixing (FWM) 25
    2.2.3 Inelastic Scattering Effects in Optical Fibers 32
        2.2.3.1 Stimulated Raman Scattering (SRS) 33
        2.2.3.2 Theory of Raman amplifiers 35
        2.2.3.3 Stimulated Brillouin Scattering (SRS) 39
2.3 PULSE PROPAGATION IN FIBERS 43
    2.3.1 Solitons 45
    2.3.1.1 Fundamental Solitons 46
    2.3.1.2 Raman Solitons 47
    2.3.2 Sources of errors during transmission and amplification 48
2.4 NONLINEAR OPTICAL FIBERS 51
    2.4.1 Photonic Crystal Fiber (PCF) 51
        2.4.1.1 Modal Behavior 54
        2.4.1.2 Nonlinearity 56
        2.4.1.3 Dispersion characteristic of PCF 57
        2.4.1.4 Loss and Attenuation 58
    2.4.2. Highly Nonlinear Fibers 59
2.5 SUPERCONTINUUM 60
    2.5.1 Pumping in Anomalous Dispersion Region 61

2.5.1.1 Effect of pulse specification in Anomalous pumping regime..............63
2.5.2 Pumping in Normal Dispersion Region 64
2.5.2.1 Effect of pulse specifications in normal pumping regime 65
2.5.3 Supercontinuum Generation with long Pulses 66

CHAPTER 3: Bi-EDF BASED LASERS AND AMPLIFIERS IN CW REGIME

3.1 BACKGROUND ON EDFA 68
3.2 GAIN AND NOISE FIGURE CHARACTERISTICS OF EDFA.........................69
3.3 LIMITATIONS OF SILICA-BASED EDFA..73
3.4 BISMUTH BASED EDFA 75
3.5 THE SPECTROSCOPIC PARAMETERS OF Bi-EDF 80
3.6 AMPLIFICATION CHARACTERISTICS OF Bi-EDFA 84
3.6.1 Luminescence Spectrum of Bi-EDFA in C-Band 86
3.6.2 Luminescence Spectrum of Bi-EDFA in L-Band 89
3.6.3 Gain in C+L-band region 91
3.6.4 Noise-Figure Characteristics of Bi-EDFA 97
3.6.5 Quantum and power conversion efficiency (QCE).......................................100
3.7 CW LASER CHARACTERISTICS 102
3.7.1 CW Tunable Ring Laser Using Bi-EDF 103
3.7.2 Bi-EDF-Based Brillouin Laser (BEFL) 105
3.7.3 Incorporation Effect of PCF in a Ring BEFL 107

CHAPTER 4: EXPERIMENTAL AND NUMERICAL INVESTIGATION OF GAIN CHARACTERISTICS OF HIGH POWER CLADDING-PUMPED Er^{3+}/Yb^{3+} FIBER LASERS AND AMPLIFIERS

4.1 MASTER OSCILLATOR POWER AMPLIFIER 110
4.2 CLADDING DESIGNS AND LIGHT INJECTION METHODS 113
4.3 ENERGY LEVELS OF Er^{+3} AND Yb^{+3} IONS 117
4.4 BASIC EQUATIONS AND MODELING..119
4.4.1 Cross Sections 122
4.4.2 Lifetime of Er^{3+} at $^4I_{13/2}$, Energy Level 124
4.5 THEORETICAL RESULTS...127
4.6 EXPERIMENTAL RESULTS...132
4.6.1 ASE Specta of Er^{3+}/Yb^{3+} Doped Cladding Pumped Fiber 132
4.6.2 DC-EYDF Laser Characteristics in a Linear Cavity....................................140
4.6.3 DC-EYDF Laser Characteristics in a Ring Cavity 145
4.6.4 Continuous Wave Er^{3+}/Yb^{3+} Doped Fibre MOPA 146
4.6.5 CW Tuneable High Power Narrow-Linewidth All Fiber-MOPA................155
4.6.5.1 Experimental Setup 156
4.6.5.2 Gain and Noise Spectra...160
4.6.5.3 Linewidth Measurements Using Brillouin Fiber Lasers 165
4.7 SUMMARY 169

CHAPTER 5: Bi-EDF BASED LASERS IN FEMTOSECOND REGIME

5.1 GENERATION OF FEMTOSECOND PULSE..170
5.2 MODE LOCKING MECHANISM 172
5.3 ACTIVE MODE LOCKING 174

5.4 PASSIVE MODE LOCKING....176
5.5 ULTRASHORT PULSE SHAPING MECHANISMS....177
5.6 INFLUENCE OF DISPERSION ON MODE LOCKING REGIME....179
5.7 PASSIVE MODE LOCKING WITH NLPR....182
5.8 PASSIVE MODE LOCKING WITH SATURABLE ABSORBER....184
    5.8.1 Saturable Absorber Structure and Technology....185
    5.8.2 Influence of Saturable Absorbers Parameters on a Mode-Locked Laser....188
    5.8.3 Mathematical Description of Loss Modulation....190
    5.8.4 Mode Locking with a Slow Saturable Absorber....191
    5.8.5 Mode Locking With a Fast Saturable Absorber....193
5.9 SOLITON PULSE REGIME....195
    5.9.1 Soliton Limits....198
    5.9.2 Quasi-Soliton Pulse Regime....200
5.10 STRETCHED-PULSE MODE LOCKING WITH NLPR TECHNIQUE....200
5.11 HYBRID MODE LOCKING....203
5.12 Q-SWITCHING INSTABILITIES AND NOISE CHARACTERISTICS....204
5.13 EXPERIMENTAL SETUP....207
5.14 EXPERIMENTAL RESULTS FOR MODE-LOCKED EDF LASER....212
5.15 EXPERIMENTAL RESULTS FOR MODE-LOCKED Bi-EDF LASER....220
5.16 POWER SCALING....230
5.17 CONCLUSIONS....232

CHAPTER 6: SUPERCONTINUUM GENERATION WITH FEMTOSECOND PULSES

6.1 EXPERIMENTAL SETUP....234
6.2 RESULTS AND DISCUSSION....238
    6.2.1 SCG Results in Photonic Crystal Fiber....238
    6.2.2 SCG Results in High Nonlinear Fiber (HNLF)....242
    6.2.3 SCG Results In Other Nonlinear Fibers....244
    6.2.4 Spectral Slicing of Supercontinuum Source....247
        6.2.4.1 Design of Temperature Sensitive Loop Mirror....249
        6.2.4.2 Multi-wavelength source by SC slicing technique....253
6.3 CONCLUSIONS....255

CHAPTER 7: CONCLUSION AND FUTURE WORK

7.1 CONCLUSION....258
    7.1.1 Bismuth-Based Optical Fibres as Different Glass Hosts....258
    7.1.2 Amplification of Narrow Linewidth and Broadband Signals....261
    7.1.3 Ultra-Short Pulse Generation....262
    7.1.4. Multi-wavelength comb and SCG with Femtosecond Pulses....264
7.2 FUTURE WORKS....267

APPENDIX

A ISI Journals....272
B Conference Papers....273
REFERENCES....275

LIST OF FIGURES

Chapter 2:

Figure 2. 1: Kerr lens mode locking effect at an intracavity focus in the gain medium. The induced lens focuses the beam in the transverse propagation due to high radial dependent intensity effect I(r), while frequency chirps in the longitudinal direction are caused by temporal dependent intensity effect I(t) which results in red shifted of the leading part and blue shifted of the trailing part. 20
Figure 2. 2: SPM effect on phase and frequency. 22
Figure 2. 3: The new frequencies generated through FWM (left) in partially degenerate case and (right) in non-degenerate case [89, 94]. 26
Figure 2. 4: Schematic of the energy levels of a molecule involved during SRS 34
Figure 2. 5: Raman gain coefficient measured in DCF with a high germanium content, TWRS, non-dispersion shifted fiber (5D)and a fiber without germanium (Pure-silica) with a 1510 nm pump wavelength [110]. 37
Figure 2. 6: Schematic diagram of the SBS process in an optical fiber 40
Figure 2. 7: (a) Variation of the Raman response function $\mathrm{h_R(T)}$ with time with arbitrary vertical unit [113] (b) SSFS rate as a function of soliton width [143]. 50
Figure 2. 8 (a): *left)* Scanning electron microscopy micrographs of a photonic-crystal fiber with silica core and *Right)* hollow core structure. 53
Figure 2. 9: Light propagation in (a) holey fiber (b) PBG. 54
Figure 2. 10: shows the number of modes in a PCF versus frequency. 55
Figure 2. 11: Effective mode area of holey fibers vs. pitch size Λ [153]. 56
Figure 2. 12: (a) Dispersion profile for different values *of d/Λ*, *Λ=2 μm* [2], (b) Dispersion profile of holey fibers with different core sizes. Comparison made to "Crystal-Fiber" [154]. 57
Figure 2. 13: (a): Relative refractive index of HNL-DSF (b) HNL-DSF characteristics. Dots show experimental results [156] 59

Chapter 3:

Figure 3. 1: The determination of noise from spectral information. 71
Figure 3. 2 :(a) Bi_2O_3 glass with a pyramidal polyhedron structure, (b) Erbium ions distribution of bismuth-based glass. 77
Figure 3. 3: The 4f energy diagram of Er^{3+} ion and the relevant transitions. 81
Figure 3. 4: cross-sections of Bi-EDF. The calculated Bismuth emission curve coincides with the measured curve where cross sections are $\sigma_{a_{max}} = 7.73 \times 10^{-25}\mathrm{m}^2, \sigma_{e_{max}} = 7.58 \times 10^{-25}\ \mathrm{m}^2$ at the 1532 nm peak (300 K). 82
Figure 3. 5: Experimental set-up for the Bi-EDFA with a (a) Forward pumping (b) Backward pumping (c) Double-pass and (d) Bi-directional pumping, configuration. 85
Figure 3. 6: Mixed Angle splicing configuration with an optimum angle of θ_2=8.2° for silica fiber and a pre-angle of θ_1=6° for Bi-EDF 86

Figure 3. 7: Luminescence spectra of EDF configured with a 49 cm long Bi-EDF for both forward and backward 1480 nm pumping scheme. The pump power is varied from 65 up to 160 mW. Inset shows ASE spectrum of the bi-directional pumped single-pass Bi-EDFA. 87
Figure 3. 8: Luminescence spectra of 49 cm long Bi-EDF for both forward and backward pumping scheme at pump wavelength of 980 nm. The pump power is varied from 32 up to 150 mW. 88
Figure 3. 9: Forward ASE spectrum configured with 215 cm long Bi-EDF for different 1480nm pumping configurations: Forward (F160B0), Backward (F0B160) and Bi-directional (F120B40 & F120B120). 89
Figure 3. 10: Gain as a function of pump power in forward pumping scheme at fixed signal power. 92
Figure 3. 11: The gain at input signal powers of -30 dBm and 0 dBm as a function of input signal wavelength for different pumping configurations............................. 93
Figure 3. 12: The gain spectra of L-band Bi-EDFA at input signal powers of -30 dBm and 0 dBm for different pumping configurations. 94
Figure 3. 13: Noise figure of C-band Bi-EDFA as a function of forward 1480 nm pump power. Signal power and signal wavelength are fixed in the figures. 97
Figure 3. 14: Noise figure spectrum for Bi-EDFA in C-band region at input signal powers of -30 dBm and 0 dBm. 98
Figure 3. 15: Noise figure spectrum for L-band Bi-EDFA at low and high input powers for different pumping configurations. 100
Figure 3. 16: Comparison of the QCE spectra at input signal power of 0 dBm between a C-band Bi-EDFA and a L-band Bi-EDFA. 101
Figure 3. 17: Configuration of the proposed Bi-EDF based tunable laser source (TLS).102
Figure 3. 18: Spectral profile of the proposed ring laser without TBF for different lengths of Bi-EDF (i.e. 49 cm, 215 cm) and various output coupling ratios. The 1480 nm pump power is fixed at 160 mW. 103
Figure 3. 19: Output power versus lasing wavelength at fixed pump power for a 49 cm long Bi-EDF laser. Inset shows the output spectra at different laser wavelengths covering from 1535 to 1580 nm by an OSA at a resolution of 0.07 nm. 104
Figure 3. 20: Configuration of a Bi-EDF based Brillouin fiber laser. 105
Figure 3. 21: Stimulated Brillouin multi-wavelength laser in 49 cm long Bi-EDF. Inset shows stimulated Brillouin stoke in 215 cm long Bi-EDF. 106
Figure 3. 22: Output spectra of the Bi-EDF based BEFL with a intracavity PCF. The BP power and 1480 nm pump power is fixed at 7 dBm and 150 mW respectively.108

Chapter 4:

Figure 4. 1: Working principle of a double-clad fiber. The pump light (Brown) propagates in the inner cladding while amplified signal or cavity power lasing (in gray) occurs in the core. 114
Figure 4. 2: (Left) Double clad EYDF with star shape silica inner cladding,(right) TFB. 116
Figure 4. 3: Energy level diagram for the EYDF amplification system. Dashed lines (d),(o) are used for spontaneous emission. Inset determines the transitions related

to the absorption and stimulated emission of pump and signal as well as energy transfer between Er and Yb. 118
Figure 4. 4: The EYDF absorption and gain specifications of Yb^{+3} ions (left) and Er^{+3} ions (right). 124
Figure 4. 5**:** Schematic of the fiber model. 128
Figure 4. 6: Theoretical gain spectrum of the EYDFA against fiber length and wavelength at input signal power of -10 dBm. 130
Figure 4. 7: Comparison of calculated output power with experimental results for the EYDFA with 10 m long EYDFA at a fixed -10 dBm input signal power and a 3.5 W forward pump power. 131
Figure 4. 8: Experimental set-up for measuring ASE. 133
Figure 4. 9: ASE spectra of the forward pumped EYDF at different pump powers. The pump powers are 250, 420 and 600 mW at 927 nm on the figure. 134
Figure 4. 10: The forward ASE spectrum from the DC-EYDFA with 10 m length of gain medium and 160-300 mWof the 1064 nm pump power. 135
Figure 4. 11: The luminescence spectra of EYDF configured with 10 m long double clad fiber for both forward and backward 927nm pumping scheme. The pump power is fixed at 670 mW. 135
Figure 4. 12: ASE power and Back traveling power as a function of pump power for forward pumping (FP), backward pumping (BP) and in a amplifier with an isolator at output (with ISO). In this experiment the input signal power and wavelength are fixed at -10 dBm and 1560 nm respectively. 138
Figure 4. 13: Back traveling power ratio as a function of signal wavelength in the forward and backward pumping scheme at a fixed pump power of 3.1W .Inset shows power ratio reduction at 1564 nm with the signal power increment. 139
Figure 4. 14: Output spectrum of the EYDFL configured without any FBG. 139
Figure 4. 15: Experimental setup for the double-clad EYDFL. 140
Figure 4. 16: Output power characteristic of the EYDFL for different schemes at different operating wavelengths. 141
Figure 4. 17: Output power characteristic of the EYDFL using BBFBG and loop mirror as a reflector, Inset shows a 0.25 nm linewidth and a spacing as narrow as 1nm for dual-wavelength performance using loop mirror. 142
Figure 4. 18: Photograph of 4 W DC-EYDFL with the cover removed. 144
Figure 4. 19: Output power as a function of pump power for laser at 1552.3nm with 38% slope efficiency. 144
Figure 4. 20: Output spectrum of the double-clad EYDFL with the 1553.6 nm FBG. Inset shows a comparision of the grating bandwidth and the laser linewidth. 145
Figure 4. 21: Experimental set-up for the EYDFA (a) Single-pass with a forward pumping scheme (b) Single-pass with a backward pumping (b) Double-pass configuration. 147
Figure 4. 22: Transmission loss spectrum of a BB-FBG. 148
Figure 4. 23: The output power of the amplified signal against the signal wavelength. 149
Figure 4. 24: The output powers of the amplified signal against 927nm pump powers for the double pass EYDFA. 150
Figure 4. 25: Measured QCE against pump power for different schemes at different operating wavelengths, FP: forward pumping, BP: backward pumping, DP: double pass Scheme. 151

Figure 4. 26: The output spectrum of the signal for different configurations at a fixed pump power of 4160 mW and a fixed signal power of -10 dBm......................... 152
Figure 4. 27: Spectrum of the tuneable C-band MOPA from 1530 nm to 1565 nm at -10 dBm input signal power and a fixed pump power of 4160 mW.................... 153
Figure 4. 28: The SMSR of signal in the C-band region. 154
Figure 4. 29: Experimental set-up for the linewidth measurement of the BFL amplified by the proposed double-pass EYDFA configuration........................... 159
Figure 4. 30: Output spectra from the BFL oscillator with different configurations. The inset shows the peak power of the BFLs against the Brillouin pump power. 161
Figure 4. 31: The output spectra of the BFL amplified at maximum pump power, with and without an interstage filter when the output power from first stage is fixed at 5dBm... 163
Figure 4. 32: Output power of the amplified BFL (with NZ-DSF) against the pump power of the DC-EYDFA at various wavelengths and input signal powers. 163
Figure 4. 33: The gain of amplified signal for different BP wavelengths and various input signal powers of the BFL. The pump power is fixed at 4.1 W. 164
Figure 4. 34: The beat spectrum using Bi-EDF based fiber laser as a seed in MOPA. 166
Figure 4. 35: The beat signal with commercial TLS in MOPA.................................. 167
Figure 4. 36: The measured heterodyne beat frequency spectrum between amplified signal from BFL seed and SMF based local oscillator at an output power of 400 mW.. 167

Chapter 5:

Figure 5. 1: Pulse sequences from a mode locked laser, (a) Random intense pulses in the laser cavity, (b) Ultra short pulses in the femtosecond regime produced when these random intense pulses add up together in phase at one instant time and (c) The corresponding peak and average power of the pulse (d) Mode locked pulses in frequency domain [327]... 174
Figure 5. 2: Active mode locking, (a) Loss modulation by external modulator, (b) Cavity loss and Pulse intensity in time domain [66]... 175
Figure 5. 3: The pulse shaping elements in a passive modelocked laser [333]. 177
Figure 5. 4: Operating regime based on the net cavity GVD...................................... 181
Figure 5. 5: (a) Passively mode locked laser using NLPR technique. (b) Schematic of the NLPR process. The wings of the pulse undergo little or no rotation relative to the peak of the pulse. This polarization difference is turned into a loss when the pulse is analyzed at the polarizer. 183
Figure 5. 6: Pulse-shaping process with a SA... 185
Figure 5. 7: Typical structure of SESAM in (a) resonant,(b) anti-resonant scheme. In R-SESAM the field in the quantum well is resonantly enhanced by about a factor of 10 in comparison to the non resonant case... 187
Figure 5. 8: (a) Reflectivity changes in SESAM as a function of the incident pulse fluence (b) Transmittance changes as a function of the incident pulse wavelength in a transmission type of SA, used in this thesis... 189
Figure 5. 9: Temporal evolution of optical power and losses in a passively mode-locked laser with a (a) slow saturable absorber, (b) fast saturable absorber [366].191

Figure 5. 10: (a) Pulse propagation in stretched pulse laser cavity, (b) Simulation. 202
Figure 5. 11: Experimental setup of the Bi-EDFL. ”WDM: Wavelength Division Multiplexer; SA: Saturable Absorber; OSC: Oscilloscope; RFSA: RF Spectrum Analyzer; OSA: Optical Spectrum Analyzer; AC: Auto-correlator; PC: Polarization Controller; PBS-Isolator: Beam Polarizing Beam Splitter integrated with Isolator; H: (Zero order)1/2- wave retarder; Q: (Zero order) 1/4- wave retarder ;ISO:Isolator”. 210
Figure 5. 12: Net cavity dispersion for various lengths of EDF in the cavity. The total length of cavity is fixed at 10.4 m. 213
Figure 5. 13: Spectra measured at different output ports for a ring cavity with 4 m long EDF (DF1500L). Pump power is fixed at 100mW. Inset shows ASE spectra in forward and backward schemes and also transmittance spectrum (%) of SA. . 214
Figure 5. 14: Autocorrelation trace of 1.17 ps pulses. Dashed curve is sech^2 fit and inset shows pulse train with a repetition rate of 9.87 MHz. 215
Figure 5. 15: (a) Spectra measured at PBS port, (b) The variation of the spectral width, and output power at the PBS port with the pump power. 217
Figure 5. 16: RF spectrum of typical pulse train without multiple pulsing for net negative GVD. The frequency axis is logarithmic. 218
Figure 5. 17: Normalized spectra of different harmonics from PBS Port as a function of the scaled offset frequency in a sub-picosecond pulse train. The RBW in RFSA is fixed at 3 kHz. Inset shows the noise structure and marks P_A, P_B, P_C and P_D. 219
Figure 5. 18: Period-doubling of multiple vector solitons: (a) Two vector solitons, (b) three vector solitons. 222
Figure 5. 19: Typical spectrum for an oscillator with a single polarization controller. Dependence of (a) output spectral width on the input power, (b) TBWP and pulse duration on the input power. 223
Figure 5. 20: Typical spectrum for an oscillator with a single polarization controller: (a) Peak power and pulse energy versus the input power (b) Comparison of output spectrum using PC and a set of retarder components. 224
Figure 5. 21: (a) Optical spectrum of oscillator with two polarization controllers for 125 mW pump power, (b) The average power versus pump power for the various rejection ports. 225
Figure 5. 22: (a) Autocorrelation trace and pulse train (inset) of the 340 fs pulses. Dashed curve: sech^2 fit, (b) The RF spectrum over a span of 1.5 GHz with a logarithmic axis. 226
Figure 5. 23: Optical spectrum of mode locked laser in linear and dB scales. The pump power is fixed at 125 mW. Inset shows pulse train with a repetition rate of 8.27 MHz. 227
Figure 5. 24: (a) Energy fluctuations as a function of pump power for both rejection ports (b) The dependency of low frequency jitter noise and energy fluctuations on pump power and spectral width. 229
Figure 5. 25: (a) Pulse spectrum of amplified signals at maximum pump powers, (b) Output Power against multi mode laser diode after amplification 231

CHAPTER 6:

Figure 6. 1: Experimental setup of the Bi-EDFL: WDM: Wavelength Division Multiplexer; SA: Saturable Absorber; PC: Polarization Controller; PBS-Isolator: Beam Polarizing Beam Splitter integrated with Isolator; H: λ/2 retarder; Q: λ/4 retarder; ISO: Isolator; MMC: multimode combiner; MM-LD: multimode laser diode; OSC: Oscilloscope; RFSA: RF Spectrum Analyzer; OSA: Optical Spectrum Analyzer; AC: Auto-correlator. 236
Figure 6. 2: Dispersion profile of different nonlinear fibers used in the experiments [396]. 237
Figure 6. 3: (a) SCG with 50 m PCF at various pump powers. The narrow curve shows the spectrum of the initial 340 fs pulse,(b) SCG extending from 500 nm to 2,2 μm. 240
Figure 6. 4: Optical spectrum of the continuum generated in 100 m length of PCF-NEG as a function of coupled power. 241
Figure 6. 5: The generated supercontinuum at different PCF lengths at fixed average pump power of 500 mW (peak power of 177 kW). 242
Figure 6. 6: (a) SC generation in 100 m HNLF at various pumping powers, (b) wide span measurement and disappearance of spectral peak at 1064nm. 244
Figure 6. 7: SCG comparison in various fibers at highest level of power (177 kW peak power). 245
Figure 6. 8: Bandwidth evolution versus launched pump power 246
Figure 6. 9: Experimental Setup of the temperature-sensitive interferometer based on multisegment Polarization Maintaining Fiber Sagnac Loop Mirrors (PMF-FLM). 249
Figure 6. 10: L_2 =2.5 m, L_1 = 1.0 m, L_{eff} =1.5 m, λ = 1037 nm, T_0=28 °C (Estimated parameters $b_1 = 2.6\times10^{-7}$ °C^{-1}, $b_2 = 1.5\times10^{-9}$ °C^{-2}, $\Delta n(T_0) = 4.07\times10^{-4}$). 252
Figure 6. 11: L_2 = 4.0 m, L_1= 2.5 m, L_{eff} =1.5m, λ = 1037 nm, T_0=28 °C (Estimated parameters $b_1 = 2.5\times10^{-7}$ °C^{-1}, $b_2 = 1.5\times10^{-9}$ °C^{-2}, $\Delta n(T_0) = 4.07\times10^{-4}$) 253
Figure 6. 12: The sliced spectra of all channels using proposed TSLM, inset shows a superposition of the spectra of 29 channels in the region of 1500 to 1549 nm with the maximum difference of 0.4 dB. 254

LIST OF TABLE

Table 2. 1: Comparison between the parameters of several types of fibers used in this work. It is to be noted here that the Raman gain coefficient around frequency shift decreases with increasing fluorine concentration. 37
Table 3. 1: Specification of Bismuth-based EDF [216, 227, 228]. 80
Table 4. 1: Transitions description in Figure 4.3. 119
Table 4. 2: The proposed cladding pumped fiber specifications and parameters used for the numerical calculations. 126
Table 4. 3: Initial Condition.. 128
Table 4. 4: The variables used in the numerical calculation.. 129
Table 4. 5: Laser threshold and efficiency for different wavelengths. 143
Table 5. 1: Specification of fibers and SA for the experimental setups. 209
Table 6. 1: Parameters and specifications of nonlinear fibers used. 237

APPENDIX

LIST OF PUBLICATIONS 272

ACRONYMS

Some jargons used in this thesis are listed as follow:

(AR)-SESAM	(Anti-Reflection-coated) SESAM
(D)SAM	(Dispersive) Saturable Absorber Mirror
(D)WDM	(Dense) Wavelength Division Multiplexing
(NZ)DSF	(Nonzero) Dispersion Shifted Fiber
A_{eff}	Effective Area
A-FPSA	Antiresonant Fabry-Pérot Saturable Absorber
AOM	Acousto Optical Modulator
APM	Additive Pulse Mode Locking
ASE	Amplified Spontaneous Emission
B(E)FL	Brillouin(Erbium) fiber laser
Bi-EDF (A)	Bismuth-Based Erbium Doped Fiber (Amplifier)
BP	Brillouin Pump
BPRS	Brillouin Pump Rayleigh Scattering
BRFL	Brillouin Raman Fiber Laser
CPA	Chirped Pulse Amplification
CUP	Co-Operative Up-Conversion
DC(F)	Double-Clad(Fiber)
DWDM	Dense Wavelength Division Multiplexing
EDF(A/L)	Erbium Doped Fiber(Amplifier/ laser)
ESA	Excited State Absorption
FBG	Fiber Bragg Grating
FROG	Frequency-Resolved Optical Gating
FSR	Free Spectral Range
FWHM	Full Width at Half Maximum
FWM	Four-Wave Mixing
GDD	Group Delay Dispersion
GSA	Ground State Absorption
GVD	Group Velocity Dispersion
HNLF	Highly nonlinear fiber

HWP	Half Waveplate
KLM	Kerr lens mode-locking
Leff	Effective Length
LMA	Large Mode Area
MBEFL(s)	Multiwavelength BEFL(s)
MBFL(s)	Multiwavelength BFL(s)
MFD	Mode-Field Diameter
MMC	Multimode Combiner
MOPA	Master Oscillator Power Amplifier
NA	Numerical Aperture
NF	Noise Figure
NLPE	Nonlinear Polarisation Evolution
NLSE	Nonlinear Schrodinger Equation
NOLM	Nonlinear Optical Loop Mirror
NPR	Nonlinear Polarization Rotation
NSE	Nonlinear Schrödinger Equation
NSR	Non-Solitonic Radiation
OC	Optical Circulator
OSA	Optical Spectrum Analyzer
OSNR	Optical Signal to Noise Ratio
PBS	Polarization Beam Splitter
PC	Polarization Controller
PCF	Photonic Crystal Fiber
PM (F)	Polarisation Maintaining Fiber
PMD	Polarization Mode Dispersion
QCE	Quantum Conversion Efficiency
QW	Quantum Well
QWP	Quarter Waveplate
RF(SA)	Radio Frequency (Spectrum Analyzer)
RIFS	Raman-Induced Frequency Shift
RP	Raman Pump
RS	Raman Stokes

SA	Saturable Absorber
SBR	Saturable Bragg Reflector
SBS	Stimulated Brillouin Scattering
SC(G)	Supercontinuum (Generation)
SESAM	Semiconductor Saturable Absorber Mirror
SHG	Second Harmonic Generation
SMSR	Side-Mode Supprestion Ratio
SNR	Signal To Noise Ratio
SPM	Self Phase Modulation
SPRS	Spontaneous Raman Scattering
SRS	Stimulated Raman Scattering
SSFS	Soliton Self-Frequency Shift
TBP	Time-Bandwidth Product
THG	Third-Harmonic Generation
TLS	Tunable Laser Source
TOD	Third Order Dispersion
TSLM	Temperature Sensitive Loop Mirror
VOA	Variable Optical Attenuator
XPM	Cross-Phase Modulation
YDFA	Ytterbium Doped Fiber Amplifier
YDFL	Ytterbium Doped Fiber Laser
ZDWL	Zero-Dispersion Wavelength

CHAPTER 1

INTRODUCTION

1.1 IMPORTANT NONLINEAR EFFECTS IN OPTICAL FIBERS

The development of silica based optical fibers led to an intense research within optical communication systems. The interaction of light with these fibers in some circumstances, (e.g. material absorption or Rayleigh scattering), leads to a loss in performance whereas in Stimulated Brillouin Scattering (SBS) or Stimulated Raman Scattering (SRS) such interaction may be beneficial. In 1922, L. Brillouin predicted light scattering from thermally excited acoustic waves [1] and in 1928, C. V. Raman reported that a small fraction of power can be transferred from one optical field to another field whose frequency is downshifted by an exact amount determined by the vibrational mode of the medium. In 1962, it has been shown that for intense pumps, most of the Raman pump energy is transferred to the Raman Stokes via SRS. Then SRS and SBS were used for generating Raman and Brillouin fiber lasers and (parametric) amplifiers [2, 3].

A new aspect in the field of nonlinear fiber optics was obtained when optical fibers were doped with rare-earth elements. The use of Erbium doped fiber amplifiers (EDFAs) led to a revolution in the design of optical systems [4]. However, power levels did not exceed 50 mW in most experiments until 1990. To improve the amplification characteristics and laser efficiency in the rare-earth doped fibers and to overcome the limitation of the doping concentration imposed by concentration quenching, several techniques such as co-doping with ytterbium, modifying the host glass with compositions (e.g.: P_2O_5 and Al_2O_3) and multiple hosts materials (e.g.: lanthanum co doped bismuth based erbium doped fiber) can be utilized [5, 6]. For instance, as demonstrated in our recent works, laser efficiencies of nearly 90% can be extracted by using the core composition of 0.2 wt % of Yb_2O_3, 1.8 wt % of Al_2O_3 and 23 wt % of GeO_2 [7-9].

Even though fiber nonlinearities are relatively weak compared to other materials, the advent of double clad fiber*s* in 1993 [10, 11], high power laser diodes [10], ultra short pulse fiber sources [12], and high-nonlinear fibers [13] provided the chance to investigate the new applications of fiber nonlinearities. Spectral broadening and the generation of new frequency components are the intrinsic features of nonlinear optics. Specifically, when an intense beam propagates inside a fiber, it introduces changes in the refractive index through the Kerr nonlinearity which imposes a nonlinear phase shift or self-phase modulation on the wave itself (SPM) [14]. This effect can be experienced by other waves co-existing inside the fiber as cross-phase modulation (XPM) [15]. It might also experience simultaneously group-velocity dispersion (GVD), which underlies the formation of optical solitons [16, 17]. Because of these novel characteristics of nonlinear optics, it is possible to produce an artificial white light (supercontinuum) with unique spectral properties and high brightness. Under such spectral broadening, an ultra short pulse propagating through a nonlinear medium experiences extreme spectral broadening.

In this thesis, a stable ultra-short pulsed fiber laser is demonstrated using a Bismuth oxide based erbium doped fiber. The SCG process with considerable flatness and low fluctuation is also investigated for different types of nonlinear fibers. This chapter is an introduction to all processes that are relevant to this thesis. The objective of this study and the outline of this thesis are also presented in this chapter.

1.2 MODE LOCKED LASER AND SUPERCONTINUUM

The required short laser pulses for continuum generation can be generated by mode locking technique. Such a train of pulses with constant phase relation between longitudinal lasing modes was demonstrated for the first time by applying acousto-optic modulator and using He-Ne laser in 1964 [18]. Thereafter, an all-fiber, unidirectional mode locked ring laser based on Nonlinear Polarization Rotation was implemented by Tamura et al. in 1992 [19]. Nowadays semiconductor saturable absorber mirrors (SESAMs) are well established for ultrafast solid state laser whereby its parameters can be engineered according to the laser design. Low noises, stable pulse train and shot to shot pulse amplitude stability are the main requirements for many applications of Mode locked lasers. This type of laser is being used in medical applications [20], telecommunication [21], microscopy, spectroscopy [22], optical coherence tomography [23, 24], optical metrology [25] and micromachining applications [26].

Simultaneously, a SCG extending from 400 nm to 700 nm was first reported in bulk BK7 glass in 1970 by using a 5 mJ picosecond pulses at 530 nm [27]. However, the SCG in bulk materials is a complex process involving an intricate coupling between spatial and temporal effects while the SCG process in optical fibers involves purely temporal dynamical process with the transverse mode characteristics determined only by waveguide properties [28]. In 1976, a SC spectrum with a 180 nm bandwidth was initially reported by launching 10 ns pulses with peak power of 1 kW from a dye laser into a 20 m long fiber [29].

It has been proven that nonlinear effects such as SRS, SPM, XPM and FWM contribute to SC generation in nonlinear fibers [30]. Depending on the dispersion characteristic of the fiber and the specification of the pump, some nonlinear effects in the experiment are more significant for the amount of SC broadening [31]. In fact, the pumping wavelength and its deviation from ZDW have a significant effect on the shape of the resulting SC spectrum [31]. The mechanism of SCG which involves several nonlinear effects is mainly dominated by soliton dynamics for when a femtosecond pulse train is used, while for wider input pulses, nonlinear Kerr effect and FWM are considered to be the dominant processes. Here it is pertinent to mention that higher-order dispersions play a significant role in modulating and controlling the spectrum in both the regimes.

The advent of Photonic Crystal Fibers (PCF) as a new class of optical waveguide in the late 1990s made it possible to support SCG owing to its flexible dispersion [32] and unique guidance properties as well as high nonlinearity [33]. SCG offers novel solutions in the field of coherent tomography [24], multiplex light sources for nonlinear spectroscopy [22], biomedical lasers [20] and atmospheric applications [34]. Some other applications of SC laser light are to realize a multi-wavelength source for Dense Wavelength Division Multiplexing (DWDM) optical communication [35], pulse compression[36], frequency metrology [37] and the generation of multiple carrier waves in optical communication systems.

1.3 MULTIPLE WAVELENGTH GENERATION

Multi-wavelength fiber lasers (MWFLs) have been advantageously utilized in spectroscopy applications, optical fiber sensors, optical component testing and in wavelength division multiplexed (WDM) systems [38-40]. To satisfy the bandwidth demand of future networks, multiplexing techniques that consist of merging several communications channels into one have been exploited [41]. One of the essential components is the creation of new low cost laser sources. There are many methods to generate multi-wavelength fiber lasers (MWFLs) such as using EDF as a gain media and immersing it in liquid nitrogen [42], using specially designed twin-core EDFs [43] and implementation of distributed feedback lasers (DFBLs). However DFBLs are sensitive to both temperature variations and back-reflections so that they have an adverse effect on output specifications, causing fluctuations in their output specifications [44]. Other systems are also not viable as they are neither well suited for practical applications nor very compact.

Recently, semiconductor optical amplifiers (SOA) have received much attention [45]. The advantage of using SOA is the possibility of multi-wavelength generation in any wavelength band where SOA is available [46].

As an alterative approach, a group of laser lines via multiwavelength Brillouin fiber lasers (MBFLs) can be generated from Brillouin Stokes as a seed signal and cascaded through SBS. To manipulate the narrow bandwidth of a nonlinear Brillouin gain in an optical fiber with a high power gain, MBFLs assisted by EDF or by semiconductor optical amplifiers are used. Thereby, a higher number of lines in comparison with MBFLs can be obtained in the optical comb. It is also possible to fabricate a MBFLs with a Raman amplifier to increase the number of Brillouin Stokes as reported in our previous work [47]. This design has a wider gain bandwidth and higher number of lines compared to its counterpart MBEFLs [48].

Alternatively, many comb-filter configurations have been proposed in accomplishing MWFLs such as Fabry-Perot and Mach Zehnder interferometers (MZI) [49], Fiber Bragg Gratings (FBG) [50] and fiber loop mirrors [51]. Among all available configurations, the polarization maintaining fiber loop mirror is one of the promising configurations as it is simple to fabricate, has a low fabrication cost and a low insertion loss in the setup as well as having the capability of creating a large number of comb lines at the output [52, 53]. In this thesis, the focus will be on the development of an MWFL using the principle of SC slicing through the use of wavelength selective filters.

1.4 SCOPE AND OBJECTIVE

Although the Bi-EDF exhibits a very high fiber nonlinearity and provides a broadband efficient amplification [54], further investigation is required in order for these applications to be commercially viable replacements to the currently utilized silica based EDFAs. In this thesis, various configurations on the continuous-wave and pulsed fiber lasers are proposed and demonstrated using the Bi-EDF to generate various seed signals for optical amplifiers and nonlinear applications.

Firstly, laser and amplification operation of Bi-EDF are investigated in the CW operating regime. In the next stage, the output of a tuneable Bi-EDFL is used as a seed signal for the measurement of the gain in EYDFA. By altering the length of Bi-

EDF in the cavity using an optical switch, the wavelength tuning range in this laser can be extended to larger than 100 nm.

In the next stage of the work, the required pulses for investigation of nonlinear effects are generated by a mode locked Bi-EDFL. The motivation behind such investigation is to improve the understanding of the physical, spectroscopical and optical properties of different glass hosts for generation of ultrashort pulses as well as applications in nonlinear optics.

In addition, the problems associated with higher dopant concentration as well as the effect of self-saturation are investigated and found to influence the noise, gain and efficiencies of the output signal. The goal of this section is to develop a near transform limited tuneable passively mode-locked Bi-EDFL. The pulse width from this seed should be continuously varied from 1.2 ps to less than 300 fs and amplified up to multi-kilowatt of peak powers. The optimized experimental configuration with the shortest and the most stable pulse train are then presented. The effect of pump power and spectral width on the Time-Bandwidth products (TBWP), pulse duration and output fluctuations in both commercially available EDF and Bi-EDF are investigated in the cavity. The optimized experimental configuration with the the lowest threshold and jitter are then presented. Following this, the performance of $\mathrm{Er}^{3+}/\mathrm{Yb}^{3+}$ double-clad fiber amplifier (DC-EYDFA) is investigated both theoretically and experimentally. In the theoretical analysis, we examine the effect of fiber length on the bandwidth of the gain spectra. In addition, the optimum fiber length is found to provide the highest and flattest possible gain in the 1545-1566 nm wavelength region. The effect of the wavelength on the performance of the DC-EYDF amplifier (DC–EYDFA) is theoretically analyzed and for both laser and amplifier configurations are experimentally demonstrated. A narrow linewidth and highly efficient tuneable BFL is constructed. Then, a master-oscillator power amplifier (MOPA) is utilized for both pulsed and CW regimes. The amplification of both ultra-narrow linewidth and ultrashort pulsed signals will also be studied to determine the detrimental effects of SPM, Raman gain and SBS on short pulse amplification as well as SBS on single-frequency amplification.

The new applications of the ultra short laser beam from a mode locked Bi-EDFL are then explored and the evolution of the SCG process at high powers is investigated. Finally, a multi-wavelength light source which incorporates the supercontinuum (SC) slicing technique and utilizes a tunable-spacing temperature sensitive loop mirror is proposed. The configurations of these two key components are investigated.

To meet the commercial expectation various aspects, such as reproducibility, production cost, and temperature sensitivity need to be improved. Pursuing this line of research, improvement of spectral spacing variation range is the next step. As a challenge, both efficient positive and negative spectral spacing detuning have been conducted [55]. By comparing conventional schemes and the proposed setup, the potential of achieving a substantial increase in the spectral spacing variation range and also in temperature sensitivity are studied. It will be also observed that multi-wavelength laser source with the spectral expansion from 950 nm to wavelengths beyond 2 μm is feasible using the presented configuration which cannot be generated by MBFLs [40, 48, 56-58].

1.5 METHODOLOGY OF RESEARCH

This research consists of two main parts, the first part is involved with the investigation of the theory of ultra-short pulse generation. It includes the physical basis of the proposed laser and the characterization of the required elements. Therefore one stage of the work is focused on: (a) improving a stable mode-locked fiber laser with wide tuneability in pulse duration (2 ps-130 fs) and (b) optimizing the experimental setup to yield the most stable near transform limited pulse train to be used in the second part of the research [59]. The mode locking is achieved using a slow and transmittance type of saturable absorber in the ring EDFL and the noise characteristic of the pulse fiber laser is thoroughly investigated in this work. As a result, the pulses with a repetition rate of 8.27 MHz and a peak power of 177.3 kW can be made feasible without using any intra-cavity or extra cavity compressor by pulsed seed signal amplification.

The second part of this work involves the investigation of the supercontinuum phenomenon in nonlinear fibers with considerable flatness and low fluctuation. Furthermore, the evaluation of spectral bandwidth at high powers is also probed [60].

Many laser schemes such as Brilluin and Brillouin–Raman Fiber Lasers based on (Bi-)EDF can be utilized to generate multi-wavelength, with a fixed channel spacing [48, 54, 56-58]. However, the homogeneous character of the erbium normally poses a major barrier to obtaining a stable multi-wavelength emission at room temperature. Other limitations include the wavelength region and unsatisfactory output stability of these lasers due to mode hopping [61]. In order to overcome stated problems, and considering all aforementioned limitations, the spectral slicing is used in this work.

There has been a great deal of resources and efforts put into development of tunable multi-wavelength sources. A discrete tuning in wavelength spacing allows a limited number of selectable wavelength spacings within a wide tuning range while a continuous tuning scheme enables fine spacing tuning within in a small tuning range [2,10,11].

In chapter six, the experimental demonstration of a temperature-sensitive interferometer based on multi-segment Polarization Maintaining Fiber Sagnac Loop Mirrors (PMF-FLM) is presented. It is constructed from a 3dB coupler and two segments of polarization maintaining fibers(PMF_1 and PMF_2)which are spliced at an offset rotation angle of 90° [55]. By exploiting the temperature dependent birefringence of the PMFs, the wavelength spacing can be continuously detuned. The wavelength spacing can be increased (positive detuned) by increasing the temperature of the PMF_2 (T_2) while the other segment is maintained at room temperature: Adversely, the wavelength spacing can be decreased (negative detuned) by increasing the temperature of PMF_1 (T_1) and maintain the temperature of the other segment (T_2) at room temperature. Consequently the wavelength spacing and tuning span can be easily configured by manipulating the PMF length parameters and temperature.

A comparison between the conventional setup [62] with experimental results, suggests that the proposed configuration can potentially achieve a substantial improvement (6.6 times more) in increasing the spectral spacing variation range and a considerable increment (337.6%) in temperature sensitivity.

1.6 THESIS OVERVIEW

This thesis is organized in seven chapters. The first chapter introduces the main topics such as nonlinear effects and multi-wavelength fiber lasers. This chapter also gives a brief historical review of supercontinuum generation (SCG) and mode locked fiber lasers.

In chapter two, the theory of nonlinear effects and fiber characteristics involved in continuum generation are described. Then, the pulse propagation in fiber and the specific pulse formation known as soliton are introduced. Finally, properties of Photonic Crystal Fiber (PCF) and Highly Nonlinear Fiber (HNLF) as tested fibers are presented.

In chapter three, a theoretical background about the fluorescence of Er^{3+} ions in glass hosts is presented briefly. Also, a description of optical glass host property, requirement and its influence on the optical amplifier and laser application is presented in detail. All the basic measurements needed for characterization of Bi-EDF and for the performance evaluation of bismuth glass host are discussed in this chapter. Using either PCF or Bi-EDF as the gain medium of BFL, new hybrid architecture is proposed to reduce the threshold power of the SBS effect as well as to increase the efficiency of the BFL. The FWM effect is then used to estimate nonlinear coefficient and refractive index coefficient of the Bi-EDF.

In chapter four, the performance of Er^{3+}/Yb^{3+} double-clad fiber amplifier (EYDFA) is investigated both experimentally and theoretically. To improve the gain and output power of the amplifier, a broadband FBG is used in the setup to allow a double-propagation of the test signal in the gain medium. In the theoretical analysis, we examine the effect of the fiber length on the bandwidth of the gain spectra and the optimum fiber length is found. A narrow linewidth, and highly efficient tuneable BFL which is amplified by EYDFA is also presented in this chapter. The linewidth specification of such narrow linewidth source is experimentally measured by the heterodyne beat technique and the result is compared with its Brillouin pump and tuneable Bi-EDF laser. Finally, the EYDFA is examined for ultrashort laser pulse amplification.

In chapter five, the theory of mode locking is reviewed and using the results of (Bi-)EDF discussed earlier in chapter four, a passive mode locked laser utilizing slow saturable absorber and nonlinear polarization rotation technique are proposed. Dispersion management and its effect on pulse shape are also reviewed in that chapter.

Chapter six focuses on the theory of SC initiation and evolution under different conditions. Subsequently, the experimental results are evaluated according to the presented theories. In this chapter, characteristic and experimental results of the proposed temperature sensitive filter are also presented when it is internally or externally used in the laser setup.

Finally, chapter seven summarizes all the results described in this thesis and outlines possible future work related to this topic. The copies of the selected published papers during the PhD in which the author was actively involved are also included in appendix A.

CHAPTER 2

LITERATURE REVIEW ON NONLINEAR EFFECTS

When an electric field is propagating through a medium, it induces a response that is dependent on the strength of the electric field. Short optical pulses and engineered nonlinear media is a powerful combination to generate new optical frequencies. As a physical phenomenon, supercontinuum generation (SCG) involves the whole catalog of classical nonlinear-optical effects, which add up to produce emission spectra, spanning over a couple of octaves. In the following subsections the nonlinear processes that are relevant to this thesis have been described in brief. Then, pulse propagation and its special case, solitonic waves, are described mathematically. Finally, the structures of photonic crystal fibers and highly nonlinear fibers which are suitable mediums for SCG and favorable gains for laser action are reviewed. For a more thorough description of nonlinear optics found in text books, see references [30, 63].

2.1 DISPERSION

Dispersion property of fiber plays an important role in pulse propagation. The performance of mode locked pulse laser is mainly determined by Kerr nonlinearity and dispersion of cavity. The most important types of dispersion are material dispersion, waveguide dispersion and polarization mode dispersion. In the presence of material dispersion, different frequency components experience different speed and it results in pulse temporal broadening. Shorter wavelengths confined in the core travel slower than longer wavelengths penetrated in the cladding because of the higher refractive index of core. Polarization mode dispersion is also of great importance when pulse broadening is caused by the difference in the refractive indices of two orthogonally polarized components of optical field.

Total dispersion is usually referred to the sum of material and waveguide dispersion of fiber. Chromatic dispersion in an optical fiber can be discussed in terms of the frequency dependence of the effective constant of propagation β around an optical carrier angular frequency $\omega_0$that is [64]:

$$\beta(\omega) = \sum_{m=1}^{+\infty} \frac{\beta_m (\omega - \omega_0)^m}{m!} = n(\omega)\frac{\omega}{c} = \frac{\beta_0}{0!} + \frac{\beta_1}{1!}(\omega - \omega_0) + \frac{\beta_2}{2!}(\omega - \omega_0)^2 + .. \frac{1}{m!}\frac{d^m\beta}{d\omega^m}\bigg|_{\omega=\omega_0}(\omega - \omega_0)^m \qquad (2.1)$$

More specifically, one has $\beta_l=n_g/c=1/V_g$ and $\beta_2 = \frac{1}{c}\left[2\frac{dn}{d\omega} + \omega\frac{d^2n}{d\omega^2}\right]$ where c, n and $n_g$are the effective refractive index, the light speed in vacuum and the group index respectively as well as v_g is the group velocity which is propagation speed of a pulse envelop in the fiber. Parameter β_1 represents the group delay per unit length of fiber while parameter β_2 is responsible for pulse broadening and is referred to as the group velocity dispersion (GVD). Hence β_2 represents the rate of variation of the group delay per unit length as a function of the radial frequency. This broadening effect is known as chromatic dispersion or group velocity dispersion (GVD).

Dispersion parameter (*D*) is also another term to describe GVD and is related to β_2 as:

$$D = \frac{d\beta_1}{d\lambda} = -\frac{2\pi c}{\lambda^2}\beta_2 \approx \frac{\lambda}{c}\frac{d^2 n}{d\lambda^2} \tag{2.2}$$

Higher order dispersion terms produce pulse distortion [65]. Parameters β_i are expressed in ps^{i}/km.

2.1.1 Normal and Anomalous Dispersion Regions

Frequency area that experiences $\beta_2>0$ is called normal dispersion region. In this regime, longer wavelengths travel faster than shorter ones. On the other hand, in the so-called *"anomalous region"*, where $\beta_2<0$, shorter wavelengths travels faster than longer ones. The frequency at which $\beta_2=0$ is known as Zero Dispersion Wavelength (ZDW). Higher order dispersions are relatively small for standard silica fibers. They become important when operating at wavelengths located near ZDW, where the amount of β_2 is comparable to higher order β.

2.1.2 Temporal Broadening Imposed by Dispersion

To understand the effect of dispersion on an initially unchirped pulse, the amount of temporal broadening imposed by dispersion for a Gaussian pulse can be expressed as follows [64]:

$$T_1(z) = T_0[1 + (z / L_D)^2]^{1/2} \tag{2.3}$$

where T_0 is FWHM of the pulse, z is propagation distance and L_D is dispersion distance which is equal to $T_0^2/|\beta_2|$.

The GVD of a medium broadens the pulse regardless of its sign. However, the sign of the GVD determines the type of imposed chirp on the pulse. In the normal dispersion region, $\beta_2>0$, the instantaneous frequency increases towards the trailing edge of the pulse and longer wavelengths (red) components travel faster than blue-shifted ones. In other words normal dispersion, for example, leads to a lower group velocity of higher-frequency components.

The condition is reversed in anomalous region. The effect of chirp and temporal broadening by GVD of one sign can be compensated by pulse propagation in mediums with the opposite sign as in the case of pulse propagation in the cavity comprising elements with opposite signs of dispersion.

2.2 NONLINEAR EFFECTS

For a nonlinear material, the electric polarization ***P*** induced by electric dipoles and its i-th component is described by:

$$\boldsymbol{P} = \epsilon_0 \chi^{(1)}.\boldsymbol{E} + \epsilon_0 \chi^{(2)}:\boldsymbol{EE} + \epsilon_0 \chi^{(3)}:\boldsymbol{EEE} + \cdots$$

$$P_i = \varepsilon_0 \sum_{j=1}^{3} \chi_{ij}^{(1)} E_j + \varepsilon_0 \sum_{j=1}^{3} \sum_{k=1}^{3} \chi_{ijk}^{(2)} E_j E_k + \varepsilon_0 \sum_{j=1}^{3} \sum_{k=1}^{3} \sum_{l=1}^{3} \chi_{ijk}^{(2)} E_j E_k E_l + \ldots \quad (2.4)$$

where ε_0 is the vacuum permittivity and $\chi^{(n)}$ is the n-th order susceptibility and a tensor of rank $n+1$. The second-order susceptibility is responsible for such nonlinear effects as second-harmonic generation (SHG) and sum-frequency generation (SFG). However, it is nonzero only for media that lack an inversion symmetry at the molecular level. The lowest-order nonlinear effects in optical fibers normally originate from the third order susceptibility $\chi^{(3)}$ and higher-order effects will not be considered here. Nonetheless, the electric-quadrupole, magnetic-dipole moments, defects and color centers inside the fiber core can generate second-order nonlinear effects (second-harmonic generation) under certain conditions.

Generally, in optical fibers most of the nonlinear effects originate from the intensity dependence of the refractive index that leads to a large number of interesting nonlinear effects. When an intense wave propagates inside a fiber, it introduces changes in the refractive index through the third-order Kerr nonlinear processes ,which imposes a nonlinear phase shift on the wave itself (self-phase modulation-SPM) [63].

Similarly, such induced nonlinear refractive-index changes can also be experienced by other waves co-existing inside the fiber via cross-phase modulation (XPM) effect. Frequency-degenerate Kerr-effect-type phenomena constitute one of the most important class of third-order nonlinear processes in fibers [66]. Such effects lie at the heart of optical compressors, mode-locked femtosecond lasers, and numerous photonic devices, where one laser pulse is used to switch, modulate, or gate another laser pulse.

If three or four waves co-propagate along a fiber, the Kerr nonlinearity can be induced by their beatings. In phase matching condition, the wave fronts of two waves catch those of the other two therefore, in-phase anharmonic motion of electrons can transfer energy from two photons to the other two (four-wave mixing or more accurately four-photon scattering) [64, 67-69].Third-order nonlinear processes include a vast variety of four-wave mixing processes, which are extensively used for frequency conversion (e.g third-harmonic generation-THG) and nonlinear spectroscopy. Unless additional steps are taken to achieve phase matching, the nonlinear processes such as THG and FWM are not efficient in ordinary optical fibers.

If optical frequencies of the four interacting photons are far below the resonant frequencies of bound electrons in silica fibers (ultra-violet region), electrons return to their original equilibrium states after interactions, resulting in an elastic scattering process [70]. Apart from the off-resonant interaction with bound electrons, optical waves can also interact with molecules inside silica fibers. In particular, when the beating between two optical waves resonates with a vibration mode of molecules, a high-frequency photon can be scattered into a low-frequency photon and an optical phonon. This phenomenon is referred to as stimulated Raman scattering (SRS) [63, 64, 71]. Similarly, optical waves can also resonantly interact with acoustic phonons and lead to stimulated Brillioun scattering (SBS) [72, 73].

In summary all the third-order nonlinear effects in optical fibers can arise due to the interaction of light waves with phonons such as SRS and SBS or optical Kerr effect. Depending upon the type of input signal, the Kerr-nonlinearity manifests itself in SPM, XPM and FWM.

2.2.1 Longitudinal and Transverse Optical Kerr Effect

In 1989, Kean and his co-workers reported that sub-picosecond pulses without any physical Saturable Absorber(SA) in the setup [74]. This mode locking approach is called Kerr-Lens Mode-locking (KLM).

For high intensities, optical fields can cause anharmonic motion of bound electrons in silica and thus induce polarization which depends on the magnitude of the optical intensity. As the secondary waves emitted by the driven bound electrons are directly proportional to the induced polarization, the total optical field experiences an extra phase retardation manifested as an intensity-dependent change in the refractive index. This phenomenon is referred to as the optical Kerr effect and is the dominant nonlinear effect inside optical fibers [63, 72]. Accordingly, the refractive index (n) increases proportionally with the radially dependent intensity $I(r,t) = |A|^2$ as:

$$n(r,t) = n_L + n_2 |A|^2 \tag{2.5}$$

$$n_2 = \frac{3}{8n_L} Re\left(\chi^{(3)}\right) \tag{2.6}$$

where n_L is the linear part of refractive index and n_2 for linearly polarized optical field as given in Equation (2.6), is nonlinear coefficient related to the third order susceptibility $(\chi^{(3)})$. This radial form of intensity $I(r,t)$, affects the longitudinal and transverse propagation of the beam. A self-focusing lens is produced in the transverse propagation direction due to the retardation of the most intense part of the plane wave front, while the self-phase modulation (SPM) which results in frequency chirps is produced in the longitudinal direction after the retardation of the central part of the optical pulse. The Kerr effect is also a self-induced effect in which the phase velocity of the wave depends on the wave's own intensity [74]. A hard or a soft aperture in the cavity allows the transmission of a more intense self-focused beam to provide the modulating electric field.

At very high intensity levels, the nonlinear response ($n(I)$) of any material begins to saturate and is given by $\tilde{n}(I) = n + n_2 f(I)$ where $f(I)$ is some known function of the mode intensity. For silica fibers, saturation of the Kerr nonlinearity occurs at quite high intensity levels.

However, if fibers are made with other materials (such as chalcogenide glasses) or if a silica fiber is doped with other nonlinear materials (such as an organic dye), the nonlinear response can saturate at practical intensity levels.

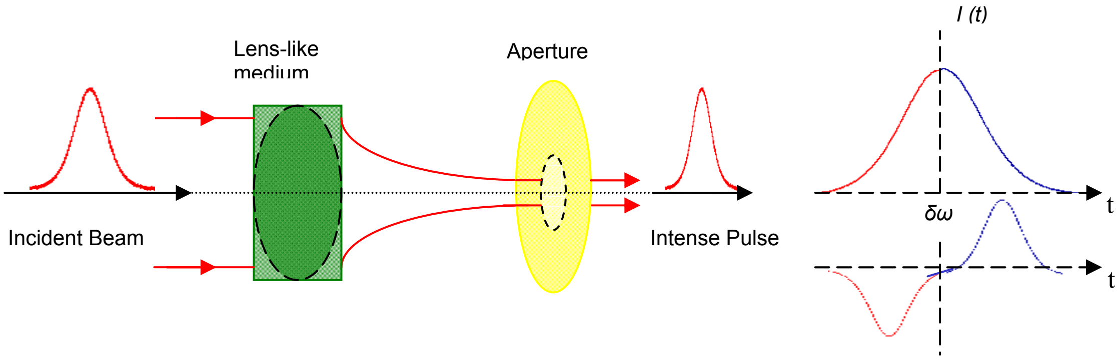

Figure 2. 1: Kerr lens mode locking effect at an intracavity focus in the gain medium. The induced lens focuses the beam in the transverse propagation due to high radial dependent intensity effect I(r), while frequency chirps in the longitudinal direction are caused by temporal dependent intensity effect I(t) which results in red shifted of the leading part and blue shifted of the trailing part.

The advantage of KLM operation is that when all of the bandwidth is engaged, it produces pulse durations less than 5 fs with broad tunability [75, 76]. However, the resonator design and the mode coupling between pump and laser modes are difficult tasks. The pulse formation is not generally self-starting and long-term stable operation is difficult to achieve in KLM lasers [77, 78].

Therefore, the challenge for alternative solutions for compact ultrafast lasers is to find better self-starting methods while avoiding any compromises to the pulse durations. Both nonlinear polarization rotation (or Polarization Additive Pulse Mode-locking PAPM), and the Nonlinear Amplifying Loop Mirror (NALM) rely on the Kerr effect in a length of optical fiber in conjunction with polarizers to cause artificial saturable absorber action [79].

2.2.1.1 Self Phase Modulation (SPM)

The Self Phase Modulation (SPM) effect is caused by an optical Kerr effect in fiber. During a pulse propagation through the fiber, different parts of the pulse acquire different values of the nonlinear phase shift φ_{NL}^{SPM} and experience different frequency shifts $\Delta\omega(t)$ which is given by:

$$\Delta\omega(t) = -\frac{d}{dt}\Delta\varphi_{NL}^{SPM} = -\frac{d}{dt}(2\pi L n_2 |A|^2/\lambda) \quad (2.7)$$

where L is the transmission distance and $|A|^2 = I(t)$ is the intensity of the pulse in the time domain. This nonlinear phase shift broadens the spectra. The nonlinear length term is then defined as the length at which the maximum nonlinear phase shift reaches the unity:

$$L_{NL} = (2\pi n_2 I_0/\lambda)^{-1} = \left(\gamma P_p\right)^{-1} = \left(P_p n_2 \omega / c A_{eff}\right)^{-1} \quad (2.8)$$

where P_p is the peak power of input pulse, A_{eff} is the effective area of propagating mode, ω is the frequency of carrier of optical field and γ is nonlinear coefficient which represents the strength of the nonlinear effect of the fiber which is also an important parameter in SPM and supercontinuum generation(SCG).

For silica based fibers ($n_2 > 0$), SPM always shifts the front (leading) edge of the pulse to the red spectral region (downshift in frequency), and the trailing edge of the pulse to the blue spectral region (upshift in frequency) [80]. This means that an initially unchirped pulse spectrally broadens and gets negatively chirped as within $L_{NL}$the pulse spectrally broadens by a factor of two. Note that, when acting alone, SPM does not change the temporal intensity profile of the pulse.

When positive GVD is then applied to this chirped pulse, the red spectral components are delayed in time with respect to the blue ones. If the right amount of dispersion is applied, the sign of the pulse chirp can be reversed to negative. Therefore the blue spectral components shift in time to the front pulse edge, while the red spectral components move to the trailing edge. When nonlinearity is applied again, it shifts the frequency of the front edge to the red spectral region and up-shifts the frequency of the trailing edge. This means that the blue front edge becomes green again, the red trailing edge also becomes green, and the pulse spectrum bandwidth narrows to its original width.

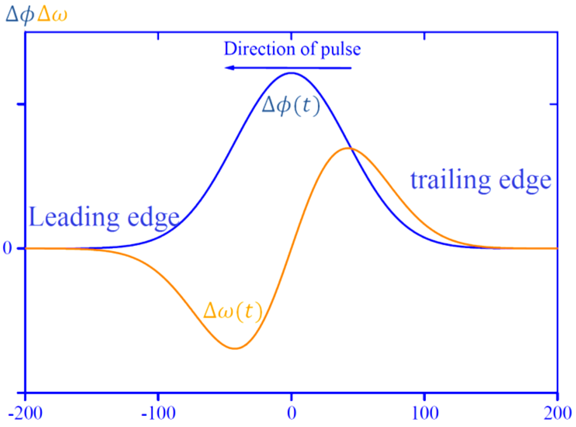

Figure 2. 2: SPM effect on phase and frequency.

In reality, the effects of dispersion and SPM act simultaneously. In soliton pulse, the pulse spectral and temporal widths stay constant with distance while the only net effect is a phase shift of 0.5 rad per dispersion length of propagation which is constant within the entire pulse [81]. However, dispersion of the fiber can intensify SPM broadening effect or distort considerably the spectral and temporal characteristics of the signal. SPM is vital in the generation of ultrashort pulses. This is because the effect gives rise to a broadening of the spectral bandwidth by distributing the intracavity power over more oscillating modes.

2.2.1.2 Cross Phase Modulation (XPM)

Several waves co-propagating in an optical fiber can interact and cause additional nonlinear effects. Induced nonlinear refractive-index changes can also be experienced by other waves co-existing inside the fiber by $\Delta n_{NL} = n_2(|A_1|^2 + b|A_2|^2)$ where $|A_i|^2$ is optical intensity of co-propagating field [30, 63]. Cross-phase modulation (XPM) is referred to the nonlinear phase shift of an optical field induced by another field with different wavelength or polarization state. This intensity dependent nonlinear phase shift depends on the intensity of each wave and is always accompanied by SPM as expressed below:

$$\varphi_i^{NL}(t) = 2\pi L n_2 {\lambda_i}^{-1}(|A_i|^2 + 2|A_j|^2) \tag{2.9}$$

where λ_i is center wavelength of co-propagating field.

As can be seen, the first term shows that XPM is always accompanied by SPM and the magnitude of second term (XPM) is twice that of SMP term. This means that for a given intensity, XPM is twice as effective as SPM.

Note that fiber dispersion affects the XPM considerably.When two or more soliton pulses propagate in the fiber at the same wavelength, the tail from one soliton pulse may overlap and interact with the other pulses due to XPM. This leads to frequency shifts in interacting solitons. The signs of the frequency shifts for the two solitons are opposites of each other. Through fiber dispersion, the frequency changes result in the changes of the soliton group velocities. However the strength of the interaction can be considered to be negligible when the separation is 4 to 5 times greater than the soliton pulse width.

The character of the interaction depends on the mutual optical phases of the solitons: when they are the same, the solitons attract each other; when they are out of phase, the solitons repel each other; when the phase difference is $\pi/2$, the solitons do not interact.XPM leads to inter-channel crosstalk in WDM systems and can produce amplitude and timing jitters [82], while SPM-induced spectral broadening can degrade the performance of a lightwave system. However, a laser pulse can be utilized to switch, modulate, compress or gate other laser pulse [83], and to realize to realize many nonlinear devices such as wavelength converters [84], through SPM and XPM. To overcome high switching power in those devices, an Bi-EDF with strong nonlinearity is required. Furthermore, when dual-wavelength continuous wave signals with wavelength separation of $\Delta\lambda$ are launched into a fiber, SPM acts on the beat envelope to create sidebands in the frequency domain. Then, the optical power ratio of the input signals (I_0) to the first sideband (I_1) is related to the nonlinear phase shift ϕ_{SPM} and can be employed, as we have demonstrated in section 3.14 to deduce the value of refractive index coefficient, n_2 of fibers [64, 85, 86].

2.2.2 Four-Wave Mixing (FWM)

FWM is a nonlinear recombination process of light waves at different frequencies in which photons from one or more waves (pump or signal) are annihilated and new photons at different frequencies (know as an idler) are generated while the net energy and momentum are conserved [64, 66].

In a general type of FWM, three laser fields with frequencies ω_1, ω_2, and ω_3 generate a fourth field with a frequency $\omega_{FWM} = \omega_1 \pm \omega_2 \pm \omega_3$. When all three laser fields have the same frequency, i.e. $\omega_{FWM} = 3\omega$, we have a third-harmonic generation (THG). However, in degenerate four-wave mixing (DFWM) process all fields have the same frequency ($\omega_{DFWM} = \omega = \omega - \omega + \omega$) and the FWM field is the phase-conjugate of one of the laser fields, referred to as optical phase conjugation. For $\omega_{CARS} = \omega_1 - \omega_2 + \omega_3$ in coherent anti-Stokes Raman scattering (CARS), $\omega_1 - \omega_2$ is tuned to a resonance with a Raman-active mode of the nonlinear medium [64].

Figure 2.3 illustrates how FWM can lead to generation of a number of extra frequencies $\omega_{ijk} = \omega_i + \omega_j - \omega_k$, from the interaction between light at three incident frequencies [87].

As shown in Figure 2.3, in the degenerate case when two waves at frequency ω_1 and ω_2 are mixed, sidebands located at $\omega_{112} = 2\omega_1 - \omega_2$ and $\omega_{221} = 2\omega_2 - \omega_1$ are symmetrically generated, which must be phase-matched along the fiber length for optimum efficiency. If a weak signal at ω_3 is also launched into the fiber with the pump, the signal is amplified while a new idler wave at ω_4 is generated [64, 72]. Similarly, three co-propagating waves will create nine new sidebands at ω_{ijk}. Both the signal and idler waves experience gain through parametric amplification [66, 88-90].

These sidebands travel along with original waves and will grow at the expense of signal-strength depletion. In general, for N wavelengths launched into fiber, the number of generated mixed products is $M = N^2(N-1)/2$ [91].

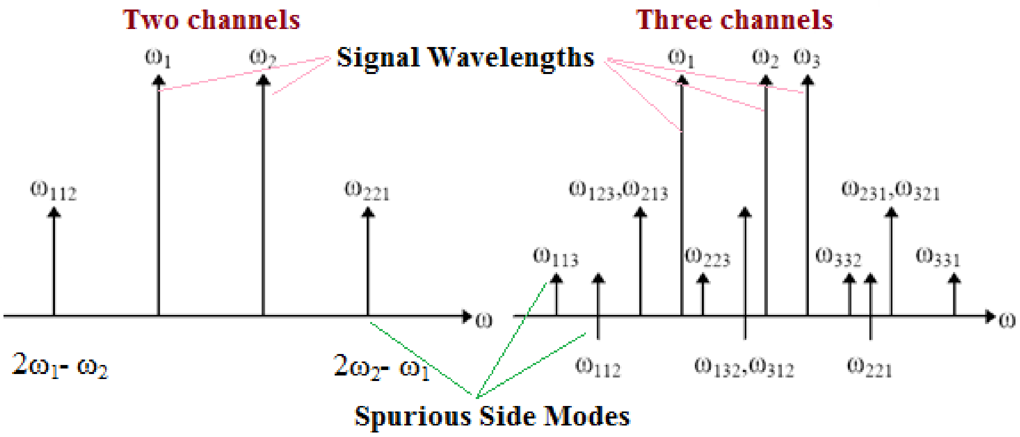

Figure 2. 3: The new frequencies generated through FWM (left) in partially degenerate case and (right) in non-degenerate case [87, 92].

In general, for non-degenerate cases of $\omega_{FWM} = \omega_1 + \omega_2 + \omega_3$, the pump and FWM fields ($\boldsymbol{E_j}$)are given by:

$$\boldsymbol{E_j} = \boldsymbol{A_j} exp\left[i\left(k_j r - \omega_j t\right)\right] + c.c. \qquad (2.10)$$

where $k_j = k_j' + i\alpha_j$ are the complex wave vectors of the pumps (j=1, 2, 3) and FWM field (j=4) while c.c. refers for complex conjugate. With no depletion of the pump fields, the slowly varying envelope approximation (SVEA) equations give the following expression for the envelope of the FWM field:

$$[A_{FWM}(z)]_i = -\frac{2\pi\omega^2{}_{FWM}}{k_{FWM}c^2}\chi^{(3)}(\omega_{FWM};\omega_1,\omega_2,\omega_3) \tag{2.11}$$

$$\times A_{1j}A_{2k}A_{3l}exp\left(\frac{i\Delta kz}{2}\right)\times exp\,(-\alpha_{FWM}z)\frac{\sin\left(\frac{\Delta kz}{2}\right)}{\frac{\Delta kz}{2}}z$$

where $[\mathrm{A_{FWM}(z)}]_\mathrm{i}$ is the i-th Cartesian component of the FWM field, k_j is the wave vector of the j-th optical wave defined before and Δk is the z-component of the wave-vector mismatch which is given by:

$$\Delta k = k_1' + k_2' + k_3' - k_{FWM}' + i(\alpha_1 + \alpha_2 + \alpha_3 - \alpha_{FWM}) \tag{2.12}$$

For a high efficiency-frequency conversion, the matching of the frequencies as well as of the wave vectors are the key requirements, as can be seen from Equation (2.11). The latter requirement is often referred to as phase matching [63] and FWM process occurs significantly only if the phase mismatch nearly vanishes.

It is worth noting that, main features of FWM can be understood by considering the third-order polarization term ($\mathrm{P_{FWM}^{(3)}}$):

$$\boldsymbol{P}_{FWM}^{(3)} = \chi^{(3)}(\omega_{FWM}\,;\,\omega_1,\omega_2,\omega_3)\,\vdots\,\boldsymbol{E}\,(\omega_1)\boldsymbol{E}\,(\omega_2)\boldsymbol{E}\,(\omega_3) \tag{2.13}$$

The induced nonlinear polarization consists of a large number of terms involving the products of three electric fields. By considering four linearly polarized optical waves propagating in the same direction with the propagation constant of

$k_j = n_j \omega_j / c$ and by substituting Equation (2.10) in Equation (2.13), P_4 in third-order polarization term as a function of $\theta_{\mp}$ can be expressed as:

$$\begin{aligned} \mathrm{P}_4 = \frac{3\varepsilon_0}{4} \chi^3 (\left|E_1\right|^2 + 2(\left|E_1\right|^2 + \left|E_2\right|^2 + \left|E_3\right|^2) E_4 \\ + 2E_1 E_2 E_3 \exp(i\theta_+) + 2E_1 E_2 E_3 \exp(i\theta_-) + \ldots) \end{aligned} \tag{2.14}$$

where phases are defined as $\theta_{\mp} = (k_1 + k_2 \mp k_3 - k_4)z - (\omega_1 + \omega_2 \mp \omega_3 - \omega_4)\, t$. The terms proportional to E_4 in P_4 are responsible for the SPM and XPM effects. The remaining terms which represent new waves at different frequencies are responsible for FWM effect. Hence, FWM efficiency depends on the phase matching between E_4 and P_4 which is governed by $\theta_{\mp}$.

The term which includes θ_+ is responsible for a condition that three photons converting energy to a single photon at frequency $\omega_4 = \omega_1 + \omega_2 + \omega_3$ and when $\omega_1 = \omega_2$ or in THG. On the meantime, the term with θ_- is responsible for creating two photons simultaneously (i.e. $\omega_1 + \omega_2 = \omega_3 + \omega_4$). The generated light utilizes optical power from the original frequencies provided that phase matching condition is satisfied. This condition is difficult to satisfy for θ_+ while the requirements for θ_- is often useful for optical fibers in the degenerate cases. In such cases, preexisting nonlinear sideband polarizations at $\omega_3 = 2\omega_1 - \omega_2$ and $\omega_4 = 2\omega_2 - \omega_1$ can experience gain in the presence of the two pump fields (i.e. $\omega_1$and ω_2). Meanwhile, sidebands will contain the phase and amplitude information of the pumps.

It is important to note that for θ_-, the phase matching conditions are given by $n_3\omega_3 + n_4\omega_4 - n_1\omega_1 - n_2\omega_2 = 0$ or $\Delta k = k_3 + k_4 - k_1 - k_2 = 0$ [92, 93], and the gain associated with FWM under these conditions, is more than twice the peak gain in SRS [69]. For a loss coefficient of α in a medium length of *L,* the sideband intensities ($I_{\omega_k}; k = 3{,}4$) are related to the pump intensities ($I_{\omega_i}, I_{\omega_j}$) through [94]:

$$I_{\omega_k} \propto (n_2\, L_{eff}/\lambda_m)^2 I_{\omega_i}(I_{\omega_j})^2 \eta exp(-\alpha L) \tag{2.15}$$

$$\eta_{FWM} = \frac{\alpha^2}{\Delta\beta^2+\alpha^2}\left[1 + \frac{4e^{-\alpha L} sin^2(\Delta\beta L/2)}{(1-e^{-\alpha L})^2}\right] \tag{2.16}$$

where L_{eff} is given by $L_{eff} = (1 - exp(-\alpha L))/\alpha$ and λ_m is defined as $\lambda_m = 4\pi c/(\omega_2 + \omega_1)$. In Equation (2.16), phase mismatch ($\Delta\beta$) is related to chromatic dispersion of D ($ps.nm^{-1}.km^{-1}$) by:

$$\Delta\beta(\omega_3, \omega_4) \approx 2\pi c\lambda_m^{-2}\,(\lambda 1 - \lambda 2)^2 [D(\lambda_m) \pm \frac{(\lambda 1 - \lambda 2)}{2} \left.\frac{dD}{d\lambda}\right|_{\lambda_m}] \tag{2.17}$$

The plus sign in this expression is used for ω_3 while the minus sign is utilized for ω_4. The coherence length also is defined as:

$$L_{coh} = 2\pi/\Delta\beta = \lambda^2/\Delta\lambda \tag{2.18}$$

where $\Delta\beta$ is the maximum wave-vector mismatch that can be tolerated. From Equation 2.16, we can infer that if the fiber length is less than the coherence length, significant FWM occurs.When the input wave is degenerated, the power of all channels is the same (P_0) and two input waves are close and near to a zero dispersion wavelength [95]. FWM signal power can be also written as [96]:

$$P_{FWM} = \frac{\eta}{9} d^2 \gamma^2 P_0^3 \exp(-\alpha L).L_{eff}^2 \tag{2.19}$$

where d is the degeneracy factor (d=3 and 6 in case of two and three channels respectively). Thus FWM effect can produce sidebands whose amplitudes and frequencies depend on the nonlinear parameter (γ).

In the degenerated case, the FWM efficiency η can be expressed as $\eta = \left[n_2(\Delta\lambda)^2 D/A_{eff}\right]^2$ where D is the dispersion parameter [97]. By employing only two laser diodes with a tuning range of less than 1 nm and a proper length of the fiber, the dispersion parameter of the fiber can also be measured via $D = c/\lambda^2 \Delta f^2 L$. In this equation, λ is the operating wavelength and Δf is the channel spacing in which P_{FWM} reaches to its first minimum [98]. Hence FWM effect provides the basic technology for measuring the nonlinearity, chromatic dispersion and nonlinear coefficient as we will employ it in chapters 3 [99].

The FWM efficiency depends on fiber dispersion, which varies with wavelength. The signal waves and the generated waves usually have different group velocities. This destroys the phase matching of the interacting waves and lowers the efficiency at which power is transferred to the newly generated frequencies. In general, the fields involved in FWM can be phase matched by using the waveguide regime in which the phase mismatch related to the material dispersion,is compensated by the waveguide dispersion component. These fields can be also phase matched by choosing appropriate angles between the wave vectors of the laser fields and nonlinear signal.

This phenomenon is employed for many applications in optical systems such as optical parametric oscillator (OPO) [100], phase conjugate optics, and the measurement of atomic energy structures and decay rates [101]. It can be also used in wavelength converters to achieve broad bandwidth supercontinuum [72, 102, 103].

To achieve a broad bandwidth supercontinuum with high conversion efficiency, chromatic dispersion variation in the longitudinal direction of the fiber should be minimized and polarization states of the pump and signals must be coincided. Additional consideration must be given to coherence length as well [99].

Indeed, low dispersion especially around ZDW of the fiber, results in better phase matching condition. On the contrary, it is difficult to maintain phase matching over a long length of fiber [104].

It is shown that for a uniform ZDW along the fiber, the phase matching condition is fulfilled when the ZDW of a fiber is at the centre of the spectrum of all interacting wavelengths [102]. In SCG high nonlinear fiber and PCFs with pumping near ZDW have been used to generate new frequency components resulting from SRS and FWM processes. These fibers have a high nonlinear coefficient and thus only a short fiber segment is sufficient to introduce significant FWM effects.

Besides the advantage of shorter fiber requirements, the use of PCFs would allow the operation of these nonlinear devices at relatively low peak powers in the wavelength regime outside that of possible using conventional fibers. This is because PCFs, unlike dispersion-shifted fibers (DSFs), can have zero dispersion wavelength ranging from 550-1550 nm. Therefore, the FWM-based devices focus on applying highly nonlinear fibers such as DSFs [102], dispersion compensating fibers and the photonic crystal fibers [105, 106].

2.2.3 Inelastic Scattering Effects in Optical Fibers

Two other main nonlinear processes that prevent high peak power obtained in optical fiber are Stimulated Brillouin Scattering (SBS) and Stimulated Raman Scattering (SRS). Both of these phenomena are related to vibrational excitation modes of silica and the transfer energy from the optical field to the nonlinear medium (inelastic).

In the Brillouin case, coherent phonons give rise to a macroscopic wave in the fiber, while in Raman scattering with optical incoherent phonons no macroscopic wave is generated.

Different dispersion relations of acoustic and optical phonons lead to differences between SBS and SRS. First, the SBS threshold power is a few miliwatts mainly in the backward direction whereas SRS can occur in the both directions with the SRS threshold power of roughly at the level of 1 W [107].

In addition, optical phonons are much more energetic than acoustical phonons and as a result, SRS produces a larger downshift of the optical frequency in comparison to the SBS.

Depending on the core composition, the scattered light with respect to the incident light is downshifted in frequency by about 10-20 GHz for SBS but by about 10–15 THz for SRS. In other words, a pump wave at 1064 nm (1550 nm) leads to the largest Raman gain at a signal wavelength of 1116 nm (1660 nm).Other difference is that the Brillouin-gain spectrum bandwidth is about 50-100 MHz [108] which is very narrow when comparing with the Raman-gain spectrum which extends up to 40 THz with a FWHM of about 5 THz [2, 71]. Meanwhile, the maximum gain coefficient g_R

for SRS in silica fibers is approximately $6\times10^{-13}\ m/W$ (at 1550 nm) which is much smaller than the peak value of the gain coefficient for SBS ($6\times10^{-11}\ m/W$) [3].

Finally for the Brillouin case, the bandwidth is related inversely to the decay time of acoustic phonons (~100 ns) while, response time in SRS is related to the optical phonon lifetime. It is important to note that fused silica exhibits a rich variety of vibration modes, dominated by the symmetric stretching motion of the bridging oxygen atom in the Si-O-Si bond [109]. Thus random Si-O-Si bond networks inside silica glass inhomogeneously broaden vibration modes, resulting in an effective phonon lifetime of about 30 fs [110, 111].

2.2.3.1 Stimulated Raman Scattering (SRS)

Vibrations or rotations of molecules, electronic motions in atoms or collective excitations of matter can interact with light, shifting its frequency through an inelastic scattering process by frequency of Ω due to Raman-active motions.The rather weak process of spontaneous Raman scattering can be turned into a highly efficient stimulated Raman scattering (SRS) in an intense field [70]. In this situation, frequency-shifted photons and pump laser photons act coherently to resonantly drive molecular motions, leading to the amplification of the Raman-shifted signal (SRS). In the SRS regime, Raman-active modes of a material act as optical modulators, forcing the driving laser field to oscillate at new frequencies.

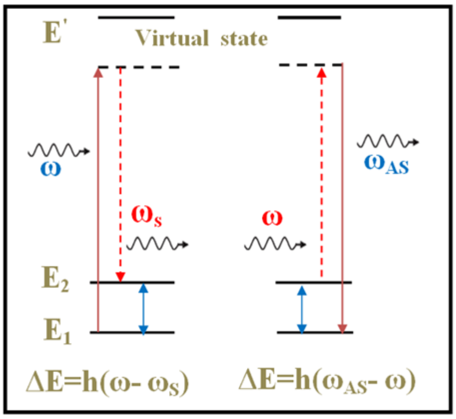

Figure 2. 4: Schematic of the energy levels of a molecule involved during SRS.

As shown in Figure 2.4 Raman Stokes scattering consists of a transition from the ground state E_1 to the final state E_2 by means of a virtual intermediate level associated with excited state $E'=h\omega+E_1$, where the system spontaneously decays to the final vibrational state state E_2 and a Stokes photon whose frequency is $v_s=(E'-E_2)/h$ is emitted with an optical phonon with the resonant frequency of $v=(E_2-E_1)/h$ remained, where h is the Plank's constant.

However, level E_2 in fact is a band of energy rather than a discrete line. Raman anti-Stokes scattering entails a transition from band E_2 to level E_1. The anti-Stokes lines with higher frequencies are typically much weaker than the Stokes lines because of thermal equilibrium [70].

The conservation of energy ($\omega_p=\omega_s+\omega$) requires that $2\omega_p \rightarrow \omega_{as}+\omega_{st}$ where ω_p, ω_{st} denote the frequency of the incident pump photon and less efficient anti-Stokes wave respectively.

Once the Raman pump and signal are presented, Raman amplification takes place. It should also be noted that the Raman gain response is much faster than the response time of the EDFA which is of the order of milliseconds.

2.2.3.2 Theory of Raman amplifiers

Nonlinear polarization vectors at the Raman Stokes (ω_s)and Raman pump frequencies (ω_p) are proportional to products of the Raman Stokes and Raman pump fields which are given by $P_{NL}^{\omega s} = \left|E_2^{\omega p}\right|^2 E_1^{\omega s}$ and $P_{NL}^{\omega p} = \left|E_2^{\omega s}\right|^2 E_1^{\omega p}$ respectively [112]. By neglecting the action of the Stokes field on the pump and assuming copolarized fields in CW forward pumping scheme $P_p(z) = P_p^0 \exp{(-\alpha_p z)}$, the Stokes signal power $P_s(L)$ and intensity $I_s(L)$ at the output of a Raman-active medium are given by [72]:

$$I_s(L) = I_s(0)\, exp\big(g_R I_0 L_{eff} - \alpha_s L\big) \tag{2.20}$$

$$P_s(L) = \bar{P}_0\, exp[\, g_R(\omega_s) I_0 L_{eff} - \alpha_s L] \tag{2.21}$$

where the pump absorption restricts the nonlinear interaction length to L_{eff} :

$$L_{eff} = \frac{1}{\alpha_p}[1 - exp\big(\alpha_p L\big)] \tag{2.22}$$

and P_P^0 (I_0) is the input pump power (intensity) at *z=0* :

$$\bar{P}_0 = \sqrt{2\pi}h\omega_s \left[I_0 L_{eff} \left|\left(\left.\frac{\partial^2 g_R}{\partial\omega^2}\right|_{\omega=\omega_s}\right)\right|\right]^{-1/2} \tag{2.23}$$

Here, α_p and α_{st} are the losses at the frequencies of the pump and Stokes fields respectively whereas g_R is the Raman gain efficiency within a length of L and related to the imaginary part of $\chi^{(3)}$ [66].The gain of amplifier G_A and small-signal gain (g_0) can be also obtained by:

$$G_A = \frac{P_{S-ON}}{P_{S-OFF}} = \exp(g_R \frac{P_P^0}{A_{eff}} L_{eff}) = \exp(g_0 L) \tag{2.24}$$

$$g_0 = g_R (\frac{P_P^0}{A_{eff}})(\frac{L_{eff}}{L}) \approx \frac{g_R P_P^0}{A_{eff} L \alpha_P} \tag{2.25}$$

where $P_{S\text{-}OFF}$ is defined by setting $g_R=0$ in Equation (2.24). This equation indicates that G_A for $\alpha_p L \gg 1$ is the fiber-length independent.

In practice, undoped fibers can be used to amplify any signal as long as $\omega_p - \omega_s$ lies within the bandwidth of the Raman gain spectrum. The Raman gain bandwidth can be extended to more than 100 nm by using multiple Raman pump sources with various frequencies.

The normalized gain profile and Raman gain bandwidth are nearly identical for an un-polarized pump near 1425 nm. Some fibers and their key parameters related to the SBS process are listed in table 2.1 (e.g. dispersion compensation fiber with a high germanium content, dispersion shifted high capacity transmission fiber with reduced dispersion slope, non-dispersion shifted fiber and Pure-silica fiber without germanium). These fibers are marked respectively with DCF, TWRS, 5D and Pure-silica in Figure 2.5.

In contrast, Raman-gain efficiency, defined by $\gamma_R \cong g_R(\upsilon)/S_{eff}$ can be very different for various fibers, since the modal field profile depend on the fiber refractive-index profile [113]. Figure 2.5 depicts that DCF in Raman amplification can be eight times more efficient than SMF due to the sufficient smaller core diameter.

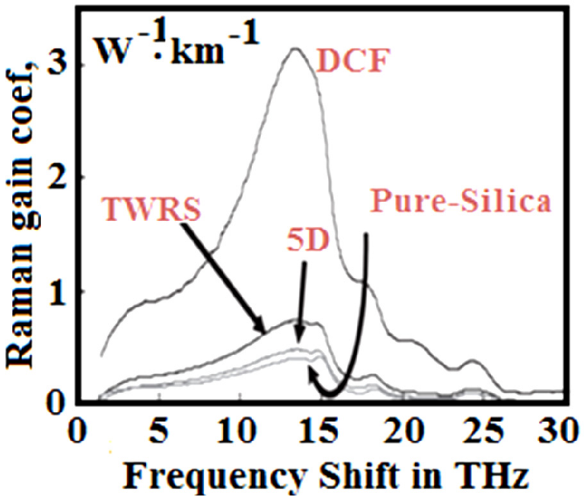

Figure 2. 5: Raman gain coefficient measured in DCF with a high germanium content, TWRS, non-dispersion shifted fiber (5D)and a fiber without germanium (Pure-silica) with a 1510 nm pump wavelength [108].

There are special DCFs with increased Raman gain, resulting from a higher doping level of germania. It is important to note that, if the pump wavelength is polarized, the Raman gain is polarization-dependent.

Table 2. 1: Comparison between the parameters of several types of fibers used in this work. It is to be noted here that the Raman gain coefficient around frequency shift decreases with increasing fluorine concentration.

Fiber	**(Second)Peak** *Shift* [*THz*]	g_R $(WKm)^{-1}$	λ_{pump} *nm*	**α (1550 nm)** *dB/km*	S_{eff} μm^2
SMF	13.2	0.34	1511	0.208	85
NZDSF	13.2	0.58	1511	0.214	52-73
DCF	13.1	3.04	1511	0.447	23
HNLF(PCF)	13	6.5	UV-IR	0.49	3
Phosphate-doped	40 (13)	1(0.5)	1370	0.24-0.7	-
Tellurite-based fiber	21(13)	55 (38)	1460	20.4	103
Fluorine-doped	13	< SMF	1452	0.19	90

However, the gain nearly vanishes when the pump and the signal are orthogonally polarized [108]. The Raman critical power is defined as that value of the input power at which the pump and the (unseeded) Stokes powers at the fiber output have the same value [114]:

$$P_{critical} \approx C S_{eff} K (g_R L_{eff})^{-1} \qquad \begin{array}{ll} C=16 & \text{Forward SRS} \\ C=20 & \text{Backward SRS} \end{array} \tag{2.26}$$

where S_{eff} is the effective mode area of the pump field and K is a factor which takes into account the pump and signal states of polarization ($K=1$ and 2 for polarized and un-polarized light respectively). Critical power $P_{Critical}$ is an useful criterion to estimate the maximum power which is able to propagate in the fiber without nonlinear scattering loss. This equation shows that $P_{Critical}$ for HNLFs [115] and holey fibers are much lower than single mode fibers due to their small S_{eff} and their extremely large Raman gains [63, 115].

When the Raman gain exceeds 70 dB, substantial power is transferred to a Stokes wave, even if there is no Stokes input to the fiber. In our experiments, it was observed that low order Stokes is generated firstly and higher-order Stokes waves are generated through cascaded SRS rapidly after arriving at the threshold for higher order Stokes. A process, in which SRS can transfer energy of high-frequency components of an ultrashort pulse to its low-frequency components, is the so called Raman induced frequency shift (RIFS) [116]. Chirped-pulse amplification (CPA) and the use of special fiber designs can suppress Raman scattering by attenuating the Raman-shifted wavelength component. There are two other ways of increasing the pump power without generating SRS. The first is to use a shorter amplifier with a higher dopant concentration and the second is to increase the effective mode area. Nevertheless SRS is one of the most important nonlinear effects for SCG.

2.2.3.3 Stimulated Brillouin Scattering (SRS)

Spontaneous Brillouin Scattering occurs when a fraction of the light wave travelling through the medium is scattered by the acoustic noise originating from thermal noise. The scattered light interferes with the forward propagating light to create a power-induced index modulation of the medium through the Kerr effect. This index modulation scatters the incoming light through Bragg reflection. Brillouin scattering occurs when the light is diffracted backward on this moving grating, giving rise to frequency shifted Stokes and anti-Stokes components. This process can be stimulated when the interferences of the laser light and the Stokes wave reinforce the acoustic wave through electrostriction. This scattering process is referred to as Stimulated Brillouin Scattering (SBS) that was discovered in 1922 and first observed in 1972 [1, 64]. As shown in Figure 2.6, the scattered light undergoes a Doppler frequency shift because of the Doppler shift associated with the grating moving at the acoustic velocity.

The energy and momentum during this event are conserved. The frequencies and wave vectors of the pump, scattered, and acoustic fields are related together as shown in Figure 2.6, where $\omega_p(\boldsymbol{k_p})$ and $\omega_s(\boldsymbol{k_s})$ are the frequencies (wave vectors) of the pump and Stokes waves, respectively.

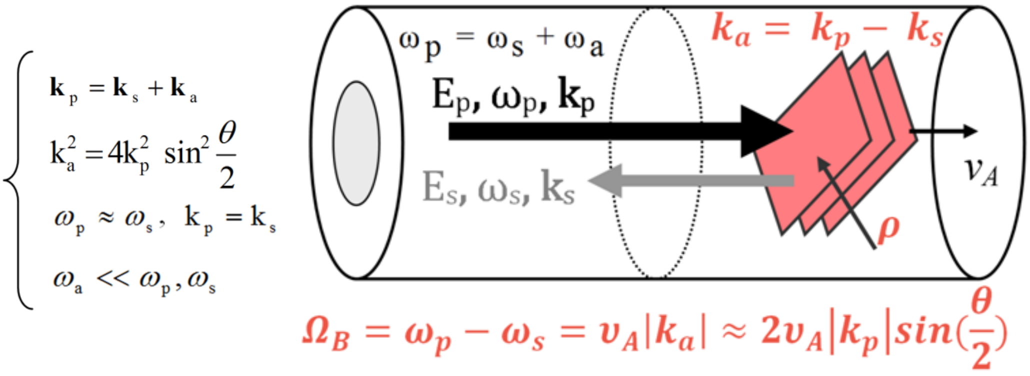

Figure 2. 6: Schematic diagram of the SBS process in an optical fiber. $\omega_p(\boldsymbol{k_p})$ and $\omega_s(\boldsymbol{k_s})$

The frequency (Ω_B) and the wave vector ($\boldsymbol{k_a}$) of the acoustic wave satisfy the standard dispersion relation while v_A is the speed of sound in the medium and θ is the angle between the pump and Stokes fields. According to the wave number and frequency relation (i.e. $\boldsymbol{k_a}=\omega_a/\nu_a$, $\boldsymbol{k_p}=\omega_p/\nu_p$) in a single-mode fiber, the relevant θ values are 0 and π. Hence, SBS occurs only in the backward direction with the Brillouin shift given by $\nu_B=\Omega_B/2\pi=(2nv_A)/\lambda_p$ where n is the modal index or refractive index of fiber core at the pump wavelength of λ_p [72, 117].

Since scattering occurs in the backwards direction and due to the fact that acoustic phonons have much low energies, the frequency shift in Brillouin scattering is found to be very small [118]. If the acoustic waves decay as $exp(-t/\tau_B)$ with an acoustic phonon lifetime of τ_B (≈100 ns) then the Brillouin gain spectrum $g_B(\nu)$ with a Lorentzian spectral shape and the peak value of the Brillouin gain coefficient (at $\nu=\nu_B$) can be determined by [64, 119]:

$$g_B(\nu) = \frac{\left(\frac{\Delta\nu_B}{2}\right)^2}{(\nu-\nu_B)^2+\left(\frac{\Delta\nu_B}{2}\right)^2} g_B(\nu_B) \tag{2.27}$$

$$g_B(\nu_B) = \frac{2\pi n^7 p_{12}^2}{c\lambda_p^2 \rho_0 \upsilon_A \Delta\nu_B} \qquad (2.28)$$

where $\Delta\nu_B=(\pi\tau_B)^{-1}$ is the 3dB spectral bandwidth, p_{12} is the longitudinal electro-optic coefficient, ρ_0 is the density of the material and *c* is the velocity of light in the fiber.

Both the Brillouin shift ν_B and $\Delta\nu_B$ can vary from fiber to fiber because of the presence of dopants in the fiber core [120]. In optical fiber communication systems, the smaller value of the spectral width source contributes to a smaller material dispersion and a better condition in optical communication [30, 121, 122]. The linewidth of the Brillouin Stokes $\Delta\upsilon_{\mathrm{BS}}$ is proportional to the Brillouin pump linewidth $\Delta\upsilon_{\mathrm{p}}$ as shown theoretically [123]:

$$\Delta\upsilon_{\mathrm{BS}} = \Delta\upsilon_{\mathrm{p}}\left(1 - \frac{\pi\ l\Delta\upsilon_B}{\mathrm{c\ Ln}(R)}\right) \qquad (2.29)$$

where $\Delta\upsilon_B$ is the Brillouin gain bandwidth, *l* is the fiber length, and *R* is the coupling ratio. Therefore, a narrow linewidth pump is used to generate a narrow linewidth BFL. On the other hand, with a broad bandwidth pump, the effective Brillouin gain coefficient is decreased by a factor of $\Delta\nu_B/\Delta\nu_p$. For pulses with a central wavelength of 1.5 μm, and a abroad bandwidth of $\Delta\lambda_p$>7 nm ($\Delta\nu_p$>1.4 THz) the effective Brillouin gain coefficient is reduced by a factor of 10^6 hence SBS is not observed in this condition (in chapter 5).

Equation (2.30) is one of the approaches to define SBS critical power ($P^{p}_{critical}$) in optical fibers [107]. It is based on the condition in which the reflected Stokes optical power at the beginning of the fiber in the absence of pump depletion equals the input pump power. Under the nondepletion assumption for a Lorentzian gain shape, $P^{p}_{critical}$ is given by [124]:

$$P^{p}_{critical} = \frac{21 S_{eff} K}{L_{eff}\, g_B(\upsilon_B)} \frac{\Delta\nu_p + \Delta\nu_B}{\Delta\nu_B} \approx \frac{21 S_{eff} K}{L_{eff} g_B|_{max}} \tag{2.30}$$

K=1 Polarized light
K=2 Unpolarized

where L_{eff} is the effective interaction length defined by Equation (2.22), g_B is the the Brillouin gain coefficient and S_{eff} is the fiber mode effective area. Here $\Delta\nu_B$ and $\Delta\nu_p$ are the Lorentztian linewidths of the SBS gain and of the pump, respectively.

As a result, $P^{p}_{critical}$ increases, when $\Delta\nu_p$ increases [3]. In other words SBS is mainly an issue in narrow-linewdth sources. The value of the factor 21 may change with the fiber length as discussed in [125]. However, $P^{p}_{critical}$ by a good approximation for $\Delta\nu_B >> \Delta\nu_p$ is summarized by $(21 S_{eff} K)/(g_B L_{eff})$ [107].

The Brillouin scattering method was employed for understanding of spectroscopic properties of materials [45, 47] and thin layers [44].The Brillouin fiber laser (BFL) also has many potential applications for microwave generation and Brillouin fiber-optic gyroscopes.

The key aspects of low threshold BFLs for most applications are the very high coherence, and the directional sensitivity of the Brillouin gain [126]. As reported in the literature and also in this thesis, a few Hz linewidth can also be generated and measured by BFLs [127-129].

In contrast, the requirement for sensor systems is reversed and the smaller spectral width contributes to a higher coherent noise [121, 130]. In this thesis, the SBS is used to generate a single and multi-wavelength laser sources that will be presented in the following chapters.

2.3 PULSE PROPAGATION IN FIBERS

The pulse propagation in fiber can be well described by a nonlinear Schrödinger equation (NLSE) derived from Maxwell's equations. By solving this equation, the evolution of a pulse in various fiber environments can be explained.

Assuming an electric field of *E(z,t)* ,with slowly varying envelop *A(z, T)* and propagation constant β at carrier frequency of ω_0:

$$E(z,T) = A(z,T).e^{-i(\beta z-\omega_0 t)} \tag{2.31}$$

NLSE is represented by following equation:

$$\frac{\partial A}{\partial z}+\frac{\alpha}{2}A-\sum_{k\geq 2} i^{k+1}\frac{\beta_k}{k!}\frac{\partial^k A}{\partial T^k}=i\gamma\left(1+\frac{i}{\omega_0}\frac{\partial}{\partial T}\right)\left[A(z,T)\int_{-\infty}^{+T}R(T')\,|\,A(z,T-T')\,|^2\,dT'\right] \tag{2. 32}$$

Here, α is the fiber loss, β_k are coefficients of a Taylor series expansion for a propagation constant around ω_0 and γ is nonlinearity of the fiber. The normalized nonlinear response function of the medium $R(T) = (1 - f_R)\delta T + f_R h_R(T)$ includes both instantaneous electronic (first term) and retarded molecular (vibrational Raman) contributions, where f_R=0.18 is fractional contribution of the delayed Raman response function $h_R(T)$, responsible for SPM, FWM and XPM effects [72]. Therefore, the left hand side of the equation represents the linear effects of the fiber in NLSE and the right hand of equation accounts for nonlinear effects.

This general equation can be simplified in some cases, especially when higher order dispersion coefficients, losses in the fiber and the delay response of the fiber can be ignored. A simplified form of the equation can be written as:

$$\frac{\partial A}{\partial z}+i\frac{\beta_2}{2}\frac{\partial^2 A}{\partial t^2}=i\gamma\,|A|^2\,A \tag{2.33}$$

where β_2 represents GVD effect and the term of $\gamma|A|^2A$ is responsible for SPM effect and temporal broadening effect.

Equation (2.33) assumes instantaneous nonlinear response as its premise. This equation describes accurately the propagation of pulses longer than 1 ps, that is roughly the nonlinear response time in silica.

For pulses shorter than 1 ps, the delayed response of $\chi^{(3)}$must usually be included, as described in Equation (2.32). Solutions of these equations lead to pulse forms known as “Soliton” provided that β_2 and γ are of opposite signs. It occurs when the phase modulation due to GVD and self phase modulation due to SMP cancel each other and result in stable pulse propagation.

2.3.1 Solitons

The effect of SPM can be canceled out with anomalous dispersion (negative β_2) and pulse propagates undistorted. This type of pulse is known as a “soliton”. Mathematically, by neglecting the higher order dispersion and attenuation as well as considering instantaneous medium response, Equation (2.33) can be rewritten in a normalized form as [72] :

$$i\frac{\partial A}{\partial z}=\frac{1}{2}sng(\beta_2)\frac{\partial^2 A}{\partial T^2}-N^2A\,|\,A\,|^2 \tag{2.34}$$

where sng refers to the sign function L_D and L_{NL} are dispersion and nonlinear length, respectively. For a given peak power and pulse width (T_0), the soliton order (N) is defined in Equation (2.35). In fact the soliton order provides a measure of the relative importance of dispersive vs. nonlinear effects. When $N^2 \ll 1$, dispersion is dominant while nonlinear effects are dominant for when $N^2 \gg 1$.

$$N=\sqrt{\frac{L_D}{L_{NL}}}=\sqrt{\frac{\gamma P_P {T_0}^2}{|\,\beta_2\,|}} \tag{2.35}$$

$$L_D=T_0^2/\,|\beta_2|^2 \quad \& \quad L_{NL}=(\gamma P_p)^{-1} \tag{2.36}$$

All these parameters are defined by input pulse parameters (P_P, T_0) and fiber parameters $(\beta_2\,, \gamma)$. In anomalous dispersion regime, i.e. $sng(\beta_2)=-1$, solitons can only exist if $N>0.5$. Equation (2.34) has analytical solution and a particular solution is solitary wave as follows:

$$A(T,Z) = N.\sec h\left(\frac{T}{T_0}\right).e^{iz/2} \tag{2.37}$$

2.3.1.1 Fundamental Soliton

For $N=1$ or the fundamental soliton, one can rewrite $L_D=L_{NL}$ to find a relationship between the soliton peak power (P_0) and the soliton pulse width (T_0):

$$P_0=A\lambda^3D/(0.3224\pi^2cn_2T_0^2) \tag{2. 38}$$

Here A is the fiber effective cross-section mode area, n_2 is the nonlinear refractive index and D is the fiber's dispersion. As long as the input parameters are not too far from the optimum values, the pulse readjusts itself (i.e. shaping into a soliton and shedding off nonsoliton components), while propagating nonlinearly [81].

For example, an unchirped pulse with pulse duration of τ and input power of P will be reshaped into a single soliton as long as $0.25P_0 \leq P \leq 2.25P_0$ [131].

Solitons are also resistant with respect to the perturbations of the pulse energy and of the fiber parameters along the transmission line. As long as the period of these perturbations (e.g. amplifier spacing) is much smaller than the soliton dispersion length (L_D),the soliton feels only the average values of these parameters. Otherwise soliton parameters follow adiabatically these changes and Equation (2.38) can be considered as a distance dependent equation. One can derive many important consequences from this equation in the following form [132]:

$$T(z)= const\left[\frac{D(z)A(z)}{P(z)T(z)}\right] =const[D(z)A(z)/E(z)] \tag{2.39}$$

As long as the whole expression in the bracket changes adiabatically with the distance, the adiabatic soliton propagation does not require that each of these parameters changes adiabatically with the distance.

Note that all soliton perturbations result in a loss of some part of the soliton energy, which is radiated into dispersive waves (DW) [133, 134].

2.3.1.2 Raman solitons

For integer values of $N>1$ in Equation (2.34), the energy of input pulse is divided among N fundamental solitons (also called "Raman solitons"). The peak power and pulse duration of these solitons are given by [135]:

$$P_k = \frac{(2N-2k+1)^2}{N^2} P_p \tag{2.40}$$

$$T_k = \frac{T_0}{2N-2k+1} \tag{2.41}$$

where k is the order of constituent soliton.

These solitons, which are higher order solitons, undergo a periodic evolution and recover their shapes at multiple soliton period of $z_0 = \pi L_D/2$, where dispersion length (L_D) is derived from Equation (2.36) and their group velocities are equal [136].However higher order solitons do not remain stable, and small perturbation due to SRS, self steepening and higher order dispersion can break up the degeneracy of the group velocities of N constituents leading to wave separation [137]. This phenomenon is known as soliton break-up or soliton decay effect.

2.3.2 Sources of errors during transmission and amplification

It should be noted that each amplifier contributes a noise with a spectral density (P_ν). This power per unit bandwidth is called the equipartition energy. At the end of a transmission line of length *L* when the amplification is equal to loss, the path-averaged spectral density (P_ν^{av}) is:

$$P_\nu^{av} = |\gamma| L n_{sp} h\nu (G-1)^2 [G ln^2 G]^{-1} \tag{2.42}$$

Here, *G* is the power gain of the amplifier, $h\nu$ is the photon energy, and n_{sp} is the spontaneous emission factor ($n_{sp} \geq 1$) that characterizes the quality of the amplifier. Equation (2.42) shows that the noise grows linearly with distance (number of amplifiers).

Moreover, for high gain amplifiers or long amplifier spacings the term in the bracket increases as well [81, 138]. To have the error probability less than 10^{-9} (10^{-15}) the ratio of the pulse energy to the equipartition energy should be, 100 (160).

There are two main sources of errors in soliton transmission systems: I) fluctuations of the pulse energies due to spontaneous emission noise of amplifiers and II) fluctuations in the pulse-arrival times (timing jitter) [133].

The adjacent pulse-to-pulse interactions can cause the pulses to shift in time which can be eliminated by spacing the solitons in time by more than 4 or 5 of their width. Another important source of the timing jitter is the spontaneous emission noise. Every time noise is added to the signal, it modulates the carrier frequencies of the solitons at random. The chromatic dispersion of the fiber then converts these frequency variations into a variation of the pulses arrival times via Gordon-Haus effect. The variance in the timing jitter produced by this effect is expressed as follow:

$$\sigma_{GH}^2 \approx 0.2 n_2 h \, \mathrm{n_{sp}} \left[\frac{(G-1)^2}{G ln^2 G}\right] \times \frac{|\gamma|}{A} \frac{D}{\tau} L^3 \tag{2.43}$$

The Gordon-Haus jitter limits the maximum bit rate and transmission distance.

2.3.3 Soliton Self-Frequency-Shift (SSFS)

Femtosecond solitons are affected by SRS when their spectrum bandwidths are comparable with Raman gain bandwidth. Generally SRS can be considered for two regimes of pump pulse bandwidth.

For narrow and moderate bandwidth pulses (i.e. $\tau > 1\, ps,\ \Delta\nu_p < 0.5\, THz$), the pump pulse is described by NLSE, but with an intensity dependent loss term to account for the energy transfer to the Stokes pulse.

However for pulses shorter than 1 ps the assumption of instantaneous nonlinear response is not accurate and the NLSE should then be modified to include the delayed response function $h_R(T)$ in Equation (2.32). In these cases the Raman gain profile is directly related to the delayed nonlinear response of the heavy nuclei. This delayed response is slower than the nearly instantaneous electronic response, which is responsible for elastic scattering [110, 111, 139, 140]. The likely significance of $h_R(T)$, can also be considered in the time domain by assessing whether the pulse duration is comparable to the response time of the medium, see Figure 2.7(a).

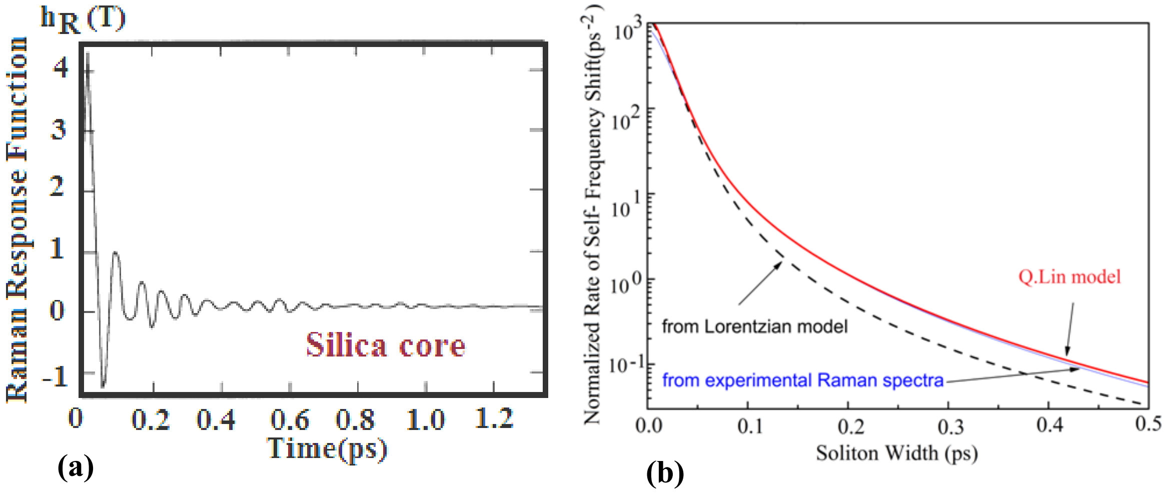

Figure 2. 7: (a) Variation of Raman response function $h_R(T)$ with time , arbitrary vertical unit [111] (b) SSFS rate as a function of soliton width [141].

For transform limited pulses of the order of 100 fs (e.g. $\Delta\nu_p \approx$ 4.4THz) , the long wavelength spectral components may experience significant Raman gain pumped by the short wavelength components in addition to the possible energy transfer to an independent Stokes pulse.

As it can be seen for a double clad amplifier in section 5.16, this intra-pulse SRS leads to a continuous center frequency shift to longer wavelengths. The intra-pulse SRS process is known as Soliton Self Frequency Shift (SSFS).

The magnitude of Raman induced SSFS using conventional single-Lorentzian model [110] is proportional to length of propagation, pulse width and central wavelength (i.e. $\Delta f \propto \lambda_0^2\, D(\lambda_0) L/T_0^4$) [72, 116]. For first order soliton, it can be expressed as:

$$|\Delta f| = 4T_R|\beta_2|L/(15\pi T_0^4) \tag{2.44}$$

where T_R is the Raman parameter related to the slope of Raman gain spectrum with the value of around 3 fs for silica fibers and $D(\lambda_0)$ is dispersion value at the wavelength λ_0. However, it is proven that the conventional model underestimates this rate by about 40% for pulse widths in the range of 100 to 500 fs ,as shown in Figure 2.7(b) [141].

It should be noted that solitons lose their power continuously due to intrinsic fiber losses and they reshape to compensate the losses. Therefore, their temporal width increases and the amount of SSFS is reduced. Moreover due to the wavelength offset the pump and Stokes pulses travel at different group velocities. The walk-off length determines the effective fiber length, over which the pump and signal can interact effectively with each other. This length is calculated by:

$$L_w = \frac{T}{\left|v_{g\_p}^{-1} - v_{g\_s}^{-1}\right|} = \frac{T}{\left|\beta_{1\_p} - \beta_{1\_s}\right|} = \frac{T}{\left|(\omega_p - \omega_s) \times \beta_2\right|} \tag{2.45}$$

Normally the walk-off length is longer than that given by Equation (2.45) and the interaction between the pump and Stokes pulses occurs over a distance of ~ 3× L_w [9]. For T=0.15 ps, and $|\omega_P - \omega_S|$=2π×13.2 THz, corresponding to the specifications of a directly amplified pulse train in section 5.16, the walk-off length can be significantly shorter than the length of the fiber (3 m). This can limit the efficiency of the Raman process. Eventually, SSFS ends when soliton spectrum does not overlap with Raman gain spectrum any longer.

2.4 NONLINEAR OPTICAL FIBERS

2.4.1 Photonic Crystal Fiber (PCF)

Photonic crystal fibers (PCF), also known as holey fibers or microstructure fibers are a new class of fibers with novel properties such as strict confinement of light in the core, high nonlinearity and manageable dispersion characteristics [142]. Some types of PCF provide endlessly single mode propagation with narrow core [143]. Narrow core PCFs are used in nonlinear optics such as SCG [144]. The extremely large mode areas of PCFs with their high numerical aperture however, are developed for high power delivery [145].

The most widely used type of PCF, known as "index guiding PCF" consists of a pure silica core surrounded by periodic arrays of air holes [146]. The air-hole arrays reduce the refractive index of the cladding and force light to be confined in the core. In actuality, the dopant materials in the core are not needed to increase the refractive index like in conventional fibers. In particular, holey fibers can have a much higher refractive index contrast than the refractive index contrast available in conventional fibers, and if this is combined with a small core size, the strong waveguide contribution to the dispersion can produce an overall anomalous dispersion at wavelengths smaller than 1.3 μm, where standard fibers have normal dispersion. Therefore holey fibers can support temporal solitons in new wavelength bands.

The guidance property and characteristics of these fibers are governed by the air hole size (d), distance between holes (Λ), and their ratio (d/Λ). In the limiting case when the operating wavelength (λ) is much greater than the pitch (Λ) of the structure, the effective refractive index of the cladding (n_{clad}) can be determined with a level of high accuracy by the weighted-mean of the refractive indices of glass and air in the structure.

(a)

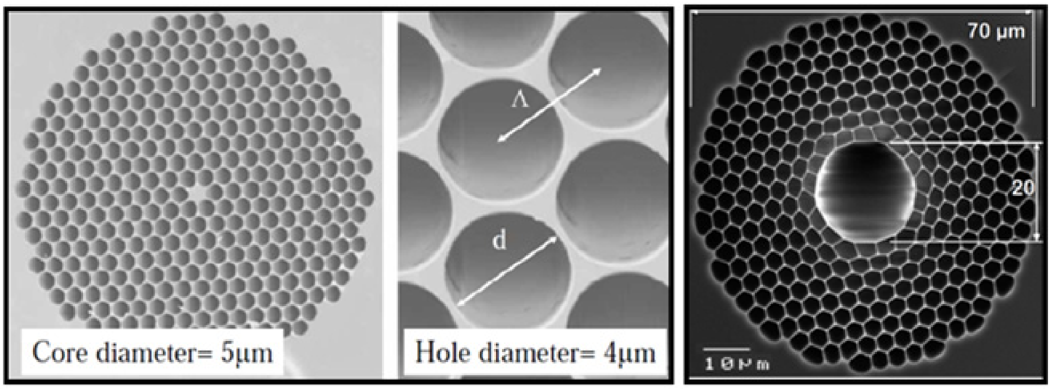

Figure 2. 8 (a): *left)* Scanning electron microscopy micrographs of a photonic-crystal fiber with silica core and *Right)* hollow core structure.

(b)

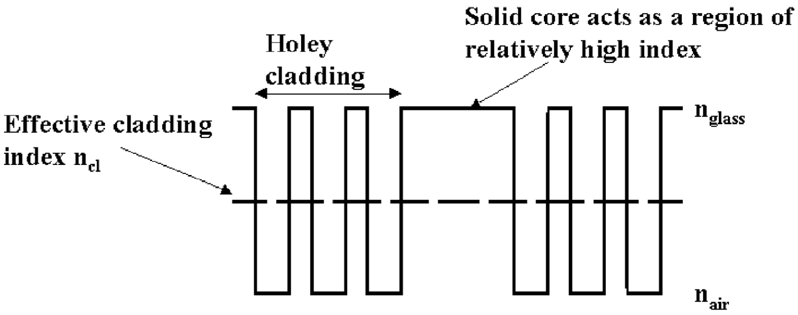

Figure 2.8(b): Refractive index profile of a holey fiber with silica core.

Some other kinds of holey fibers are fabricated with the hollow core providing low light loss and small nonlinearity as well as providing the option of filling the core with suitable gasses or liquids to change the fiber's characteristics [146, 147].

Figure 2.8(a) shows a cross section of a holey fiber with both silica solid and hollow core and Figure 2.8(b) shows the refractive index profile of the PCF with a solid core characteristic.

Another type of PCF is the photonic band-gap fibers (PBG) where light is confined through band-gap effect [148]. Photonic crystals with two or three dimensional periodicity can be seen as a generalization of Bragg mirrors, where the band-gap occurs for all directions of propagation either in the plane of periodicity or in the full space, respectively.

If a longitudinally extending central defect (e.g. a hole) is introduced in the infinite lattice, localised defect states for isolated frequencies within the bandgap can emerge. In this case reflection (at the defect boundary) is guaranteed for some frequency regardless of the refractive index of the material inside the defect [19].

Light propagation through air in a hollow fibre allows high power delivery as well as eliminates or greatly reduces the problems of nonlinearities, surface damage, and, when free-space coupling is used, end-reflections. Figure 2.9(a) and (b) illustrate the light propagation inside holey fibers and PBG, respectively.

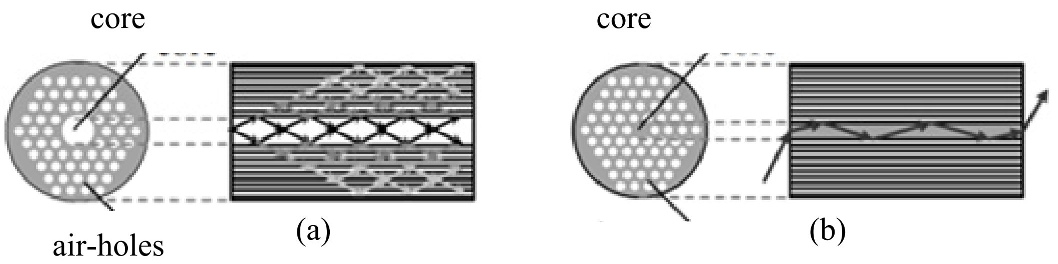

Figure 2. 9: Light propagation in (a) holey fiber (b) PBG.

2.4.1.1 Modal Behavior

The number of modes (N) supported by PCF scales by V-number. V-number depends on air hole diameter (d), pitch size (Λ) and λ as given in the following equation:

$$\sqrt{N} \approx V_{eff} = \frac{2\pi D(\Lambda)}{\lambda}\sqrt{n_{core}^{2} - n_{clad}^{2}(\lambda)} = \frac{2\pi D(\Lambda)}{\lambda} NA \tag{2.46}$$

where D is the effective core radius, n_{core} is the refractive index of silica and the effective cladding index (n_{clad}) is defined as the effective modal index of the lowest-order cladding mode. Unlike conventional fibres, the small dimensions of the microstructure make the effective cladding index a strong function of wavelength such that decreasing λ causes the effective cladding index to approach the core index. It is shown that for $V_{eff}<4.2$ only a fundamental mode propagates inside a holey fiber while V number for a standard single-mode fiber is 2.405 [149]. It makes holey fibers suitable for single mode operation in short wavelengths.

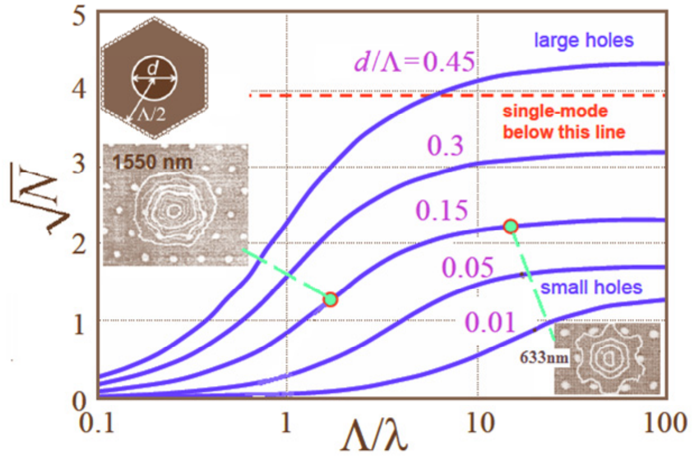

Figure 2. 10: Number of modes in a PCF versus frequency.

It has been also shown that a holey fiber with the hole-diameter to pitch of $d/\Lambda<0.48$ (low air fill fraction) can be single-moded regardless of the operating wavelength [148, 150]. Figure 2.10 shows the number of modes in a PCF as a function of Λ/λ (frequency) [143].

2.4.1.2 Nonlinearity

Figure 2.11 shows the effective mode area of holey fibers (A_{eff}) against pitch size at different ratios of d/Λ [151]. It is clear that the ability to confine light in a small A_{eff} renders such devices capable of generating strong nonlinear interactions. For instance, NL-1.5-670 with pure silica core from Blaze Photonics has a material-related nonlinear coefficient (n_2) of 2.5×10^{-20} m^2/W and a nonlinear coefficient ($\gamma=2\pi n_2/A_{eff}\lambda$) of 190 W^{-1}km^{-1}, which is 169 times greater than that of a standard silica fiber [151]. For a given value of d/Λ, the effective mode area (A_{eff}) increases as the pitch size (Λ) is raised except for small pitch size values. At low pitch size, A_{eff} increases again because of the fact that the fundamental mode is not confined in the core any longer and begins to leak into the cladding. Also, for a given value of pitch size, A_{eff} increases if d/Λ ratio increases.

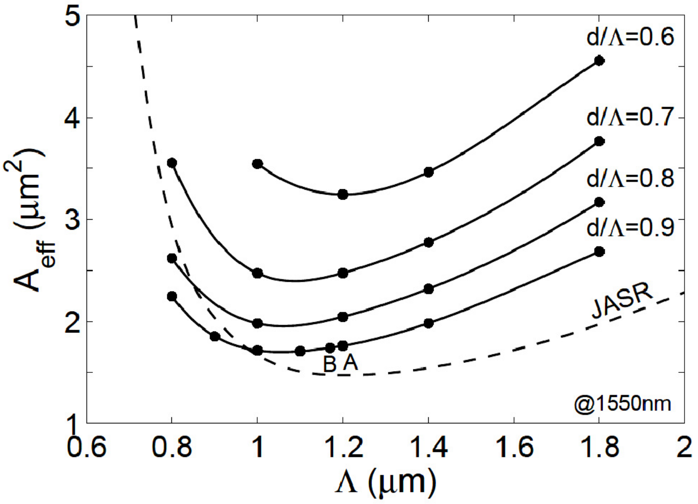

Figure 2. 11: Effective mode area of holey fibers vs. pitch size Λ [151].

2.4.1.3 Dispersion characteristic of PCF

It is possible to fabricate PCF with a shifted ZDW. Dispersion shifted PCF, dispersion compensating PCF and dispersion flattened PCF are the kinds of fibers with managed dispersion. The following equation implicitly shows that GVD is easily calculated from effective refractive index (or fiber structure) versus the wavelength by [152]:

$$GVD = (-\frac{c}{\lambda})(\frac{d^2 n_{eff}}{d\lambda^2}) \tag{2.47}$$

Figure 2.12(a) compares the dispersion profile of holey fibers with different hole sizes when the pitch size is fixed at $\Lambda=2\mu m$ [153]. As the hole size is increased, the magnitude of dispersion is enhanced. When the hole size is small, the GVD is dominated by material dispersion.

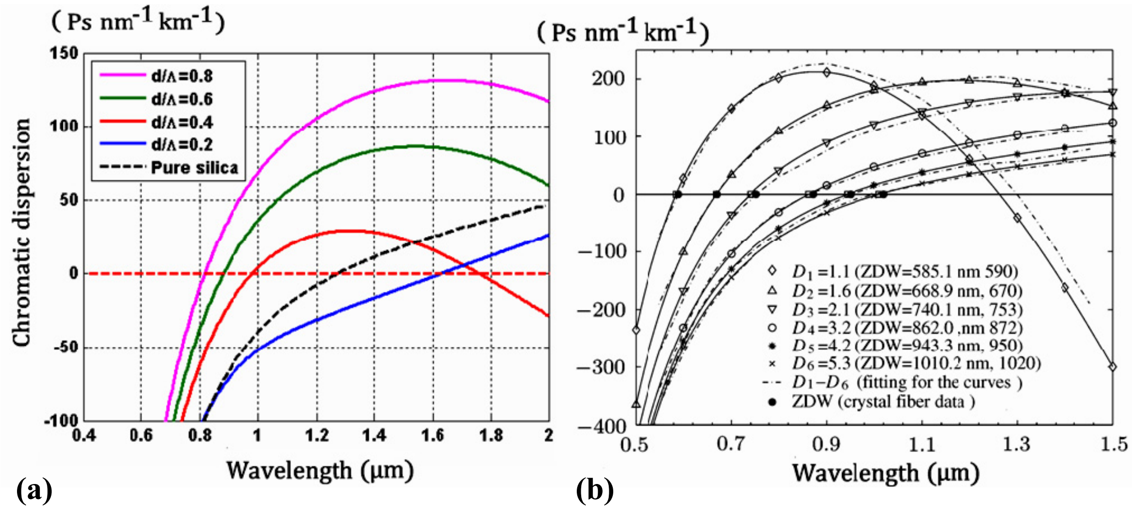

Figure 2. 12: (a) Dispersion profile for different values of d/Λ, with $\Lambda=2\mu m$ [153], (b) Dispersion profile of holey fibers with different core sizes. Comparison made to "Crystal-Fiber" [152].

A dispersion-shifted and flattened curvature are obtained for *d/Λ*=0.3 with a dispersion slope of 0.01 $ps/nm^2.km$. For large hole sizes, anomalous dispersion can be provided at a shorter wavelength, which is useful for soliton propagation employed in telecommunications.

Figure 2.12 (b) shows the theoretical and the experimental measurement of ZDW and dispersion profile in PCFs when *d/Λ* kept at a constant value [152]. As shown in the figure, by increasing core diameter (*D*), ZDW shifts to longer wavelength and the dispersion slope becomes flatter. On the other hand, shifting the ZDW to shorter wavelengths provides anomalous dispersion for a wider wavelength range, which is suitable for solitonic propagation application [154].

2.4.1.4 Loss and Attenuation

The main loss mechanisms in PCFs are scattering and absorption [145]. Rayleigh scattering is the dominant loss mechanism for the wavelength range of 500-1600 nm, where it is proportional to λ^{-4}. For shorter and longer wavelengths than this range, UV and IR absorption of silica become significant, respectively. In addition, peak absorption around 1400 nm due to OH contamination becomes considerable which can be reduced by altering core materials. For hollow core holey fibers, these losses are significantly lower than solid holey fibers. On the other hand the critical bend radius for solid core holey fibers is governed by $R_c \sim \Lambda^3/\lambda^2$ that limits critical bending radius for short wavelength compared to $R_c \sim \lambda$ for conventional SMF [149]. However, hollow PCFs are experimentally much less sensitive to bending loss [149]. Holey fibers also suffer from light leakages into the cladding layer, due to their small size and the fact that they are made from a single material for core and cladding. This loss is more critical for holey fibers with small core size and large air-hole sizes. For a fixed amount of d/Λ adding more air-hole rings around core area can reduce the loss due to leakage [149].

2.4.2 Highly Nonlinear Fibers

To achieve high contrast refractive indices in conventional fibers as well as to have highly nonlinear fibers (HNLFs) with small dispersion or dispersion slope, germanium doping in the core and fluorine doping in the cladding area has been used.

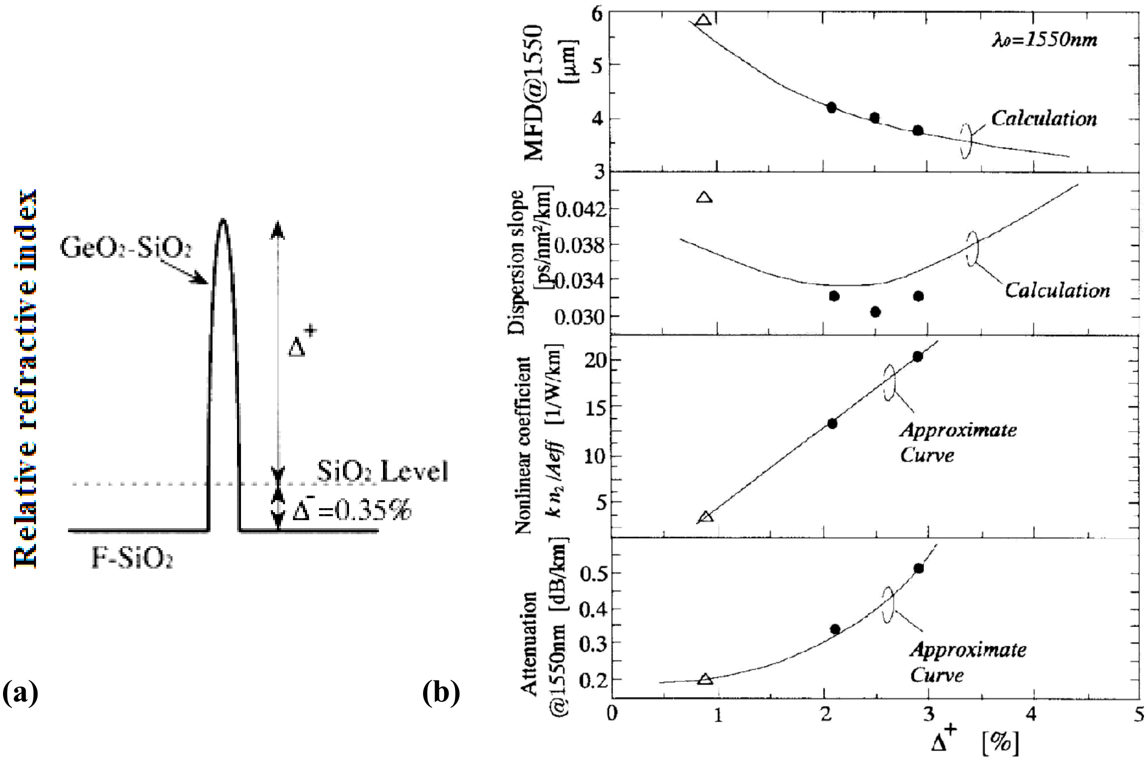

(a) (b)

Figure 2. 13: (a): Relative refractive index of HNL-DSF (b) HNL-DSF characteristics. Dots show experimental results [155].

Figure 2.13(a) shows a typical relative index of HNL-DSF where Δ^+ and Δ^- respectively indicate refractive index difference between the center of the core and the cladding from pure silica level. As reported by Okuno et al. [155] and shown in Figure 2.13(b), when Δ^+ becomes large, the mode field diameter decreases and the nonlinear refractive index, n_2 increases. At the same time, the loss increases rapidly.

2.5 SUPERCONTINUUM

Supercontinuum (SC) is an extremely broad spectrum of light generated by lasers in a nonlinear medium. This can be achieved by launching short pulses into fibers with high nonlinear characteristics. Single and dual core photonic crystal fiber (PCF) [156], highly nonlinear fiber (HNLF), tapered fiber, and even SMF have been used as nonlinear medium for SCG. Tapered PCFs with a zero dispersion wavelength (ZDW) decreasing along the fiber length, will enable SCG extension to shorter wavelengths [157].

Since nonlinear effects in fibers are a function of light intensity, pulse lasers exhibit a better nonlinear behavior in fibers. In fact, the pumping power level determines the degree of broadening of the continuum since different nonlinear effects participating in the formation of the continuum are involved at different pumping power levels. The mechanism of SCG is mainly dominated by SPM and soliton dynamics when a femtosecond pump is used, whereas in parametric FWM, SRS and nonlinear Kerr effect are considered to be the most important processes in the formation of SC for nano or picosecond pumping regimes. In both the cases, the presence of higher order dispersions (HODs) leads to the transfer of energy from soliton to non-solitonic radiation (dispersive waves). In fact the dispersion profile of a specific fiber can control the generation of DWs and HODs play a significant role in blue-component generation in the SC process. In this section, the different aspects of SCG in different dispersion regions are reviewed and effect of pumping power, pumping wavelength and pulse width are discussed.

2.5.1 Pumping in Anomalous Dispersion Region

For a pump wavelength in the anomalous dispersion regime, the SC originates from higher order solitons [158]. Input pulses with sufficiently high power corresponding to the *N-th* order soliton is initially compressed temporally due to SMP [72, 159]. This effect creates an initial broadening in pulse spectra. For more propagation, perturbation of this *N-th* order soliton by the SRS effect and higher order dispersion leads to the break up the pulse into several fundamental solitons (see Equation (2.40)) [158, 159]. These solitons have different temporal width. This difference also results in a change in group delay.

Due to the relatively wide spectrum of fundamental solitons they are amplified by the SRS effect and their central frequencies are shifted to longer wavelength (SSFS). As the solitons shifts to longer wavelengths, their group velocities are reduced and they are separated further and further from the main pulse. The amount of shift is weaker for broader solitons with smaller peak power. As seen in Equation (2.44), the narrowest soliton pulse experiences the longest shift in the frequency domain and the most delayed pulse in the time domain [160]. The spectra of narrower solitons then extend to the normal dispersion region, resulting the generation of DWs at the blue wavelength side. In other words, Raman solitons which are generated through fission process and perturbed by higher order dispersion, emit "*Non Solitonic Radition*" (NSR) in the form of DWs in the short wavelength region of the spectrum in the normal dispersion region. The wavelength of NSR is governed by phase matching condition as:

$$\sum_{m=2}^{\infty} \frac{\beta_m(\omega_s)}{m!} \Omega_d^m = \frac{1}{2} \gamma P_s \tag{2.48}$$

where P_s is the peak power of the Raman soliton formed after soliton fission, β_m is the GVD at the soliton central frequency and Ω_d is frequency difference between the DWs and the soliton. The frequency difference between the fundamental soliton and the frequency component which receives the most shaded energy can be approximated by:

$$\Omega_d \approx -\frac{3\beta_2}{\beta_3} + \frac{\gamma P_s \beta_3}{3{\beta_2}^2} \tag{2.49}$$

Further broadening and more peaks are generated by nonlinear interaction between Raman solitons and anti Stoke waves through FWM and XPM. In fact, XPM occurs when Raman soliton and NSR overlap temporally during propagation in fiber at different speeds if their group velocity mismatch is relatively small. This phenomenon is called "*soliton trapping*" in which Raman solitons trap and drag the NSR along. They then interact through XPM [72]. FWM also contribute to the generation of spectral components especially when pumping wavelengths lie near to ZDW, where phase matching condition is fulfilled for small value of GVD [144, 161, 162].

2.5.1.1 Effect of pulse specification in Anomalous pumping regime

Equation (2.35) shows clearly that an increase in the peak power of the ultrashort pulse launched into the fiber results in the enhancement of soliton order (N) in the pulse train. .In turn, the number of fundamental solitons generated through soliton fission and the number of stoke peaks at long wavelengths of spectrum are increased [72, 144]. On the other hand the relationship in Equation (2.41) indicates that it reduces the temporal width of these fundamental solitons. Consequently, the amount of SSFS related to those solitons increases (Equation 2.21). The overlap of solitons and resonant waves also becomes larger, which increases the magnitude of the anti stokes components.

As shown in Equation.(2.49) the location of stoke and anti stoke components depends on the input power [159]. From the phase matched condition, soliton waves and NSR components move in opposite directions as the power is increased. Additionally, a broader spectrum is generated but this comes at the expense of more gaps between the stokes and anti stokes components (see section 6.3) [144, 163]. A further increase in power actually makes the SC spectrum smoother due to the higher number of solitons present.

The pumping wavelength and its deviation from ZDW also have a significant effect on the shape of the SC spectrum [144, 159, 164]. For example, pumping near ZDW in the anomalous regime results in an increase in the *N* value due to the smaller amounts of GVD as seen in Equation.2.35. A higher soliton order simultaneously generates more stokes peaks in the spectrum.

It should be noted that in this case, the wavelengths of the resultant phase matched resonant waves lie near the ZDW in the normal dispersion region and fill the “gaps” around the pumping wavelength and make the spectrum smoother. Consequently, the overlap between solitons and resonant waves is greater, leading to an increase in the magnitude of the anti-stokes components. This greater overlap, nevertheless, lowers SSFS because of an increase in the loss of soliton energy. The generated spectrum is finally narrower than that of pumping wavelengths which are further away from the ZDW but it is flatter and smoother.

The relationship in Equation (2.35) indicates that the soliton order is proportional to the pulse width .Hence, a broader pulse leads to more solitons generated by the soliton fission process. These solitons have a broader width which reduces the amount of SSFS and overlap between the solitons and the dispersive waves. As a result, less number of anti stokes peaks in the short wavelengths are expected to be generated [159, 165].

2.5.2 Pumping in Normal Dispersion Region

SC generation in the normal region is different from that of the anomalous region because solitons cannot propagate in this region. The main nonlinear effects that contribute to spectrum broadening are SPM and SRS. Initially, the spectrum is symmetrically broadened by SPM at short distances [144, 159, 166]. By further propagation, the pulse experiences temporal broadening due to normal dispersion and this reduces the pulse peak power. It decreases the amount of spectrum broadening, especially when pumping wavelength lies deep in the normal region [167]. There is therefore a narrower continuum compared to the anomalous pumping scheme. At higher powers, new frequencies appear on the red side of spectrum, which results in an asymmetric broadening through Raman scattering [13]. In most cases in which the wavelength difference of the pump and ZDW are comparable to the bandwidth of spectrum, further increases in power makes the spectrum broader but unstable [144].

2.5.2.1 Effect of pulse specifications in normal pumping regime

The spectrum keeps growing through SPM and SRS when lies in the normal dispersion region, as the degree of broadening is governed by the pump power. It should be noted that in the vicinity of ZDW, the SPM effect is considerable due to the smaller dispersion value. Hence pumping near ZDW is of interest because of its complex interaction of nonlinear effects.

For pumping wavelengths deep in the normal region, the increase in power leads to spectrum broadening, mainly due to SRS [159, 166] .By increasing the power, if the spectrum extends over ZDW into the anomalous region, solitons are created in the anomalous region through soliton fission. The SRS, XPM and FWM effects are then involved in spectrum generation [144]. It should be noted that spectrum broadening beyond ZDW experiences spectral vibrations because of the pulse breaks up the solitons [144, 168, 169].

In other words the spectral components near ZDW act as a “seed” for efficient FWM and spectral components in the anomalous region grow until soliton fission occurs and extends the spectrum to the anomalous pumping region.

For a constant average power as the pulse width is reduced, the peak power is increased and SC extends more to red and blue side of spectrum due to increased effect of SPM [144].

2.5.3 Supercontinuum Generation with long Pulses

The mechanism of SCG is mainly dominated by soliton dynamics when a femtosecond pulse is used as a pump, whereas FWM and nonlinear Kerr effect are considered to be the most important processes for wider input pulses [31].

Due to the larger pulse width, nonlinear effect of SPM becomes negligible. Thus, the main nonlinear effects involved in spectrum broadening are SRS and FWM [159, 170]. SRS generates side bands around the pump wavelength as stokes and anti stokes bands. These components are then coupled by the FWM effect and result in spectrum broadening on both sides. The FWM is more efficient when the pumping wavelength is located near the ZDW of the fiber since the phase matching condition is more easily satisfied. Furthermore, XPM effect helps to smooth the spectrum by broadening the sidebands around the pump wavelength [171].

The SC can be also generated due to the cascade SRS by using a high energy nanosecond laser [172]. However due to the small peak power, a longer fiber is needed to form a SC. In this situation the components separated by 13.2 THz, are amplified by the SRS effect.

The FWM effect also contributes to broadening to longer wavelengths if the pumping wavelength is near the ZDW of fiber [159, 161, 162]. A nearly symmetric, broad and smooth spectrum forms at sufficiently high power due to strongly coupled stokes and anti stokes components by FWM. They further interact through XPM and SRS.

CHAPTER 3

Bi-EDF BASED LASERS AND AMPLIFIERS IN CW REGIME

In this chapter, a brief theoretical background of the fluorescence of rare earth ion in glass host is discussed and a detailed description of optical glass host property, requirement and its influence on the optical amplifier and laser application are presented. Particularly the performances of the Bismuth-based Erbium-doped fiber amplifiers (Bi-EDFAs) with various pumping schemes and configurations are comprehensively reviewed as an alternative medium for optical amplification in both C and L-band regions. The Bi-EDFA is characterized and its performance is compared with conventional silica based EDF (Si-EDF). A number of experiments and configurations setup are introduced in order to determine the noise characteristics and to achieve a high gain-flattened amplifier covering wavelengths from C-band to the extended L-band region.

The Bi-EDFs are then used to demonstrate tunable fiber lasers. The Bi-EDF used also exhibits a high nonlinearity, which will be used for realizing new narrow linewidth nonlinear devices based on Brillouin effect. In this chapter a performance of Bi-EDF based Brillouin fiber lasers is also demonstrated to generate a single-wavelength or multi-wavelength comb like output.

The motivation for this research is to improve the understanding of Bi-EDFs from the point of view of their physical, spectroscopic and optical properties for the generation of ultrashort pulses as well as applications in nonlinear optics. In addition, the problems associated with a very high dopant concentration and the effect of self-saturation are found to influence the gain, noise and efficiencies of the output signal.

3.1 BACKGROUND ON EDFA

The scattering and absorption mechanisms in an optical fiber can cause a progressive attenuation of light signals as they travel along a fiber. Thus the signal tends to lose power and cohesion. Consequently optical amplifiers have become essential to increase the scale and performance of communication systems [173].The fiber amplifiers investigated so far belong to three main categories: (a) Rare earth-doped fiber amplifiers which are based on stimulated emission, (b) nonlinear fiber amplifiers which are based on phonon-photon interaction and finally, (c) fiber optics parametric amplifiers which are based on four-wave mixing [30, 64].

In EDFA and Raman fiber amplifier, pumping can be achieved in either or both propagation directions, while pumping must be forward in parametric fiber amplifiers and backward in Brillouin fiber amplifiers. This work focuses on the development of the rare-earth doped fiber lasers and amplifiers.

The addition of rare earth ions into a silicate glass to produce laser action in a fiber was first shown in 1964 by Snitzer and Koester [174]. Rare earth element, such as Erbium, Ytterbium or Thulium, is doped in silica glass fibers for many practical applications, including fiber laser devices and amplifiers. Devices that provide gain must have low intrinsic and extrinsic loss properties, low absorption and low scattering losses, so the broader emission and absorption spectra of rare earth doped glasses lead to many applications [175] .

The following characteristics are the current major requirements of optical amplifiers [176-178]: precise control of fiber mode and refractive-index profile in the radial direction, higher doping concentration, low up-conversion, low cost fabrication process, high chemical and physical/mechanical stability and durability. An ideal optical amplifier should have high power conversion efficiency (PCE), high saturated output power and high input saturation power.

Furthermore, optical amplifiers should have a uniform or flat gain [179] in order to ensure the maximum applicable amplification bandwidth.

3.2 GAIN AND NOISE FIGURE CHARACTERISTICS OF EDFA

Gain as the most important parameter in optical amplifier is actually constrained by several physical effects such as the limit due to the energy conversion principle and the finite number or Erbium ions that exists in the medium. In practice, EDFA gain properties are also limited by commonly called second-order physical effects including pump ESA, self saturation by ASE, concentration quenching, and inhomogeneous broadening.

Therefore, the optical gain, G(dB) is defined as $10\times log_{10}\,((P_{out} - P_{ASE})/P_{in})$ where P_{in} and P_{out} are the amplifier input and output signal powers respectively and P_{ASE} is the ASE power.

An optical amplifier is actually a concatenation of many amplifier segments where the gain element $(g(z))$ within length of Δz and total gain (G) within a length of L in a three-level laser medium are given by following equations:

$$g(z)=\Gamma_s[\,\sigma_e N_2(z) - \sigma_a N_1(z)] \tag{3.1}$$

$$G=exp[\,\Gamma_s(\sigma_e N_2 - \sigma_a N_1)L] \quad (3.2)$$

where $N_1, N_2,$ are the ground state and the metastable level population density ,respectively. Also Γ_s , σ_e and σ_a are the confinement overlap integrals factor, the stimulated emission cross-section and absorption cross-section respectively.

The maximum signal gain or the limiting value of gain occurs during complete inversion in which spontaneous emission factor $\sigma_e N_2/(\sigma_e N_2 - \sigma_a N_1)$, become unity (minimum).

The spontaneous emission factor (n_{sp}) measures the quality of inversion of the gain media and become unity when complete inversion ($N_1 \approx 0$) occurs. The limiting values for output power (P_{out}^{max})and gain G_s are related to signal parameters as [61, 180]:

$$P_{out}^{max} = 1 + (\lambda_p P_p^{in}/(\lambda_s P_s^{in})) \quad (3.3)$$

$$Gs=exp[((\sigma_{es}/\sigma_{as} - \sigma_{ep}/\sigma_{ap})\alpha_s L))/(1 + \sigma_{ep}/\sigma_{ap})] \quad (3.4)$$

where α_s is the Bi-EDF absorption coefficient at signal wavelength, L is the Bi-EDF length and σ is the absorption (a) or emission (e) cross section at signal (s) or pump wavelength (p).

Noise figure is also a crucial parameter for optical amplifiers since this effect is cumulative and it is the ultimate limiting factor in the number of amplifiers that can be concatenated. As the ions have a finite excited state lifetime (τ=10 ms), some of the ions spontaneously return to the ground state and as a result the gain medium will emit spontaneous emission at the signal wavelength that manifests itself as noise to the signal. These photons have no coherence characteristics with respect to the incoming signal light. They are amplified as it travels down the fiber. Hence, they are stimulated more photons (with the same mode of the electromagnetic field as the original spontaneous photons) from excited ions. This process occurs at any frequency within the fluorescence spectrum of the amplifier transitions. This reduces the gain from the amplifier. In a small signal gain regime, this amplified spontaneous emission (ASE) as a background noise has an output power of $P_{ASE}^{\pm}$ in a given bandwidth of Δv in an amplifier with gain of *G*. Hence we have

$$P_{ASE}^{\pm} = n_{sp}^{\pm} h v_s (G-1) = n_{eq}^{\pm} h v_s \Delta v G \tag{3.5}$$

where $n_{sp}^{\pm}$ and $n_{eq}^{\pm}$ are the spontaneous emission factor and the equivalent input noise, respectively, corresponding to forward and backward propagation directions. In addition *h* is Planck's constant, *v* is signal frequency. The optical noise figure represents a measure of the signal-to-noise ratio (SNR) degradation experienced by the signal after passing through the amplifier.

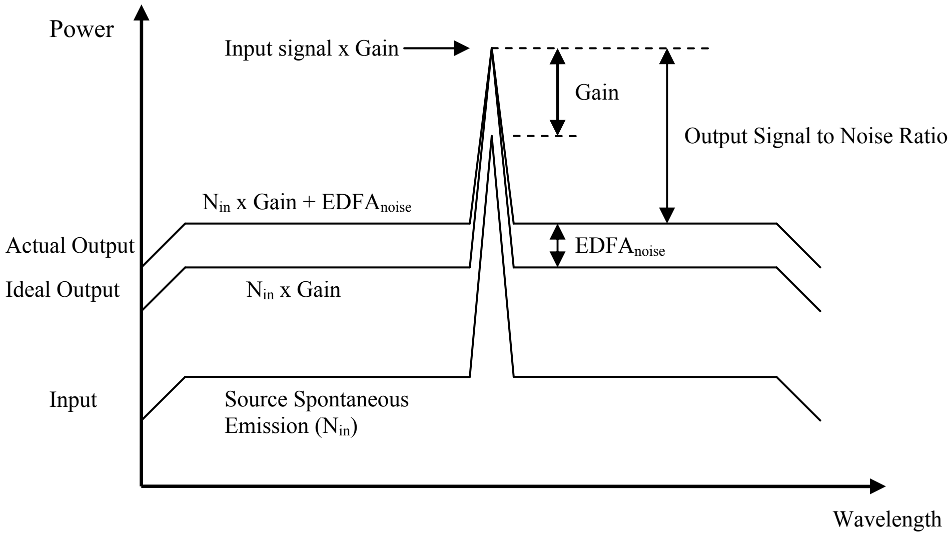

Figure 3. 1: The determination of noise from spectral information.

The original formula of noise figure defines it as SNR_{in} / SNR_{out} [61, 181, 182] where the SNR_{in} and SNR_{out} are signal-to-noise ratio at input and output of an amplifier respectively. Figure 3.1 shows the spectral information required for determination of EDFA noise.

A commonly used definition of noise figure is the quantum-beat-noise-limited noise figure, which excludes the output SNR due to spontaneous-spontaneous beat noise, ASE shot noise. That is [61, 181] :

$$NF = [P_{ASE}/(h\nu G \Delta\nu_s)] + 1/G \tag{3.6}$$

where, $\Delta\nu_s$ is optical frequency band of photo detector system. The first term is the signal-spontaneous beat noise and the second term is the signal shot noise.Note that the $P_{ASE} = 2n_{sp}h\nu[G(z)-1]B_0$ is summed over all the spatial modes that the fiber supports in an optical bandwidth B_0 [181].

The noise figure can be then expressed as a function of n_{sp} by:

$$NF(z) = 2n_{sp}[(G(z)-1)/G] + (1/G(z)) \tag{3.7}$$

In the high gain limit the signal noise can be ignored and consequently NF would be reduced to $NF = 2n_{sp}$.The $NF_{\min}$ and $n_{\mathrm{sp}}^{\min}$ at signal wavelength, λ_s are given by:

$$\begin{aligned} NF_{min} &= 2n_{sp}^{min} = 2 \times [1 - (\sigma_{as}\sigma_{ep}/\sigma_{es}\sigma_{ap})]^{-1} \\ &= 2 \times [1 - exp(hc(\lambda_{p-}\ \lambda_s)/K_B T)]^{-1} \end{aligned} \tag{3.8}$$

where T is the temperature and k_B is the Boltzmann constant. Note that n_{sp} is equal to 1 for fully inverted amplifier and otherwise is $1.4 < n_{sp} < 4$. Using a 1480 nm pump excitation (two-level laser system), σ_{ep} is non-zero which consequently produces NF_{min} of higher than 2.

Thus, a 1480 nm pump is less preferred when compared to a 980 nm pump for an excitation in a low noise EDFA design. A double pass amplifier has a higher *NF* compared to that of the single pass system [182]:

$$NF(z)_{total} = NF_1 + [(\mathrm{L}'(\lambda)^{-1} - 1)/\mathrm{G}] + [(NF_2 - 1)/(G\mathrm{L}'(\lambda))] \tag{3.9}$$

where $NF_1(\lambda)$ and $NF_2(\lambda)$ are the *NF* of the first and the second stage of the double pass EDFA. This Equation shows that the total noise figure is made up of the noise at the first stage EDFA, the insertion loss of the feedback loop and the accumulation of the cascaded amplifiers.

3.3 LIMITATIONS OF SILICA-BASED EDFA

EDFAs have several advantages such as having: a polarization insensitive high gain (>30 dB) in C-band, a high saturation power, a low signal noise (4-5 dB), a low crosstalk between different signals and data bit-rate independent. However, higher output creates adverse nonlinear effects in the EDFA such as four-wave mixing (FWM) and cross-phase modulation (XPM) etc. that result in signal distortion [183, 184].

By exploiting signal and ASE re-absorption properties in longer EDF length, the amplification bandwidth is expanded to the L-band region. However this technique increases the optical nonlinearity in the system [64]. The gain of the signal is also small [61, 185, 186] due to the effects of excited-state absorption (ESA) being far from the Er^{3+} ions emission cross-section and the low pump power conversation efficiency.

The ability to have high concentration RE doping is crucial in producing higher signal gain per pump power ratio without extending the EDF length [187, 188]. High RE solubility also leads to new research advancements for ultrafast generation and soliton amplification [189]. A highly doped erbium fiber laser (EDFL) with shorter length shows lower cavity loss and dispersion.

The Er^{3+} ion distribution should ideally be uniform in the centre of the fiber core to achieve maximum signal gain per launched pump power [188, 190]. Due to low RE solubility which causes high concentration RE silica glass to form ion clustering easier, the maximum Er^{3+} concentration is limited before concentration quenching occurs. Concentration quenching triggers an interionic energy processes such as energy migration, cross-relaxation and up-conversion [61, 184, 186].

As the cluster distance and distribution becomes closer, the energy transfer process can happen very fast in a sub-microsecond timescale that lowers the population inversion [191]. These energy processes cause the gain coefficient per unit length of silica-based EDFA to be lower compared to other glass host. In addition, this can generate undesirable effects such as the reduction of the fluorescence bandwidth and lifetime [61, 187, 188, 190].

Based on these factors, optical engineers have developed several techniques to widen the optical bandwidth and to overcome the doping concentration limit. Alkali-metals as co-dopants glass modifiers which alter the glass matrix coordination are capable of increasing the amount of non-bridging oxygens [192, 193], thus reducing the Er^{3+} ion clustering capability.

Using direct nanoparticles deposition (DND) for dopants has also shown smaller amount Er^{3+} ion clustering in silica glass [194, 195].

3.4 BISMUTH BASED EDFA

Due to numerous limitation of silica-based EDFA, other host glass such as tellurite based fiber, antimony silicate fiber, fluoride-based glass, phosphate and bismuth, glass are being studied [177, 198-200]. Tellurite-based EDF has a flat and broadband gain of 75 nm from 1535 to 1610 nm. However it cannot be fusion-spliced to the standard communication fiber [199].

Glasses such as bismuth and phosphate have also shown better thermal stability and chemical durability compared to fluoride-based glass such as ZBLAN. Beside their high RE solubility, glasses such as phosphate and ZBLAN glasses are difficult to fabricate due to their hygroscopic and devitrification properties that may result in many difficulties in fabrication process and during optical amplifier's deployment [186, 200].

The Bi-EDF has a very high fiber nonlinearity, which can be used for realizing many applications in fiber laser devices and has significant advantages in which other host glass EDFAs can not compete [201-203]. The Bi-EDF co-doped with Lanthanum (La) has allowed erbium ion doping of up to 13,000 wt.ppm before Erbium ions starts to cluster together. It means a shorter interaction length with much lower accumulated dispersion.

Several authors have recently studied on the properties of Bismuth borate glasses in a restricted composition range, un-doped [204], Er^{3+} doped or Nd^{3+} doped

[205]. The bismuth-based EDFA has a low melting temperature which makes it easier to be fabricated, good thermal stability and chemical durability. Furthermore it is capable of supporting high Er^{3+} ion concentrations more than 10-100 times compared to conventional silica based EDF [200, 206-208]. Also, this fiber shows a broad and flat emission due to a large emission cross-sections as well as low excited state absorption due to the smaller vibration energy of the bismuth glass lattice. Optical amplifiers using bismuth host are capable of exhibiting a high signal saturation power that is preferred in the design of a compact high power system [5]. A high power Bi-EDF laser in the wavelength range of 1300–1500 nm has been reported by Firstov et al. [209].

In this work, a newly developed nonlinear Bi-EDF from Asahi Glass Company in Japan is introduced and its application in optical amplifier and nonlinear fiber laser is described. Table 3.1 lists the main physical properties of the propose Bi-EDF that we employed in this thesis.

This fiber has an Er^{3+} ion concentration of 7.6×10^{25} ions/m^3 or 3,250 (wt.ppm), which is obtained from the weight ratio of erbium oxide (Er_2O_3) to other starting materials (Bismuth oxide) during the fabrication process. The pyramidal polyhedron structure of Bismuth glass whereby the faces and the base of the structure are triangular and converge on the apex is shown in Figure 3.2(a).This host is capable of incorporating and bonding with more active ions via non-bridging oxygen atoms(see arrows), because of a high oxygen atom ratio in the vicinity of the heavy bismuth atoms [210, 211].

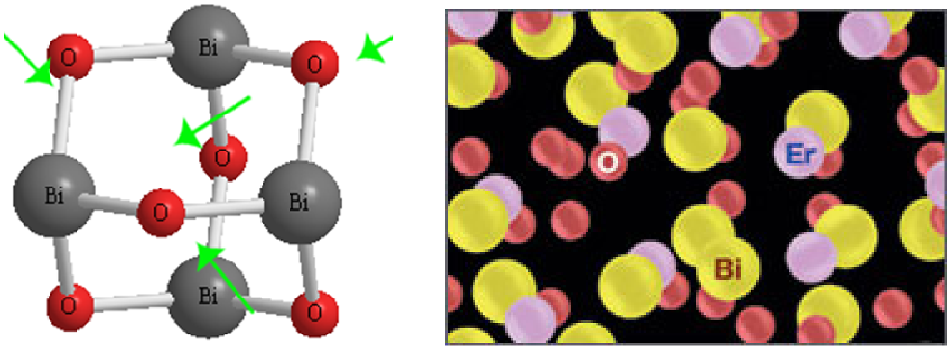

(a) (b)

Figure 3. 2 : (a) Bi_2O_3 glass with a pyramidal polyhedron structure, (b) Erbium ions distribution of bismuth-based glass.

It is showed that the efficiencies of the Bi-EDFA can be improved by suppressing the upconversion process through lanthanum (La) and boron (B) addition into the glass host [212]. Hence a La/Er^{3+} co-doped Bi_2O_3-based glass (perform) with a Lanthanum (La) ion co-dopant concentration of approximately 4.4 wt % was prepared using a modified chemical reaction deposition (MCVD) process [213].By utilizing three glass former elements, i.e. bismuth oxide Bi_2O_3, silica SiO_2 and alumina/aluminium oxide Al_2O_3, the local glass basicity near the Er^{3+} ions sites would be expanded as reported in [193, 214], effectively increasing the crystal field (Ligand field) of the glass. This has the benefit of enhancing the 1530 nm fluorescence bandwidth and making it comparably broader than that obtainable with a silica glass host. This special Er^{3+} ions distribution in the Bi-EDF also reduces the concentration quenching effect [215, 216] of the Er^{3+} ions, thus increasing the quantum efficiency [193, 214, 217].

The analysis from the Energy Dispersive X-Ray Microanalysis (EDX) with JEOL JSM6460LA) has disclosed that the proposed Bi-EDF glass network formers and modifiers. As shown in the Table 3.1 besides Er_2O_3 as the activator of the 1.55

μm transition, there are small percentages of network modifiers such as phosphorus oxide and potassium oxide in the glass.

Indeed various relevant properties such as the refractive index can be tuned by the addition of heavy metal oxide such as TeO_2, PbO, Ga_2O_3 and Bi_2O_3 [218]. From the Judd-Ofelt theory, the effect of the glass composition is explained by the $\Omega_{2,4,6}$ coefficients[61, 211, 219]. As presented in the table the refractive indices of cladding and core at 1.55 μm are 2.02 and 2.03, respectively, while these values for standard single mode fiber are around 1.45.

The large Judd-Ofelt intensity parameter (Ω_6) and the higher refractive index of the Bismuth-based glass results in broader emission bandwidth [220] and larger emission cross section which are desirable for network systems [221]. However, the lifetime of $^4I_{13/2}$ level in Bismuth-based glass is relatively shorter due to such a high refractive index.

Having a core radius of 2.55 μm, the MFD of the proposed fiber can be determined from Marcuse equation to be about 6.1 μm which is 0.2 μm larger than that of typical Si-EDF. This larger MFD is accompanied by a lower NA in the Bi-EDF (0.02 lower than the Si-EDF) .This comparatively higher refractive index, leads to higher single-mode cut-off wavelength and a nonlinear refractive index (n_2) which is so much higher than silica-based fiber.

The presented effective area (A_{eff}) is another parameter that determines the threshold power for stimulated Brillouin scattering in the next sections.

Nonlinear scattering processes such as SRS and SBS are mainly determined by two important factors, i.e. nonlinear gain coefficient and gain spectrum. The nonlinear parameter (γ) is important parameter for the nonlinear Kerr effect. This parameter (γ) is proportional to the nonlinear refractive index of the material (n_2) and inversely proportional to the fiber core cross-section ($2\pi n_2/\lambda A_{eff}$).

All these parameters depend both on the composition of the glass material and on the MFD. Besides reducing the A_{eff}, using a glass material whose n_2 is high can enhance the fiber nonlinearity. Fibers with a value γ of more than 10 $(W/km)^{-1}$ is referred to as a highly nonlinear fiber [64].

In practice, the value of γ has an order of magnitude of 2.7 $W^{-1}km$ for a standard single mode SiO_2 based fiber whereas largest values of γ for a conventional fiber made from a Bismuth borate glass lies in the range of 1360 $W^{-1}km^{-1}$ [222]. The high nonlinear performance of Bi-EDF leads to many applications in fiber laser devices such as super-continuum generation.

The dispersion of the Bi-EDF is relatively flat, within a large wavelength range of 1200 nm to 1800 nm. However, the large normal dispersion of the Bismuth fiber, provides the ultimate limit on spectral broadening. As presented in the Table 3.1, the proposed Bismuth fiber also has a large value of normal group velocity dispersion (GVD), which is mainly due to the material dispersion of the high refractive index of the glass [223].

A number of techniques have been developed to measure nonlinear parameters in fibers based on different effects of the nonlinearity, including SPM, XPM, and modulation instability. Using the spectrally resolved or by two beam coupling technique the n_2 value is measured [226]. From a FWM method and by employing a two beam coupling technique in this fiber, γ and n_2 around 1600 nm were measured to be 59.16 (W^{-1} km^{-1}) and 4.40×10^{-19} (m^2/W), respectively. The details of the results presented in this section have been published by the authors as regular papers in [54, 227].

Table 3. 1: Specification of Bismuth-based EDF [213, 224, 225].

Parameter	Value
Background loss, signal	40 dB/km
Cutoff wavelength	<1450(nm)
Erbium ions concentration	3250 wt. ppm
Mode-field diameter (MFD)@1550 nm[3]	6.12 μm
A_{eff}	29.4 μm^2
Numerical aperture (NA)	0.20
Core dia / cladding diameter @1550 nm	5.4/125 μm
La ion Co-dopants concentration[12]	4.4%
Peak absorption around 980(1480) nm	73(83) dB/m
Peak Absorption around 1530(1560) nm	133 (44.11) dB/m
Absorption cross-section at 1532 nm	7.73×10^{-25} m^2
Emission cross-section at 1532 nm (Peak)	7.58×10^{-25} m^2
Fluorescence Lifetime $^4I_{13/2}$	2.84 ms
Mass percentage of Bi_2O_3	67.80 $\mp$1.88 %
Mass percentage of SiO_2	14.24$\mp$0.81 %
Mass percentage of Al_2O_3	16.96$\mp$ 0.87 %
Mass percentage of Er_2O_3	0.42$\mp$ 1.67 %
Mass percentage of K_2O	0.05 $\mp$ 0.29 %
Mass percentage of P_2O_5	0.53$\mp$ 0.64 %
Nonlinearity (γ)	58.3 $(w.km)^{-1}$
Core/cladding refractive index 1550 nm	2.03/2.02
Numerical aperture (NA)	0.20
Dispersion Bi-EDF at λ=1545 nm	+140±0.21 Ps^2/km
non-linear refractive index	4.23×10-19
V-number	2.18
melting temperature	817^oC

3.5 THE SPECTROSCOPIC PARAMETERS OF Bi-EDF

Figure 3.3 shows the 4f energy level diagram of Er^{3+} ion and the transitions involved for amplification. In this figure amplified spontaneous emission [61, 228], 1550 nm band spontaneous emission, excited state absorption [229], cooperative upconversion [230] and nonradiative decay are shown by ASE, 1550 nm-SE, ESA, CUP and NA respectively.

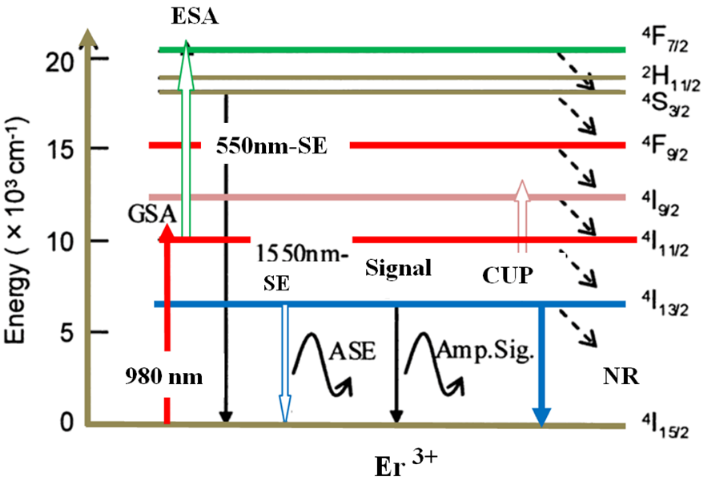

Figure 3. 3: The 4f energy diagram of Er^{3+} ion and the relevant transitions.

Two commonly-used bands for pumping of Bi-EDF are 980 nm and 1480 nm. The 980 nm band with a higher absorption cross-section is generally used for low-noise performance. However, a wavelength stabilized laser source is needed for this absorption band since this band is relatively narrow. On the other hand with a lower absorption cross-section, the 1480 nm band is broad and generally used for high power amplifiers.

Figure 3.4 shows the normalized emission cross sections $\sigma_e(\lambda)$ obtained from the McCumber theory which are compared with the measured values [61]. The emission cross-sections were calculated from absorption cross sections σ_a (λ), provided by Asahi Glass Co. Ltd.

The ratio of emission to the absorption cross-section (η) is also depicted in the figure inset as a comparison. The comparison factor (η) is given by:

$$\eta = \sigma_e/\sigma_a = exp[(-hc\,(\lambda^{-1} - \lambda^{*-1})/\,k_B T] \qquad (3.10)$$

where λ* is the wavelength at which the emission and absorption cross sections are equal.

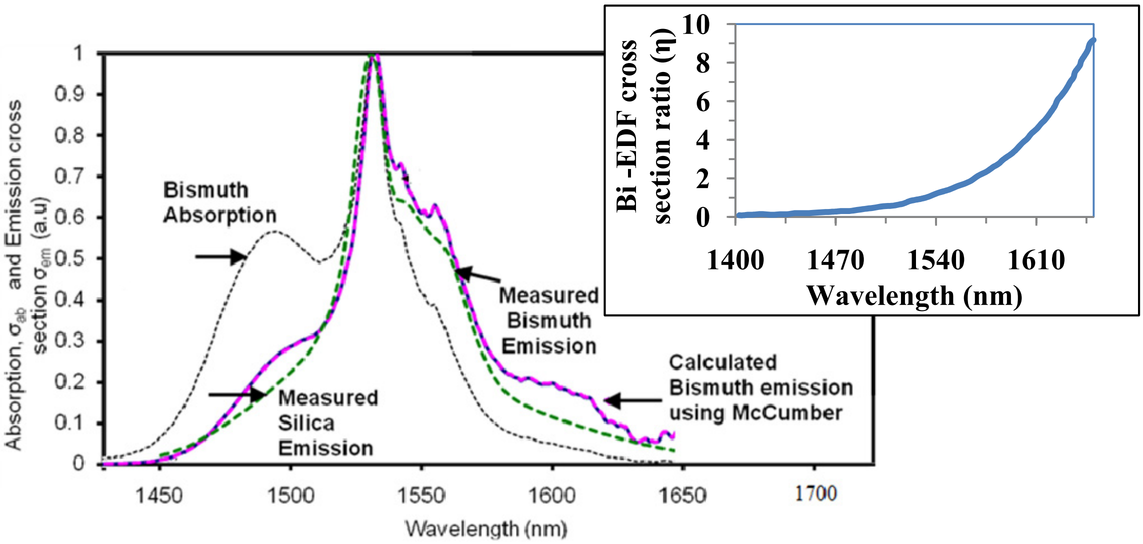

Figure 3. 4: cross-sections of Bi-EDF. The calculated Bismuth emission curve coincides very well with the measured curve where cross sections are $\sigma_a{}^{max} = 7.73 \times 10^{-25}\text{m}^2$, $\sigma_e{}^{max} = 7.58 \times 10^{-25}\ \text{m}^2$ at the 1532 nm peak (300 K).

The emission peak at 1530 nm is obtained due to the population inversion between the $^4I_{13/2}$ and $^4I_{15/2}$ energy levels.

The Bi-EDF has a higher absorption cross-section peak at 1530 nm (7.58×10^{-25} m^2) as compared to the Si-EDF (which is only 4.39×10^{-26} m^2). In addition, it has a wider emission spectra. This is due to the Stark level of the Er^{3+} ions in this glass host is separated to a larger degree because of the larger ligand field.

The lifetime (τ) of fluorescence emitted from Er^{3+} ions at the $^4I_{13/2}$ level is calculated from radiative decay rate (w_{21}^{R}) and non-radiative decay rate (w_{21}^{NR}) as follows:

$$\tau = 1/W_2 = 1/w_{21}^{R} + 1/w_{21}^{NR} \qquad (3.11)$$

The lifetime is an essential parameter to specify the characteristic of the glass host local environment. In general with longer Er^{3+} ion metastable level lifetime an optical amplifier is capable of maintaining its excited state population inversion longer and consequently is capable of producing a higher energy conversion efficiency.

Having the average transition wavelength (λ) , the refraction index (n) and the oscillator strength of transition (f_{osc}), the lifetime can be calculated by [231, 232]:

$$\tau_0 = 1.51 g^2 \lambda^2 / (g^1 f_{osc} n^2 \chi\,) \qquad (3.12)$$

where χ is the Ligand field correlation with the theoretical value of $(n^2+2)^2/9n$ and g^1 is the statistical weights of the excited state.

From the above equation and measurement obtained from the time-resolved spectroscopy technique, the lifetime is found to be about 5.45 ms and 2.84 ms, respectively [214, 233, 234] which is much more shorter than the results obtained for the lifetime of an Er^{3+} in conventional silica host glass [177].

The reasons for the shorter lifetime of $^4I_{13/2}$ level in bismuth-based glass are due to the effect of the Er^{3+} ions radiation quenching, having a high refractive index and the addition of bismuth oxide that reduces the overall glass phonon energy.

With lower phonon energy, the non-radiative decay rate at the $^4I_{13/2}$ level was found to be shorter leading to a significant increase in up-conversion process and the multi-phonon relaxation rates. Hence, these effects convert and waste the pump photons to the visible light and heat via multi-phonon processes that lead to reduction in the important 1.55 µm radiative emission.

3.6 AMPLIFICATION CHARACTERISTICS OF Bi-EDFA

In this section, the common amplification parameters are measured and studied in details for the Bi-EDFA evaluation in four configurations: a) forward pumping b) backward pumping, c) double Pass and d) bi-directional schemes.

As illustrated in Figure 3.5, the experimental setups used for the Bi-EDFA consist of wavelength selective coupler (WSC), variable optical attenuator (VOA) and a piece of Bi-EDF where optical isolators are used to avoid the reflection and ensure unidirectional operation in the amplifier. The WSC is used to pump the Bi-EDF and to combine the pump light with test signal.

The double-pass operation can be obtained by using a broadband mirror or fiber Bragg grating (FBG) at the output end of the amplifier. Tuneable laser source (TLS) is used in conjunction with an optical spectrum analyzer (OSA) to characterize the Bi-EDFA. A VOA is incorporated immediately after the TLS to control the input signal power into the optical amplifier.

The insertion loss of the Bi-EDF is estimated to be approximately 0.82 dB and 0.55 dB/m at 1550 nm and 1310 nm respectively using a cut-back method. The total splice loss of the Bi-EDF is a sum of a loss due to mode-field diameters mismatch (~0.047 dB), reflections and also due to lateral misalignment between the fibers.

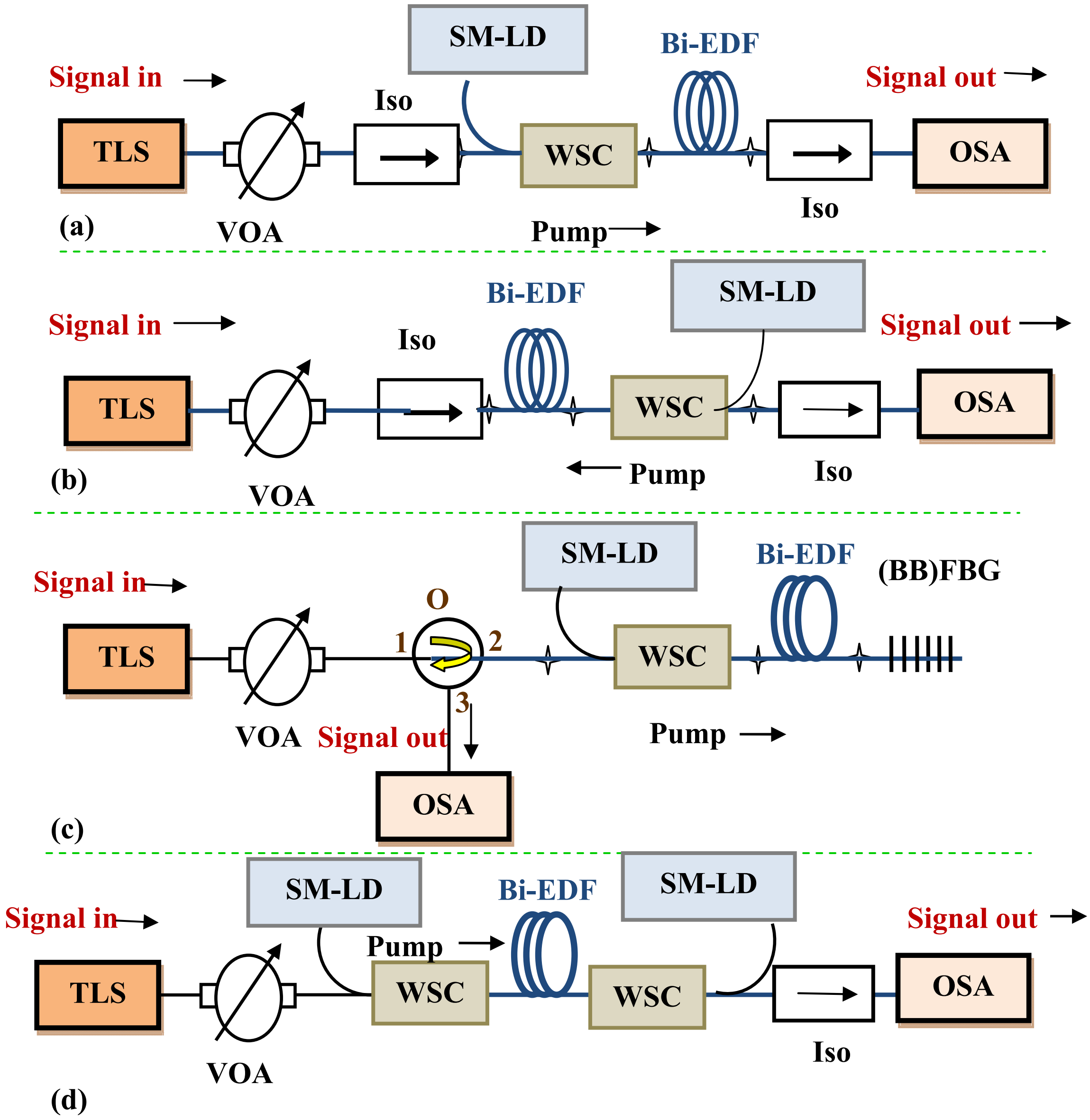

Figure 3. 5: Experimental set-up for the Bi-EDFA with a (a) Forward pumping (b) Backward pumping (c) Double-pass and (d) Bi-directional pumping, configuration.

The major problem of Bi-EDF is fusion splicing to standard silica fibers. The melting point of Bi-EDF (~800 ^{o}C) is much lower than that of silica fiber (>1000 ^{o}C). The splice losses in Bi-EDFA can be minimised by using multiple dummy fibers with higher refractive index and spliced using angle splicing method. Hence Bi-EDF before splicing to single mode fiber was first angle spliced to high numerical aperture fiber (Nufern 980-HP) with an average splice loss was estimated to be less than 0.5dB/point. The mixed angle fusion splicing is critical for Bi-EDFA to reduce reflection and splicing loss due to large index differences between Bi-EDF and silica fibers [224].

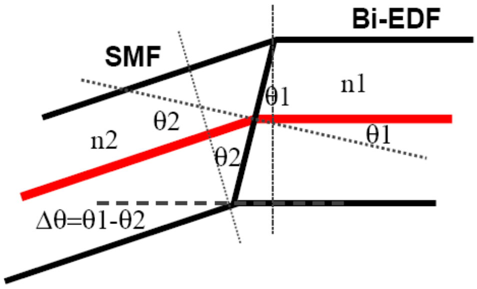

$$\theta_1 = 45^o - \frac{1}{2}\arcsin\left[\frac{n_{clad}}{n_{core}}\right]$$

Figure 3. 6: Mixed Angle splicing configuration with an optimum angle of θ_2=8.2^o for silica fiber and a pre-angle of θ_1=6^o for Bi-EDF [225].

Actually the large refractive index difference (approximately 0.5-0.6) between Bi-EDF and SMF fiber introduces Fresnel reflection loss of about 2.8% . As shown in Figure 3.6, to reduce the coupling loss, the incident angle θ_2 must be greater than the pre-angle θ_1=6^o [225]. However, the incident angle θ_2 cannot be too large as it would increase splicing loss and it is optimum for the proposed case at 8.2^o.

3.6.1 Luminescence Spectrum of Bi-EDFA in C-Band

To fully understand the effect of the pump configuration, and pump power ,the ASE spectrum of the EDF using a piece of 49 cm long Bi-EDF are measured for both forward and backward pumping scheme. The forward ASE spectrum is measured longitudinally at the output end of the Bi-EDF using an OSA. The backward ASE spectrum is measured by incorporating an optical circulator at the input port of the Bi-

EDFA to tap the backward propagating ASE. For both forward and backward pumping scheme, the maximum pump power of 160 mW is used. The results are displayed in Figure 3.7 by F160-1480 and B160-480 respectively.

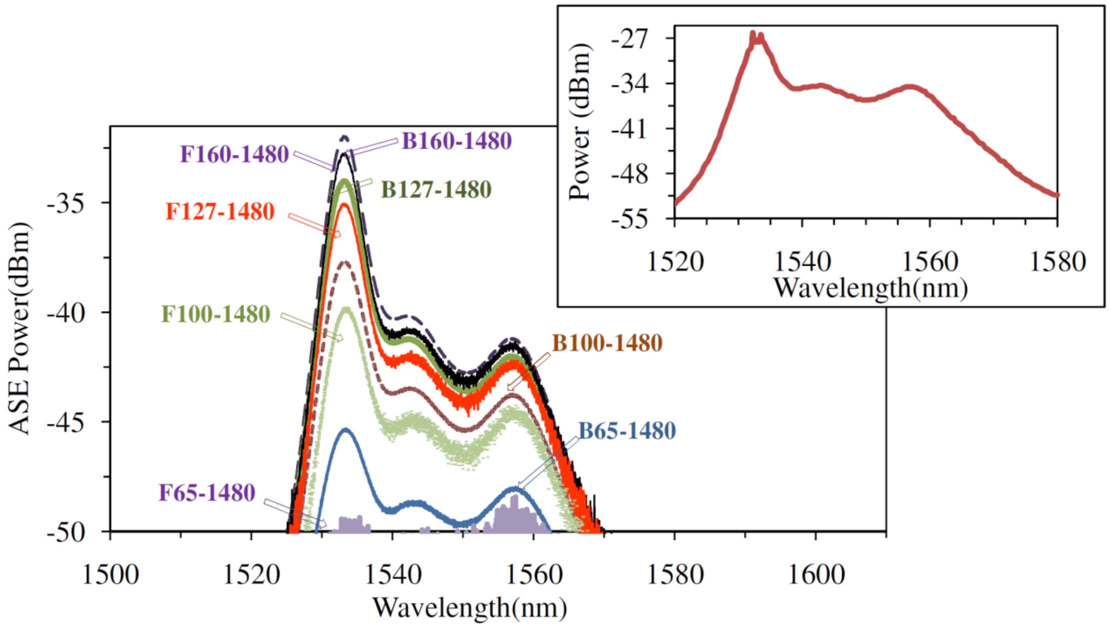

Figure 3. 7: Luminescence spectra of EDF configured with a 49 cm long Bi-EDF for both forward and backward 1480 nm pumping scheme. The pump power is varied from 65 up to 160 mW. Inset shows ASE spectrum of the bi-directional pumped single-pass Bi-EDFA.

It can be seen from Figure 3.7 that for pumping at 1480 nm, the ASE power increases with pump power while the spectral shape remains constant. In addition the ASE power from the backward pumping generates the highest power despite being pumped with the same amount of pump power.

For a given high pump power at 1480 nm, if the population inversion is relatively flat across the fiber, then ASE power and spectra would be equal in both schemes. As shown in this figure, ASE has two peaks at 1532 nm and 1556 nm which are not sensitive to the pump power. However the intensity of the forward ASE at

1532 nm is very sensitive to the pump power. As shown in Figure 3.7 in forward scheme, ASE at 1530 nm band is initially weaker than the ASE at 1556 nm band. However, it then surpasses the other band while the 1530 nm band is always stronger in the backward scheme.

In the inset figure, the ASE spectrum of the 49 cm long Bi-EDF configured with bi-directional pumping is demonstrated. The experimental setup is shown in Figure 3.5(d) where the Bi-EDF is pumped by two 1480 nm laser diodes. This inset shows the forward ASE of the amplifier, when both pump powers are fixed at 100 mW. The spectrum is relatively wider and it is also flat within the wavelength region from 1540 to 1560 nm whereas peaks at 1535 nm. A flat ASE spectrum demonstrates the ability of the Bi-EDF to act as a wide-band optical amplifier for DWDM optical telecommunications systems [235, 236].

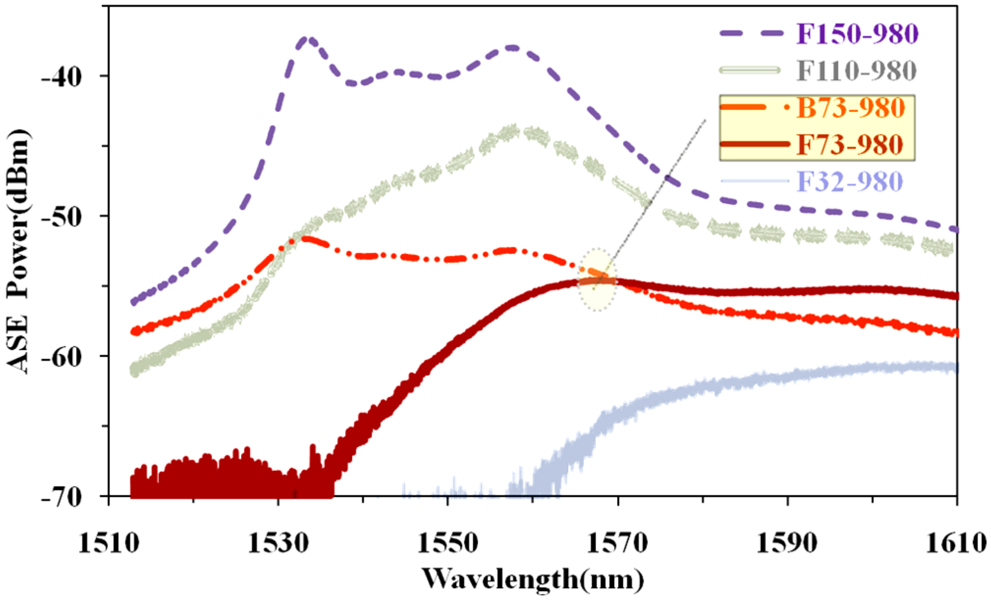

Figure 3. 8: Luminescence spectra of 49 cm long Bi-EDF for both forward and backward pumping scheme at pump wavelength of 980 nm. The pump power is varied from 32 up to 150 mW.

For comparison purposes, the experiment is repeated for the 980 nm pumping scheme. As shown in Figure 3.8, the ASE spectrum is observed at the wavelength region between 1510 to 1610 nm in which the ASE at 1535 nm band, coincides with the maximum emission region of Erbium ion in the EDF.

The total ASE power is observed to increase with the pump power. The ASE spectrum is also observed to be moved towards a shorter wavelength region as the pump power increases from 32 to 150 mW.

3.6.2 Luminescence Spectrum of Bi-EDFA in L-Band

In this section, the luminescence spectra of a 215 cm long Bi-EDF configured with bi-directional pumping are measured and presented in Figure 3.9 for different 1480 nm pump power ratios. In this experiment ASE is measured after the isolator and a maximum pump power of 160 mW was used for back or front laser diode.

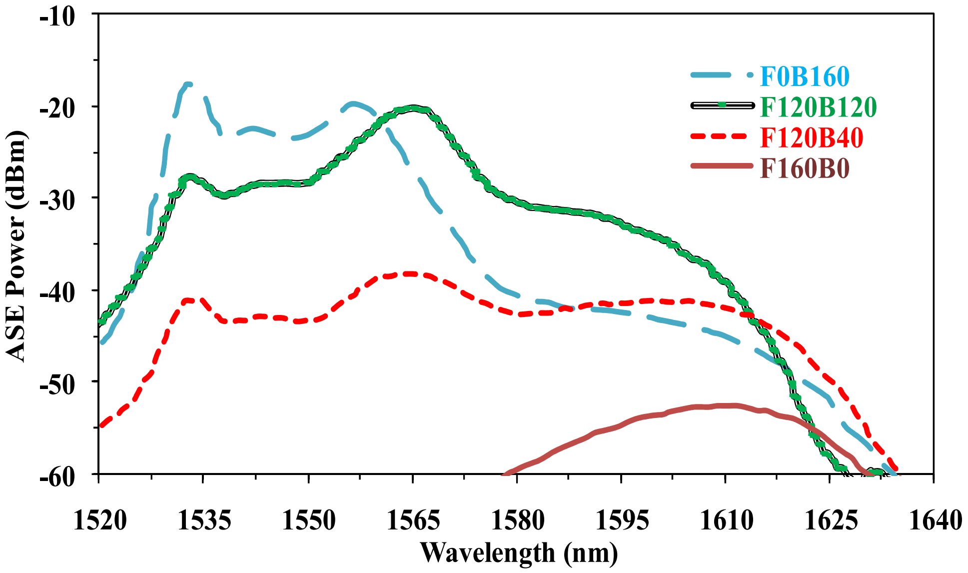

Figure 3. 9: Forward ASE spectrum configured with 215cm long Bi-EDF for different 1480nm pumping configurations: Forward (F160B0), Backward (F0B160) and Bi-directional (F120B40 & F120B120).

For forward pumping, displayed in the figure by (F160B0), ASE operates at L-band region and peaks at 1608 nm. In this case, the ASE power suffered greater attenuation in reaching the end of the fiber as compared to the backward pumping configuration (F0B160). This is due to the fact that the pump light is only capable of producing high population inversion at limited lengths of the input portion of the fiber. As a result the ASE power from the forward pumping (F0B160) generates the lowest power.

Indeed the weak C-band fluorescence is a result of high absorption of light in C-band region. Figure 3.9 shows that the C-band ASE obtained from the input part of the fiber section is dominant in the F0B160.

For bi-directional pumping, the ASE spectrum is the mixer of the forward and backward ASE. As observed in Figure 3.9, the forward to backward pump power ratios of 120:40 mW (F120B40) and 120:120 mW (F120B120) are the effective combinations of pumping which capable to produce a more flatter ASE.

Hence, the Bi-EDFA gain bandwidth covers the region up to the extended L-band region and is also much wider than that of the standard Si-EDFA. This is attributed to the suppression of excited state absorption (ESA) effect by the incorporation of La ions in the Bi-EDFA. The suppression of ESA reduces the dissipation of pump energy and increases the population inversion especially at extended L-band region.

The ASE spectrum gives a good indication of the gain profile. Higher ASE level indicates higher population inversion.

The ASE power in a double-pass scheme is improved by more than 8 dB at the wavelength region of 1530 to 1600 nm as compared to the ASE power of the single-pass scheme.In order to gauge the behaviour of the Bi-EDF in optical amplification, Bi-DFA characteristics are evaluated by measuring the signal gain and noise figure by an OSA using the ASE interpolation technique [237].

3.6.3 Gain in C+L-band region

Signal output power and EDFA gain are usually measured as functions of input signal power (P_s^{in}) and wavelength (λ_s). More specifically, there are three important gain regions. In the under-pumped region the gain is smaller than one.

In the incomplete inversion region, the gain steeply increases with pump power by increasing population inversion. However, as the pump power further increases, the gain approaches the limiting values at the near-complete inversion region.

In the experiment, a piece of 49 cm long Bi-EDF is used as a gain medium for C-band region. To fully understand the effect of the input signal power and wavelength on the gain spectrum experimental, verification is done under forward, backward and double pass pumping schemes. Figure 3.10 shows the gain characteristic of the Bi-EDFA against 1480 nm pump power in forward pumping scheme.

As shown in this figure, the gain starts to saturate at 80 mW of pump power at a low input signal power of -30 dBm. At a fixed pump power the gain decreases as the input signal power increases.

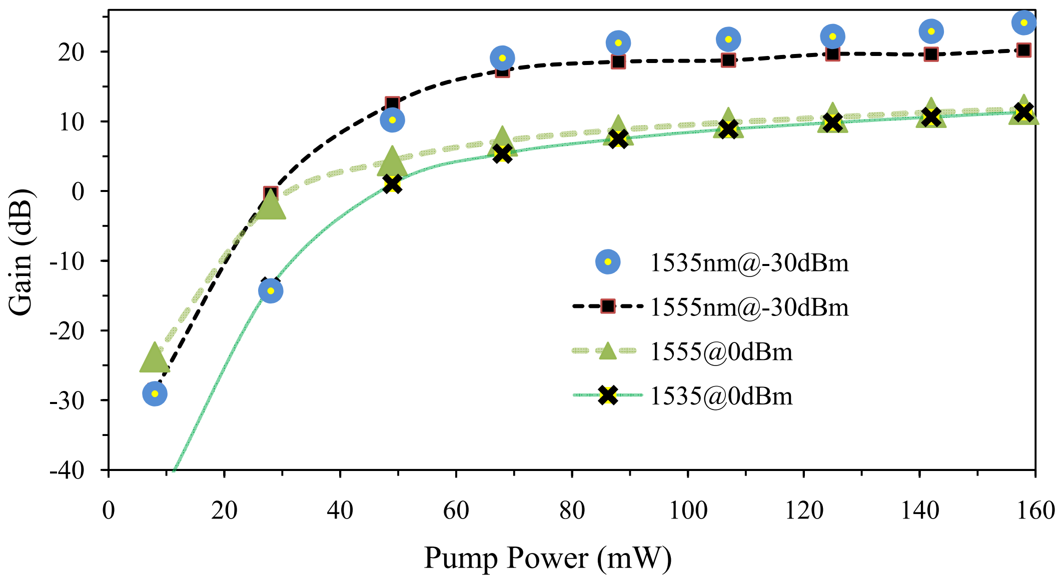

Figure 3. 10: Gain as a function of pump power in forward pumping scheme at fixed signal power.

Figure 3.11 shows the gain spectra at the input signal powers of -30 dBm and 0 dBm, while the 1480 nm pump power in uni-directional scheme is fixed at 150 mW.

From the result obtained for the forward pumping scheme, a gain bandwidth of 30 nm (from 1530 to 1560 nm) with the gain peak of 22.6 dB is obtained at 1535 nm for input signal power of -30 dBm. While the Bi-EDF has a wider gain bandwidth (40 nm) especially at the longer wavelengths (1530 nm to 1570 nm) for 0 dBm input signal, with a flat-gain of 10.9 dB with gain flatness of less than 1.1dB within the spectral bandwidth.

In the backward pumping scheme at low input signal power (-30 dBm), the gain peak at 1535 nm is about 3.51 dB higher than that of the forward one. Meanwhile a flat-gain spectrum with a gain peak of 11.9 dB is obtained at 1565 nm with a 0 dBm input signal power, which is not a major change in comparison with the forward pumping scheme.

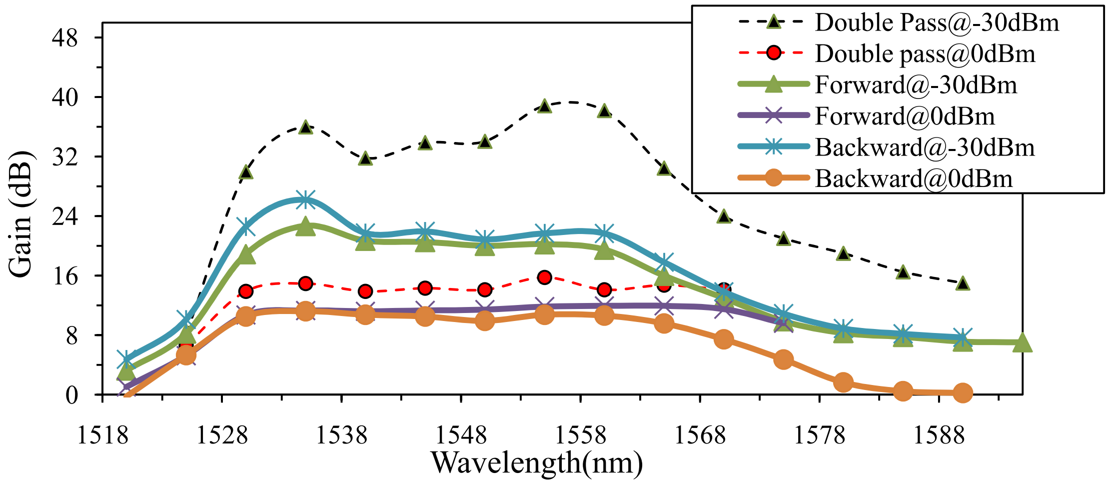

Figure 3. 11: The gain at input signal powers of -30 dBm and 0 dBm as a function of input signal wavelength for different pumping configurations.

A broadband FBG has been used in a double-pass scheme to enhance the gain of Bi-EDFA. Compared with the single-pass operation the gain is increased by 12.6 dB at -30 dBm. At this small input signal power the gain peak of 38.8 dB is achieved at 1555 nm. Again a flat-gain of 14.8 dB with gain flatness of less than 1.1 dB is observed within the bandwidth of 1530 -1565 nm at 0 dBm input signal power.

The performance of Bi-EDFA in C-band region is also investigated with the bi-directional pumping scheme as configured in Figure 3.5(d). At input signal powers below -20 dBm, the experimental results for a given pumping power ratio show a small variation on gain. However, the gain reduces as the signal power further increases. Nevertheless with input signal powers ranging from -30 to 0 dBm the gain at 1555 nm at least 3 dB is higher than that of the gain at 1530 nm. Similar to the other schemes at input signal power of 0 dBm, the gain spectrum is almost flat. In this case a flat-gain of 10.43 dB with a gain variation of less than 3dB is observed within the bandwidth of 1530 - 1570 nm when the pump power is fixed at 100 mW for both pumps. In contrast to the case of 0 dB at input signal power of -30 dBm, the gain spectrum has two peaks at 1535 nm and 1555 nm. A maximum gain of 25 dB is obtained at 1535 nm.

We repeated the procedure leading to Figure 3.11 for a piece of 215 cm long Bi-EDF and the results are shown in Figure 3.12.

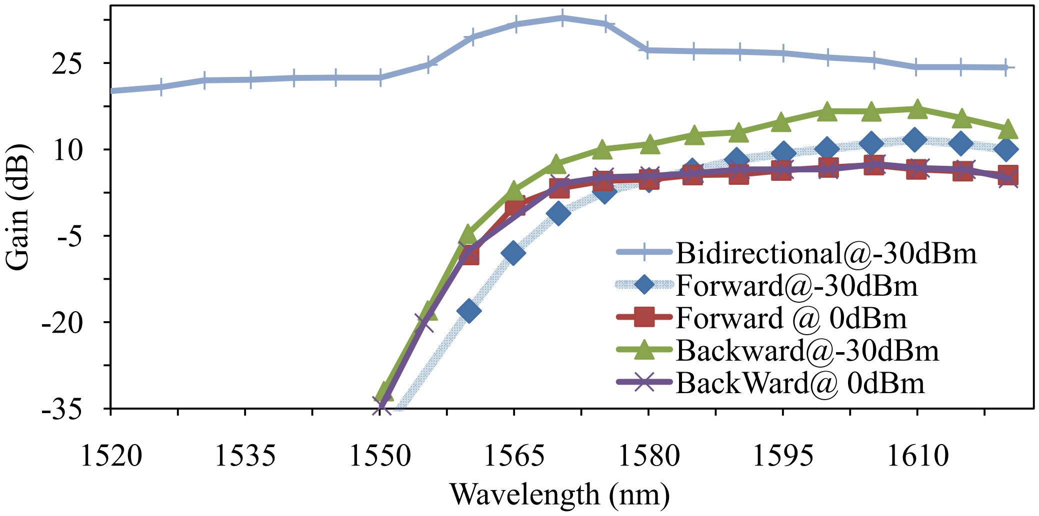

Figure 3. 12: The gain spectra of L-band Bi-EDFA at input signal powers of -30 dBm and 0 dBm for different pumping configurations.

At a 215 cm long Bi-EDF, the gain spectrum of a unidirectional scheme shifts to the L-band. Using a given pumping scheme for instance forward scheme and a given pump power for instance 160 mW, the gain further increases as the input signal power reduces. However, for an input signal power below −25 dBm (−20 dBm) the experimental results show a small gain variation at wavelength of 1610 nm (1590nm). In this condition, the gain at 1610 nm varies from 8.5 dB to 12.3 dB by decreasing the input signal power from −10 to −40 dBm.

The gain spectra at input signal powers of 0 dBm and −30 dBm are shown in this figure while the 1480 nm pump power is fixed at 150 mW. For all input signal powers tested in a uni-directional scheme, the gain at longer wavelengths is higher than that at shorter wavelengths. From the result obtained for the forward scheme a small gain variation within 1575–1620 nm is observed. The gain peak for low and high input signal power is measured to be 11 dB and 7 dB at 1610 nm and 1605 nm respectively.

In the backward scheme at low input signal power the maximum gain is approximately 5 dB higher than that of the forward pumping. In contrast at high input signal power, the maximum gain is not much different when compared to that of the forward scheme.

Using a double pass configuration and a low input signal power, the gain can be increased to more than 9 dB within 1565-1600 nm. However, at a high input signal power, the gain from both configurations remains unchanged.

From the result obtained for the unidirectional configurations, the gain increases as the pump power increases. However a pump power of 160 mW is not capable of carrying the Bi-EDF into a complete inversion regime. In fact, for a complete inversion region given in Equation 3.1 and 3.2, the estimated gain value at 1610 nm is about 21.8 dB at signal power of 0 dBm. However for forward pumping scheme, the gain is measured to be below 4.8 dB at maximum pump power of 160 mW.

There are two kinds of saturation that affects optical amplifier performance. Signal-induced saturation occurs due to an insufficient number of pump photons to excite the RE ions in order to amplify a high power input signal, whereas ASE self-saturation is due to a high ASE power that dominates and competes with the signal photons. At low pump power the generated ASE is low. Therefore the effect of the signal-induced saturation is more significant. As the pump power increases, the inversion of the Bi-EDF is improved and generates a larger ASE power and overpowers the input signal. It is important to note that the backward ASE power is few times higher than the forward ASE power. Our results show that, an increase in the pump power at the input end will increase ASE power at input end. As a result this high power backward ASE acts as broad-band saturating signal that is capable to saturate the input signal, intensifies the ASE self-saturation effect and causes the gain to decline [61, 238-240]. Whereas adding an extra pump to the output end in backward pumping scheme leads to a gain growth because the ASE power distribution is more at EDF output end.

Utilising a high power pump source for the uni-directional scheme is not largely efficient for a long length of Bi-EDF although it can reduce the attenuation effects. According to Desurvire et. al. [180], the onset of ASE self-saturation is when the power ratio between saturated signal power P_{sat} and ASE power (P_{ASE}) is $P_{ASE}/Psat \approx 0.6$. The transition between signal induced saturation and ASE self-saturation for a signal power of 0 dBm (1 mW), can be evaluated by the pump power in which the backward ASE power is about 0.6 mW. Hence the gain for bi-directional pumping greatly depends on pump powers configuration.

Using maximum pump power for each pump and a minimum of −30 dBm for input signal power, a maximum gain of 32 dB around the peak of ASE spectrum is obtained for a bi-directional scheme. In this condition the gain of more than 20 dB is obtained within C+L band region. By increasing the input signal power to 0 dBm, the gain between 1560-1590 nm drops to 6.1-7.9 dB.

These results show that the ESA of Erbium ion in Bi-EDF is shifted to longer wavelengths compared to other host. This enables Bi-EDF to exhibit high flat-gain operation within a double bandwidth compared to Si-EDFA.

3.6.4 Noise-Figure Characteristics of Bi-EDFA

To fully understand the effect of pump power and signal wavelength on the noise figure (NF), experimental measurements are done first using a piece of 49cm long Bi-EDF for various schemes. Later, NF measurements that are needed to be done for the determination of the performance evaluation of a longer length of Bi-EDFA are presented.

Figure 3.13 shows that for a forward 1480 nm pumping scheme and a 49 cm long Bi-EDF the noise figure reduces with increasing pump power. The noise figure is observed to depend on the signal gain; wavelength and power whereby noise figure is lower if the gain is higher (see Figure 3.11).

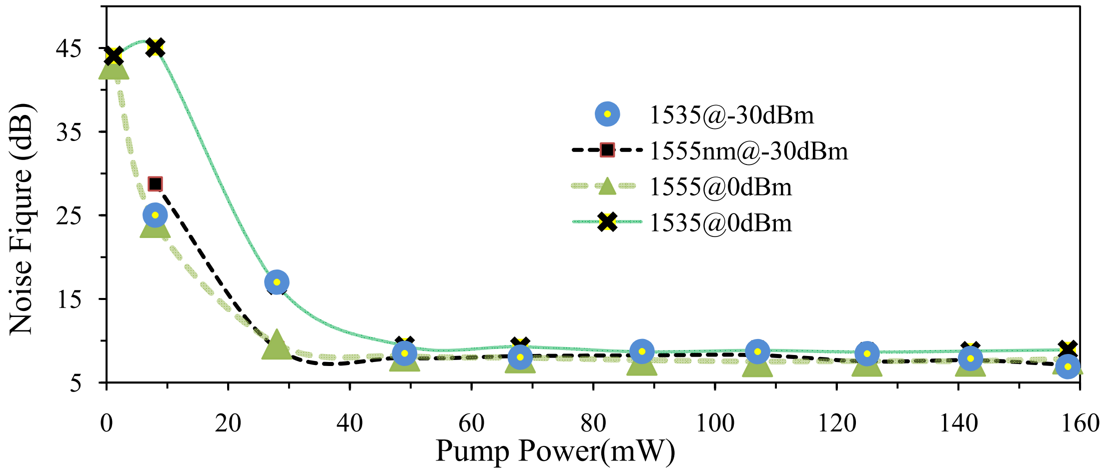

Figure 3. 13: Noise figure of C-band Bi-EDFA as a function of forward 1480 nm pump power. Signal power and signal wavelength are fixed in the figures.

The minimum noise figure of 6.8 dB is achieved for maximum pump and signal power at 1555 nm.

Figure 3.14 shows the noise figure spectra at low and high input signal powers (-30 dBm and 0 dBm) while the uni-directional pump power is fixed at 150 mW.

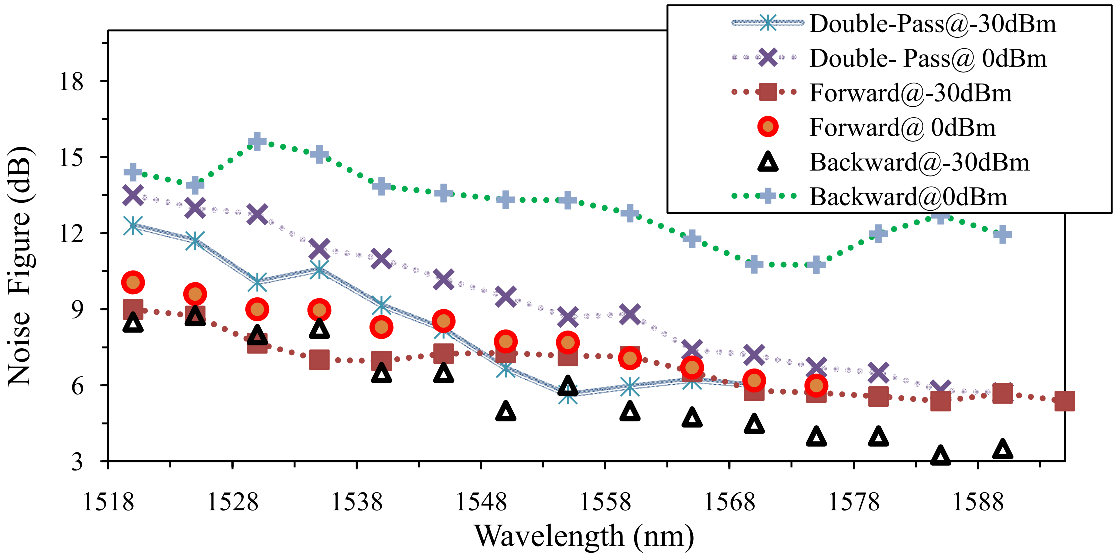

Figure 3. 14: Noise figure spectrum for Bi-EDFA in C-band region at input signal powers of -30 dBm and 0 dBm.

The maximum noise figure of 15.62 dB is observed at 1530nm region for a backward pumping scheme where the power of ASE is highest. In all schemes noise figure reduces with increase of the signal wavelength and reducition of the signal power. The noise figure is lower at -30 dBm compared to 0 dBm due to the enhanced gain at a lower signal power.

The noise figure performance in a double pass scheme is poor compared to forward pumping configuration due to the double-propagation of signal in the gain medium, which increases the ASE at the input part of the amplifier. This will reduce the population inversion, which in turn increases the noise figure. For a bi-directional scheme, noise figures at input powers of 0 and -30 dBm are respectively measured to be 6.1 and 5.8 dB when both pump powers are fixed at 100 mW.

We repeated the procedure leading to Figure 3.14 for a piece of 215 cm long Bi-EDF and the results are shown in Figure 3.15. Similar to the results obtained for C-band configurations, the noise figure is reduced with an increase of the pumping power. Thus the minimum noise is obtained at the maximum power. The noise figure spectra at input signal powers of 0 dBm and -30 dBm are displayed in the figure when the 1480 nm pump power is fixed at 150 mW for unidirectional schemes. For bi-directional pumping scheme, both pumps are fixed at 100 mW. From the figure, it is obvious that the noise figure reduces as the signal wavelength increases.

As illustrated in Figure 3.9, the ASE power for L-band Bi-EDFAs is highest at the 1560 nm region, which contributes to a higher noise figure at this region. Note that, the noise figure decreases as the input signal power decreases due to the higher gain obtained at lower input signal powers. However, for input signal power of less than -20 dBm the experimental results show a small variation of less than 0.5 dB in the noise figure. At this constant gain region the minimum noise figures at 1610 nm are measured to be approximately 3.0 dB for a forward pumping scheme.

In the case of the backward scheme, the noise figure is slightly higher with small input signal power and the minimum noise figure of 4.4 dB is observed at 0 dBm input power.

On the other hand, the double pass system has a higher noise figure compared to that of the single pass system particularly at 0 dBm. The NF penalty observed within 1550- 1610 varies from 3.3 to 5.8 dB nm. This penalty is attributed to higher counter-propagating ASE at the input part of the amplifier which reduces the population inversion particularly at the high input signal power.

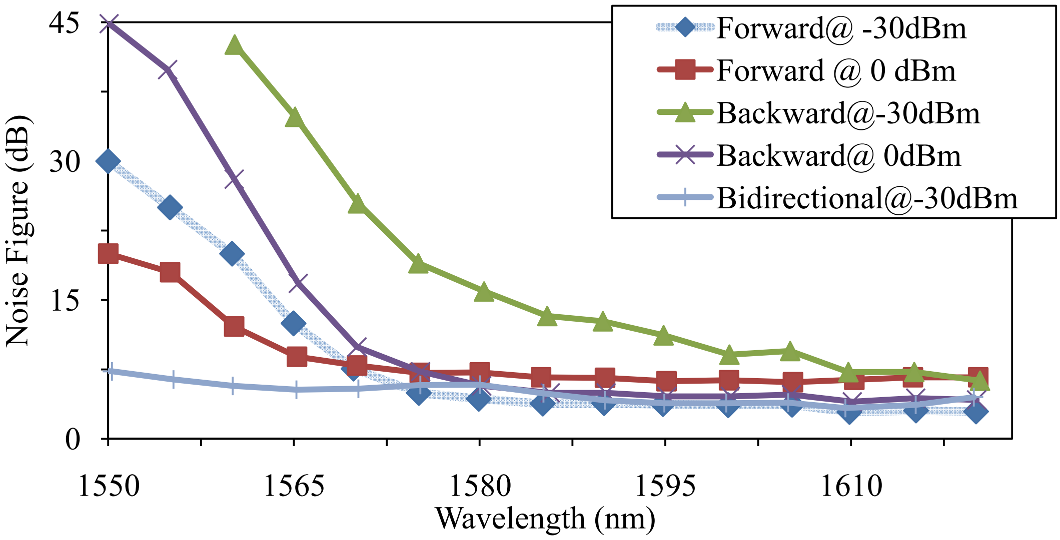

Figure 3. 15: Noise figure spectrum for L-band Bi-EDFA at low and high input powers for different pumping configurations.

For a bi-directional system a noise figure of less than 9 dB is obtained within the spectral bandwidth. Using a signal power of -30 dBm in this experiment, the total pump power is fixed at 240 mW. However, above -15 dBm the gain is much smaller and thus increases the noise figure.

3.6.5 Quantum and power conversion efficiency (QCE)

Another feature of interest is the quantum conversion efficiency (QCE) which is conversion efficiency of pump photons into signal photons. The L-band or C-band Bi-EDFA performance can be expressed in terms of optical QCE. The QCE is defined as:

$$QCE = (\lambda_s/\lambda_p)((P_s^{out} - P_s^{in})/P_p^{in}) \qquad (3.13)$$

where λ_p and λ_s are the pump and signal wavelengths, P_s^{out} and P_s^{in} are the signal output and input powers, respectively and P_p^{in} is the pump power [61]. The QCE of the Bi-EDF reveals a dependence on pump configuration rather than the amount of launched pump power. A comparison of QCE spectra for two different lengths of Bi-EDF at the highest value of the forward pump power, i.e. 160 mW is shown in Figure 3.16.

Although the 1480 nm pump wavelength has been reported [182, 241] as an optimum pump band for high conversion efficiency of the conventional EDF, in a high Er^{3+} ion concentration, the maximum QCE for 49 cm and 215 cm long of Bi-EDF are estimated to be approximately 17.0% and 23.5% which is obtained at 1560 nm and 1605 nm.

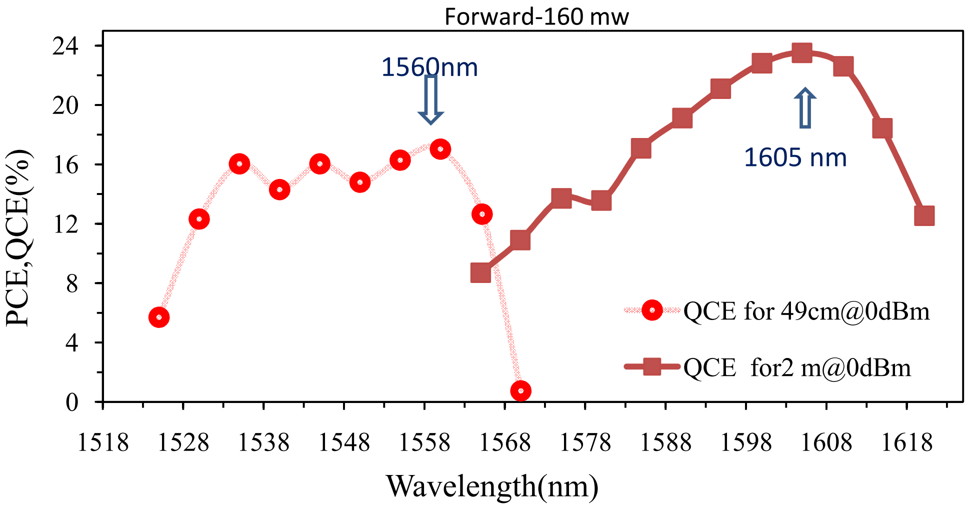

Figure 3. 16: Comparison of the QCE spectra at input signal power of 0 dBm between a C-band Bi-EDFA and a L-band Bi-EDFA.

3.7 CW LASER CHARACTERISTICS

This section, demonstrates a Bi-EDF ring laser using all components shown in Figure 3.17, with the exception of a tunable band-pass filter (TBF) which is incorporated in the next setup to provide tunability in the output wavelength.

The proposed laser consists of an isolator, a piece of Bi-EDF, a wavelength selective coupler (WSC) and an output coupler. The Bi-EDF is backward-pumped by a 1480 nm laser diode, via a WSC to provide a gain in either C or L-band region depending on the length used. The laser output is tapped from coupler and characterized by an OSA with a resolution of 0.07 nm. In the figure, the ratio represents the percentage of oscillating laser power, which is extracted from the laser system. The experiment is carried out for various coupling ratios of the output coupler.

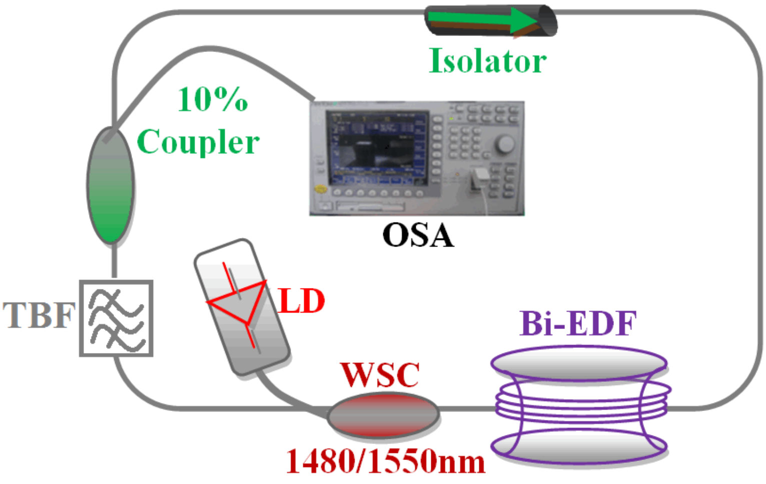

Figure 3. 17: Configuration of the proposed Bi-EDF based tunable laser source (TLS).

The slope efficiency and operating wavelength of the laser is determined by the Bi-EDF gain spectrum and the cavity loss. As shown in Figure 3.18 at a fixed pump power (of 160 mW) the operating wavelength shifts to a shorter wavelength as the extraction ratio or cavity loss increases. Also, as shown in the Figure, the operating wavelength shifts toward the longer wavelength with using longer Bi-EDF. This is due to the fact that the gain spectrum of the Bi-EDFA peaks at the longer wavelength in the longer length of the fiber. The gain peak of 1535 nm for 49 cm long Bi-EDF is shifted to 1595 nm for 215 long Bi-EDFA. Similarly, the gain peak is shifted to a longer operating wavelength in a resonator as shown in the figure, due to the wavelength dependence of the insertion losses for used components and an increase of the effective fiber length.

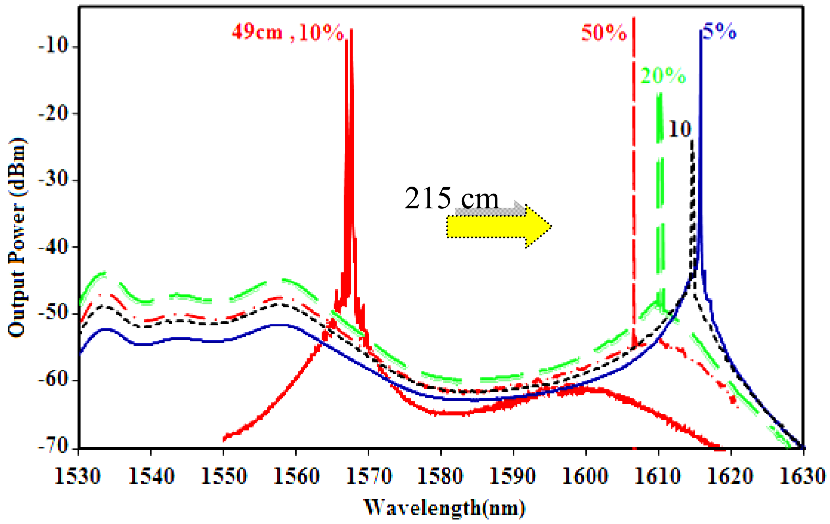

Figure 3. 18: Spectral profile of the proposed ring laser without TBF for different lengths of Bi-EDF (i.e. 49 cm, 215 cm) and various output coupling ratios. The 1480 nm pump power is fixed at 160 mW.

3.7.1 CW Tunable Ring Laser Using Bi-EDF

Recently, EDF based ring fiber lasers have also been demonstrated with a tunable single wavelength operation [242]. These lasers provide a high signal to noise ratio within wide tuning range. In this section, a ring resonator is presented using a reduced length of Bi-EDF to generate narrow-bandwidth tunable laser signals. A configuration of the proposed laser is shown in Figure 3.17. The proposed tunable fiber ring laser can be continuously tuned at high speed using just one TBF and a proper length of Bi-EDF. The thin film coating interference filter in the TBF has a high tuning resolution of 0.05 nm. This TBF will be also used as a inter-stage component for sideband noise suppression [243] in the next chapter. Figure 3.19 shows the output power and spectra at different laser wavelengths for maximum pump power.

With a unidirectional pumping scheme and using a 49 cm (or 215 cm) long Bi-EDF in the setup, the operating wavelength can be tuned from 1535 to 1575 nm (or 1540- 1620 nm). The tuning range for a 49 cm long Bi-EDF can be extened larger than 70 nm using bi-directional scheme. Finally by using an optical switch in the setup the Bi-EDF length can be altered and the tuning range can be extended to a range larger than 100 nm.

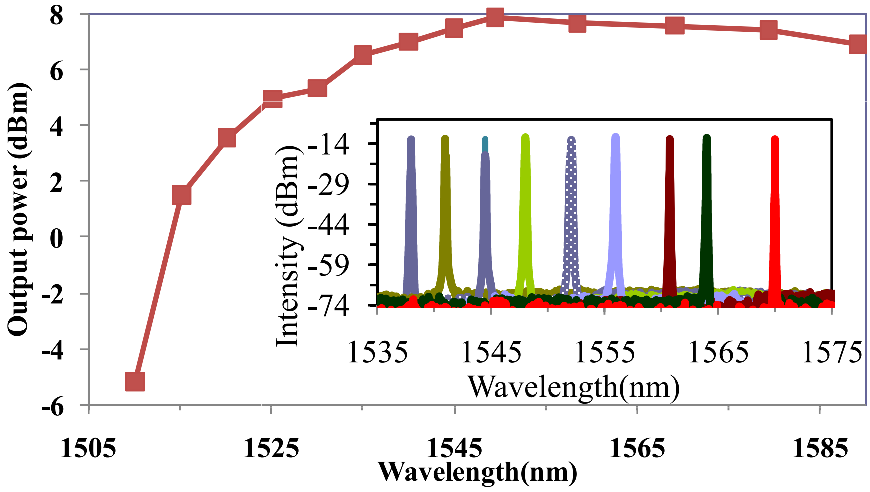

Figure 3. 19: Output power versus lasing wavelength at fixed pump power for a 49 cm long Bi-EDF laser. Inset shows the output spectra at different laser wavelengths covering from 1535 to 1580 nm by an OSA at a resolution of 0.07 nm.

As shown in the figure, the extinction ratio of better than 55 dB is achieved throughout the entire tuning range. The measured bandwidth (FWHM) of this multi-longitudinal mode laser is 0.09 nm. The output is suitable for testing and gain measurement in the next chapter.

3.7.2 Bi-EDF-Based Brillouin Laser (BEFL)

To reduce the length of the gain medium of BFL, a single wavelength BFL is proposed and successfully demonstrated using only a short long Bi-EDF as the gain medium. The experiment is carried out for two different Bi-EDF lengths (i.e. 49 cm and 215 cm) for operations in both C- and L-band regions.

The experimental setup of the Bi-EDF based BFL (BEFL) is shown in Figure 3.20.

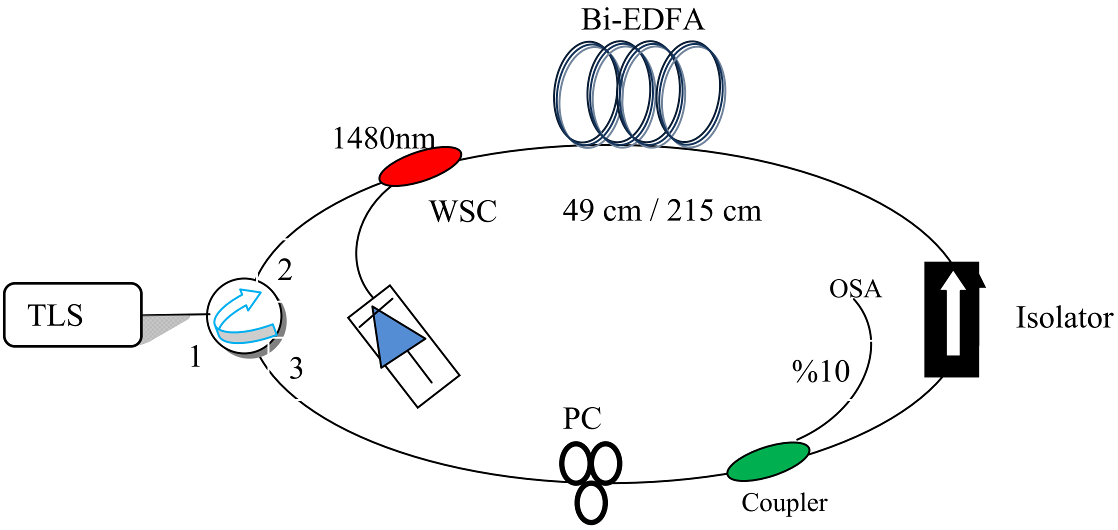

Figure 3. 20: Configuration of a Bi-EDF based Brillouin fiber laser.

To generate and amplify the backward-propagating Brillouin Stokes, a signal power acting as a Brillouin pump (BP) from an external-TLS is injected into the ring cavity via optical circulator. The output of this TLS has a linewidth of approximately 20 MHz. The output of the cavity is tapped from the 90/10 coupler and characterized by an OSA.

To avoid the FWM effect, and also to prevent the generation of anti-Stokes and to ensure a unidirectional operation of the BFL, an isolator is used in the cavity.

In the proposed scheme a short length of the Brillouin gain is used. However, due to the small Brillouin gain and the SBS threshold requirements, the pump power cannot be efficiently converted to the Stokes unless the operation wavelength is set near the free-running laser peak. Hence, the BP wavelength is injected to cavity at 1615.7 nm and 1567 nm for 49 cm and 215 cm long Bi-EDF respectively.

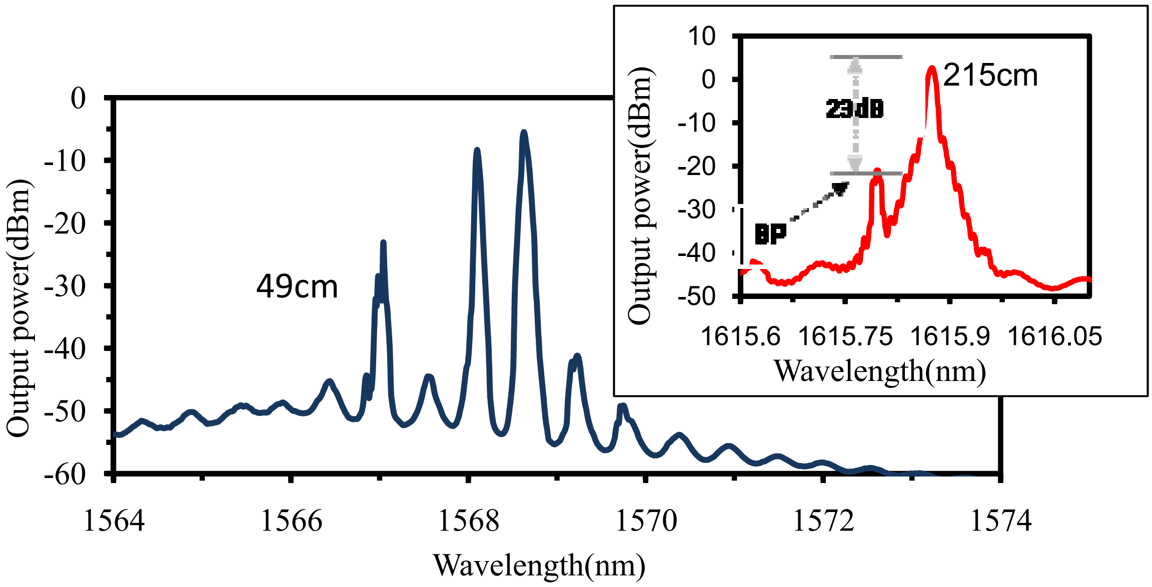

Figure 3. 21: Stimulated Brillouin multi-wavelength laser in 49 cm long Bi-EDF. Inset shows stimulated Brillouin stoke in 215 cm long Bi-EDF.

Figure 3.21 shows the output spectrum of the BEFL for two different lengths of Bi-EDF at the maximum pump power of 150 mW. For a piece of 49 cm long Bi-EDF, and a BP wavelength of 1567 nm, the output spacing is obtained at around 0.50

nm. Meanwhile, anti-stoke is also generated through FWM between the stoke lines and BP.

The number of lines in the spectrum is limited by the availability of the 1480 nm pump power, insufficient gain, fiber nonlinearity, coherence length and polarization filtering effect in the cavity as well as the length of the ring cavity.

By using a 215 cm long Bi-EDF, stimulated Brillouin scattering appears under BP wavelength of 1615.77 nm. This length of Bi-EDF is nearly four times longer than the previous case. Compared to the short long case this setup has about twice threshold power. Single stimulated Brilluoin scattering with a SMSR higher than 23 dB and an output spacing of about 0.08 nm is achieved above threshold power of 87 mW.

The spacing between the BP and the BFL is obtained at approximately 10-11 GHz, which is equivalent to the Stokes shift in the SMF. Brillouin multi-wavelength generation has two distinct advantages over other multi-wavelength method; a constant spacing and narrow linewidth.With optimizing the state of polarization and employing a dispersion compensator fiber, the numbers of generated lines increases up to 15 lines due to efficient phase-matching [57].

3.7.3 Incorporation Effect of PCF in a Ring BEFL

The effect of PCF incorporation on the BEFL performance is also investigated. Since the Brillouin gain coefficient (between $4.5\text{-}5.0\times10^{-11}$ m/W) in the standard SMF is very small, the PCF as a nonlinear gain medium is replaced with existing SMF between PC and the circulator to improve the FWM process in the system.

The 20 m long PCF used as a nonlinear gain medium has a cut-off wavelength of 1000 nm, a MFD of 4.2 μm near ZDW of 1040 nm, and a fiber nonlinearity (γ) of more than 11 $(W.km)^{-1}$.

Under 1480 nm pumping and a power of 150 mW, the BP wavelengths of 1559.1 nm and 1611.3 nm are injected into this new configuration. A single wavelength BEFL is successfully achieved using only a 49 cm long Bi-EDF with a peak power of -11.84 dBm at a BP power of 7 dBm. The narrow linewidth output is expected to have a low technical noise.

As shown in Figure 3.22, a SMSR around 12.4 dB and an output spacing of 0.08 nm are obtained in this setting. It was observed that at BP power below 0.5 dBm, there is no SBS. The threshold power is also observed to be lower when a longer PCF is used. It was also found that the Stokes power begin to saturate as the BP power increases above 4 dBm.

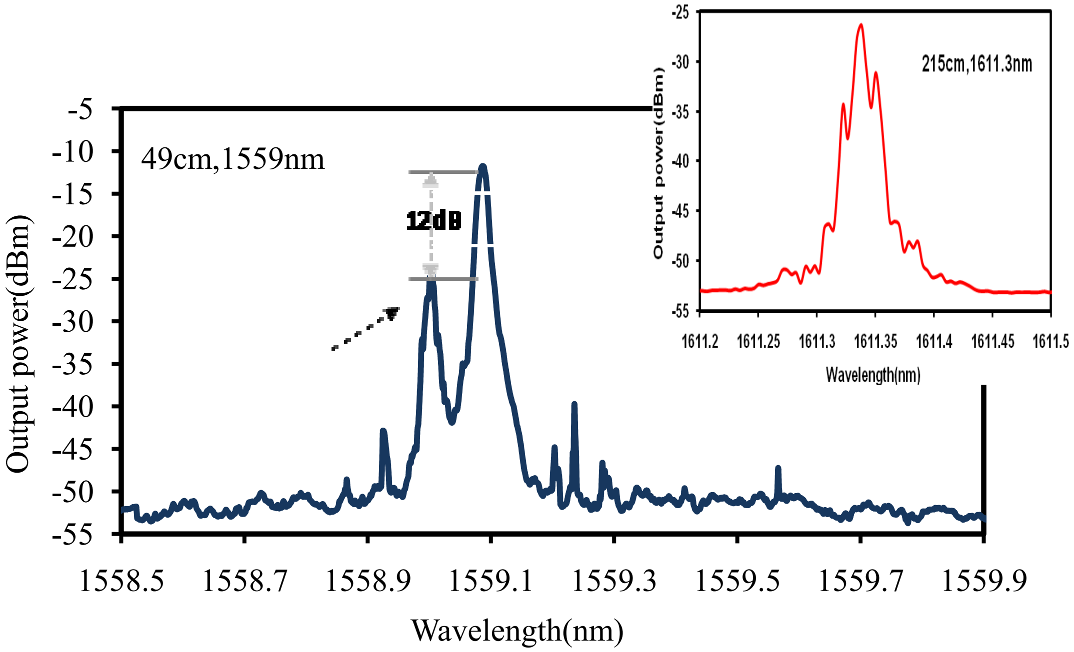

Figure 3. 22: Output spectra of the Bi-EDF based BEFL with a intracavity PCF. The BP power and 1480 nm pump power is fixed at 7 dBm and 150 mW respectively.

The odd-order Stokes and anti-Stokes lines appeared weak due to, the counter propagating feature of SBS process, and the unidirectional aspect of the ring cavity. For a longer Bi-EDF in the cavity pump power is not sufficiently high and and thus no Stokes is achieved.

No lasing was observed when only a 20 m long PCF is used in the setup. Although the longer PCF in the cavity increases the cavity's loss however, it provides a better nonlinearity characteristic to achieve an efficient SBS. The side mode suppression ratio of the BFL and the number of anti-Stokes lines are also increased when a longer PCF is used.

In chapter five, the theory of mode locking is reviewed and using the result of Bi-EDF discussed, passive mode locked laser utilizing saturable absorber and nonlinear polarization rotation technique are described. The optimized experimental configuration with the shortest and the most stable pulse train are then represented.

CHAPTER 4

EXPERIMENTAL AND NUMERICAL INVESTIGATION OF GAIN CHARACTERISTICS OF HIGH POWER CLADDING-PUMPED Er^{3+}/Yb^{3+} FIBER LASERS AND AMPLIFIERS

Fiber lasers have multiple scientific applications in research areas including: sensing, atom cooling, interferometry, spectroscopy and nonlinear optical conversion. They also are useful in medicine applications such as microsurgery and optical coherence tomography, which requires broadband sources [244].

Recently, research on CW single transverse mode fiber lasers and amplifiers has opened up new opportunities for developing microphotonic devices such as resonators, couplers, sensors and loop interferometers. CW single transverse mode lasers and amplifiers have been demonstrated with output powers in the kilowatt regime and linewidths of about 10-20 nm [245]. Multi-mode output have also been developed to achieve output powers in several tens of kilowatts, while in the pulsed regime, MW peak power and multi-mJ energy have been achieved [246]. These broad linewidth pose no problems in materials processing and are mainly obtained in the 1-1.1 μm [247].

4.1 MASTER OSCILLATOR POWER AMPLIFIER

The Master Oscillator Power Amplifier (MOPA) approach allows the scaling of lasers to high powers while preserving the spatial and temporal coherence of the master oscillator. However, oscillators are very effective in extracting high output power due to their relatively simple and compact arrangement. MOPA are also employed because they are highly refined and show excellent control on output characteristics [248].

The advances in MOPA are planned to be utilized as compact sources which offer many options (e.g. frequency-tuning, single-frequency, plane-polarized, or pulsed sources with various durations and repetition rates). Hence, low power seed sources are designed accordingly to meet these options. Recently, high power fiber systems with good atmospheric transmission in eye-safe wavelength region have also received great attention. Amplifiers in this region have many potential applications in booster amplifier for long haul repeaterless optical links, in head end amplifiers for CATV distribution architectures and as amplifiers for 1× N loss less splitters [249]. However, coherent laser sources with both low intensity and frequency noise are an essential requirement in many applications such as coherent optical communication and LIDAR detection, wavelength conversion, high-resolution spectroscopy, interferometric sensing and fiber gyros. On the other hand, some applications such as gravitational wave detection, gyroscopes [126], temperature sensors [250], and digital or analogue optical transmission require high power narrow linewidth lasers and in some other applications there is a need for stable electric signals ranging from hundreds of gigahertz to terahertz with dual frequency narrow linewidth lasers [251].

Generation or amplification of light pulses to high energy levels is another interesting feature of RE doped fibers, which is difficult in Yb-free erbium doped fibers. There are some other key issues such as suppression of nonlinear scatterings (e.g. SBS, SRS, SPM, and XPM) and add-on options for the spectral or temporal control of such high-power sources.

The high output power can be achieved by exploring efficient, high power pump light sources, co-dopants and novel fiber designs for effective absorption of pump power[252].

Optimization of fiber material to improve the effectiveness of absorption can be achieved by co-doping Ytterbium ions into the erbium-doped fiber as a sensitizer and double cladding the fiber structure for expanding the aperture of the pump light[253]. Such a fiber is called Erbium-Ytterbium doped fiber (EYDF) and has several advantages [254].The double clad structure increases the amount of pump power coupled to the fiber.

In this chapter, the performance of double-clad structure high power EYDF laser and amplifier, pumped by using 927 nm multimode laser diodes are investigated experimentally and theoretically. The systems are capable of driving up to three laser diodes so that depending on the operating regime, different operation modes are available.

The EYDFA operates efficiently using multistage configurations. Instead of multistage configuration, the double pass scheme is proposed in this work to increase the pump conversion efficiency of the amplifier. A broadband fiber Bragg grating is used in the double-pass EYDFA to allow a double-propagation of the test signal in the gain medium and thus improves the gain and output power characteristics of the amplifier.

In the theoretical analysis, the energy levels, transitions, the rate and power propagation equations are presented and solved to examine the effect of fiber length on the bandwidth of the gain spectra as well as to find the optimum fiber length. It is shown that the calculated output power is in good agreement with the experimental results, verifying the feasibility of our theoretical model.

A narrow linewidth, and highly efficient tuneable Brillouin fiber laser amplified by Er^{3+}/Yb^{3+} co-doped double-clad fiber amplifier (EYDFA) is also demonstrated. The linewidth specification of the output spectrum of such narrow linewidth source is experimentally measured by heterodyne beat technique and compared with its Brillouin pump and presented Bi-EDF based (tuneable ring) fiber laser. The proposed EYDFA is also utilized for ultrashort laser pulse amplification. The results presented in this chapter have been published by the author as regular papers in [255-257].

4.2 CLADDING DESIGNS AND LIGHT INJECTION METHODS

Fiber lasers based on double-clad fibers can be seen as brightness converters. which convert light from multi-mode semiconductor pump source into sources with high beam quality suitable for tight focusing as well as long working distances,.Double-clad fibers have a secondary lower index, outer, cladding which provides a multimode waveguide for, high power multiple multimode laser diodes. The pump light propagates in the fiber and is absorbed in the core region for the amplification of the signal (see Figure 4.1).

In general, the advantage of cladding-pumping schemes is that they have a high thermal tolerance for high-power operations. Particularly for high thermal resilience all-glass double-clad fibers with RE-doped pure-silica core, fluorine doped silica glass outer cladding and pure silica inner cladding, one can achieve a low propagation loss for pump light with a maximum numerical aperture of about 0.3.

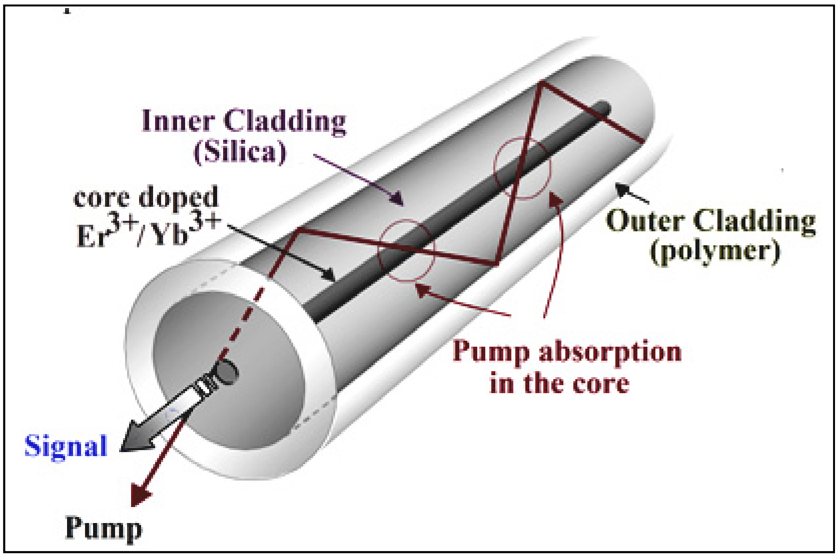

Figure 4. 1: Working principle of a double-clad fiber. The pump light (Brown) propagates in the inner cladding while amplified signal or cavity power lasing (in gray) occurs in the core.

With a fluoro-acrylate or a silicone polymer outer cladding, numerical aperture can be increased up to 0.5 and up to more than 0.7 in case of a Jacketed Air-Clad fiber [258, 259]. It is important to note that, the low brightness of the pump source and the maximum ion concentration permissible in silica fiber, leads to a low pump absorption in a double-clad fiber, specially [260] for low peak absorption cross-section of Er^{3+} ions.

Power scaling at 1.5–1.6 µm relies on the double-clad fiber structure together with ytterbium co-doping. Co-doping, which is particularly important in systems with significant ground-state absorption, improves the undesirably low pump absorption, reduces the threshold power, prevents the formation of Erbium clusters and effectively controls the upconversion from $^4I_{13/2}$ level so that a higher doping level can be used [261, 262]. The pair induced energy transfer from Ytterbium to Erbium provides an efficient indirect pumping mechanism. Ytterbium ions, which have a high absorption at wavelengths between 900 nm and 1000 nm, absorb pump light and transfer their energy to erbium ions through a non-radiative cross-relaxation effect [263].

The pump absorption rate in a cladding-pumped scheme is much lower than the intrinsic core absorption because of the small overlap between the pump beam and the doped core. Cladding absorption of the pump is proportional to the ratio of core area (A_{core}) over the inner cladding area (A_{clad}). Thus, it can be expressed as $\alpha_{clad} = \alpha_{core} \times A_{core} / A_{clad}$ where α_{core} is the pump absorption coefficient in the core. This can result in the degradation of pump conversion efficiency and also limits the range of operating wavelengths in so far as ground-state absorption is significant. For very high power systems, large and slightly multimode cores can be used to reduce the intensity of the core center and to increase pump conversion efficiency. Hence these fibers will enhance the SRS and SBS threshold powers and postpone the output power rollover caused by nonlinear effects to a later stage in power scaling.

Another important aspect of the cladding design is to use inner cladding shapes that do not support skew modes for efficient mode mixing [264]. For example by eliminating the skew propagation in the cladding which does not contribute to pumping process, the pumping efficiency over the rare earth-doped core increases. An additional advantage of star shape inner cladding is improving splice ability.

Depending on the fiber geometry, the choice of pumping scheme (e.g. side pumping, end pumping and hybrid schemes) is important as this, together with the pump brightness, determine the maximum coupled pump power. With a passive tapered fiber bundle (TFB) scheme [265], the maximum number of injection points is limted to the two fiber ends of double clad RE-doped fiber. For other injection methods such as V-groove side pumping [266], colinear coupling [267, 268] and fused taper side coupling [269], the power scaling ability is poor or they are quite similar to the tapered fiber bundle in their design and handling capabilities. However, all-fiber schemes such as TFB are preferred as it reduces the number of bulk optic components.

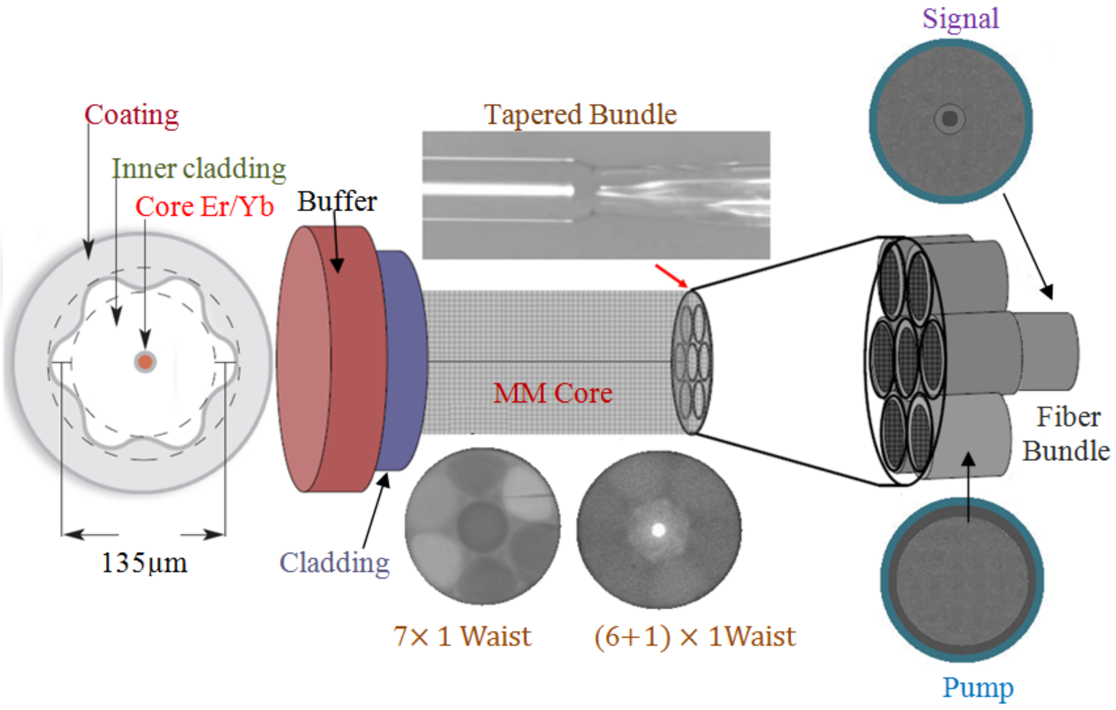

Figure 4. 2: (Left) Double clad EYDF with star shape silica inner cladding,(right) TFB.

All the active and passive double clad fibers tested in this chapter have star inner claddings with polymer outer claddings as the fibre coating. Their tough, low-index polymer coatings maintain their strength and give them a high cladding numerical aperture (NA) of ~0.45 while their small core NAs of ~ 0.17 lead to a small beam size and high power single mode operation. As shown in Figure 4.2, the double clad EYDF spliced to TFB has a star shape silica inner cladding with a wide pump wavelength window from 910 to 1060 nm.

4.3 ENERGY LEVELS OF Er^{+3} AND Yb^{+3} IONS

In this section, we proposed a versatile analytical technique for investigating the characteristics of the EYDF which follows the approach of cooperative energy transfer from Ytterbium to Erbium ions [253]. Figure 4.3 shows the energy level diagram for the EYDF amplification system.

Depending on the pump wavelength pump photons ($h\nu_p$) can be absorbed by Yb^{+3} ions in the level $^2F_{7/2}$ and/or Er^{3+} in the $^4F_{15/2}$ level and excite them into the $^2F_{5/2}$ level. From there, a cooperative energy transfer process between the Yb^{3+}excited state and the Er^{3+}ground state in the $^4I_{15/2}$ level excites the Er^{3+} to the $^4I_{11/2}$ level, while simutantuosly de-excites the Yb^{3+} to its ground state. Since the excited energy level of $^4I_{11/2}$ is unsteady, Er^{3+} ions quickly relax to the meta-stable level $^4I_{13/2}$. Compared to the lifetime of the $^4I_{13/2}$ meta-stable state (τ_{Er}), the lifetime of the $^4I_{11/2}$ excited state (τ_{32}) is in the order of ns which is very short.

In contrast, in the glass hosts with various co-dopants, τ_{Er}varies in the range of 8–10 ms. Co-doping with phosphorus is required to shorten the lifetime of $^4I_{11/2}$ and to increase the nonradiative relaxation rate of $^4I_{11/2}$ to $^4I_{13/2}$ compared to the back transfer process. This work can increase energy transfer efficiency up to 85%. However, EYDFs are significantly less efficient than ytterbium-doped ones [7]. This is mainly due to the relatively large quantum defect and some problematic issues related to spurious Yb emission at 1–1.1 μm and excessive thermal load. There is another energy transfer process between two ions at the $^4I_{13/2}$ metastable level as a cooperative upconversion (CUC) process. The energy transfer mechanism including (CUC) process is shown and marked with (g) in Figure 4.3.

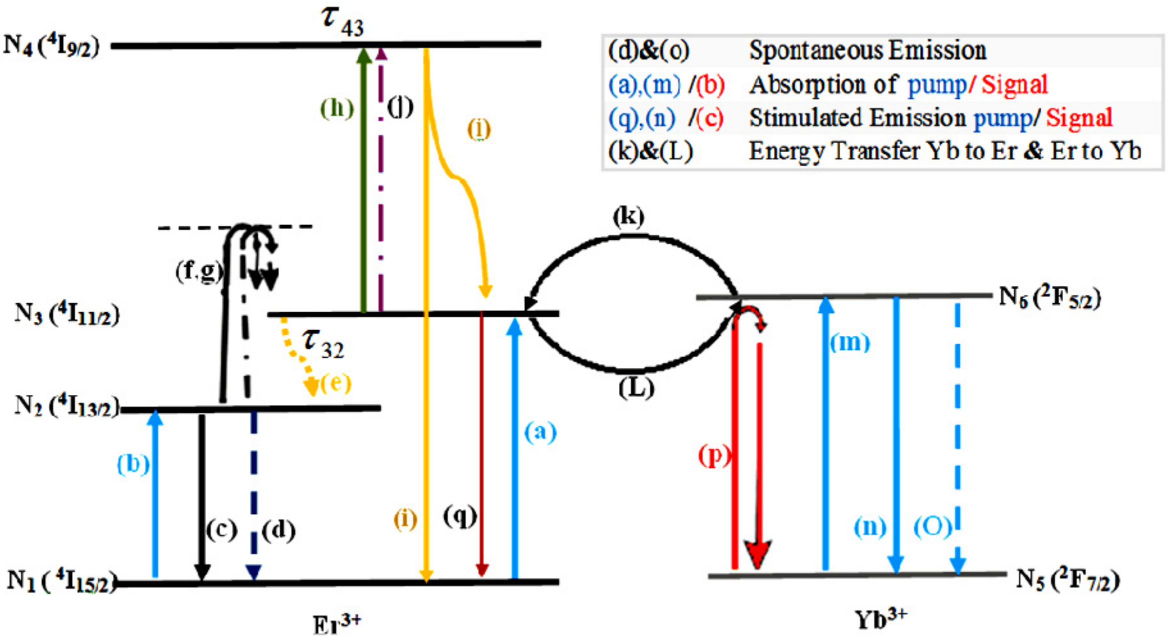

Figure 4. 3: Energy level diagram for the EYDF amplification system. Dashed lines (d),(o) are used for spontaneous emission. Inset determines the transitions related to the absorption and stimulated emission of pump and signal as well as energy transfer between Er and Yb.

Besides, the emission at our targeted transition band, detrimental emissions (R_{41}) in the visible can be also obtained due to Er^{3+} cooperative upconversion processes, which allow energy to be transferred to excited Er^{3+} ions so that they depopulate ions at the $^4I_{13/2}$ level, however. These transitions can be useful for upconversion lasers and temperature sensing [270]. Glass hosts with low phonon energies such as bismuth glass (≈ 500 cm^{-1}) have an efficient pump photon energy transfer process that produces the upconversion of visible fluorescence. However, as explained by Oprea et al., they waste pump photons as vibrational energy and therefore less pump energy can be transferred to the signal [271]. As a result, these glass hosts can be used in optical amplifiers with a wide fluorescence bandwidth and a moderate gain [272].

The main transitions are shown in inset of Figure 4.3 and the mechanisms behind other transitions have been summarized in Table 4.1. In the figure $h\nu_s$, $h\nu_{green}$ and the unassigned $h\nu$ indicate photons at the signal wavelength, at the observed green region and at any possible spontaneous emission wavelength, respectively.

Table 4. 1: Transitions description in Figure 4.3.

(#) Type of Transition	Detail of Transition
(E) Non-radiative Decay	$Er_3 \rightarrow Er_2$ +phonons
(F) ESA (Signal) and Fast Decay	$Er_2 + h\nu_s \rightarrow Er_3$ + phonons
(g) CUC and Fast Decay	$Er_2 + Er_2 \rightarrow Er_1 + Er_3$+ phonons
(h) ESA (Pump)	$Er_3 + h\nu_p \rightarrow Er_4$
(i) Radiative and Non-radiative Decay	$Er_4 \rightarrow Er_3 + h\nu_{green} + Er_1$+phonons
(j) CUC	$Er_3 + Er_3 \rightarrow Er_1 + Er_4$
(p) Absorp & Nonrad.Trans.In Quenched Ions	$Yb_5 + h\nu_p \rightarrow Yb_5$ + phonons

4.4 BASIC EQUATIONS AND MODELING

The Er^{3+} system consists of four levels as shown in Figure 4.3. However, the $^4I_{9/2}$ level can be assumed to be empty. This is because, τ_{43} is actually almost instantaneous. Let us denote the $^4I_{15/2}$, $^4I_{13/2}$, $^4I_{11/2}$ and the $^4I_{9/2}$, states of Er^{+3} as levels 1, 2, 3, and 4, and the $^2F_{7/2}$ and the $^2F_{5/2}$ states of Yb^{+3} as levels 5 and 6 and their electron concentrations of energy levels as N_1, N_2, N_3, N_4, N_5 and N_6, respectively.

The total concentrations of Er^{+3} and Yb^{+3} are $N_{Er}=N_1+N_2+N_3$ and $N_{Yb}=N_5+N_6$, respectively where under the uniform dopant and the steady state condition, the numbers of Er^{3+} and Yb^{3+} ions on the corresponding levels are functions of the longitudinal coordinate Z of the fiber.

Moreover fractional excitated Er^{+3} and Yb^{+3} ions population respectively are defined as $n_{Er} = N_2^{Er} / N_{Er}$ and $n_{Yb} = N_2^{Yb}/N_{Yb}$. For efficient energy transfer, the concentration ratio is chosen between $10 < N_{Yb}/N_{Er} < 20$ because the low Yb^{3+} concentration will not prevent the formation of Er clusters. Hence, they will act as quenching centers where rapid upconversion takes place. On the other hand a very high ratio changes the properties of the silica glass medium and energy will be lost to Yb^{3+} fluorescence. The rate equations are simplified to [273-275] :

$$\frac{dN_1}{dt} = \frac{N_2}{\tau_{21}} - W_{12}N_1 + W_{21}N_2 - R_{13}N_1 + C_{up}N_2^2 + C_{up}N_3^2 - C_{cr}N_1N_6 \tag{4.1}$$

$$\frac{dN_2}{dt} = \frac{N_3}{\tau_{32}} - \frac{N_2}{\tau_{21}} - W_{21}N_2 + W_{12}N_1 - 2C_{UP}{N_2}^2 \tag{4.2}$$

$$\frac{dN_3}{dt} = -\frac{N_3}{\tau_{32}} + R_{13}N_1 - C_{cr}N_3N_5 + C_{cr}N_1N_6 - 2C_{UP}{N_3}^2 \tag{4.3}$$

$$\frac{dN_6}{dt} = -\frac{N_6}{\tau_{65}} + R_{56}N_5 - R_{65}N_6 + C_{cr}N_3N_5 - C_{cr}N_1N_6 \tag{4.4}$$

where τ_{ij} denotes the spontaneous transition rate between levels i-th and j-th. Here W_{ij} and R_{ij} terms represent the stimulated transition rates. In particular, W_{12} and W_{21} are the signal absorption and emission rates of Er^{3+}, respectively. Moreover R_{13}, R_{56} and R_{65} are the pump absorption rate of Er^{3+}, the pump absorption and emission rates of Yb^{3+}, correspondingly. While, the cross-relaxation or energy transfer coefficient from Yb^{+3} to Er^{+3} ions and up-conversion coefficient are given by C_{cr} and C_{up}, respectively [276]. In the model, C_{up} is calculated using Snoek's method [276] .

In the above equations the expressions account for uniform up-conversion are displayed with $C_{up}\times N_2^2$ and $C_{up}\times N_3^2$ while the $C_{cr}\times N_3N_5$ and $C_c\times N_1N_6$ terms represent the energy transfer between Er^{3+} to Yb^{3+} and Yb^{3+} to Er^{3+}, respectively [276]. The field distribution of the LP_{01} mode ($E(r,\nu)$) can be normalized and its value can be calculated using:

$$2\pi\int_0^\infty \left|E(r,\nu)\right|^2 rdr = 1 \tag{4.5}$$

Therefore, the transition rates are given by:

$$\begin{aligned} R_{ij}, W_{ij} = {} & \tfrac{\sigma_{ij}(\nu_{p,s})}{h\nu_{p,s}} p_{p,s}(z)\left|E(r,\nu_{p,s})\right|^2 + \\ & \int_0^\infty \tfrac{\sigma_{ij}(\nu)}{h\nu}[P_{ASE}^{+}(z,\nu)+P_{ASE}^{-}(z,\nu)]\times\left|E(r,\nu)\right|^2 d\nu \end{aligned} \tag{4.6}$$

and the steady state evolutions of signal, pump and ASE powers along the EYDF are described by the power propagation equations:

$$\frac{dP_S}{dz} = [\Gamma(\nu_s)(\sigma_{21}(\nu_s)N_2(z)-\sigma_{12}(\nu_s)N_1(z))-\alpha_S(\nu_s)]P_S(z) \tag{4.7}$$

$$\frac{dP_P}{dz} = [\Gamma(\nu_p)(\sigma_{65}(\nu_p)N_6(z)-\sigma_{56}(\nu_p)N_5(z)-\sigma_{13}(\nu_p)N_1(z))-\alpha_P(\nu_p)]P_p \tag{4.8}$$

$$\begin{aligned} \frac{dP^{\pm}{}_{ASE}(z)}{dz} = {} & \pm h\nu_p\Delta\nu\Gamma_p(\nu_p)\sigma_{65}(\nu_p)N_6(z)\pm \\ & [(\Gamma_p(\sigma_{65}(\nu_p)N_6(z)-\sigma_{56}(\nu_p)N_{56}(z)))-\alpha(\nu_p)]P^{\pm}{}_{ASE} \end{aligned} \tag{4.9}$$

where h, c, υ_P and ν_S denote Planck's constant, the speed of light in vacuum, the pump and signal frequencies respectively. The frequency-dependent background loss of the active fiber $\alpha(\nu)$, power filling factors for pump Γ_P and signal (Γ_S) lights are also set from table 4.2. The evolution of the signal ($P_S(z)$) and pump ($P_p(z)$) powers in the fiber are given by Equations (4.7)-(4.8) and the signs of ‘‘+’’ and ‘‘-’’ in the above equations indicate the propagation directions of the ASE light ($P_{ASE}^{\pm}(z)$).

In the set of coupled equations, $\sigma_{12}(\nu_s)$and $\sigma_{21}(\nu_s)$ are the absorption and emission cross-sections at the signal frequency (ν_s) for the Er^{3+} ions while $\sigma_{56}(\nu_P)$ and $\sigma_{65}(\nu_P)$ are the absorption and emission cross sections for the Yb^{3+} ions at the pump frequency (ν_P).The subscript of ASE stands for the ASE and $\sigma_{13}(\nu_P)$ is the absorption cross-section of Er^{3+} ions at pump frequency (ν_p). Finally in the ASE equation, $\Delta\nu$ represents the effective ASE bandwidth that is the resolution of the measuring device (e.g. OSA).

4.4.1 Cross Sections

Typical values of cross sections of single ions in glasses are in the range of $10^{-20} - 10^{-18}$ cm^2, but due to inhomogeneous broadening, the average cross sections of the ions in a glass are often several times smaller. In order to model doped fiber sources reasonably, it is important to accurately determine the absorption and emission cross sections at the pump and laser wavelengths. The cross sections influence not only the achievable pump absorption and gain, but also the saturation behavior and the rates of spontaneous transition processes. A technique for modeling a gain media, with spectrally overlapping transitions is to use effective cross sections, which can be directly calculated from spectroscopic measurements (i.e. absorption and emission spectra).

Absorption cross sections are often obtained from the absorption spectra, if the concentration of the ions is known. For example absorption of Er^{3+} ions can be measured using a white source and employing the cut-back method afterwards, the absorption cross-section (σ_{abs}) at relevant frequency (υ) can be directly related to the absorption spectrum by $\sigma_{abs}(\upsilon) = \alpha_{abs}(\upsilon)/N$ where $\alpha_{abs}(\upsilon)$ and N represent the absorption coefficient and the volumetric density of the ions. On the other hand the emission cross-section (σ_{emi}) can be either measured via fluorescence spectra or calculated from absorption cross-section. The absolute values of emission cross sections can be calculated from Füchtbauer–Ladenburg or McCumber equations. They can be also estimated from absorption cross sections using the Judd–Ofelt theory. In the specific case of Er^{3+} doped glass, the McCumber theory has been refined to give a relationship for the $^4I_{13/2}$ to $^4I_{15/2}$ transition as [61, 185, 231]:

$$\sigma_{emi}(\upsilon) = \sigma_{abs}(\upsilon)exp[(h\varepsilon - h\upsilon)/K_BT] \tag{4.10}$$

where hε is the net thermo-dynamical free energy to excite one Er^{3+} ion at temperature T and K_B is the Boltzmann constant. The emission (σ_{emi}) and absorption (σ_{abs}) cross-sections are equal only at frequency of $\nu_o=\varepsilon/h$ and they are offset at other frequencies. It should be noted that the absorptions shift to higher frequencies and emissions to lower frequencies.

The ground and exited state core absorption as well as core gain spectra for high erbium concentration EYDFA used in this thesis is shown in Figure 4.4. Note that in the range of 900-1100 nm, the absorption is mainly due to Yb^{3+} ion, because it has an absorption cross-section almost of an order of magnitude higher than that of the Er^{3+} ion. The absorption band of Yb^{3+} is about 200 nm but it has a high peak centered at 975 nm with a narrow bandwidth of 5 nm.

All the other absorption peaks are from Er^{3+} transitions. The core absorption for ytterbium ion in the region of 914-950 nm was approximately constant and equal to 300-320 dB/m. Therefore, the clad absorption coefficient for ytterbium ion was approximately 0.5 dB/m at 915-950 nm. The erbium peak absorption for the core is 30dB/m at a wavelength of 1535 nm and it is is equal to 7.5and 3.75dB/m for 1530nm and 1570nm respectively. At the wavelength region 1200-1450nm, both Er^{3+} and Yb^{3+} ions are transparent and the associated background losses are presented in Table 4.2.

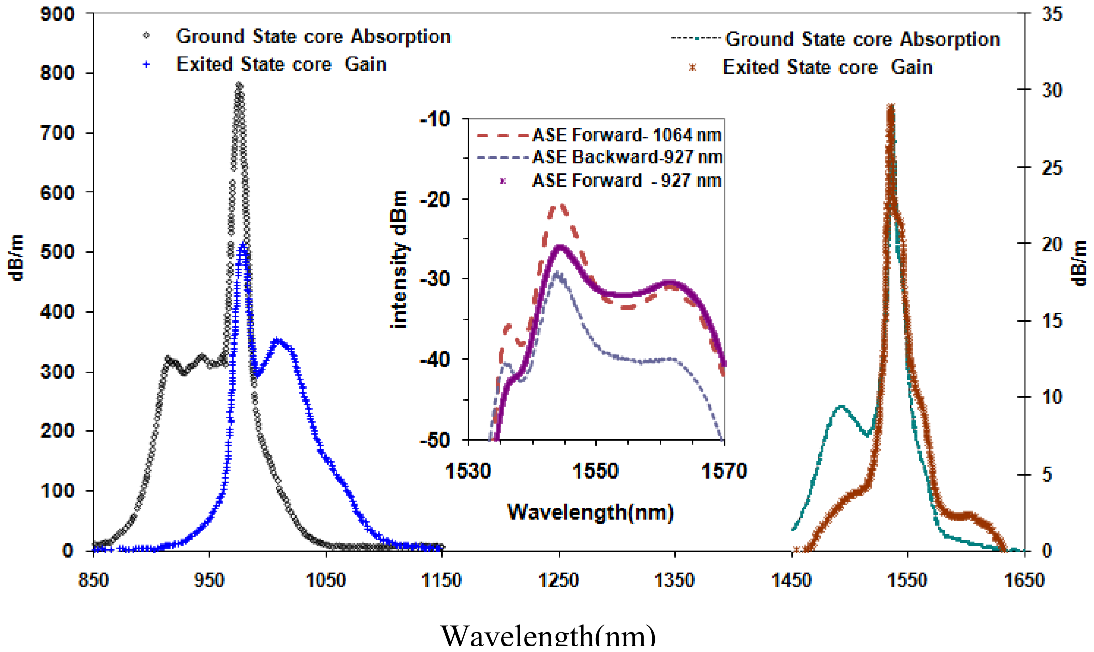

Figure 4. 4: The EYDF absorption and gain specifications of Yb^{+3} ions (left) and Er^{+3} ions (right).

4.4.2 Lifetime of Er^{3+} at $^4I_{13/2}$, Energy Level

The main laser transition of interest in Er^{3+} is the $^4I_{13/2}$ to $^4I_{15/2}$ transition centered around 1.5 µm with a a large energy gap. Therefore the lifetime of the upper lasing level that is filled through fast decay by ions from $^4I_{11/2}$ level, is long and mostly radiative. This lifetime depends on the host glass and the Er^{3+} concentration. It is an important criterion to judge the probability for the laser transition. The lifetime of the excited states of ions is usually given by the decay of spontaneous emission. Even though quantum noise processes determine the rate of spontaneous emission, it is also proportional to the emission cross section and bandwidth. A gain media with high emission cross sections and /or broad gain bandwidth tends to have a low upper-state lifetime because of strong spontaneous emission. Similarly, in a gain media with high concentrations, the probability for cooperative upconversion increases and concentration quenching dramatically shorten the lifetime [277].

Unlike fiber amplifiers which require doping concentrations as high as possible, laser fibers can only be doped up to the level that the upper lasing level lifetime and consequently laser efficiency are not drastically reduced by the cooperative upconversion. This is the reason why higher Er^{3+} doping level isn't pursued for the laser application [6].

Lifetime measurements are obtained using time-resolved spectroscopy techniques, in which the optical amplifiers are pumped by a pulsed laser diode and the time decay of the fluorescence is measured. A square wave at 70 Hz with a 7% duty cycle and pulse width of 1 ms is suitable for modulating of a laser diode. The modulated pump should be switched off for a period which is several times longer than the decay time of spontaneous emission of interest. The fall time of modulated pump also should be shorter than the decay time of spontaneous emission of interest [61]. The required setup is similar to the setup which is used for observing the the emission spectrum except that the signal from the fast photo detector is sent to an oscilloscope The fluorescence decay curve is recorded and exponentially fitted to obtain the Er^{3+} lifetime.

Table 4. 2: The proposed cladding pumped fiber specifications and parameters used for the numerical calculations.

Parameter	**Unit**	**Symbol**	**Value**
Background loss ,clad	dB/m	$\alpha(\nu_p)$	0.15
Numerical Aperture core/Cladding	--	NA	0.17/0.45
Core/Cladding diameter	µm	a/b	6.1/135
Fiber Length	M	L	10
Background loss,core(signal)	dB/m	$\alpha(\nu_s)$	0.19
Planck's constant	m^2kg/s	h	6.63×10^{-34}
Effective area	m^2	A_{eff}	28.46×10^{-12}
Pump coupling efficiency	%	η	80
Light speed in vacuum	m/s	c	3×10^8
Er concentration	m^{-3}	N	4.5×10^{25}
Yb concentration	m^{-3}	N	6×10^{26}
Spontaneous emission	S	τ_{21}	11×10^{-3}
Spontaneous emission lifetime	S	τ_{32}	1×10^{-9}
Spontaneous emission lifetime(Yb^{3+}	S	τ_{65}	1.5×10^{-3}
Er up-conversion coeffiecient	m^3/s	C_{up}	3.5×10^{-23}
Cross relaxation coefficient	m^3/s	C_{cr}	3.5×10^{-22}
ASE bandwidth	nm	$\Delta\nu_8$	Fig 4.11
Signal. abs & Stimulated emission cross	m^2	σ_{sa}, σ_{se}	Fig 4.4
Yb Clad Absorption@975(927)nm	dB/m	α_{Yb}	1.6(0.5)
Yb Clad Gain@975(927)nm	dB/m	g_{Yb}	1(0.06)
Yb Clad Absorption@975/915nm	dB/m	α_{Yb}	2.34/0.5
Er Core absorption@1535nm	dB/m	α_{Er}	20.7
Er Core Gain@ 1535nm	dB/m	g_{Er}	20.3
Yb absorption cross section (927nm)	m^2	$\sigma_{56}(\nu)$	2.3×10^{-25}
Yb emission cross section (927nm)	m^2	$\sigma_{65}(\nu)$	0.1×10^{-25}
Er absorption cross section (927nm)	m^2	$\sigma_{13}(\nu)$	1.5×10^{-26}
Mode overlap factor@1550nm	-	Γ_P	0.76
Pump coupling efficiency	%	η	79
Non-radiative transition-marked with(i) [278]	S^{-1}	R_{43}	14×10^5
Radiative (green light) transition indicated	S^{-1}	R_{41}	10^3
Phonon lifetime in silica glass	ns	τ_B	4.5

The proposed cladding-pumped fiber specification and other spectroscopic parameters used in our analysis are carefully chosen from the literature [279, 280] and is summarized in Table 4.2.

To have a clear measurement trace on the oscilloscope, the energy of the pump pulse must be sufficient and the ASE and reabsorption must be avoided using short fibers. To verify that the fluorescence decay is free from up-conversion processes and ASE, the pump power level must be varied. Moreover the fluorescence light is filtered from other emissions [281]. From the fitting line, the average lifetime can be found to be about 11 ms which is somewhat close to the results obtained by [282]. This long lifetime allows population inversion to be induced by a relatively weak pump power density.

4.5 THEORETICAL RESULTS

The theoretical results are obtained by numerical methods. All of the equations used for pump and signal powers are first order differential equations and a Runge-Kutta-based iteration method [283] is used to solve these equations numerically by using the ode 45 built in Matlab® function. In order to solve the population rate in a steady state condition, the time derivatives of Equations (4.1) to (4.4) are set to be zero. The pump and input signal powers are fixed at 3.5 W and 0.1 mW, respectively. Table 4.3 shows the initial conditions which are set for pump power, signal power and the ASE spectrum.

Table 4. 3: Initial Condition

Initial condition	**Wavelength(nm)**	**Initial condition**
$P_{P1}(z=0)=P_{P1}$	927	Pump at z=0
$P_S(z=0)=P_S$	$1530<\lambda<1570$	Signal at z=0
$P^{+}_{ASE,Yb}(z=0,v)=P^{-}_{ASE,Yb}(z=l,v)=0$	927	Ytterbium ions
$P^{+}_{ASE,Er}(z=0,v)=P^{-}_{ASE,Er}(z=l,v)=0$	$1530<\lambda<1570$	Erbium ions

The EYDF with length of L is divided into N segments along the z direction, as shown in Figure 4.5. The light intensity of the pump, signal and ASE power propagating in the first segment (segment 0) is calculated using the above initial conditions. For the subsequent segments (segment 1 to N-1), the output intensity from the preceding segment is used as the input for the following segment. A relaxation method is used to achieve an accuracy of 0.01 % for all the pump, signal and ASE powers.

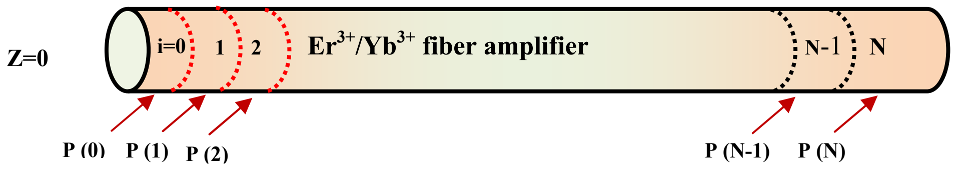

Figure 4. 5: Schematic of the fiber model.

With considerable experimental information on the double clad EYDF lasers and amplifiers, it seems that further theoretical work is still needed for further improvements. This work focuses on the characterization of the spectral gain, which is an important factor in the generation of a stable high power amplifier with an optimal gain.

Figure 4.6 shows a three dimensional diagram of the theoretical gain spectrum with the variation of the EYDF length ranging from 0.5 to 10 m at the wavelength region between 1520 and 1600 nm. The gain spectrum is simulated by numerically solving the coupled equations where the input signal and forward pump powers are set at -10 dBm and 3.5 W, respectively.

A similar procedure for backward pumping scheme can be used to solve the equations numerically. To run the program for each operating wavelength, the absorption and emission cross-sections are obtained from Figure 4.4. The variables used in the numerical calculation and their corresponding values are shown in Table 4.4.

Table 4. 4: The variables used in the numerical calculation

Parameter	**Unit**	**Symbol**	**Value**
Signal wavelength	nm	Λs	Varying
Pump wavelength	nm	Λp	927
Forward pump power	mW	P_p	3500
Input signal Power	dBm	P_{s_in}	10

Figure 4.4 shows that under the above-mentioned initial conditions, the optimum length for operation in the C-band is between 5 to 8 m. At optimal length a gain of higher than 40 dB can be achieved with a pumping power of 3.5 W whereas for longer fibers, the gain is decreased due to 1535 nm ASE recombination and for this reason, in a 10 m long EYDF the small signal gain varies from 37.2 to 32.4 dB.

There are two other physical reasons in the variation of the signal gain with the fiber length. The first reason is that the signal gain increases linearly with the fiber length according to the linear gain regime.

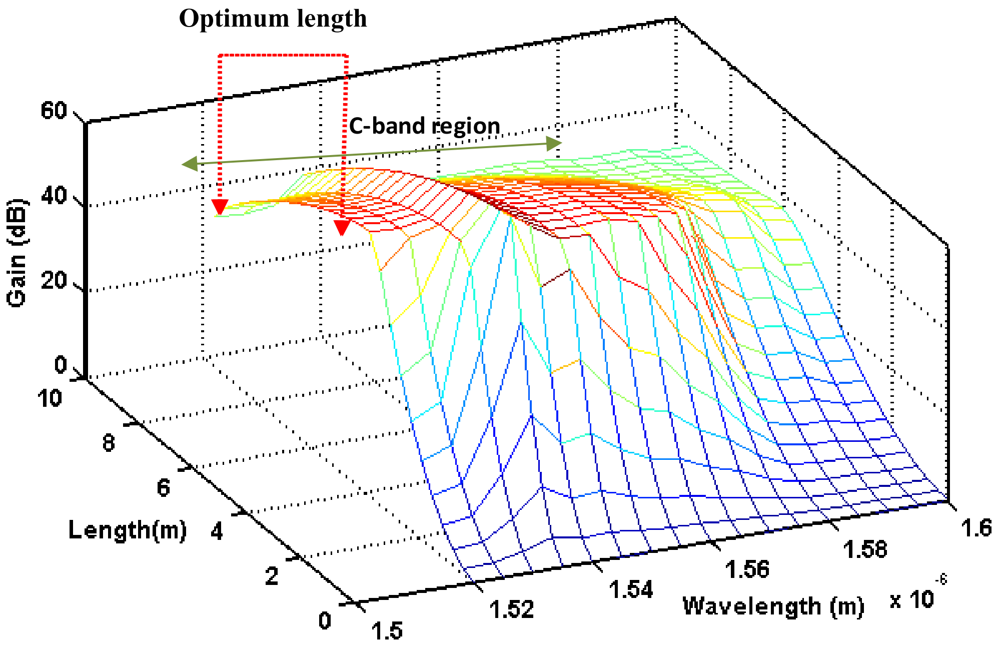

Figure 4. 6: Theoretical gain spectrum of the EYDFA against fiber length and wavelength at input signal power of -10 dBm.

The pump power should be sufficient to keep the amplifier performance in the linear gain regime. The second reason is that the signal gain decreases due to high absorption of pump power by Yb^{3+} ions.

To verify the simulated results, the output powers from a piece of 10m long DC-EYDFA are experimentally measured and compared in Figure 4.7 with numerical results. An output power of about 23 dB with a flat profile and a power variation of less than 2 dB is obtained experimentally at wavelength region between 1541 to 1565 nm. In particular, the maximum output power of 23.6 dBm which corresponds to the gain of 33.6 dB is obtained at wavelength of 1548 nm.

It is shown that the experimental data are in good agreement with the calculated values confirming our theoretical model. However, the experimentally determined gain is observed to be 4 dB lower than the theoretical prediction. This is expected due to the presence of unwanted reflections in the system, such as those that might occur from scattering in the fiber, reflections from connectors or from fiber splices which was ignored in the theoretical analysis. The spurious reflection generates the spurious lasing, which suppresses the attainable gain of the EYDFA. The insertion loss of the EYDF, splicing and connector losses also contribute to the gain suppression which was neglected in our theoretical model.

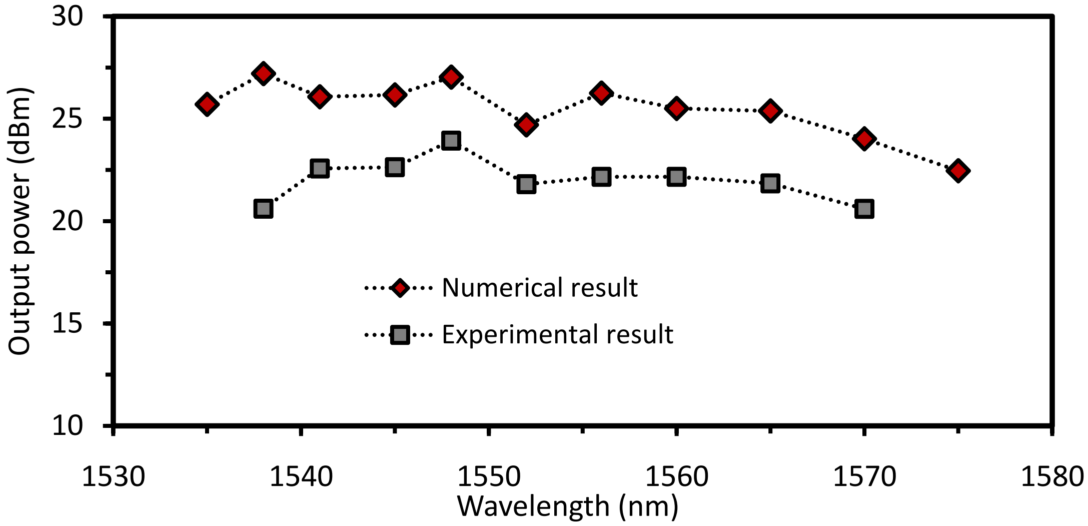

Figure 4. 7: Comparison of calculated output power with experimental results for the EYDFA with 10 m long EYDFA at a fixed -10 dBm input signal power and a 3.5 W forward pump power.

The noise figure can be also calculated by the equation:

$$NF(\lambda_s) = 1/\mathrm{G}(\lambda s) + P_{ASE}\lambda_s \times (hc\Delta\nu\mathrm{G}(\lambda_s))^{-1} \quad (4.11)$$

where G and P_{ASE} are gain and ASE power at the relevant wavelength and $\Delta\nu$ is the signal spectral resolution. This equation contains two important terms that contribute to the noise of the EYDFA. The first term or shot noise of the active medium has a larger influence on the NF values while the noise generated from the mixing of the signal and ASE (known as the spontaneous emission factor) in the next term sets the limit of minimum noise of an EYDFA. The smallest spontaneous emission factor is achieved when the gain becomes weakly dependent upon the launched pump power and approaches its maximum value which corresponds to the regime of maximum inversion[177]. This equation shows that NF reduces as the gain increases which is in agreement with the results.

4.6 EXPERIMENTAL RESULTS

4.6.1 ASE Specta of Er^{3+}/Yb^{3+} Doped Cladding Pumped Fiber

By pumping the EYDF with laser diodes, the ytterbium ions are excited to the upper level state of $^2F_{5/2}$, the energy from the excited Yb^{3+} ions is then transferred to the $^4I_{11/2}$ state followed by the $^4I_{13/2}$ state which undergoes a nonradiative transition and finally form a population inversion generates an ASE. The ASE has a short coherence time and length but in RE-doped single mode fiber the media can exhibit perfect spatial coherence. The ASE bandwidth of a high gain media usually is smaller than its gain bandwidth. Also note that normally, multi mode fiber with higher numerical aperture and larger core area has a higher ASE power.

Alternatively, stimulated emission is prompted by the arrival the signal light. As a result, additional photons are created with the same optical phase and direction as the incident photon. Spontaneous decay of excited ions which did not participate in amplification becomes a source of optical noise. This noise is then amplified along with the incident light and results in amplified spontaneous emission (ASE). In a high-gain single stage fiber amplifier, ASE tends to limit the gain achievable to the order of 40–50 dB and can contribute significantly to the noise of the amplified signal. ASE for a fiber laser can also prevent lasing at extreme wavelengths, if the gain at other wavelengths is high enough for generating strong ASE.

Unwanted ASE can be suppressed using photonic crystal fibers, with special attention to fiber length or doping level and using a four-level media. The luminescence spectrum is also known as ASE spectrum. The ASE power can differ strongly from that of leaving the fiber ends in a transverse direction, because of wavelength-dependent amplification and reabsorption. Moreover the spectral shape of ASE can depend on the pump intensity level.

The pump power is injected into the EYDF cladding via a TFB with a flat wavelength transmission characteristic between 927nm and 980 nm, and is fusion spliced to the DC-EYDF. The TFB and the EYDF are meticulously chosen to avoid extra losses from mismatch.

The insertion loss of the TFB at the signal and pumping wavelength are about 0.2 dB and 0.4 dB respectively. A coupling efficiency of 86% are obtained at the pumping wavelengths of 927and 937 nm, using this TBF. The experimental setup for measuring ASE is illustrated in Figure 4.8.

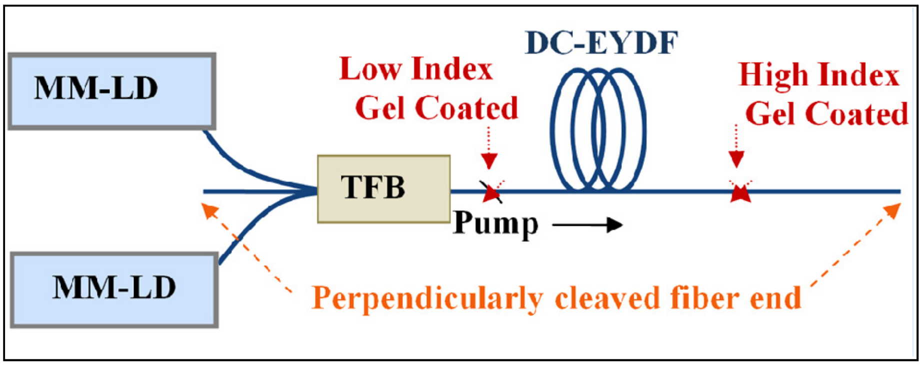

Figure 4. 8: Experimental set-up for measuring ASE.

Figure 4.9 shows the ASE spectra of the forward pumped DC-EYDF at different 937 nm pump powers. As shown in this figure, the ASE spectrum is observed at wavelength region between 1535 and 1570 nm. The total ASE power is observed to increase with the pump power. The peak of the ASE spectrum is also observed to move towards a shorter wavelength region as the pump power increases from 250 to 600 mW. The ASE from the ytterbium ions is quite weak and represents less than 1% of the total output power.

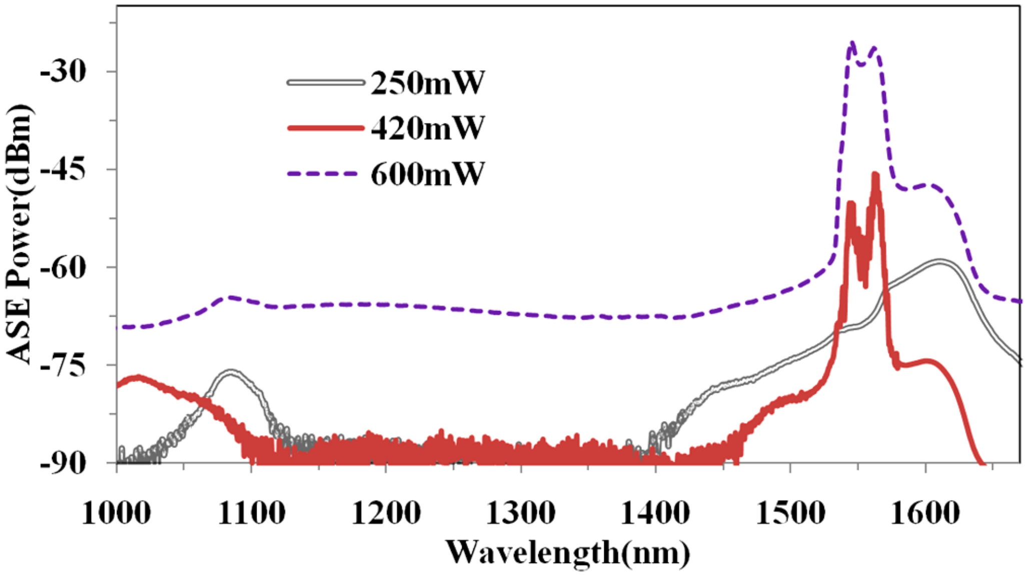

Figure 4. 9: ASE spectra of the forward pumped EYDF at different pump powers. The pump powers are 250, 420 and 600 mW at 927 nm on the figure.

The ASE spectrum for a pumping wavelength of 1064 nm is also shown in Figure 4.10. The similar spectral shape for ASE at pumping wavelength of 925 nm and 1064 nm is justified in view of the cross sections of these two wavelengths.

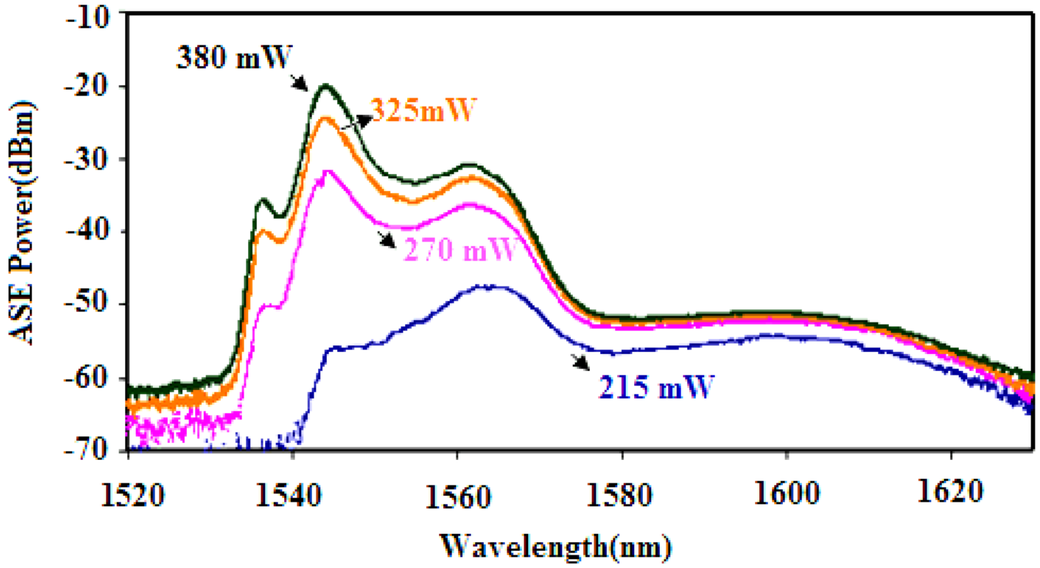

Figure 4. 10: The forward ASE spectrum from the DC-EYDFA with 10 m length of gain medium and 160-300 mW of the 1064 nm pump power.

For comparison purposes, the ASE spectrum of the forward and backward pumped EYDF under 927 nm pumping and a pumping power of 670 mW are displayed in Figure 4.11.

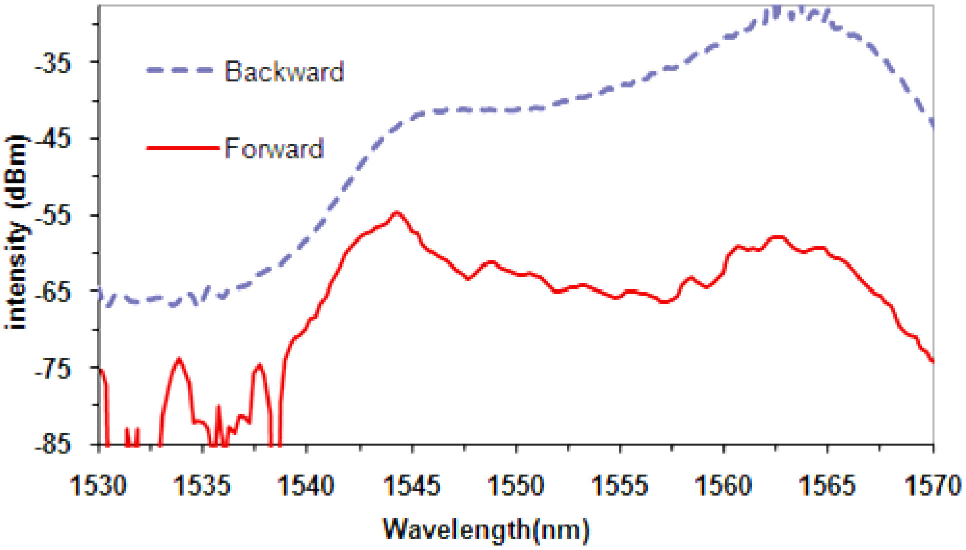

Figure 4. 11: The luminescence spectra of EYDF configured with 10 m long double clad fiber for both forward and backward 927nm pumping scheme. The pump power is fixed at 670 mW.

As shown above, the forward and backward ASE have two peaks at 1545 nm and 1565 nm. In Figure 4.11 and Figure 4.9, it is clear that the forward ASE peak at 1545 nm is very sensitive to the pump power. In both configurations, as the pump power is increased to 850 mW, the 1545 nm ASE band catches up with and then surpasses the 1565 nm ASE band, similar to the gain behaviour. In fact, in the forward configuration with a pumping wavelength of 1064 nm, the peak of the ASE is moved towards a shorter wavelength region at lower pump powers**.**

Performance of an amplifier is degraded by parasitic oscillations, pre-lasing, Rayleigh scattering and more seriously by ASE which can also propagate backwards into the seed oscillator, affecting its performance and destabilizing the signal laser, potentially damaging it.

All of the above mentioned processes will decrease the energy available for laser radiation in amplifier. In long high-gain amplifiers, ASE can have a high enough intensity to partially (self) saturate the gain. In general ASE can be reduced by controlling dopant concentration, operating the amplifier in the deep saturation regime and assuring that the population inversion is as high as possible. Double-pass and segmented configurations as well as interstage isolators are also used.

The result is that possible lasing, gain quenching and noise arising from back-scattered light or from ASE can be lower than those of a single fiber amplifier of the combined lengths. In order to allow the forward signal to reach a higher power and reduce the amplification of the ASE in the MOPA, different stages are isolated using polarization independent optical isolators and spectral band pass filters. A time gating elements such as AOMs which is synchronised to the arrival of each pulse can be also used.

As shown in Figure 4.11, the ASE power from the backward pumping generates the highest power while forward pumping is only capable of generating a low ASE power. This is because the pump light is only capable of producing high population inversion at limited lengths of the input portion of the fiber. As a consequence, the ASE power from forward pumping (FP) suffered greater attenuation by the end of the fiber as compared to the backward pumping (BP) configuration. When the power of pump at EYDFA is increased, the backward ASE power was intensified and competes with the actual input signal. This ASE behaved in a similar manner to a high power pseudo-signal, competing with the input signal and as a result, reduced the available gain for the signal.

In order to provide monitoring of the power traveling backward from the input signal power, an optical circulator (OC) is placed between a wide tunable laser source based on Bi-EDF and EYDFA. The output characteristics of this stable Bi-EDF based fiber laser have been explained with all details in chapter 3.

The optical spectrum of the back traveling light can be monitored simultaneously and continuously during the experiments. It can also be useful to observe the onset of the parasitic oscillations which are capable of damaging the system.

Figure 4.12 shows the ASE power against the input pump power for forward pumping (FP) and backward pumping (BP) schemes. From the figure, the backward ASE power is higher than the forward one and the power traveling backward can be suppressed using a configuration which includes an isolator (see FP-EYDFA with ISO case in the figure).

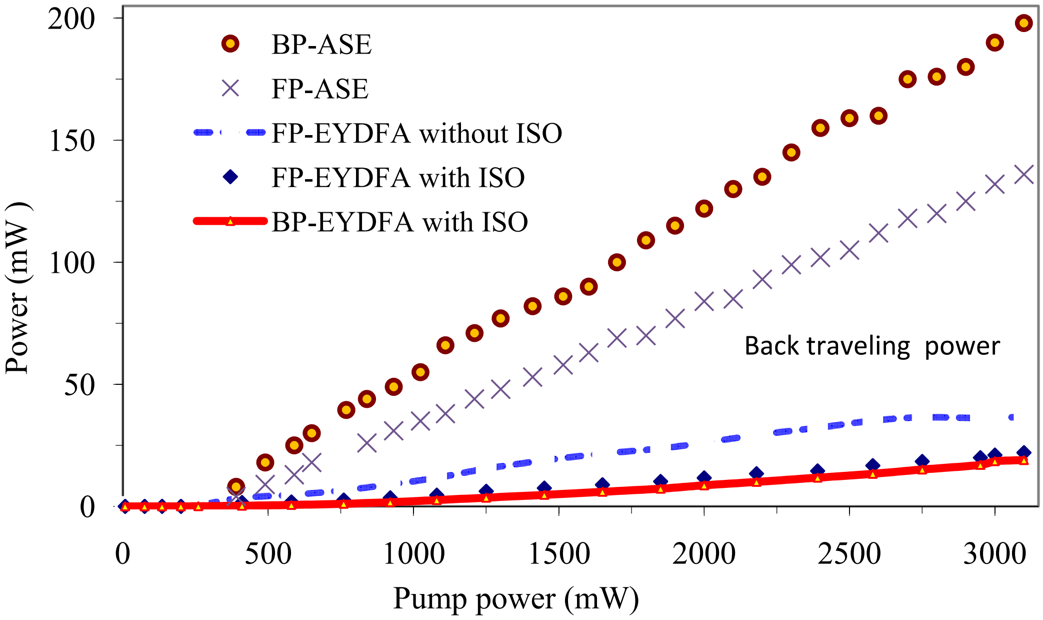

Figure 4. 12: ASE power and Back traveling power as a function of pump power for forward pumping (FP), backward pumping (BP) and in a amplifier with an isolator at output (with ISO). In this experiment the input signal power and wavelength are fixed at -10 dBm and 1560 nm respectively.

However, for a given pump power the ratio of amplified signal power to the backward travelling power is strongly dependent on the signal wavelength and amplifier configuration.

Under a pump power of 3100 mW and input signal power of -10 dBm, Figure 4.13 compares the experimental results for both FP and BP scheme with an isolator. The inset figure however, shows that a further power ratio reduction is possible by using a 10 dB increment in the signal power. The signal wavelength is fixed at 1564 nm in inset figure.

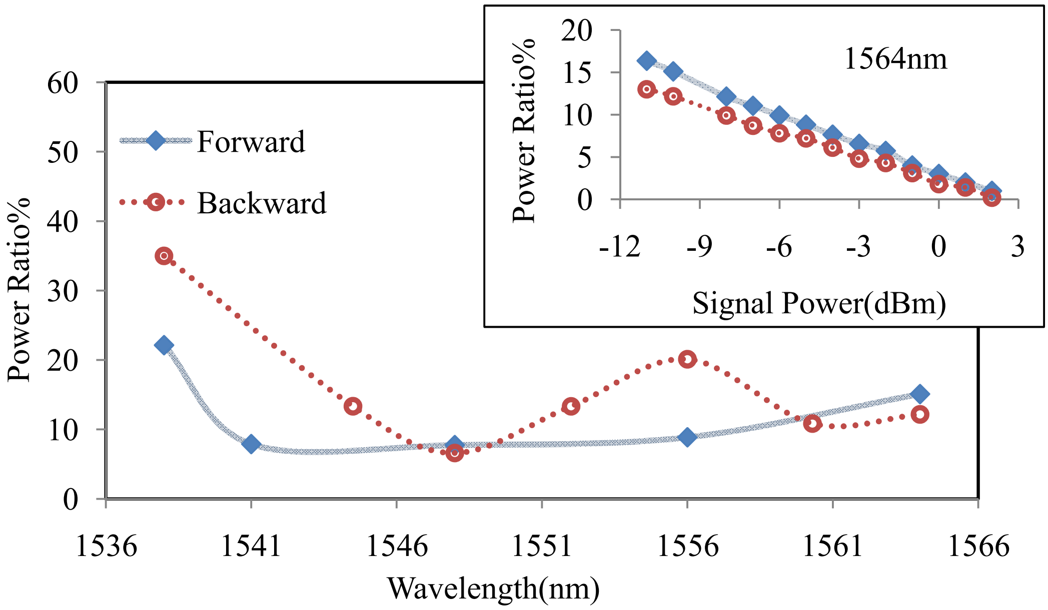

Figure 4. 13: Back traveling power ratio as a function of signal wavelength in the forward and backward pumping scheme at a fixed pump power of 3.1W. Inset shows power ratio reduction at 1564nm with the signal power increment.

A double-sided laser operation with a 42% slope efficiency can be achieved with 4% reflections at bare facets of both EYDF ends. Figure 4.14 shows the spectrum of double-sided laser measured with a resolution bandwidth (RBW) of 0.07nm at a pump power of around 4 W.

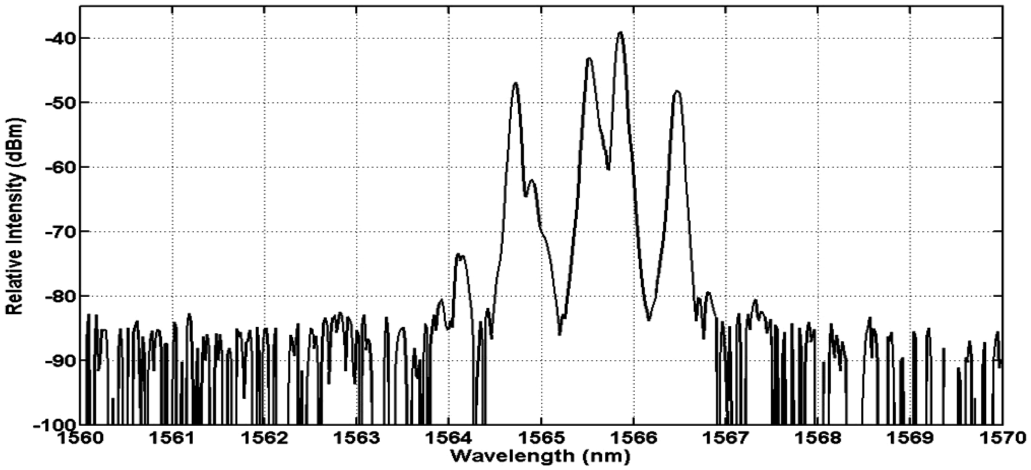

Figure 4. 14: Output spectrum of the EYDFL configured without any FBG.

Owing to the OSA power detection limit, additional loss is required. Thus the intensity on OSA represents a relative, rather than absolute intensity. By combining the output power at both sides a total power of 2.5 W is obtained at a pump power of 6.5 W. However, the laser operation without FBGs has a higher laser threshold which is measured to be approximately 480 mW. Note that, the operating wavelength is determined by the cavity loss and the gain spectrum. Consequently, the output spectrum peaks at 1565.8 nm with a few lower peaks within this wavelength region.

4.6.2 DC-EYDF Laser Characteristics in a Linear Cavity

In the laser cavity the ASE propagates through the single mode core and oscillates to generate a laser via stimulated emission. Efficient operation of the EYDFL can be conveniently achieved using a FBG in a linear cavity as a wavelength selective filter which operates in the amplification region. In this section, high power EYDFLs configured with and without a FBG are described using a Multi Mode laser Diode scheme (MM-LD). A FBG is fusion spliced to the TFB in forward scheme (Figure 4.15) or to EYDF in backward scheme with a splice loss less than 0.5 dB.

Figure 4. 15: Experimental setup for the double-clad EYDFL.

Thus, an all fiber laser cavity is formed between the FBG and the perpendicular cleaved fiber. The experiments are carried out for different FBGs and two pump wavelengths.

The incorporation of a fiber Bragg grating in the cavity restricts the laser operation to the bandwidth of the grating. All FBGs used have the peak reflectivity of nearly 100% and a 3 dB bandwidth of approximately 0.2 nm. In comparison, the laser radiation is much narrower than that of the FBG bandwidth, due to the linewidth narrowing that occurs in multiple pass amplification.

The output power characteristics for different lasing schemes are compared in Figure 4.16 for different grating wavelengths. The pump power was not increased further for fear of potential damage to EYDF–SMF splice region.

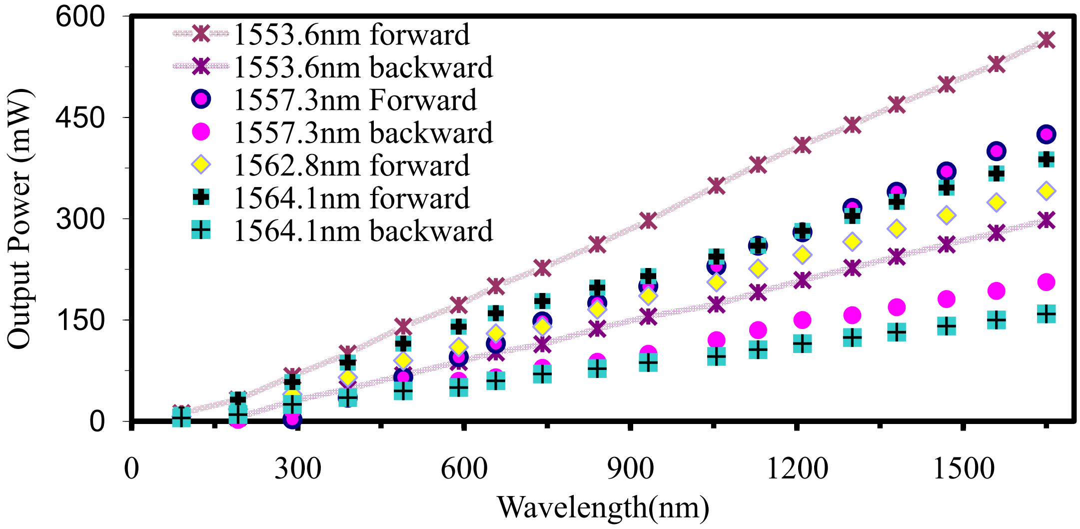

Figure 4. 16: Output power characteristic of the EYDFL for different schemes at different operating wavelengths.

Clearly for a given wavelength, forward pumping schemes provide higher output powers and higher slope efficiencies than backward pumping schemes. As can be seen in Figure 4.16 the most efficient laser operates at shorter wavelengths because the ASE spectra of the EYDF peaks at 1545 nm and the gain characteristic of the EYDF is highest at this wavelength.

The output power of 520 mW is obtained at a pump power of 1700 mW for this wavelength. The laser light is shown to have a sharp bandwidth of 0.2 nm at the Bragg wavelength with a signal to noise ratio of more than 25 dB.

Figure 4.17 shows how wavelength dependent loss can affect laser operation. From the figure a broad band-FBG (BBFBG) with a lower transmission loss near 1560nm (see Figure 4.22) results in a laser spectrum with single sharp peak located at 1560nm. Whereas a high power dual wavelength laser with the same slope efficiency can be simply achieved using a loop mirror as a comb filter in which the wavelength region can be varied using a polarization controller (PC). The inset figure shows the balanced dual-wavelength spectrum of EYDFL with a pump power of 1500 mW.

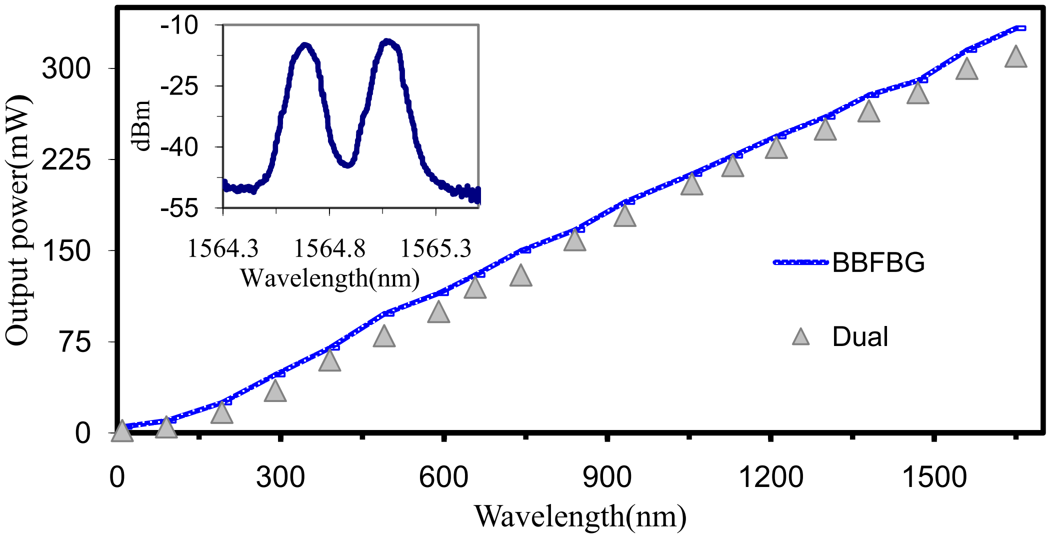

Figure 4. 17: Output power characteristic of the EYDFL using BBFBG and loop mirror as a reflector, Inset shows a 0.25 nm linewidth and a spacing as narrow as 1nm for dual-wavelength performance using loop mirror.

The slope efficiencies and the laser thresholds for different wavelengths are listed in Table 4.5.

Table 4. 5: Laser threshold and efficiency for different wavelengths.

Wavelength	Forward Threshold	Backward Threshold	Forward Efficiency	Backward Efficiency
1553.6 nm	102mW	150 mW	36%	20%
1557.3 nm	282mW	171 mW	31%	14%
1562.8 nm	89 mW	115 mW	22%	8%
1564.1 nm	30 mW	55 mW	24%	10%

It should be evident that the slope efficiency with respect to the launched pump power does not change at higher output power and the maximum output power is limited by the available pump power, nevertheless the laser is expected to have a higher efficiency if its operating wavelength is changed to 1545 nm.

After optimizing the cavity loss, the laser efficiency is expected to improve. The efficiency of the proposed EYDFL was improved to up to 3% using polymer coating at the splicing regions. For this purpose, the FBG was fusion spliced to input signal port of the TFB. Subsequently, on the other side of TFB, the splice region with EYDF is covered in low-index gel.

Furthermore, to remove the cladding modes and to have a laser with M^2 value of close to one, the far end of the doped fiber was spliced with a single-mode fiber, while the other end of SMF-28 is perpendicularly cleaved to provide 4% feedback for the laser.

It should be noted that, the multimode beam propagates mostly in the cladding. Therefore, to protect the SMF from unabsorbed pump light, the splice region at the output end is covered with high-index gel layer.

This method is proven to be very effective in protecting the SMF from damage. When the high index gel is not used, the residual pump power is enough to burn and destroy the SMF coating. A photograph of EYDFL with the cover removed has been shown in Figure 4.18.

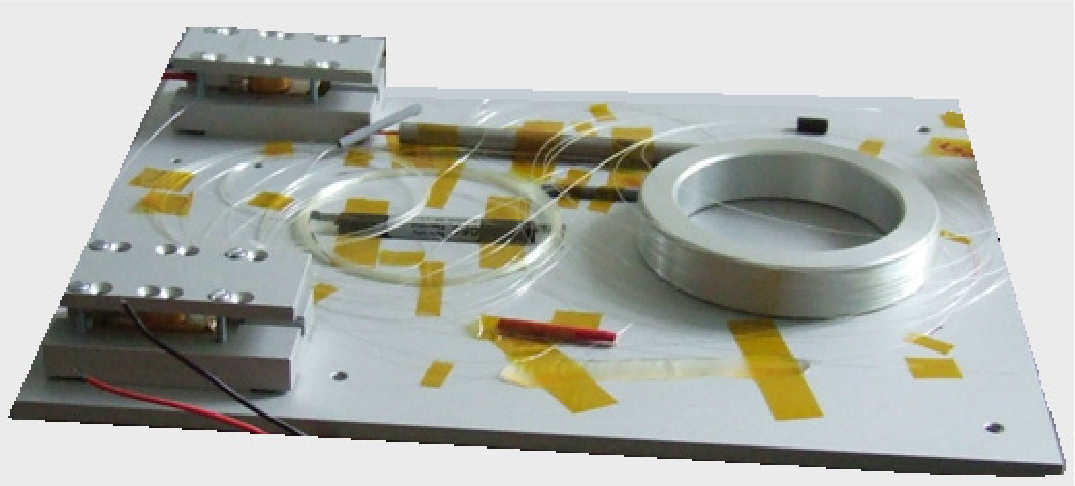

Figure 4. 18: Photograph of 4 W DC-EYDFL with the cover removed.

In this situation a slope efficiency of 39%, with an output power 4 W are obtained at operating wavelength of 1552.3 nm with pumping power of 10 W (see Fig. 4.19).

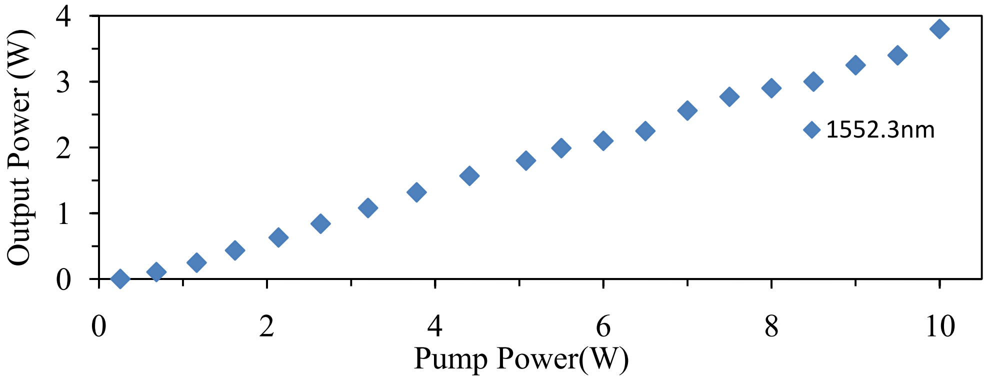

Figure 4. 19: Output power as a function of pump power for laser at 1552.3 nm with 38% slope efficiency.

The experiment shows a significant capacity for power-scaling with no sign of the efficiency downfall. Figure 4.20 shows the EYDFL output spectrum with a 1552.3 nm FBG in the setup at a fixed pump power of 4W. The residual pump power is not observed in the spectrum (at 937 nm) which indicates that the output power measured by the power meter is mainly from the laser power. Again the Y-axis represents relative and not absolute values. The inset shows the enlarged laser spectrum and the FBG bandwidth at the 1553 nm region.

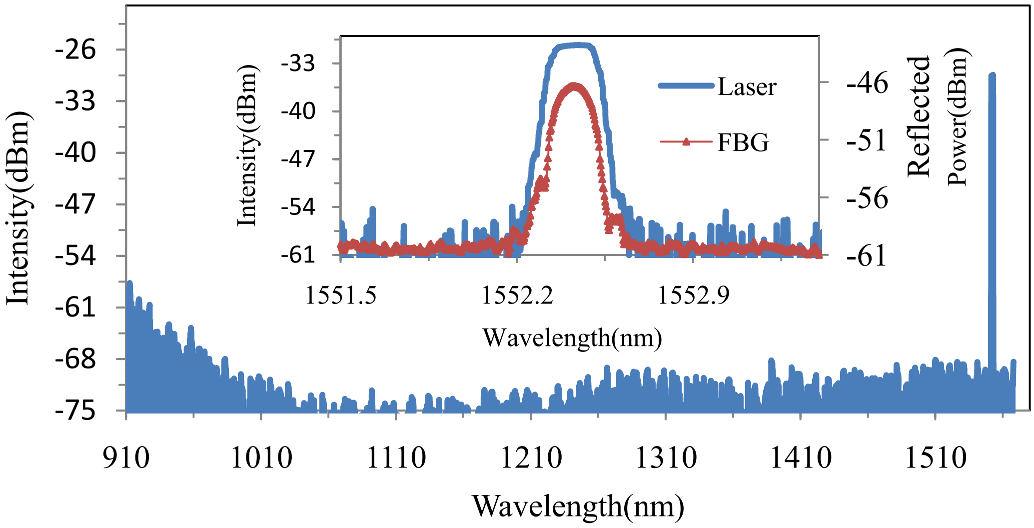

Figure 4. 20: Output spectrum of the double-clad EYDFL with the 1553.6 nm FBG. Inset shows a comparison of the grating bandwidth and the laser linewidth.

4.6.3 DC-EYDF Laser Characteristics in a Ring Cavity

For an all fiber DC-EYDF ring setup as the output coupling ratio is decreased, the peaks in the short wavelength region of the ASE spectrum disappears and the peaks in the long wavelength region continues to shift to even longer wavelengths.

This result indicated that, increasing the reabsorbing effects along the fibre could be regarded as a new pump source that excites longer wavelength emission. Hence, the fibre gain shifts towards longer wavelengths and only powers at longer wavelengths can compensate for cavity losses.

In our experiments, as the coupling ratio decreased, the laser threshold varied from 300 mW to less than 150 mW. In setups with lower thresholds, the resulting competition between the various modes reduced the quality of laser output due to the smaller threshold for all modes.

4.6.4 Continuous Wave Er^{3+}/Yb^{3+} Doped Fiber MOPA

In this section, the output power, amplification bandwidth and NF are measured and studied in detail for performance evaluation of DC-EYDFA in different configurations**.**

The pumping configuration can be identified in three schemes. As shown in Figure 4.21(a), a single pass forward pumping is when the pump light source is combined at the input ends of the erbium-doped fiber (EDF) and travels in same direction with the signal light. The splice region between the EYDF and TFB is shown by the "star points" and is covered by a low-index gel layer.Alternatively as depicted in Figure 4.21(b) a single pass backward pumping scheme is obtained by changing the location of TFB to a point after the EYDF section.

An optical isolator is used in the single-pass configurations to prevent the oscillation of spurious reflections in the system. A Bi.-directional configuration on the other hand is a combination of both forward and backward pumping schemes. The single-pass in the above mentioned configurations means that the signal is amplified only once while a double-pass as illustrated in Fig.4.21(c) implies that the signal will be reflected and passed back to experience amplification for a second time.

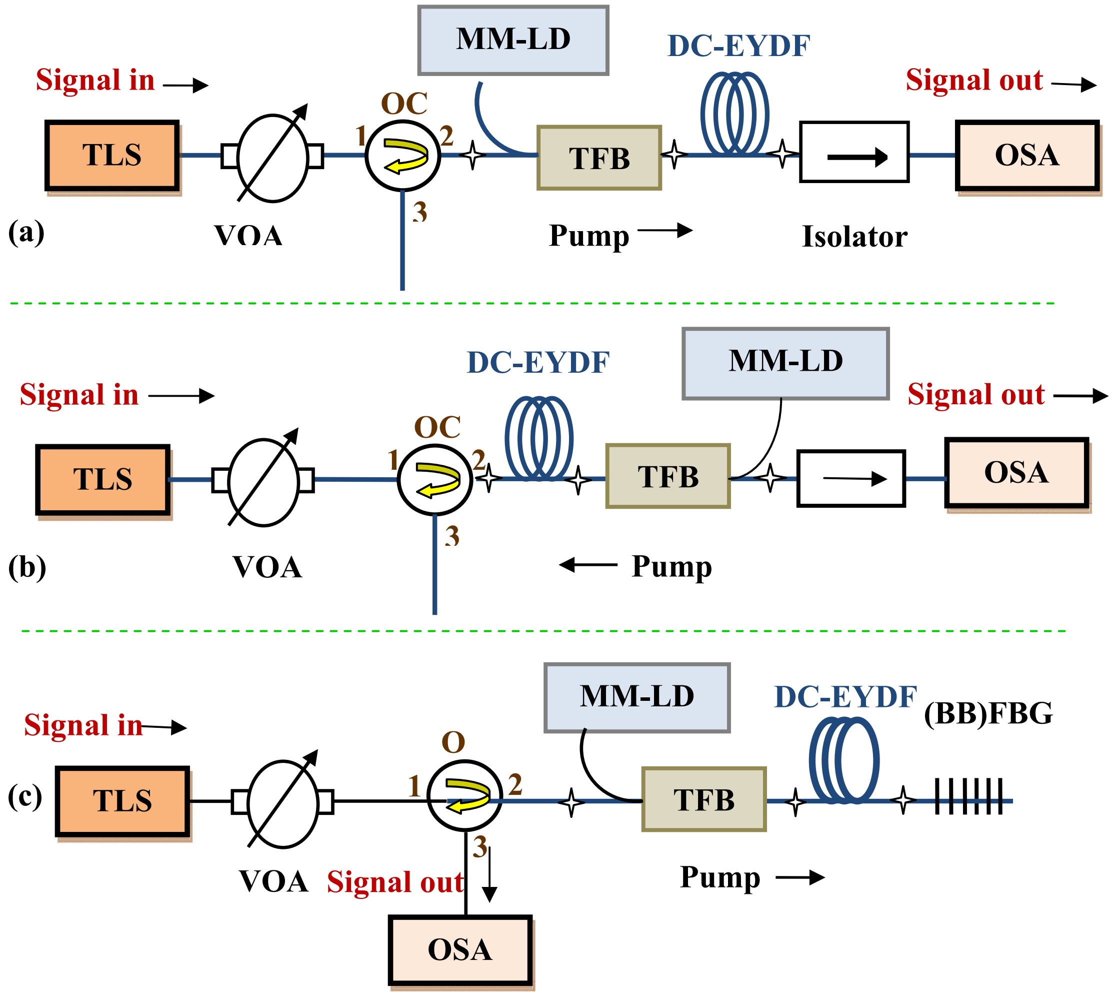

Figure 4. 21: Experimental set-up for the EYDFA (a) Single-pass with a forward pumping scheme (b) Single-pass with a backward pumping (c) Double-pass configuration.

A BBFBG is fusion spliced at output end of the EYDF to act as a reflector for the test signal in a double pass configuration. The FBG used operates at a wavelength region between 1527 nm and 1567 nm with the average reflectivity of nearly 100% and a bandwidth of 40nm. The transmission spectrum is shown in Figure 4.22.

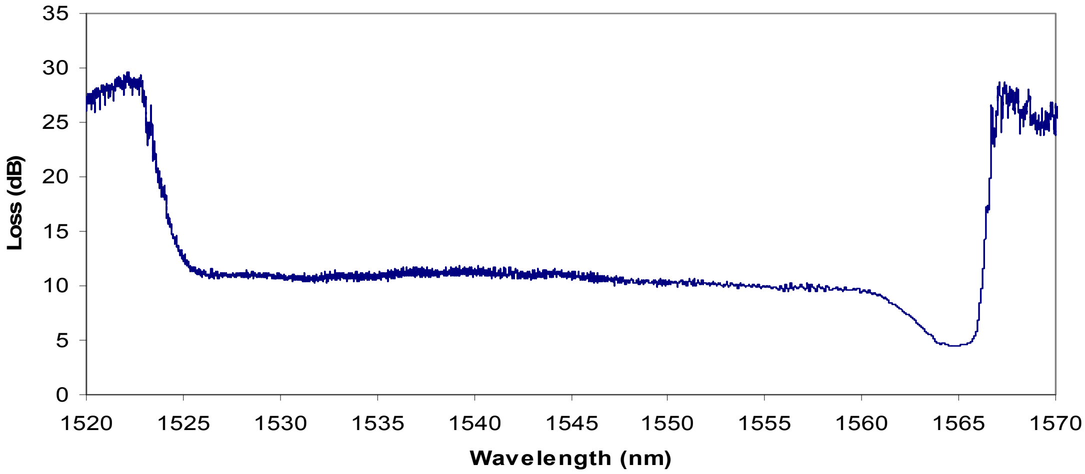

Figure 4. 22: Transmission loss spectrum of a BB-FBG.

The input signal power from a Bi-EDF based fiber laser is controlled by a variable optical attenuator (VOA) and injected to the DC-EYDF via an optical circulator (OC). The gain, NF and output power ranging from 1520 nm to 1620 nm are then measured after the isolator (ISO) in the case of single pass configuration and after the OC in the case of double pass configuration. Figure 4.23 shows the output power of the EYDFA for both single-pass and double-pass configurations while the input signal and 927 nm pump power are fixed at -10 dBm and 3.1 W respectively.

As shown in Figure 4.23 for the single-pass configurations, the backward pumping provides higher output power than the forward pumping because the stronger pump power at the output delays the onset of gain saturation.

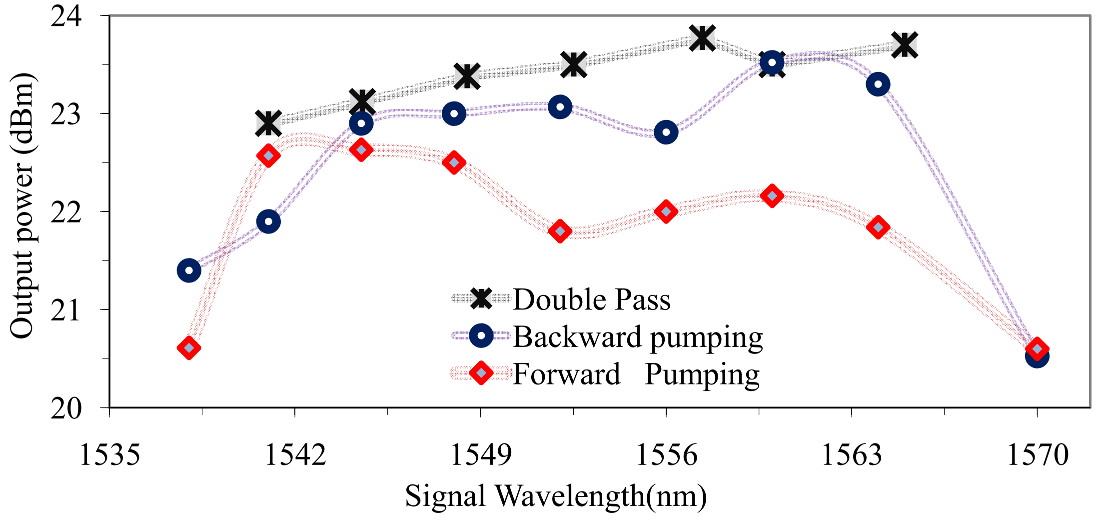

Figure 4. 23: The output power of the amplified signal against the signal wavelength.

This is true for intermediate signal input powers. In addition, this scheme is also favoured due to the increased threshold of nonlinear effects and better power efficiency. Nevertheless, the noise figure for this scheme is usually higher as shown in Figure 4.28.

On the other hand, the double pass EYDFA has a higher gain and output power compared to the single-pass due to the double-propagation of the test signal in the gain medium. We note that, the operation of the amplifier at wavelengths longer than 1566 nm is limited due to specifications of used BB-FBG. Under the same conditions for pump and signal, a flat gain of 33.5 dB with a variation of less than 1 dB is observed for the double pass configuration. Furthermore, an output power of 23.8 dBm that corresponds to a gain of 33.8 dB is attained at wavelength of 1557.4 nm and seed power of -10 dBm.

Clearly, as the seed power decreases, the gain increases such that at the seed power of -30 dBm and for a pump power of 3.1 W, the gain reaches about 53 dB. However, the peak gain or bandwidth can be changed by optimizing the fiber length and amplifier configuration. Figure 4.24 shows the output power against input pump power for the double-pass EYDFA at various input signal wavelengths and powers.

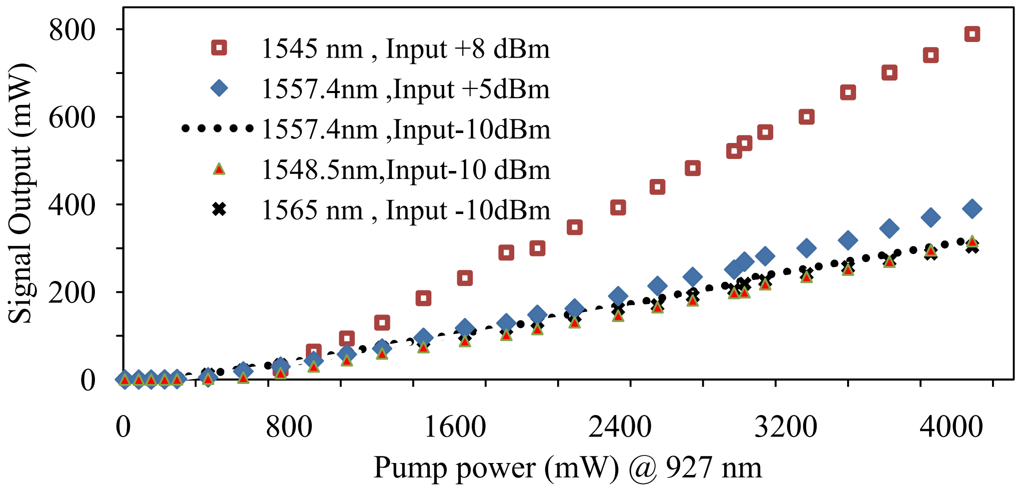

Figure 4. 24: The output powers of the amplified signal against 927 nm pump powers for the double pass EYDFA.

In order to further improve the output power, a higher input signal and pumping power is required. As demonstrated in Figure 4.24, the double pass amplifier is expected to have a much higher efficiency for longer signal wavelengths.

A high power pump can transfer a significant fraction of its power to a signal, resulting in an output power that can reach to several watts when the signal input is large enough to extract the gain at the expense of the ASE. In the double pass configuration an output power of up to 800 mW is obtained for a pump power of 4.1 W and a seed power of +8 dBm, which translates to a quantum conversion efficiency (QCE) of 32 %.

An increase in the pump and signal powers should yield to an even higher QCE. Nevertheless, in a double pass configuration the efficiency and the power scaling are mainly limited by damage threshold of the circulator (~800 mW).

Therefore, we were constrained to set the pump, signal and output powers to 4160 mW, 8 dBm and 800 mW respectively.

For a 10 m long DC-EYDF the single pass forward pumped configuration shows the lowest quantum conversion efficiency as shown in Figure 4.25. With lower background losses, higher quantum conversion efficiency is expected.

Adding an auxiliary 1040 nm signal with a power of 10 mW from the pump end was helpful to stabilize output by suppressing parasitic lasing. The power and wavelength of this auxiliary signal takes the energy that will be lost in the form of ASE (in 1040 nm band), otherwise back to the pump direction. This signal is reabsorbed completely at the later part of the fiber, and behaves as the pump for the Er-band signal in the later part of the gain fiber.

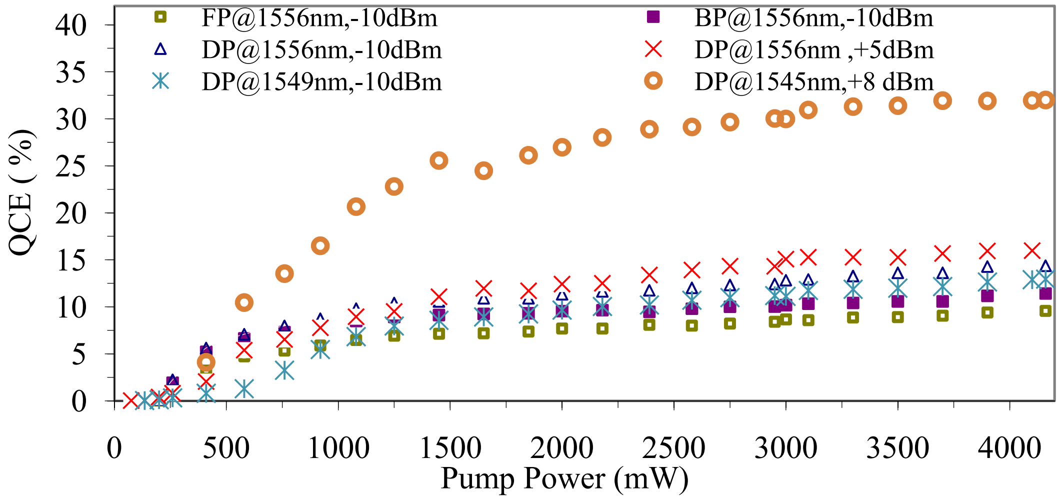

Figure 4. 25: Measured QCE against pump power for different schemes at different operating wavelengths, FP: forward pumping, BP: backward pumping, DP: double pass Scheme.

At lower pump power, this auxiliary signal has only a slight influence on the output power. However, with the increase of the pump power, the output power in

1040-nm assisted amplifiers is improved to up to 20%. Also the output power of the auxiliary signal was observed to be much lower than that of the main signal.

Figure 4.26 shows the attenuated output spectra for different configurations at the same pump power and input signal power. The output signals have a 3 dB bandwidth of less than 0.1 nm while for input signal 3 dB bandwidth is observed to be about 0.09 nm. When compared to the backward pumping scheme [238], the forward pumping scheme suffers a much less signal-spontaneous beat noise [284, 285], due to higher signal amplification at input end and also smaller ASE self-saturation [238, 239]. In figure 4.26, the forward pumping scheme shows the lowest ASE level which indicates the lowest noise figure. In contrast, the double-pass configuration shows the highest power of ASE, which translates to the highest noise figure.

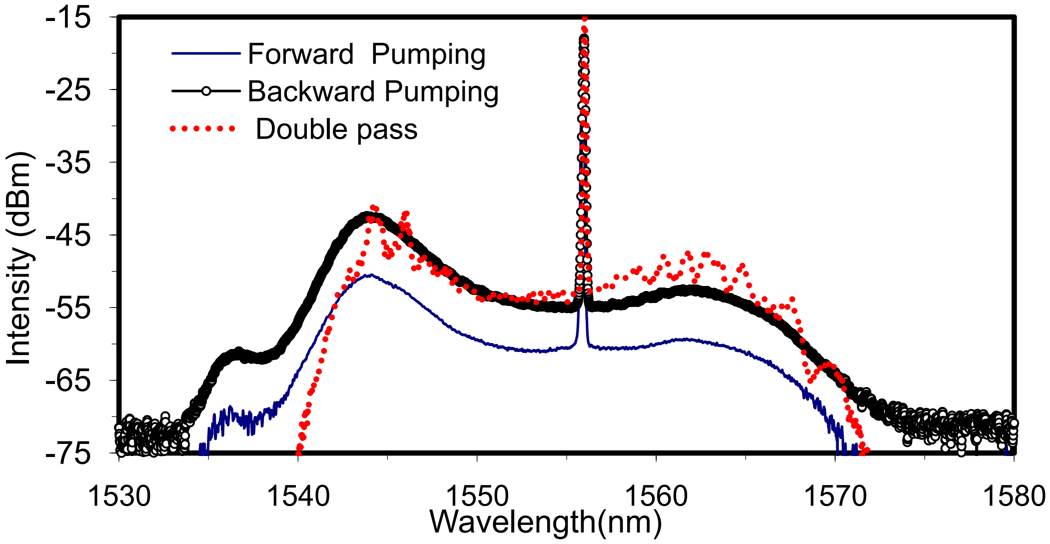

Figure 4. 26: The output spectrum of the signal for different configurations at a fixed pump power of 4160 mW and a fixed signal power of -10 dBm.

Although the forward pumping configuration is the most desirable configuration for low noise optical amplifiers [286], low signal gains and efficiencies forced optical amplifier designers to pick the bi-directional or double pass pumping configuration for high power applications since these pumping configuration has a better pump power distribution [287]. The use of a SBS mirror instead of a highly reflective mirror is an effective means of suppressing ASE in a double-pass amplifier.

The backward pumping spectra usually have a high noise figure but this configuration is favored due to the increased threshold of nonlinear effects. Nevertheless, the results shown in Figure 4.27 illustrate a peak power to noise level ratio more than 15 dB in C-band region and indicates that the measured output power is mainly from the peak region of the amplified signal. In this experiment the signal and pump power are fixed at -10 dBm and 4160 mW respectively.

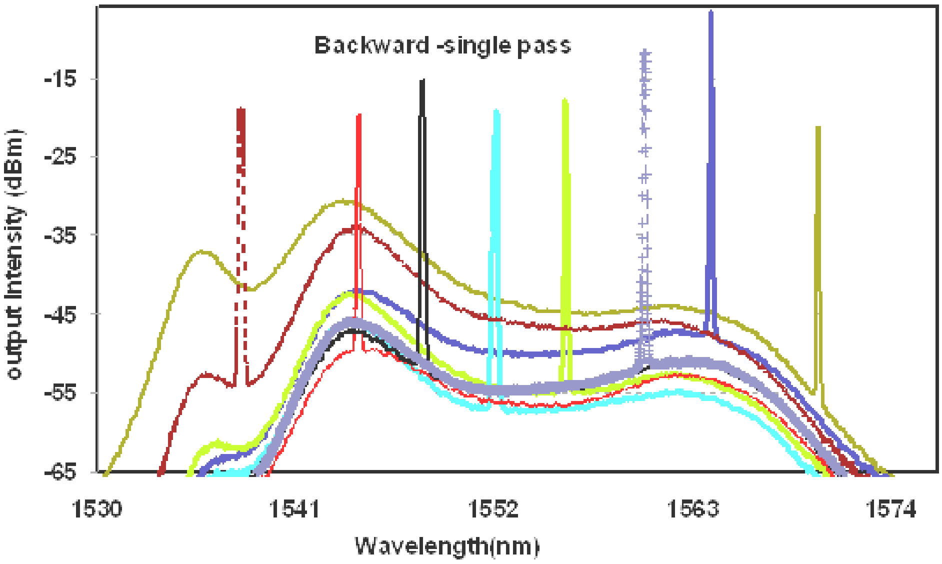

Figure 4. 27: Spectrum of the tuneable C-band MOPA from 1530 nm to 1565 nm at -10 dBm input signal power and a fixed pump power of 4160 mW.

From the results in Figure 4.28, the side-mode suppression ratio (SMSR) at amplifier output has a similar slope with signal gain due to its dependence on the signal gain. The measurement of SMSR was performed by OSA built-in functions.

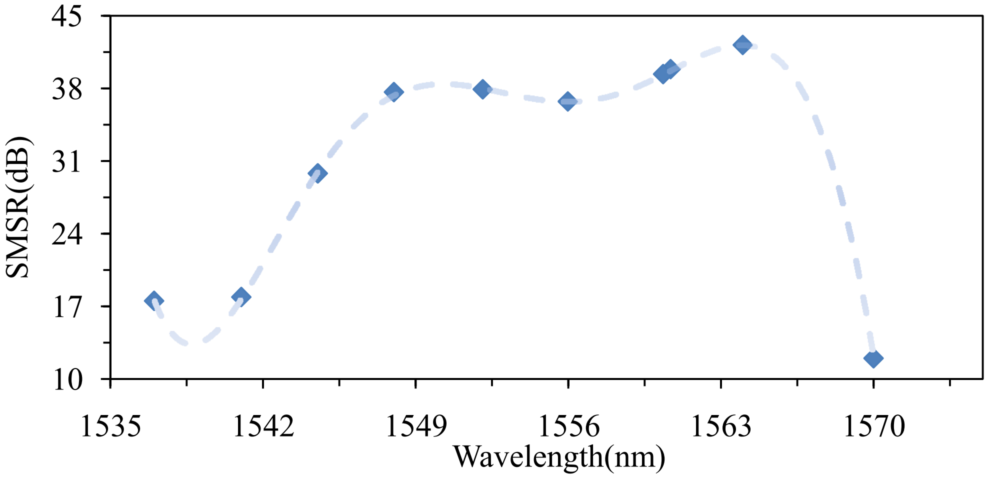

Figure 4. 28: The SMSR of signal in the C-band region.

Input signals at longer wavelengths have better SMSR because the ASE power level at this region is lower than for shorter wavelengths The highest SMSR was found to be 42.18 dB at wavelength of 1564 nm. However, the noise level of the DC-EYDF optical amplifier was found to be higher at signal wavelengths longer than 1564nm. This is because at longer wavelengths, the noise level of the DC-EYDFA, which originated from the shot-noise and ASE beat noise, is affected by the signal excited-state absorption process [177, 229] that came from the $^4I_{13/2}$ to $^4I_{9/2}$ energy transition in Er^3 ions. Furthermore, the SMSR and consequently *NF* values are strongly dependent on the amount of pump power launched into the EYDF. With a maximum gain, a low NF value is achieved if the input end of EDF is fully inverted.

There is a threshold for pump power in which the DC-EYDFA starts to amplify and amplification mechanism would be efficient beyond this threshold. Under the backward pumping scheme and an input signal power of -10 dBm, this threshold is found to vary between 200 to 260 mW. In general, a lower threshold is obtained for longer wavelengths. Note that besides pump direction, the threshold is related to the pump absorption coefficient, fiber length and the signal power.

4.6.5 CW Tuneable High Power Narrow-Linewidth All Fiber-MOPA

Single-frequency solid-state lasers are the best known low-noise coherent seed laser with a spectral linewidth ranging from hundreds of kilohertz to as narrow as a few kilohertz [288]. High power fiber lasers provide the best wall-plug efficiencies, and are simplest to implement. However, the fiber lasers usually have a broad spectrum and operate in a multi-longitudinal mode regime. The development of single-frequency fiber lasers is of great interest. However there is spectral broadening of the laser oscillator linewidth due to the phase noise introduced by the spontaneous emissions.

There are several efficient methods to generate narrow-linewidth fiber lasers, such as using one section of gain fiber as the saturable absorber which acts as a very narrow filter, twisted-mode technique to restrain spatial hole burning effect in the laser material, and fiber Bragg grating (FBG) [289-291].

Single-frequency Brillouin fiber laser is another type of highly coherent light source whose linewidth could potentially be only a few Hz [129]. Unlike conventional fiber lasers, single-frequency fiber lasers can be coherently beam combined for power scaling. Being relatively safe and immune to electromagnetic disturbance, the narrow linewidth fiber lasers can produce near-quantum-limited intensity noise by using an electronic feedback loop and amplitude squeezed pump diode.

Some applications such as digital or analogue optical transmission need high power tunable single-frequency fiber lasers [292]. Because of the cavity-free travelling-wave nature of the amplifiers, they can maintain the spectral purity of the seed source with a minimum additive phase noise. In coherent communication systems, amplitude noise is not a critical attribute. However, the phase noise has the most critical contribution and depends mainly on the spectral width of the amplified signal. A semi-classical model predicts a phase noise which is negligible for narrow linewidth signals [293]. The effect of phase noise introduced by fiber amplifiers was first measured in 1990 and was found to broaden the linewidth of the amplified signal [294]. However Desurvire [45] derived the semi-classical model, which predicts spectral broadening much smaller than those measured.

Möller reproduced the experiments and showed that [295]spectral broadening due to fiber amplifier was not as large as predicted in [296]. Consequently, more detailed experimental and theoretical investigations have been undertaken to solve this problem.

This section is confined to amplification of narrow linewidth sources .Hence the gain of amplifier and the output characteristics of the amplified signal in term of linewidth and output power are presented.

4.6.5.1 Experimental Setup

The configuration of the proposed high power narrow linewidth BFL, which is amplified by the EYDFA is shown in Figure. 4.29. It consists of three main parts, namely a tunable narrow linewidth BFL oscillator, a single mode pre amplifier EDFA and a double pass DC-EYDFA. The pump light from a 927 nm multimode laser diode (MMLD) is coupled into a 10 m long DC-EYDF by a multimode combiner (MMC).

Since the ASE from the EDFA becomes a source of optical noise, a combination of the isolator and filter is used between the two stages. Note that in contrast to the isolator that removes most of the backward-traveling ASE, the filter rejects ASE traveling in both directions.

The combination of both filter and isolator provides a slight improvement over that of the filter alone, which itself is more effective than the isolator alone. A notch interstage filter which acts as a band pass filter can also be used to flatten the gain spectrum of the amplifier. The band pass filter passes the wavelengths at the signal frequency while for a short wavelength at 1550 nm region the notch filter rejects the 1530 nm ASE source. The tunable band pass filter (TBF) used in this work has a transmission bandwidth of 1.0 nm and insertion loss of around 0.5 dB in the setup (Figure 4.29).

The simplest structure for fiber lasers is the Fabry-Perot resonator, but it normally does not generate a single-frequency beam because of the large gain spectrum and spatial hole burning [287]. This effect can be suppressed using very short cavities, but will result in poor pump absorptions and low efficiencies. Moreover, the resulting linewidths are too large compared to the requirements of coherent communication systems.

A piece of unpumped doped fiber as a saturable absorber has been applied to EDFL [297] and YDFL but the emission wavelength for these lasers depend on the length of the cavity [298] and on the pump wavelength [299], such that it may be difficult to select our desired range. In addition, the conventional linear cavity BFL usually suffers from problems such as the higher-order Stokes generation [129].

For this reason, we looked for alternative solutions, such as traveling wave loop and Fox-Smith resonators. The advantage of the traveling wave operations that it eliminates spatial hole burning and prevents multi-mode operation [300]. Furthermore it is easier for the ring fiber laser to achieve a narrow linewidth fiber laser compared to linear cavity based fiber laser. A stable single frequency tunable fiber laser at 1.55 μm can be realized by combining the above mentioned principle with a saturable absorber and narrow band feedback using a Bragg grating [289].

In this work, a ring BFL oscillator is used as a seed (see Figure 4.29). The BFL seed consists of an optical circulator, an optical coupler and a piece of Brillouin gain medium. For Brillouin gain, we have utilized 25 km long SMF, 10 km long NZ-DSF and 49 cm long Bi-EDF. A commercial tunable laser source with a maximum pump power of around 9 dBm is used as a Brillouin pump in the setup. The Brillouin pump power is launched into the Brillouin gain to create the narrow linewidth Stokes in the opposite direction. This Brillouin pump can be tuned from 1520 nm to 1620 nm with a stable output linewidth of approximately 5MHz. Therefore the output wavelength of all BFLs can be tuned within this spectral range.

The coupler allows a certain ratio of the light to oscillate in the ring cavity and the remainder is coupled out through the circulator. For SMF-based BFL, the SMF used has a mode field diameter (MFD) of 9.36 μm, a cut-off wavelength of 1161 nm, a ZDW of 1315 nm, and an attenuation coefficient of 0.187 dB/km at 1550 nm. The NZ-DSF used in NZ-DSF based BFL has an MFD of 8.5 μm, a cut-off wavelength of 1171 nm and a positive dispersion of about 4.0 ps/(nm.km) at 1550 nm.

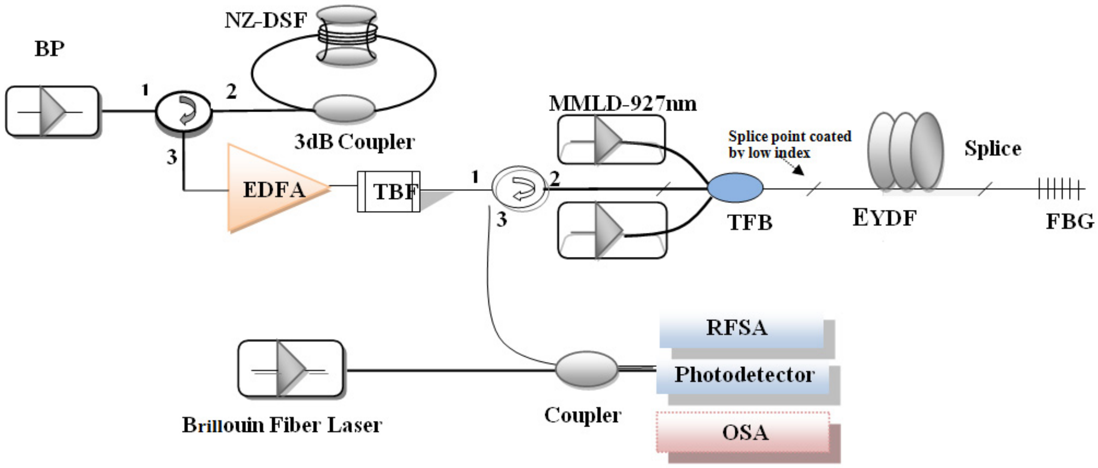

Figure 4. 29: Experimental set-up for the linewidth measurement of the BFL amplified by the proposed double-pass EYDFA configuration.

The EDFA employed a 3 m long highly doped Erbium-doped fiber (EDF) with an absorption rate of 13 dB/m at 975 nm, numerical aperture of 0.23 and background loss of 40 dB/km, which is forward pumped with a 980 nm pump. Then the pre-amplified BFL is injected into the EYDFA from port 1 through port 2 of the optical circulator and this circulator also functions to route the amplified BFL into port 3 as an output. A broadband FBG is used to allow the input BFL signal to double-propagate in the gain medium.

The output power and attenuated spectrum of the amplified BFL are measured by a power meter and an OSA (AQ6317B-ANDO), respectively. In the experiment, the input signal power of EYDFA and the multimode 927 nm pump power are fixed at 5 dBm and 4 W, respectively. Although laser linewidth can be measured by the homodyne method in which a signal is mixed with its time-delayed replica, achieving incoherent self-mixing of BFL is difficult in practice since the coherence length is estimated to be at least hundreds of kilometers [288]. Besides, this method is sensitive to environment perturbations even though it is insensitive to fluctuations in the frequency of the laser itself [301].

In our work, the laser linewidth measurement is done by evaluating the beat signal resulting from the interference of the BFL with another uncorrelated BFL (local oscillator) using a heterodyne beat technique [178]. This method requires another laser either with a comparable and well-known spectrum or with an extremely narrow and negligible linewidth.

The linewidth of the amplified BFL is measured by attenuating and combining the signal with another uncorrelated BFL via a 3dB coupler. The combined output is converted into an electrical signal by a fast response photo detector and the generated radio beat frequency signal is analyzed by a radio-frequency spectrum analyzer (RFSA). The photo detector used has a bandwidth of about 6 GHz while the RFSA (ANRITSU MS2683A) has a resolution bandwidth of 300 Hz to 3 MHz and frequency range of 9 kHz to 7.8 GHz.

The accuracy of the linewidth measurement is limited by the resolution of the RFSA. It is expected that the BFL is able to demonstrate a linewidth in the range of less than a few hundred MHz to a few Hz. The advantage of the proposed technique is its simplicity.

4.6.5.2 Gain and Noise Spectra

The output spectra from four different seeds used for MOPA are compared in Figure 4.30. The experiment is carried out for different kinds of seeds specifically commercial TLS, NZ-DSF based BFL, SMF based BFL and Bi-EDF based fiber laser. As shown in the figure, the line spacing between Brillouin pump reflection and Stokes lines is measured to be approximately 0.083 nm in all BFLs. The 3-dB bandwidth of the all Stokes lines in BFLs are measured to be less than 0.015 nm limited by the OSA resolution. The SMSR of 29 dB and 30 dB are achieved with the usage of SMF and NZ-DSF, respectively and the SMSR decreases with the reduction of the 1480 nm pump power.

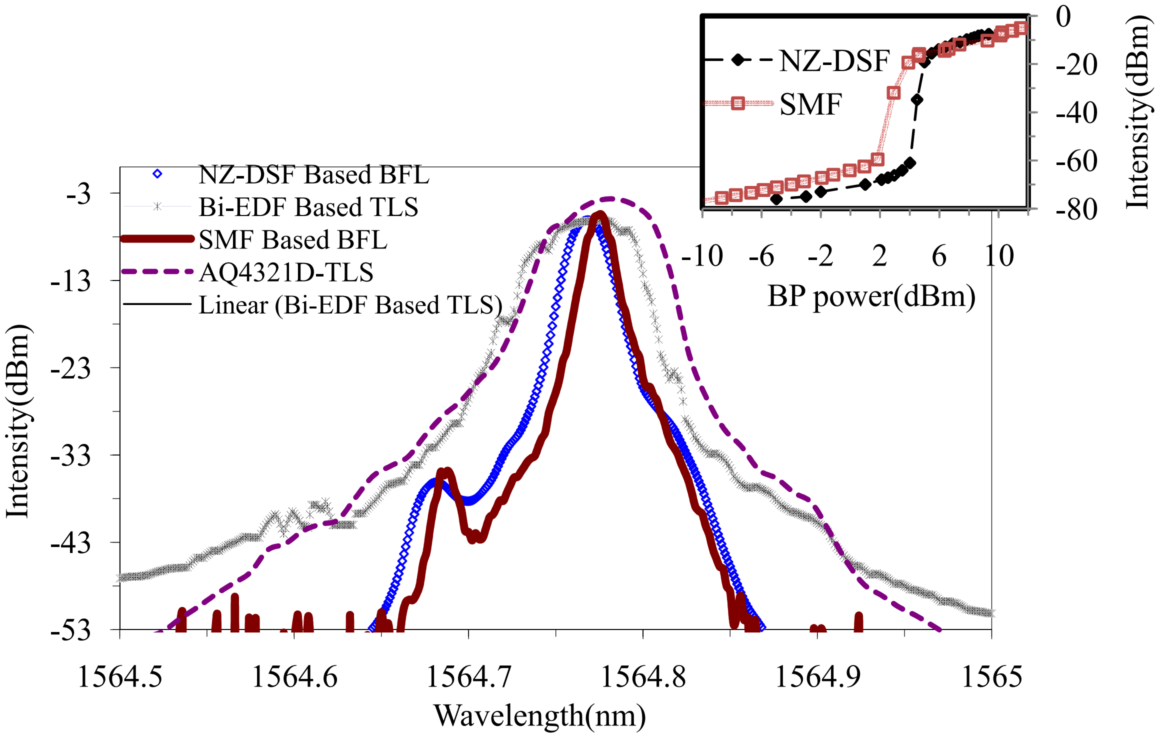

Figure 4. 30: Output spectra from the BFL oscillator with different configurations. The inset shows the peak power of the BFLs against the Brillouin pump power.

The inset of Figure 4.30 shows the peak power of the BFLs against the Brillouin pump power. As shown in the inset, the SBS peak power for all lasers increases with the Brillouin pump power. All peak powers start to saturate at Brillouin pump power of 10 dBm due to the generation of the higher order Stokes and the power transfer to them, which co-propagate with the Brillouin pump.

At lower Brillouin pump powers, only a single-wavelength or the first Stokes line is obtained, as shown in Figure 4.30. The SBS threshold power is determined from [302] the input Brillouin pump power at which a sudden jump of the BFL's peak power is observed. Therefore, the SBS threshold is measured to be around 5 dBm and 4 dBm for NZ-DSF and SMF respectively. From this experimentally determined threshold values, one can estimate the Brillouin gain coefficient [64] which is about 1.253×10^{-11}m/W for the NZ-DSF. It is also observed that the threshold is relatively unchanged with the operating wavelength. The threshold change with wavelength can be neglected.

Figure 4.31 compares the attenuated output spectrum of the proposed BFL, which is amplified by the double-pass EYDFA in the MOPA system with and without a TBF. Without the TBF, the forward ASE of the pre-amplifier enters the double-pass EYDFA, which reduces the attainable gain and increases the noise figure inside the amplifier.

The high noise figure in turn reduces the signal to noise ratio (SNR) of the amplified BFL. However, with the incorporation of the TBF, the SNR is improved from 41 dB to 50 dB. These SNR values indicate that the measured output power is mainly from the peak region of the amplified signal.

In this situation there is no significant ASE for input signals larger than 5 dBm, therefore the second stage will act as a booster for the signal, without introducing further ASE. These values can be improved remarkably using another TBF between BBFBG and EYDF.

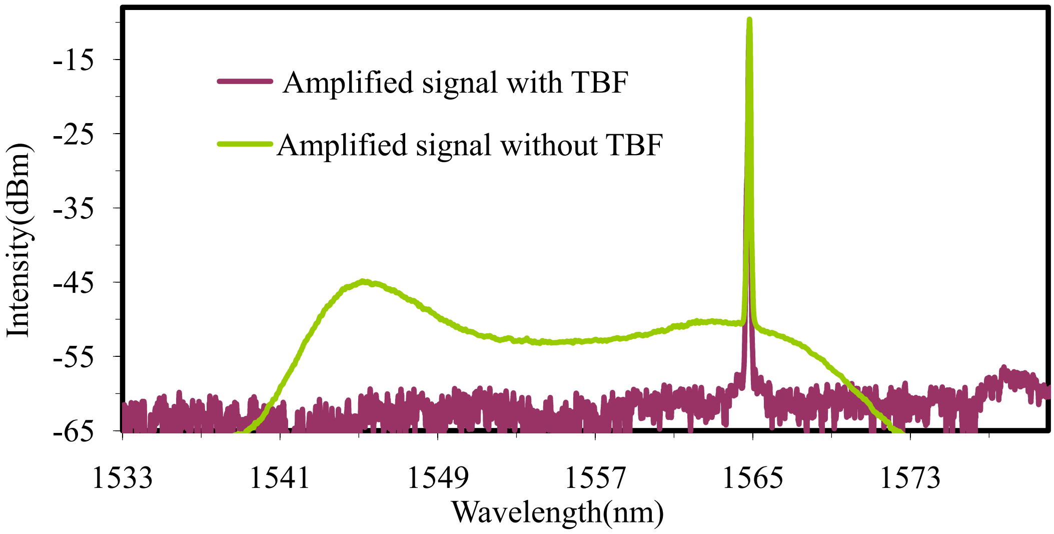

Figure 4. 31: The output spectra of the BFL amplified at maximum pump power, with and without an interstage filter when the output power from first stage is fixed at 5dBm.

Figure 4.32 shows the output power of the amplified BFL versus pump power in double-pass EYDFA. The power of the first stage EDFA and the wavelength are illustrated in the Figure.

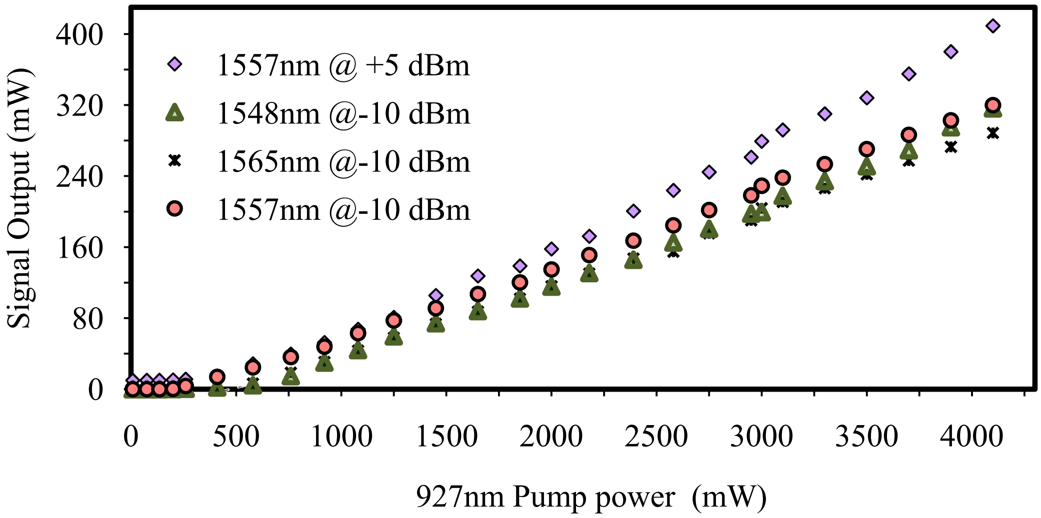

Figure 4. 32: Output power of the amplified BFL (with NZ-DSF) against the pump power of the DC-EYDFA at various wavelengths and input signal powers.

This experiment demonstrates that the output power at the wavelength of 1557.4 nm increases from 320 mW to 400 mW as the input power increases from -10 dBm to 5 dBm. As shown in the figure, an output power of 400 mW, corresponding to the gain of 33.6 dB is achieved in this wavelength when the multi-mode pump power and the Brillouin pump power are fixed at 4.1 W and 5 dBm, respectively.

Figure 4.33 shows the signal gain of EYDFA at different wavelengths of Brillouin pump and various input signal powers when the pump power is fixed at 4.1 W. As shown in this figure, the flat gain of 33.5 dB is observed with a gain variation of less than 0.8dB within a wavelength region of 1545 nm to 1566 nm especially at the input signal BP power of -10 dBm.

A gain enhancement of 5.5 dB is obtained using TBF. Note that, for high input signal powers, the gain for shorter wavelength is higher than that at longer wavelengths while for low signal powers, the maximum gain value is obtained at 1565 nm.

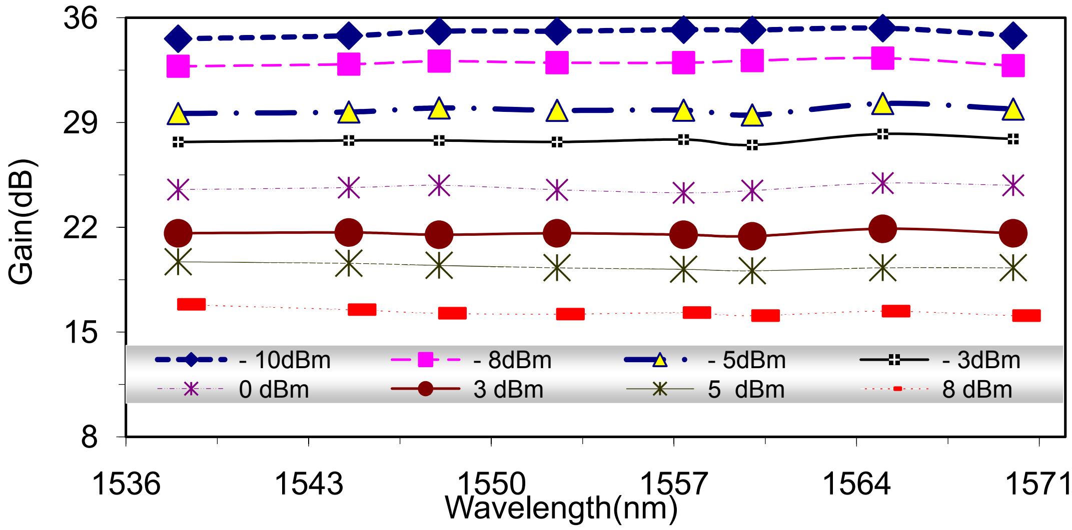

Figure 4. 33: The gain of amplified signal for different BP wavelengths and various input signal powers of the BFL. The pump power is fixed at 4.1 W.

4.6.5.3 Linewidth Measurements Using Brillouin Fiber Lasers

The frequency of uncorrelated BFL should be very close to frequency of the output BFL. The wavelength separation between both signals should be small enough such that the frequency of the beat spectrum is within a RFSA frequency region [303]. To identify signals in the RF spectra and to ensure the accuracy of the measurement, the resolution bandwidth (RBW) in RFSA was selected to be less than the separation of the signals. Furthermore, powers of both signals are fixed at nearly similar level during the measurement.

Assuming an ultra-narrow Lorentzian line shape, the laser linewidth at 3 dB down from the maximum point can be derived from the full width at 20 dB down value i.e. FWHM linewidth=20 dB width/(2√99). Any deviation of the spectra from a Lorentzian shape is attributed to the frequency noise of the lasers [64].

As shown theoretically in chapter 2, the linewidth of the Brillouin Stokes is given by $\Delta\nu_{Bs} = \Delta\nu_p \times[1-(\pi l \Delta\nu_B/\nu \, ln(R))]^{-2}$ and is proportional to the Brillouin pump linewidth $(\Delta\nu_p)$ where $\Delta\nu_B$ is the Brillouin gain bandwidth, l is the fiber length, ν is the velocity of light in the fiber and R is coupling ratio [123]. Therefore, a BP with narrower linewidth and a longer fiber is used to generate a narrower laser linewidths. Moreover the BFL Stokes linewidth slightly shrinks and its Lorentzian line shape changes to gaussian shape as the BP power increases [304].

To generate an uncorrelated BFL as a local oscillator with a linewidth narrower than the amplified signals, we used narrower BP linewidths, longer fiber and maximum BP power. Hence we employed a 25 km long SMF for the Brillouin gain medium and a BP linewidth of 5 MHz (FWHM) for local oscillator. By changing the coupling ratio, the local oscillator linewidth can be further improved.

The heterodyne spectra of the amplified signals are investigated for three kinds of tuneable seeds in MOPA which are NZ-DSF based BFL, commercial TLS and Bi-EDF based fiber laser. To achieve coherent detection, the frequencies of the local and the master oscillators must be locked. This is only possible for lasers with good spectral quality.

Figure 4.34 shows the beat spectra of the amplified Bi-EDF based fiber laser and an uncorrelated BFL. As shown this spectrum has many random components with multiple frequency noise peaks. The full width at half maximum (FWHM) of the each line shown in the inset of Fig. 4.34 is measured to be around 8.8 kHz.

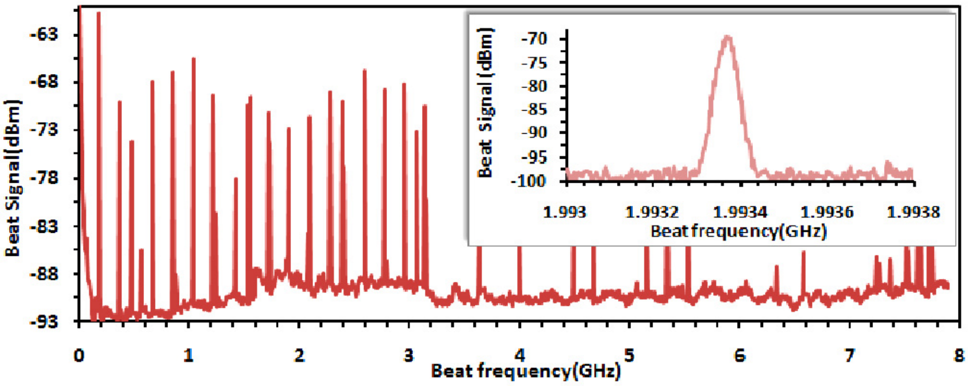

Figure 4. 34: The beat spectrum using Bi-EDF based fiber laser as a seed in MOPA.

The linewidth, for commercial TLS (or BP) as a seed, is measured to be around 3.5 MHz when the output signal power is fixed at 0 dBm in the 1565 nm region. In this setting, the linewidths of the amplified signal at the maximum pump power of 4.1 W are obtained at 4.765 and 6.79±0.001 MHz by using of SMF-BFL and NZ-DSF-BFL local oscillator (see Figure 4.35). It is therefore concluded that the amplified signal linewidth is broadened as it propagates inside the EYDFA. However, it is observed that no remarkable spectral broadening could be measured.

Hence our results confirm the measurement reported by Moller et al. [295] and demonstrate that phase noise do not apply in a way similar to line broadening in laser cavities. In a single pass configuration, the spectrum of the backward propagating light was observed and the power level in the backward direction did not exhibit any sudden increase which indicates that we are still below the SBS threshold in EYDF.

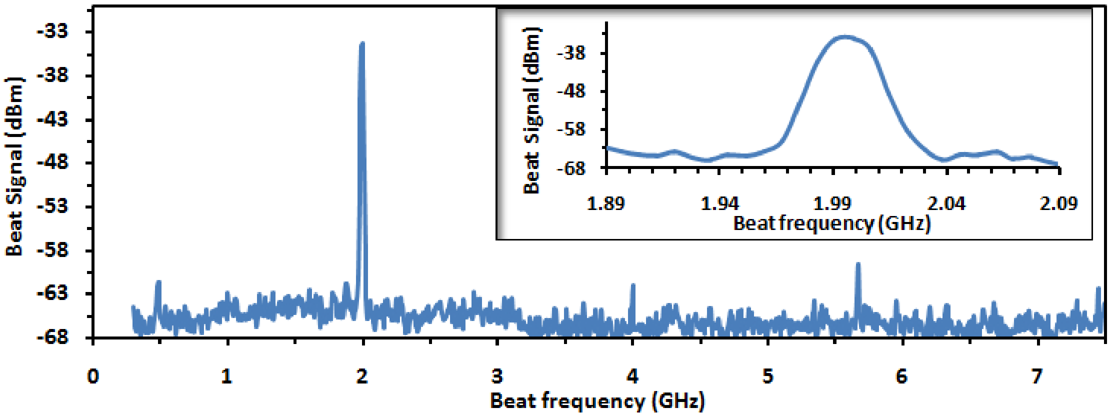

Figure 4. 35: The beat signal with commercial TLS in MOPA.

It is important to note that the multiple frequency noise peaks appeared in the beat spectra are due to environmental vibration and power supply electrical noises (60 Hz and its harmonics).

As a final result the beat spectrum of a narrow linewidth NZ-DSF based BFL which is amplified by a cladding pumped MOPA is shown in Figure 4.36. The linewidth of amplified BFL is measured to be about 10 kHz between 1545 to 1566 nm In the measurement, the BP linewidth and coupling ratio were fixed approximately

5±0.001 MHz and 0.5±0.1 respectively. The laser linewidth of local oscillator for a Brillouin gain bandwidth of 20 MHz is approximately less than 1 KHz.

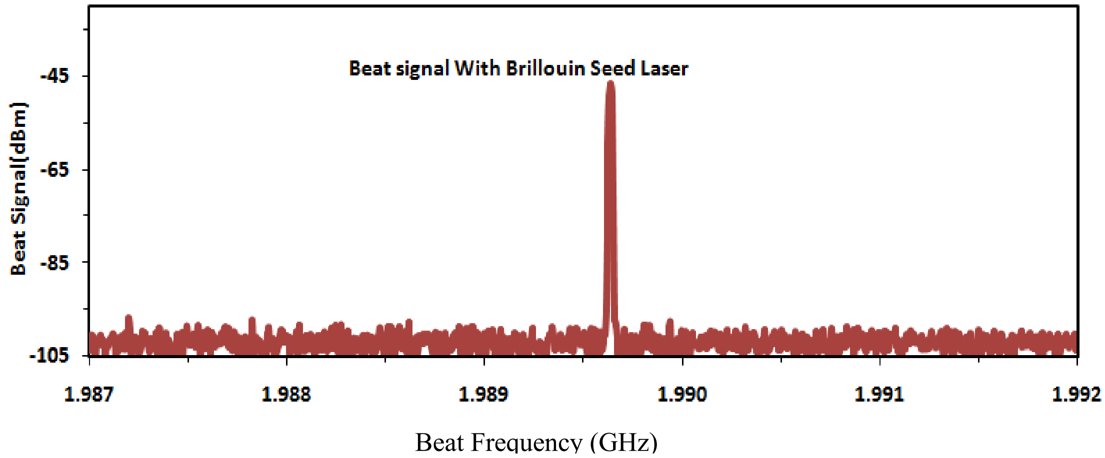

Figure 4. 36: The measured heterodyne beat frequency spectrum between amplified signal from BFL seed and SMF based local oscillator at an output power of 400 mW.

In actuality, in the BFL, the oscillation frequency that experiences the highest gain is temperature dependent as it follows the gain curve centre and the free spectral range (FSR) as well as frequency pulling and nonlinear Kerr effects which determine the frequency stability of the BFL system [305].

In conclusion, the construction of a high gain two-stage single mode amplifier was successfully accomplished to achieve a high power single-frequency emission with a low ASE, which is required in many applications. The amplification may be simply scaled to a few watts, by increasing the pump power. When the amplifier is working in the complete saturation regime with an input power of more than 5 mW, the output power is no longer sensitive to intensity variations of the input signal and the ASE power reduces to less than 1 % of the total output power.

4.7 SUMMARY

High-power cladding-pumped EYDFA was theoretically analyzed and the experimental outputs in the same condition were compared with the theoretical results. The slope efficiencies and the laser thresholds were also listed for different wavelengths in the laser operation. It was found that the efficiency is higher for shorter wavelengths. In MOPA configuration, the ratio of amplified signal power to the backward traveling power was found to be dependent on the signal wavelength and amplifier configuration.

The performance of a narrow linewidth BFL, which was amplified by this cladding pumped EYDFA in a MOPA system was also experimentally demonstrated. The tuneable amplified BFL has achieved the maximum output power of 400 mW with a laser linewidth of 10 kHz and and an optical signal-to-noise ratio of more than 45 dB in the wavelength region from 1545 to 1566nm. With a Brillouin pump linewidth of 5±0.001 MHz, a coupling ratio of 50% and a Brillouin gain bandwidth of about 20 MHz, the laser linewidth of the local oscillator can be estimated to be less than 1 KHz. No significant temporal degradation was observed after a short length of Bi-EDFA or a 10 m long DCEYDFA, even at an output power of 18 dBm for Bi-EDFA or 27 dBm for double cladding scheme. However, using a Si-EDFA (5-7m) the spectrum is started to distort at 5 dBm of average output power.

CHAPTER 5

Bi-EDF BASED LASERS
IN FEMTOSECOND REGIME

In this chapter, the theory of mode locking is reviewed. The dispersion management consideration for having stretched pulse is also described. In addition a mode-locked fiber laser is demonstrated by employing a 49 cm long Bi-EDF and using additive mode locking with nonlinear polarization rotation methods, whereby a slow saturable absorber (SA) is used. The goal of this chapter is to develop a MOPA system seeded by tunable mode-locked Bi-EDFL for investigating SCG process. The pulse width from this seed can be continuously varied from 1.2 ps to 130 fs. The pulse train is then amplified up to an average power of of 177.3 kW.

5.1 GENERATION OF FEMTOSECOND PULSES

Short optical pulses can be generated by employing mode locking, gain switching or by gating continuous wave light with an electro-absorption modulator. Mode locked laser is a train of pulses with a constant phase relation between the longitudinal lasing modes. These pulses are typically much shorter than the cavity round trip, and the repetition rate, which varies from tens of megahertz to a few hundreds of gigahertz, is determined by cavity round trip. The first mode locked laser was demonstrated by applying acousto-optic modulator using He-Ne laser by Hargrove et al. [18]. At the same time, the first frequency modulated (FM) mode locked laser was reported by Harris et al. [306]. The first passively mode locked laser with a stable pulse train was first demonstrated by Ippen et al in [307]. Generation of mode locked laser in fiber offers many advantages such as: having compact sizes, being maintenance- and alignment-free, possessing superior thermal handling, inherent stability and immunity against thermo-optical issues. This became feasible in 1980s [308, 309]. In Mollenauer's experiment, mode locked "soliton laser" was generated by adding an auxiliary fiber cavity to a mode locked laser. Later on, the first frequency modulated (FM) mode locked fiber laser [310] and the first amplitude modulated (AM) mode locked fiber laser using ring geometry were demonstrated [311].

In the following years, there was an explosion in fiber laser development. Hofer et al. presented a passively mode locked laser based on nonlinear polarization rotation (NLPR) [312]. An all-fiber, unidirectional mode locked ring laser based on NLPR was then implemented by Tamura et al [19]. At the same time, the use of semiconductor saturable absorber mirrors (SESAMs) as a pulse shaping element made a breakthrough in passively mode locked fiber laser with self starting and stable operation modes [313].

Femtosecond pulses have durations with the period of molecular oscillations and many scientific and commercial applications would benefit from mode locked fiber laser. This type of laser is being used in medical applications [314, 315], telecommunication [316, 317], microscopy [318, 319], spectroscopy [320], optical coherence tomography [321], optical metrology [322] and micromachining applications [323]. A femtosecond pulse's interaction with an electronic wave packet under well-defined conditions can give rise to the generation of higher-harmonics, up to the soft X-ray region, with pulse durations reaching the attosecond region. The required short laser pulses for continuum generation can be also generated by mode locking technique.

5.2 MODE LOCKING MECHANISM

The frequency spacing between longitudinal modes in laser cavity is given by $\Delta\nu=\dfrac{c}{L}$ where L is the optical length of one round trip in the cavity [64]. The total optical field in the cavity is then given by

$$E(t)=\sum_{m=-M}^{M} E_m \exp(i\phi_m - i\omega_m t) \qquad (5.1)$$

where E_m, ϕ_m and ω_m are amplitude, phase and frequency of the *m-th* mode among *N=2M+1* modes respectively. Mode locking occurs when the longitudinal modes within the gain bandwidth are synchronized, and relative phase differences of neighboring modes are a constant value of ϕ satisfying $\phi = \phi_m - \phi_{m-1}$. By rearranging Equation (5.1), the total intensity can be written as [324]:

$$|E(t)|^2 = \frac{\sin^2[(2M+1)\pi\Delta\nu t + \phi/2]}{\sin^2(\pi\Delta\nu t + \phi/2)} . E_0^2 \qquad (5.2)$$

Therefore, the mode locking results in a train of pulses with a repetition period of *2L/C=1/*$\Delta\nu$. Where $\Delta\nu$ is the frequency difference between longitudinal modes which is equal to the cavity round-trip time. In other words, the optical spectrum of a mode-locked pulse train consists of discrete lines with constant spacing which is equal to the pulse repetition rate. The pulse width can be also approximated from Equation (5.2) by:

$$\tau_P = \frac{T}{N} = \frac{1}{N\Delta\nu} = \frac{{\lambda_0}^2}{2c\delta\lambda} \tag{5.3}$$

As shown in Figure 5.1, the number of all phase locked modes (N) is related to the stimulated emission bandwidth ($\delta\lambda$) by $N=4L\delta\lambda/(\lambda_0)^2$. According to above arguments, as the spectral width becomes broader, the generated pulse becomes shorter.

This behavior is a consequence of the relationship between the time domain and the frequency domain described by the Fourier transform.

The product of the FWHM in time of the pulse $\mathrm{E(t)}$ and the bandwidth of the frequency evolution of the electric field (i.e. $E(\omega)$) depends only on the pulse shape.

The magnitudes of this product in a perfectly mode locked laser for Gaussian, Hyperbolic Secant, Lorentzian and Exponential pulse shapes are 0.441, 0.315, 0.221 and 0.142 respectively. Such Fourier-transform limited pulses, are the shortest pulses (Δt_{FWHH}) that can be generated for a given gain-spectrum ($\Delta\nu_{FWHH}$). In all the aforementioned cases, the spectral phase is a linear function of the frequency. However owing to group velocity or material dispersion, the spectral phase has a more complicated form of $\phi(\omega) = \sum_0^\infty \frac{1}{n!}\frac{d^n\phi}{d\omega^n}\Big|_{\omega_0}(\omega-\omega_0)^n$. Hence, dispersion in the cavity must be managed to have pulses as short as possible [65].

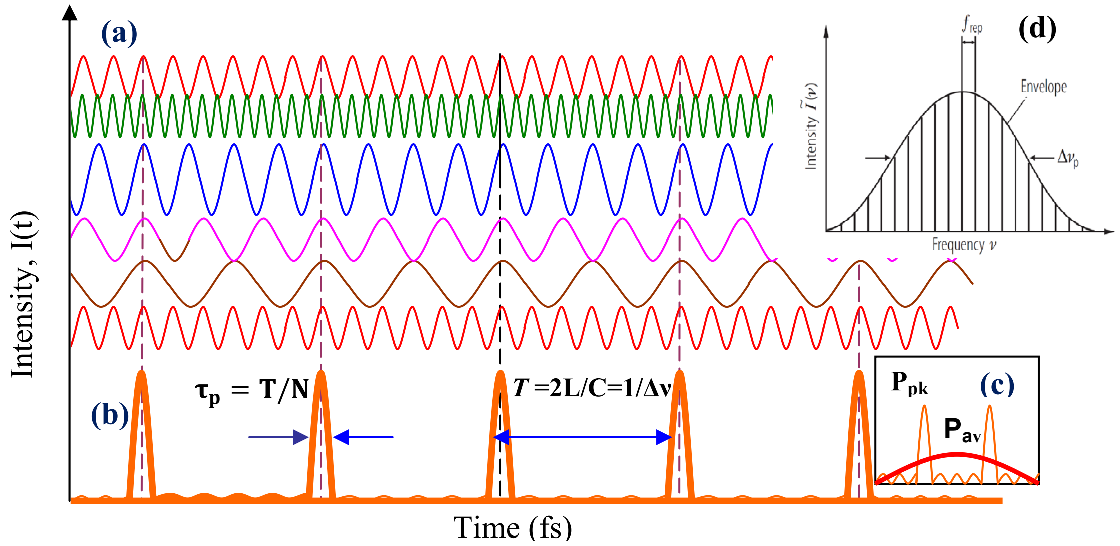

Figure 5. 1: Pulse sequences from a mode locked laser,(a) Random intense pulses in the laser cavity, (b) Ultra short pulses in the femtosecond regime produced when these random intense pulses add up together in phase at one instant time and (c) The corresponding peak and average power of the pulse (d) Mode locked pulses in frequency domain [325].

5.3 ACTIVE MODE LOCKING

Active mode locking can be achieved by using the periodic modulation of the resonator losses or by using the round-trip phase change. To that end, the amplitude or the phase of operating modes are modulated by a frequency of f_m which is equal to the mode phase difference Δv or is a multiple of that.

This modulation generates sidebands separated by f_m. These sidebands overlap with neighboring modes and are synchronized to them. For amplitude modulation specifically, the modulator alters the medium loss and causes the laser to operate in minimal loss, which leads to the pulsed operation of the laser in time domain as depicted in Figure 5.2 [64, 325].

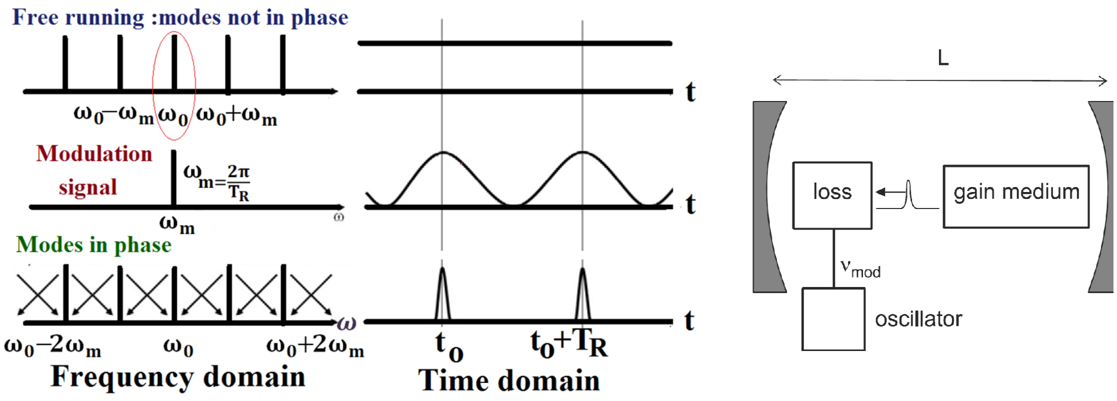

(a) (b)

Figure 5. 2: Active mode locking, (a) Loss modulation by external modulator, (b) Cavity loss and Pulse intensity in time domain [64].

An acousto-optic or electro-optic loss modulator is modulated by an external signal which produces loss modulation with a period given by the cavity round trip time (see Figure 5.2) [325]. The saturated gain supports the net gain just at the minimum loss and then supports pulses which are shorter than round trip time. The pulse shape and precise pulse width in fiber lasers can be calculated by the Ginzburg-Landau equation [64] or the Haus master equation [326]. The loss exerted by the modulator can be expressed as $\alpha = \alpha_c + \alpha_M[1-\cos(\omega_M t)]$ where α_C represents all cavity losses and α_M is the periodic loss at frequency of ω_M generated by the modulator. In the absence of GVD and SPM effects, the laser system emits a Gaussian pulse with FWHM of [325, 327]:

$$T_P = 1.655\times\left[2g_C/(\alpha_M \Omega_g^2 \omega_M^2)\right]^{1/4} \qquad (5.4)$$

where g_C is the saturated gain and Ω_g is the gain bandwidth. The pulse width then, depends on the gain bandwidth, modulation frequency (ω_M) and longitudinal frequency spacing. Introducing GVD and SPM effects in the cavity causes nonlinear perturbation leading to changes in pulse shape and width. SPM shortens the pulse as well as introduces chirps to the pulse. On the other hand, an excessive amount of SPM destabilizes the laser [325, 328].

5.4 PASSIVE MODE LOCKING

In passive mode locking, an intensity fluctuation without external control is utilized to modulate the cavity loss with low noise. In comparison to active mode locked laser, passive mode locking generates much shorter pulses due to the fact that the external modulation pace is slower than the intra-cavity modulator which is driven by the pulse itself [325].

Several mechanisms can be used for passive mode-locking such as saturable absorbtion (SA), NLPR, nonlinear mirror device containing a frequency-doubling crystal ,Colliding Pulse and Kerr lens mode-locking [325]. The NLPR or polarization additive pulse mode-locking (P-AMP) as well as the nonlinear amplifying loop mirror (NALM) techniques rely on the Kerr effect in the length of optical fiber. These techniques are employed in conjunction with polarizers to introduce artificial saturable absorber action [19, 79].

NLPR exhibits extremely fast absorption behavior with wide tunability and does not put any practical limitations on the pulse duration or operating wavelength. On the other hand, NALM forming a figure-8 shape cavity displays a tendency for operation with bursts of multiple pulses due to its long cavity length [329].

As a third method, saturable absorber layers were introduced in optical devices to examine their nonlinear optical property of an intensity dependent absorption for ultrafast all-optical switching [330]. Although passively mode-locked lasers usually produce shorter pulses than actively driven systems do, they may suffer from instabilities due to amplitude fluctuation, timing jitter and Q-switching.

5.5 ULTRASHORT PULSE SHAPING MECHANISMS

A comprehensive understanding of the pulse shaping mechanisms is essential for the laser design. This section describes how a short optical pulse propagates and is shaped by the time-varying and nonlinear dynamics which produce modelocking in a cavity consisting of active and passive fibers as well as an output coupler, and a saturable absorber. As shown in Figure 5.3 the basic elements of pulse shaping are: bandwidth limiting , self-phase modulation, self-amplitude modulation, gain and loss.

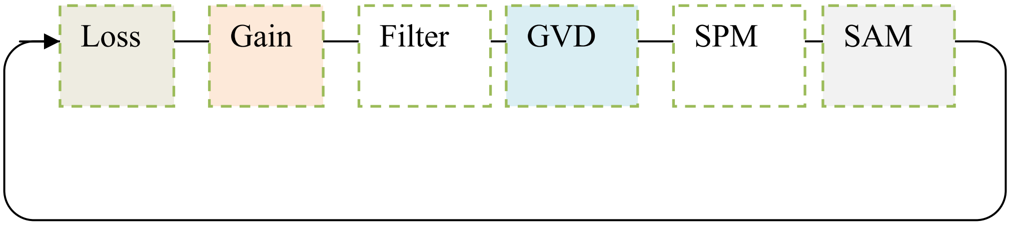

Figure 5. 3: The pulse shaping elements in a passive modelocked laser [331].

When simulating active fibers in mode-locked lasers, the gain saturation and gain filtering have to be taken into account. The gain saturation simply depends on the total pulse energy by the following relation:

$$g(z) = g_0 / \left(1 + \frac{\mathcal{E}_{pulse}(z)}{\mathcal{E}_{sat}}\right) = g_0 / \left(1 + \frac{p_{ave}(z)}{p_{sat}}\right) \qquad (5.5)$$

where g_0, $\mathcal{E}_{Sat}$, P_{Sat} , $\mathcal{E}_{Pulse}$ and P_{ave} are the small signal gain, saturation energy, saturation power, interacavity pulse energy and interacavity average power, respectively. Furthermore, we have the following relations, $P_{Sat}=\mathcal{E}_{Sat}/\tau_g$ and $P_{ave}=\mathcal{E}_{Pulse}/T_R$, where τ_g is the gain recovery time. Loss, pulse broadening by bandwidth limiting as well as pulse broadening and chirping by GVD are simply assumed to be time-independent linear effects [332].

In the time domain, the passage input pulse *E(t)* through the gain turns into *E'(t)* and a single pass through an element with GVD changes an incident input pulse E' into a broadened and chirped output pulse E'':

$$E'(t) = (1 + g(1 + ({\omega_g}^{-2})\frac{d^2}{dt}))E(t) \tag{5.6}$$

$$E''(t) = \left(1 + jD\frac{d^2}{dt}\right)E'(t) \tag{5.7}$$

Hence a fractional increase of $\Delta\tau/\tau=2g/{\omega_g}^2\tau^2$ in pulse width is produced per pass by the bandwidth limiting effect [333], while GVD term rapidly chirps the pulses and produces an increase of $\Delta\tau/\tau=2D^2/\tau^4$ and keeps the spectral bandwidth intact. So some sort of nonlinearity or pulse shortening modulation is required to generate short pulses.

The pulse duration obtained from a simple scheme with a SA, especially in the picosecond regime, depends strongly on the parameters of the SA. The shaping process often is the result of a steady state between the pulse-shortening effect of the SA and gain narrowing [334]. In fiber lasers, the fiber nonlinearity is often stronger than what is desirable and excessive nonlinear phase shifts can destabilize the pulses or limit the achievable pulse durations. In brief the stability limit not only depends on the gain bandwidth, but also on the total intracavity losses, the strength of nonlinearities and other factors.

The Haus master equation [335] and the nonlinear Ginzburg-Landau equation or the generalized nonlinear Schrödinger equations (NLSE) [336] describe the propagation of ultrashort pulses. It is possible to distinguish three stable operation regimes among the solutions that depend on the dominant pulse shaping mechanisms in the laser cavity:

I. Soliton pulse regime determined by the balance between anomalous dispersion and self-phase modulation resulting from Kerr nonlinearity and has no additional requirements on the cavity stability regime, such as KLM.
II. Stretched-pulse regime determined by dispersion-managed solitons and
III. Self-similar pulse regime determined by the interrelation of normal dispersion and finite-bandwidth gain.

In general, for zero SPM the minimum pulse width (τ_0) occurs at zero GVD and has a value consistent with a simple balance of the SA pulse shortening and filter broadening. As SPM increases, the point of the minimum pulse width moves to negative GVD where the chirp is compensated. As a final remark, the proper balance between GVD and SPM reduces the pulse duration by a factor of 2.75 [331].

5.6 INFLUENCE OF DISPERSION ON MODE LOCKING REGIME

The pulse characteristics and its formation in the cavity are strongly dependent on the net-dispersion in the cavity and proper dispersion management in fiber lasers is essential for the production of clean pulses. Under the influence of strong optical nonlinearities, the concept of resonator modes becomes questionable. Even though the lines in the spectrum of a mode-locked laser are related to the resonator modes, it is not advisable to use term modes for these lines.

In the gain medium, the mode-locking mechanism forces the laser to emit in frequencies which can to some extent deviate from the frequencies of the resonator modes. These longitudinal modes must be kept equally spaced in frequency and frequency deviations may not be arbitrarily high.

In addition, a single pulse propagating around the laser cavity must have the same shape after one round trip. Chromatic dispersion causes the modes to be spaced unequally in frequency, and leads to output pulse durations which are longer than the minimum duration supportable by the amplifier bandwidth. Therefore, the generation of a broadband spectra is usually possible only if the resonator dispersion is sufficiently small, so that the resonator mode frequencies are approximately equidistant.

Clearly, this dispersion will cause the pulse to broaden. The nonlinear mode-locking mechanism balances this broadening tendency to some extent, though minimizing linear dispersion is still necessary [337]. It is generally useful to classify mode locking regimes that involve nonlinear phase modulations based on the net dispersion in the cavity.

With only anomalous dispersion, soliton formation can occur for any value of GVD. As a result nearly bandwidth-limited soliton-like pulses can be easily obtained when the GVD balances the self-phase modulation (SPM). In soliton like pulse shaping, self amplitude modulations mostly play a secondary role, namely starting and stabilizing the mode locking. For a large net anomalous GVD, the pulses approximate static solitons, but as the net GVD approaches zero the solutions breath. Most femtosecond lasers have segments of normal and anomalous GVD such that the cavity consists of a dispersion map (DM). With a dispersion map, the solutions are generally DM solitons. DM solitons can even exist at small net normal GVD.

The broadening of the pulse width using net positive (i.e. large net normal) GVD is an effective approach to increase the pulse energy from oscillators without external amplification. These include so-called self-similar laser [338] and the chirped pulse oscillator (CPO) [339, 340]. Highly chirped pulses generated from a CPO preserve the form during circulation in the cavity due to the weak dispersion map (DM) while highly chirped pulses are produced with a notable breathing ratio in a self-similar laser cavity due to strong DM. However, the pulse energy would be limited by over-driving the nonlinear polarization evolution (NPE) [325, 341].

Ultimately, stable pulses with notable high energy are generated in an all-normal dispersion (ANDi) fiber laser [342]. Remarkably, no anomalous dispersion is required in ANDi design. Such ANDi lasers containing interacavity spectral filters provide additional self-amplitude modulation, and also exhibit a variety of pulse shapes and evolutions by reducing the strength of the NPE [343].

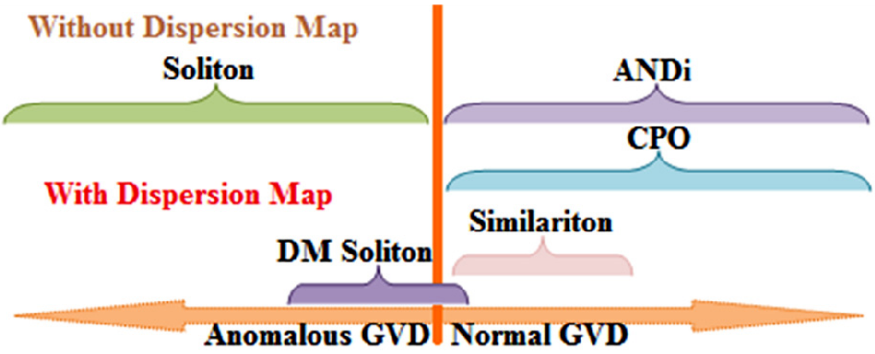

Figure 5. 4: Operating regime based on the net cavity GVD.

To fundamentally shape the pulse (as opposed to just starting and stabilize it), the mode locking regimes at large normal GVD rely on dissipative processes such as spectral filtering. The generated pulses from this ANDi fiber laser are found to balance not only phase modulation but also gain and loss. Thus they constitute dissipative solitons [344]. Mode locking regimes based on the net cavity GVD are shown in Figure 5.4.

5.7 PASSIVE MODE LOCKING WITH NLPR

Several different schemes have been used successfully to form artificial saturable absorbers [345]. One of the methods to generate short pulses from a solid-state laser is via Kerr-lens mode-locking (KLM). In conjunction with some kind of apertures, the nonlinear indexes of the laser crystals as the Kerr medium are utilized to synthesize the simplest embodiment of KLM. The optical Kerr effect produces a non-resonant artificial saturable. In fact, the fastest optical nonlinearities are reactive and non-resonant. They are relatively weak but inherently broad band. The nonlinearity in glasses has also a response on the order of a few femtoseconds [346] and it may be utilized over a wide range of wavelengths. In the fiber lasers, NLPR (P-AMP) and nonlinear fiber loop mirror are convenient methods to utilize Kerr nonlinearity.

Passive mode locking can be achieved by exploiting the changes in intensity dependent states of polarization, caused by SPM and XPM in a cavity. In a ring cavity, a polarizing isolator and one or two polarization controllers act as artificial saturable absorber as shown in Figure 5.5 [327, 347, 348].

The light pulse leaving the polarizer has linear polarization. The polarization controller after the polarizing isolator changes the polarization state slightly to an elliptical state. Hereinafter, the orthogonally polarized components experience nonlinear changes in the fiber sections of the cavity, which act as Kerr medium.

This nonlinear change is intensity dependent and is due to SPM and XPM induced phase shift during the pulse propagation through the fiber sections. The second polarizer placed before the isolator, is adjusted to change the polarization of the central part of the pulse to a linear state.

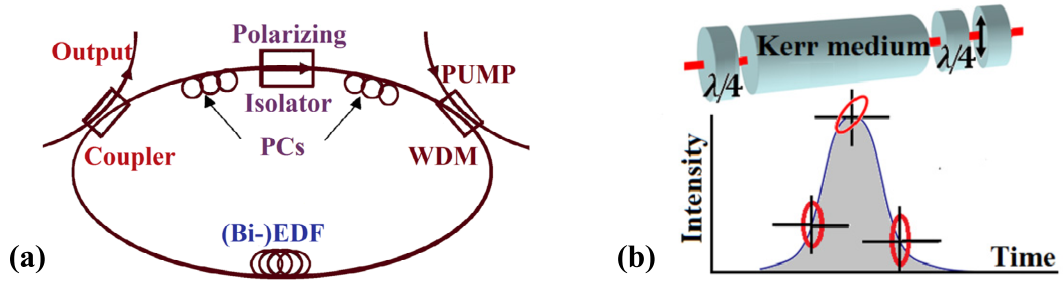

Figure 5. 5: (a) Passively mode locked laser using NLPR technique. (b) Schematic of the NLPR process. The wings of the pulse undergo little or no rotation relative to the peak of the pulse. This polarization difference is turned into a loss when the pulse is analyzed at the polarizer.

Note that, the state of polarization is nonuniform across the pulse due to the intensity dependent induced nonlinear phase shift. Finally, the isolator allows the intense linear central part of the pulse to propagate through the polarizing isolator while it absorbs the low intensity wings. It results in a slight pulse shortening in one round trip similar to a fast saturable absorber. This phenomenon is illustrated in Figure 5.5.

A combination of wave plate polarizer and fiber loop retarder can be used as polarization controller. Meanwhile, a polarizing beam splitter (PBS) integrated with an isolator can be applied as a polarizer and isolator that only allows the linear polarized part (of the light pulse) to pass. The main advantage of this method is that it generates self starting short pulses through adjusting the polarization. However, such approach demands regular adjustment of the structure to operate in the optimum condition. In fact, this method suffers from some issues. The first issue is that randomly changing birefringence in the fiber, changes the polarization of the pulse. Consequently, the propagation time would be altered in an unknown way. These changes which degrade mode locking are due to thermal changes or mechanical stresses. The second issuse is time-varying linear and nonlinear phase delays between the eigenmodes of the fiber [349].

5.8 PASSIVE MODE LOCKING WITH SATURABLE ABSORBER

A saturable absorber is an optical material or setup that ensures an absorption, which is reduced with optical intensity. A pictorial schematic that describes the principle of pulse shortening provided by a saturable absorber is presented on Figure 5.6.

The top left corner of the Figure 5.6 illustrates a typical transmission curve of an absorber, which shows that the transmission increases as the power of the incident pulse increases. Pulse formation in a cavity using SA initiates from spontaneous emission and stochastic noise fluctuations. When such an absorbing element is used within a laser cavity, these emissions continuously grow and reduce the loss. This process will be completed when the formed intense pulse saturates the absorber. However, due to the dispersion inside the cavity and the nonlinear frequency pulling of the axial modes (caused by spurious reflections), these noise spikes have finite coherence times. The nonlinear modulation must be large enough to continue the sharpening and growth of each spike, before it decays. The SA promotes the pulse formation with an increased peak power and suppresses the lower-intensity CW light. Because the laser tends to operate with a minimum cavity loss per round-trip, the longitudinal modes of the lasers become phase-locked.

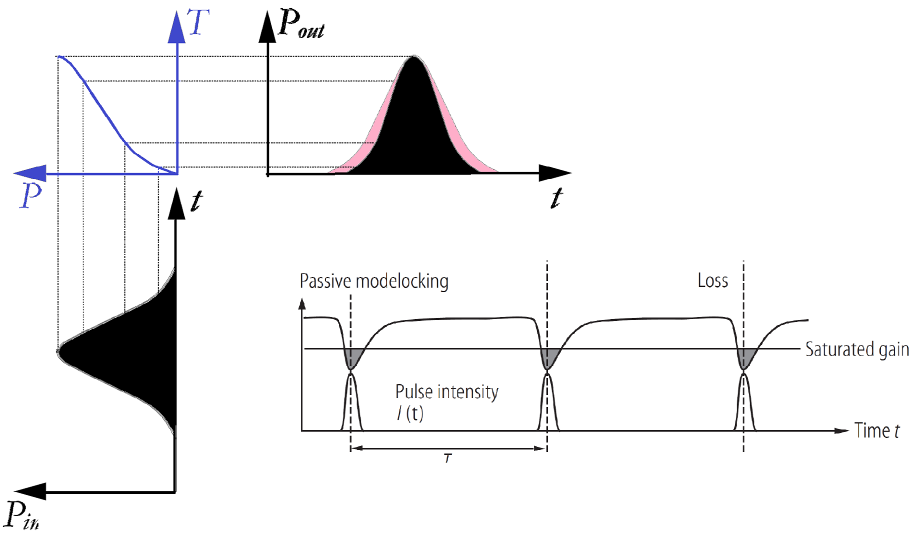

Figure 5. 6: Pulse-shaping process with a SA.

5.8.1 Saturable Absorber Structure and Technology

A saturable absorber is a nonlinear component which has a decreasing light absorption ability with increasing light intensity. Saturable absorbers are used for intracavity purposes such as passive mode locking and Q switching, or used externally for nonlinear filtering. The most important type of absorber for mode locking of solid state lasers is the semiconductor saturable absorber mirror (SESAM). In some lasers, a saturable absorber (SA) section is created simply by not pumping that region. SA materials such as bismuth chromium or samarium dopants in the form of optical fibers are used for Q-switching [11]. Other absorbers such as lead sulfide suspended in glasses or single-wall carbon nanotubes are based on quantum dots or carbon nanotubes [9]. One drawback of single-wall carbon nanotubes as saturable absorbers is its strong scattering and thus strong non-saturable losses [14,15].

SESAMs are designed in resonance (R-SESAMs) and antiresonance structures and they can be designed as reflective components along with a circulator inside the cavity or as a intracavity transmittance component. These kinds of structures can be used in various laser configurations.

The concept of a resonant Fabry–Perot microstructure is well known [350]. The structure of the R-SESAMs typically consists of an active region corresponding to the Fabry–Perot cavity, a bottom and a top distributed Bragg reflector (DBR). As shown in Figure 5.7(a), R-SESAM is designed as a resonant Gires–Tournois interferometer with absorber layers positioned at the antinodes of the optical field inside the setup [351, 352]. Depending upon the reflectance of partially reflective mirror they can be used as a noise suppressor, a pulse picker and a passive mode-locker.

A close to-resonant Fabry–Perot saturable absorber structure, referred to as the D-SESAM (dispersive SESAM or SA) is used to optimize both negative group-delay dispersion (GDD) and the nonlinear modulation to construct more compact femtosecond sources without further dispersion compensation or special cavity design [330, 353].

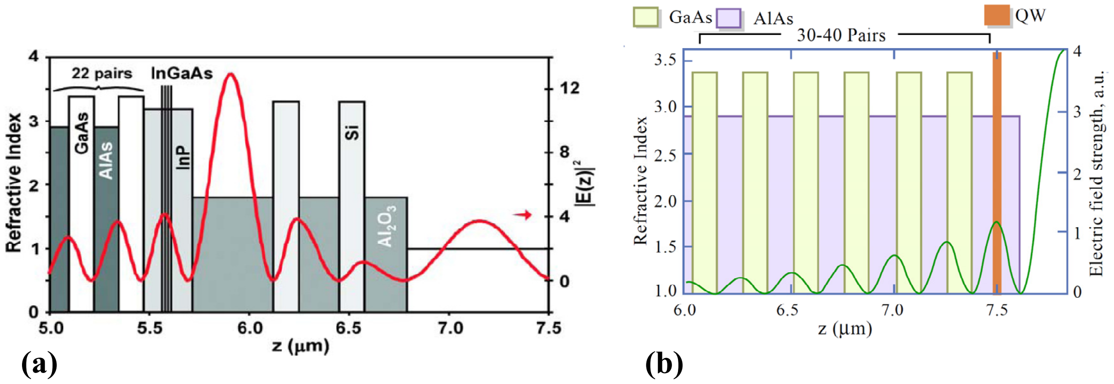

(a) **(b)**

Figure 5. 7: Typical structure of SESAM in (a) resonant,(b) anti-resonant scheme. In R-SESAM the field in the quantum well is resonantely enhanced by about a factor of 10 in comparison to the non resonant case.

An antiresonant SESAM with absorbance value between 20 % to 50 %, depending on the fiber gain can be used to generate femtoseconds pulses. An A-FPSA as show in Figure 5.7(b) is typically formed by the lower semiconductor Bragg mirror and a dielectric top mirror, with a SA and possibly transparent spacer layers in between. The thickness of the total absorber and spacer layers are adjusted such that the Fabry-Perot is operated at anti-resonance. The top reflector is an adjustable parameter that determines the intensity entering the SA and the effective saturation intensity [330, 354, 355].

Compared with devices with an anti-reflection coating, A-FPSA designs have a lower field penetration into the absorber [313]. In general, an antiresonant SA exhibit a more or less constant degree of saturable absorption and for transmission applications can lead to a high-repetition-rate cavity with fewer required components and without significant dispersion influence of the SA. Operation at antiresonance leads to a device that is broad-band and has minimal group velocity dispersion. In this thesis, a transmission type of SA has been utilized. The proposed fiber butt coupled

SA consists of a group of absorbing InGaAs quantum wells on a semiconductor wafer like GaAs, covered on both sides with an antireflection coating [13].

5.8.2 Influence of Saturable Absorbers Parameters on a Mode-Locked Laser

Saturable absorbers are characterized by a subset of parameters which depend on the SA structure and materials. The most important parameters of a SA are transmittance and absorbance. The absorbance of the SA consists of two parts: saturable absorption and non-saturable absorption.

Figure 5.8 shows saturation characteristics and relative parameters of a typical SA. In the figure, ΔR_{NS} is non saturable loss and it is the remaining loss in absorber after getting bleached by highly intense pulse [325, 334]. Note that, the ratio between the saturable part and the non-saturable part of the absorption depends mainly on the relaxation time of the excited carriers in the absorbing quantum wells.

Another effective parameters is modulation depth (ΔR), which is the maximum change in absorption or reflectivity of the absorber. Large modulation depth leads to stronger pulse shaping and shorter pulse width and hence, reliable self staring. However, an excessively large modulation depth might cause Q switching instability.

An important limiting factor of a SESAM is its saturation fluence [355]. The saturation fluence, F_{sat} (j/cm^2), is the energy per unit area that determines the strength of pulse to reduce the absorption. To prevent the destruction of SA from high pulse fluences, the saturation fluence must be low. The saturation intensity of a SA is also defined as the optical intensity that it takes to reduce the absorption to one half its unbleached value.

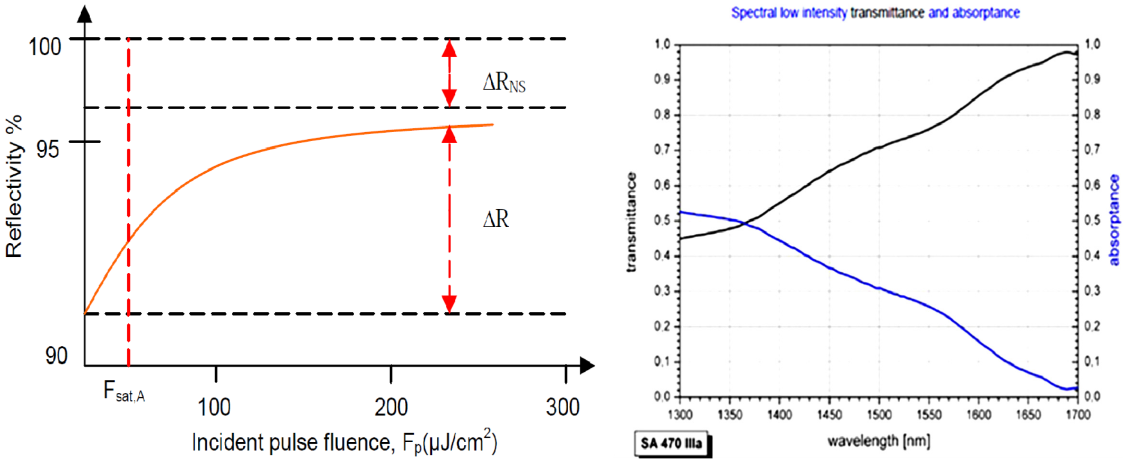

(a) **(b)**

Figure 5. 8: (a) Reflectivity changes in SESAM as a function of the incident pulse fluence (b) Transmittance changes as a function of the incident pulse wavelength in a transmission type of SA, used in this thesis.

The SA layer consists of a semiconductor material with a direct band gap slightly lower than the photon energy. During the absorption, electron-hole pairs are created in the film. The relaxation time of the carriers has to be a little bit longer than the pulse duration to prevent Q-switching. The recovery time is the main factor that determines the speed of the absorber to recover after excitation by pulse.

Changes in loss, gain spectrum, internal cavity power, etc, of each laser, necessitate slightly different absorber characteristics. For a mode-locked fiber laser, the absorption recovery time is below 25 ps [356].

A resonant designs have a higher modulation depth, a larger saturable absorption, a smaller bandwidth, a lower saturation fluence [357] and finally a lower damage threshold when compared to an anti-resonant design. Lower saturation fluence is particularly desirable for fundamentally mode-locked lasers with an ultra-high pulse-repetition rate (i.e. PRR>>1 GHz) [358-360]. Furthermore, the threshold for continuous-wave mode locking without Q-switching instabilities (QML threshold) is decreased with a low saturation fluence [361].

5.8.3 Mathematical Description of Loss Modulation

A mathematical description of saturable absorbers enables us to investigate their effects on pulse shape and predict the resultant output pulse, e.g. the narrowest pulse [325, 362, 363]. The behavior of saturable absorbers is modeled by following general equation:

$$\frac{dq(t)}{dt} = -\frac{q(t)-q_0}{\tau_A} - \frac{q(t)P(t)}{E_{sat,A}} \tag{5.8}$$

where $q(t)$ is the saturable amplitude loss coefficient, $P(t)$ is time dependent incident power, $E_{sat,A}$ is the saturation energy (saturation fluence times the incident beam area) and τ_A is the recovery time.

The unsaturated amplitude loss coefficient in this equation is denoted by q_0. In dealing with pulses, if the absorber recovery time is well below the pulse duration, the absorber is called a fast absorber. Otherwise it is called a slow absorber. Hence the same device may be either a fast or slow absorber. Fast absorber dynamics produce an ever increasing pulse shortening rate and differ from the slow absorber case in which the shortening rate is independent of pulse width [347].

5.8.4 Mode Locking with a Slow Saturable Absorber

As shown in Figure 5.9(a), a slow SA causes a loss modulation which is fast for the leading wing of the pulse, whereas recovery of the absorber takes some longer time. Thus, the slow absorber attenuates the leading edge of the pulse much more than the trailing edge [65]. Consequently, the pulse is shifted backwards in time with every propagation through the absorber.

As a result with slow SA there is a temporal range with net gain just after the pulses in which the absorber is still in the saturated state. Noise is amplified during this window. This noise grows due to its higher gain compared to the pulse. Since the pulse moves backwards due to the slow interaction of absorber, it is shifted on top of the growing noise, which causes noise to be suppressed.

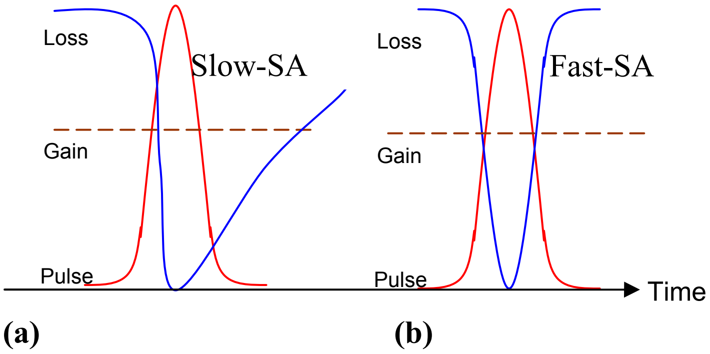

Figure 5. 9: Temporal evolution of optical power and losses in a passively mode-locked laser with a (a) slow saturable absorber, (b) fast saturable absorber [364].

In the case of slow saturable absorbers, Equation 5.8 reduces to:

$$\frac{dq(t)}{dt} \approx -\frac{q(t)P(t)}{E_{sat,A}} \tag{5.9}$$

The absorption is now saturated by time-dependent energy *E(t)* or the integrated pulse intensity (instead of the instantaneous intensity). Therefore, for a given incident pulse fluence ($F_{P,A}$), the intensity-dependent, time-averaged loss can be expressed as:

$$q_p(F_{p,A}) = \int q(t) f(t) dt = \alpha_0 + q_0 \frac{F_{sat,A}}{F_{p,A}} (1 - e^{F_{P,A}/F_{Sat,A}}) \tag{5.10}$$

Here, q_0 is the unsaturated amplitude loss coefficient and α_0 accounts non-saturable losses. It is also useful to introduce the saturation parameter as $S=F_{p,A}/F_{sat,A}$ to express the strength of incident pulse to saturate the absorber. With a $S>3$ the minimum pulse width resulted from a slow SA without gain saturation and soliton formation can be given by:

$$\tau_{p,\min} \approx \frac{1.5}{\Delta\upsilon_g} \sqrt{\frac{g}{\Delta R}} \tag{5.11}$$

where $\Delta\nu_g$ is the FWHM of gain bandwidth, g is saturated amplitude gain coefficient and ΔR is modulation depth. In solid state lasers ΔR can be related to the unsaturated amplitude loss coefficient q_0 by $\Delta R=2q_0<<1$. Again similar to the case of fast SA the effects of Kerr nonlinearity and dispersion in the cavity, phase changes on the absorber and spatial hole burning in the gain medium have been neglected.

Simulations have proven that SPM alone in the positive dispersion regime should always be kept small because it always makes pulses longer and even destabilizes them, particularly for absorbers with a small modulation depth. A rule of thumb is that the nonlinear phase shift for the peak should be at most a few mrad per 1% of modulation depth. In fact in the sub-picosecond domain, SPM could hardly be made weak enough. Hence, the soliton regime is commonly needed in this domain, for there the nonlinear phase changes can be much larger(see section 5.9) [325, 363].

In a simple scheme of having a SA, especially in the picosecond domain, a large modulation depth supports shorter pulses, but there is an upper limit for ΔR due to the stability limit. Accordingly to have a stable ps pulse train, the critical intracavity pulse energy $E_{p,c}$ with certain approximations is recommended as $E_p^2 > E_{p,c}^2 = E_L^{sat}.E_A^{sat}.\Delta R$ [361], where E_p is the intracavity pulse energy, E_L^{sat} is the saturation energy of the gain medium, E_A^{sat} is the saturation energy of the saturable absorber, and ΔR is the modulation depth of the absorber. This relation shows that the modulation depth cannot be increased arbitrarily since it could cause QSML and high, non-saturable losses. In order to have a clean single pulse and an effective gain saturation, the gain must be saturated after the saturation of the absorber or E_L>E_A where E_L is the saturation energy of the gain and E_A is the saturation energy of the absorber. Moreover, the gain lifetime must be shorter than or comparable to the cavity round trip time and the absorber must recover faster than the gain.

5.8.5 Mode Locking With a Fast Saturable Absorber

In fast absorbers, the loss modulation basically follows the variation of the optical power as shown in Figure 5.9. As a consequence, as the pulse becomes shorter, the loss modulation would become faster. A fast absorber can suppress any weaker pulses and continuous background light. It constantly attenuates the leading wing of the circulating pulse. If the absorber recovers at sufficiently quick rate, then the trailing wing may also be attenuated. With a gradual decrease in the pulse duration, the effective saturation fluence of the absorption would also decrease at this limit. The fast absorber with short recovery time is preferred for shaping short pulses as it is efficient in the rejecting of long pulses that suffer large saturation fluence [365]. On the contrary the starting capability of a fast absorber is poor compared to the slow absorber. In the case of a fast saturable absorber, Equation 5.8 for $q(t)$ are changed to:

$$-\frac{q(t)-q_0}{\tau_A}-\frac{q(t)P(t)}{E_{sat,A}}=0 \tag{5.12}$$

$$q(t)=\frac{q_0}{1+\frac{I_A(t)}{I_{sat,A}}} \tag{5.13}$$

where we used the fact that $P_{sat,A} = E_{sat,A} / \tau_A$ and $P(t) / P_{sat,A} = I_A(t) / I_{sat,A}$. With a fast saturable absorber and by neglecting dispersion and nonlinear effects, the unchirped solution for NLSE takes the form of $P(t)=P_0 \times sech^2(t/\tau)$ in which P_0 is the intracavity peak power and τ is obtained from[325]:

$$\tau^2=8gI_{Sa}\,S_{eff,A}\,/q_0P_0\,\Omega_g^2 \tag{5.14}$$

which leads to a soliton pulse duration (FWHM) of $\tau_p=1.7627\times\tau$. In this equation Ω_g is the total homogenous bandwidth, g is the saturated amplitude gain coefficient and $S_{eff,A}$ is the effective area of the saturable absorber. For a $sech^2$ shape pulse and an ideal fast absorber, the absorber saturates linearly with the pulse intensity over the full modulation depth that is: $q(t) = q_0 - \gamma_A P(t)$ and $\gamma_A = q_0/I_{sat,A}A_A$. In this case total loss is expressed by:

$$q_p(F_{p,A})=\frac{1}{F_{P,A}}\int q(t)I_A(t)dt=q_0(1-\frac{1}{3}\frac{F_{p,A}}{\tau.I_{sat,A}}) \tag{5.15}$$

In general for a laser medium with a gain dispersion of D_g, the transform limited pulse duration is given by:

$$\tau_{p,\min} = \frac{1.76}{\Omega_g}\sqrt{\frac{2g}{q_0}} \approx \frac{1.12}{\Delta\upsilon_g}\sqrt{\frac{g}{\Delta R}} \tag{5.16}$$

where Ω_g is HWHM of gain bandwidth, and ΔR is modulation depth. An additional pulse shortening (with a factor of 2) is predicted by accounting for GVD and SPM, i.e. soliton formation. The unchirped soliton pulses are obtained only at certain negative dispersion value given by $|D| = D_g\ \delta_L/\gamma_A$ where δ_L is the SPM coefficient.

5.9 SOLITON PULSE REGIME

The spectrally dependent group delay of a standard optical fiber can lead to a sizable lengthening of sub-picoseconds pulses after a propagation of over less than one meter of fiber. The simultaneous action of SPM and chromatic dispersion can generate a variety of behaviors, from the formation of stable soliton pulses to distortions and pulse break-up [65]. Under certain circumstances, apart from a constant phase delay per unit propagation distance, the effects of Kerr nonlinearity and dispersion can exactly cancel each others and the pulse might propagate with a constant temporal and spectral shape even over long propagation distances [16]. Fundamental soliton pulse propagation in a lossless medium with a positive value of the nonlinear coefficient (n_2), requires the anomalous chromatic dispersion, and a constant group delay dispersion (no higher-order dispersion). Solitons are very stable and can adiabatically adapt their shape to slowly varying parameters of the medium, provided that these changes occur over distances which are long compared with the so-called soliton period .This period is defined as the propagation distance in which the constant phase delay equals to $\pi/4$.

Soliton mode locking with a quasi-soliton circulating pulse can be generated in laser cavities with a net anomalous round-trip dispersion. In this regime, in which the pulse shaping is done solely by soliton formation, the pulse duration is determined by the balance of the dispersion (GVD) and Kerr nonlinearity (SPM), without a significant direct influence of the gain bandwidth and other parameters. However an additional loss mechanism such as a saturable absorber or an acousto-optic modulator is necessary to start the mode-locking process around the proposed wavelength and in order to stabilize it [325].

Due to the gain dispersion and losses in the cavity, the soliton pulse loses its energy. This lost energy is called a continuum. The continuum would actually grow until it reaches the lasing threshold which instabilizes the soliton. The dispersion causes the background to broaden temporally. Thus, the energy in those parts which drift into the time regions with net loss would be permanently lost. However, we can stabilize the soliton by introducing a slow SA to add sufficient additional loss for the growing continuum that spreads in time during its build-up phase so that it no longer reaches the lasing threshold. The improvement is particularly large for absorbers with a relatively low modulation depth. Indeed, soliton pulses with durations in order of 40 times shorter than the absorber recovery time have been demonstrated. Even with saturable absorber, SPM can make the system unstable unless sufficient dispersion is introduced at the same time. Haus's master differential equation can be solved analytically using soliton perturbation theory. A stable solution for negative GVD and positive SPM is given by:

$$A(z,t) = A_0\, sech\,(t/\tau) e^{-i\Phi_s(z)} \tag{5.17}$$

where I_0 is the peak intensity inside the SPM medium and the phase shift of the soliton during propagation along the z-axis is given by:

$$\Phi_s(z) = kn_2 I_0 z/2 \equiv \Phi_{nl}(z)/2 \tag{5.18}$$

The soliton pulse duration (FWHM) is given by τ_p =1.7627 × τ and the time bandwidth product could be computed by $\Delta\nu_p \times \tau_p$ =0.3148. With an intracavity pulse energy of E_p , a shorter pulse duration is achieved with a smaller magnitude net GVD in an anomalous dispersion regime [366]:

$$\tau_p = 1.7627 \times \left(2|D|/(\delta_L E_p)\right) \tag{5.19}$$

The naturally occurring chromatic dispersion is often in the normal dispersion regime. For optimum pulse generation, it is often beneficial to overcompensate the normal chromatic dispersion in order to utilize the regime of anomalous dispersion or even close to zero dispersion, where soliton effects can help to obtain shorter pulses which may also have a higher pulse stability and weaker pedestals.

By accounting SPM coefficient, based on the phase shift of the soliton per cavity round trip ($\Phi_s = \delta_L P_0$) and the intracavity peak power (P_0), the minimum pulse duration (τ_p^{min}) can be predicted as:

$$\tau_p^{min} \approx 0.45 \times (\,1/\Delta\upsilon_g)^{\frac{3}{4}}\,(\tau_A/\Delta R\,)^{\frac{1}{4}}(\,g^{\frac{3}{8}}/\Phi_s{}^{\frac{1}{8}}) \tag{5.20}$$

In the case of soliton mode-locking, unlike the ideal fast saturable absorber, an unchirped transform-limited soliton is obtained for all dispersion levels as long as the stability requirement against the continuum is fulfilled. This means that only higher-order dispersion increases the pulse duration.

It should be noted that soliton shaping effects can allow the generation of significantly shorter pulses, compared to cases without SPM. It is important to adjust the ratio of dispersion and SPM to obtain the desired soliton pulse duration.

Moreover, their absolute values should be kept in a reasonable range where the nonlinear phase change is in the order of some tens to a few hundred mrad per round trip (i.e. significantly larger than what is acceptable in cases without negative dispersion) [334]. In this situation, soliton mode locking allows a band width limited ultrashort pulses with low chirp .

The shortest soliton pulse extracted from fiber lasers has a durations of 500 fs [348]. With a broadband gain media, the minimization of pulse duration below roughly 30 fs essentially relies on compensation of the cavity dispersion to as many orders as possible. This can be achieved by employing a prism pair, GRISMs [367] or special fibers such as PCFs, multi mode fibers and chirped fiber Bragg gratings [75]. Higher order dispersion compensation by proper dielectric multi-layer mirror design is also being pursued as a means for getting pulses of a few cycles or less.

5.9.1 Soliton Limits

For a given pulse duration of τ_p and a group delay dispersion of β_2, the soliton period (Z_s) is defined as the propagation distance in which the nonlinear phase delay of a fundamental soliton reaches to the value of $\pi/4$:

$$Z_s \approx \pi\left(\tau_p/1.76\right)^2/(2|\beta_2|) \approx \tau_p^2/(2|\beta_2|) \qquad (5.21)$$

In fact, higher-order solitons also reproduce their temporal and spectral shape with this period.

In a cavity, solitons are disturbed with a nonlinear phase shift per round trip periodically. If the ratio of this disturbance period to the soliton period is well below unity, then solitons essentially experience just the average values of the chromatic dispersion and Kerr nonlinearity. Too small amounts of the nonlinear phase shift result in a stronger pulse shaping details of the SA.

For the picosecond regime, the nonlinear phase shifts are strong enough and soliton mode locking works well. However, the achievable pulse energy is limited to a few picojoules.

On the other hand, excessively strong nonlinear phase shifts per round trip can create Kelly sidebands in the spectrum and destabilizes the pulses due to the periodic disturbance on a length scale which is not much shorter than the solitons period. Generally this effect is a signature of soliton pulse losses. In other words, for an excessively short pulse when nonlinear phase shift reaches to the value of 2π at Z_s =0.125× L_{cavity}, resonant scattering would occur at the center frequency of the soliton. Hence increasing loss to the encroaching sidebands limits the energy and stops the shortening process [331].

In addition to the aforementioned limits, the soliton will eventually reach the limit imposed by additive pulse mode-locking saturation in the figure-8 configuration and long ring cavities. In these cases, nonlinear effects at high pump powers cause wave breaking which leads to multiple and uncontrolled pulse operation [368].

Consequently the stability of the circulating solitons requires a very strong saturable absorber in the femtosecond regime. Despite fairly small pulse energies, soliton operation is desired because it is possible to construct lasers that emit nearly transform-limited pulses directly from the cavity. This low chirp pulse minimizes dispersive temporal broadening, which is very desirable in SCG [369].

5.9.2 Quasi-Soliton Pulse Regime

As opposed to most soliton mode-locked lasers, the balance between the dispersion and nonlinearity is not fully preserved along the propagation path in the case of quasi-soliton pulses. Furthermore, the dispersion and nonlinearity usually come in discrete portions and the laser beam only experiences the averaged dispersion and nonlinearity of the resonator. The resulting pulse energy and the pulse duration exhibit oscillations during a resonator round trip. Nevertheless, the pulses may behave like solitons if the periodic deviations from the balance are not too large during one round trip.

5.10 STRETCHED-PULSE MODE LOCKING WITH NLPR TECHNIQUE

A dispersion-managed mode locked laser or a stretched pulse fiber laser cavity consists of sections with anomalous and normal dispersion causing the chirp to change from positive to negative and back, during one round trip [370]. In this configuration, dispersive and nonlinear effects can become so strong that the pulses' spectral and temporal widths undergo large variations (breathing) during each resonator round trip. The stretched pulses then can tolerate nonlinear phase shifts an order of magnitude higher than ordinary solitons without breaking into multiple pulses. As a result, both pulses with lower width and/or higher energy can be produced [338, 348] .In addition timing jitter of stretched-pulse laser can be lower than the soliton fiber laser [371].

Figure 5.10 illustrates a simple ring configuration which consists of EDF with positive dispersion, and a segment of passive fiber with negative dispersion. The waveplates are adjusted to provide the elliptic polarization necessary for NLPR [372]. Considering a pulse starting at the PC after the polarizer, it passes through the SMF fiber section and begins broadening and getting chirped with the concentration of higher frequencies in leading edge of the pulse.

In this case, the pulse energy decreases. However this highly chirped long pulses can acquire an increased energy from the gain material [81] .When it enters the doped fiber section, the opposite dispersion sign begins to chirp the pulse in the reverse direction. The pulse is then amplified and recompressed until it reaches the middle of the doped fiber. Hereinafter, over-dispersion compensation occurs and the pulse initiates broadening and chirping again. By entering the anomalous dispersion section, the dispersion sign is reversed again and the pulse gets compressed once more until it reaches the original position.

To have a complete stretched pulse laser, precise lengths of fiber sections and their dispersion values must be chosen. The stability of highly chirped solutions, the positions of the minimal pulse in the cavity, the lack of sideband radiation and the Gaussian-shaped spectra have been predicted and formulated for stretched-pulse mode locking in [373, 374].

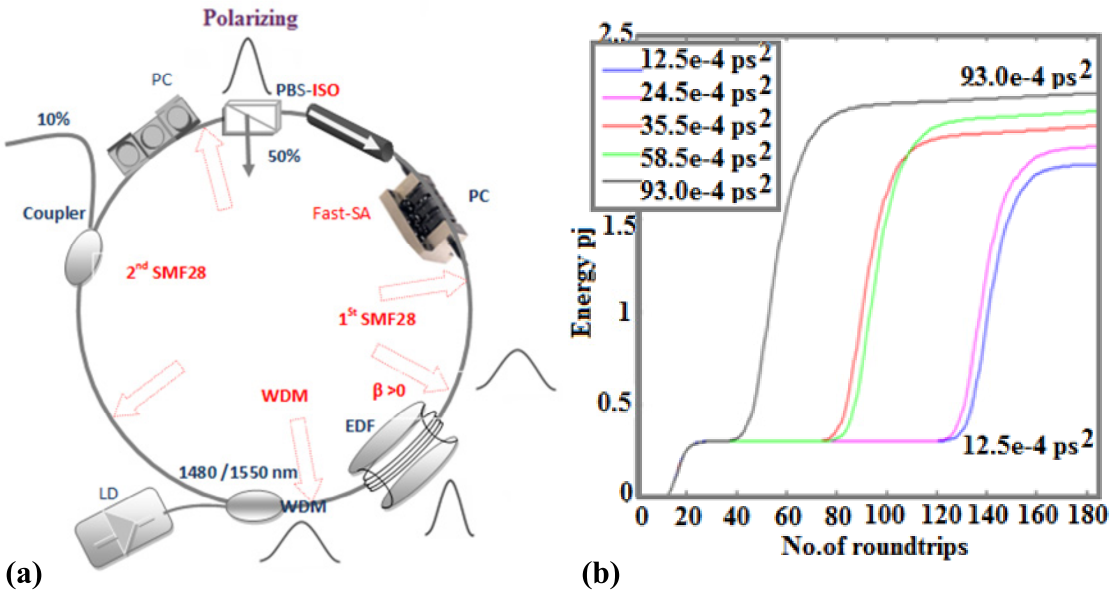

Figure 5. 10: (a) Pulse propagation in stretched pulse laser cavity, (b) Simulation.

It should be noted that the highest pulse energies in conjunction with strong chirp can be generated with a large net normal dispersion. In contrast, the cleanest and shortest pulses can be obtained from a cavity with low net normal dispersion [375].

Compared to a setting which has less stretching, nonlinear saturation can be avoided and the pulses with significantly higher energies can be achieved in a setup with a higher degree of pulse stretching. With steep edges and a broad spectral width (that may exceed 50 nm), the spectrum tends to form as a sharp top-hat shape with increasingly large chirp parameter, in the net normal dispersion regime [376]. However mode-locking in this regime is more unstable and is difficult to initiate. To certain extent, such problems may be tolerated either by using of slow and fast saturable absorbers in the cavity simultaneously or working in self-similar pulse regime [377].

It is interesting to note that the net GVD in the cavity can be a low anomalous value as well. In this case, one can produce short pulses at the cost of low pulse energy [348, 362, 378]. In contrast to soliton mode locking, the phase modulation is only partially compensated in this dispersion map. This leads to a relatively large local chirp within the cavity. Stretched pulse fiber lasers, operating near ZDW generate the shortest Gaussian pulses with suppressed temporal wings and no spectral sidebands [378]. One approach to obtain near-zero cavity net-dispersion ($\sum_i D_i L_i \approx 0$) is adjusting the length of active section of cavity or SMF section of the cavity [213].

As discussed by Tamura et al. [379], the pulse energies in a cavity with a polarizing beam splitter as the the rejection port can be further increased. This method has been exploited successfully for the generation of pJ-energy sub-picosecond pulses [380]. Meanwhile, the generation of nJ-energy pulses with a duration shorter than 100 fs would be feasible with high pumping powers as reported in [381]. Finally, it should be noted that, it is hardly practical to generate picosecond transform-limited pulses using this method, since large breathing would require very large amounts of GVD in this case.

5.11 HYBRID MODE LOCKING

Depending on required pulse characteristics and degrees of freedom to adjust parameters, a combination of the above techniques is also used to achieve mode locking. Employing the NLPR technique in conjunction with SA can enhance pulse shortening [382]. To achieve the broadest mode locked pulse spectrum and to compensate any degradation of pulse quality due to environmental effects, NLPR is utilized in hybrid mode locking to provide adjustment accessibility. In this thesis two types of passive mode locking will be used in a ring laser comprised of two segments of oppositely dispersive fiber to circumvent spectral sideband generation and saturation of the P-APM soliton lasers [370].

5.12 Q-SWITCHING INSTABILITIES AND NOISE CHARACTERISTICS

A mode-locked laser may generate multiple pulses, or pulses which are accompanied by various kinds of noises even without particular instabilities. These noises include phase noise and intensity noise. These sources induce small changes, from pulse to pulse, in timing (timing jitter), energy, phase, carrier frequency, width, and chirp in some systems [383]. Timing jitter or simply jitter is a type of phase noise that can occur in a short time scale. Jitter is defined as the short deviations of the significant instants of a timing signal from those in a perfectly periodic pulse train.

The origin of this noise can be widely different. Some noise sources are gain fluctuations, length and refractive index fluctuations, pump noise, and ASE fluctuations. However, owing to the excited states of the erbium ions having long relaxation times, the output pulses are not directly sensitive to gain fluctuations except at low frequencies. Moreover, the ring laser is not sensitive to pump noise and gain fluctuation except at low frequencies. It has been proven that instability can also be attributed to the sensitivity of the birefringence of the fiber to changes in the environment such as changes in temperature, accidentally applied pressure, unintentional bending and so on.

Another harmful effect that may occur in the systems is the fact that the SA reduces the damping of the relaxation oscillations. The relaxation oscillations become undamped when this “damping reduction” effect is strong enough. In this case the pulse energy undergoes large oscillations. Such large oscillations represent the Q-switched mode locking (QML). It is noted that, for lasers operating in very high output powers or very high pulse repetition rates the suppression of Q-switching instabilities is difficult or it may require compromises, such as accepting longer pulse durations, lower laser efficiencies, or a high thermal load on the saturable absorber [361]. Above a certain Q-switched mode locking (QML) threshold, it is possible to derive a criterion for stable mode locking without Q-switching instabilities as noted earlier [361, 384] .

In this section, laser stability in terms of the timing jitter as well as shot to shot pulse stability are quantitatively analyzed through the RF spectrum. The power spectrum of an optical pulse without any jitter consists of discrete modes with a frequency spacing of $n\omega_c$ where ω_c is the longitudinal mode spacing of the laser cavity and *“n”* is the mode number. The absence of spurious side bands around the frequency components in the RF spectrum reveals the high stability of the laser pulses. However, output pulses in any practical mode-locked laser exhibit some random behaviour. Due to jitter, sidebands are created around discrete modes of power spectrum.

Each harmonic consists of sum of a constant amplitude noise spectrum due to the pulse energy fluctuations and a component from pulse duration fluctuations and timing jitter. All of these noises can be characterized distinctly, even if they occur at the same time. If the pulses are totally uncorrelated or the uncorrelated noise of the laser is well-below the noise floor of the RFSA, side bands caused by energy fluctuations are independent of “*n*”. While, the jitter caused by phase variation causes the power in the side bands to increase with n^2. In fundamentally mode-locked lasers, the position and amplitude of neighbouring pulses are highly correlated since the same pulse recirculates through the laser cavity, giving up a fraction of its photons each time. Namiki et al. [385] reviewed the Haus–Mecozzi theory of amplitude fluctuations and timing jitter in a mode-locked laser with negative GVD [386].

To obtain the phase and energy jitter, the simplified relations from the Von der Linde method is used [18]. Based on the definitions for the "*n-th*" order frequency component, P_A, P_B and P_D represent the absolute maximum powers of the signal spike, structure with frequency width (FWHM) of Δf_j and the broad noise band structure with a FWHM of Δf_A (see inset Figure 5.17).

On the other hand, a detailed analysis in low-resolution spectra shows that the lowest noise bands represented by the ratios P_D/P_A are actually the sum of two different contributions: (i) middle narrow noise bands due to a fast temporal jitter with the power of P_C and a frequency width of $\Delta f'_j$ and (ii) constant broad noise bands (noise floor) due to amplitude fluctuations with a power level of P_D and a frequency width of Δf_A. All experimental power values represent integrals of the power densities over the spectral resolution Δf_{res} of RFSA (Resolution Bandwidth- RBW). The energy fluctuations and low frequency jitter noise (timing jitter Δt) are evaluated from the first frequency component and high harmonic components of the RF spectrum, according to following equations:

$$\Delta E/E = [(P_D/P_A)_f \, \Delta f_A/\Delta f_{res}]^{½} \tag{5.22}$$

$$\Delta t/T = (2\pi n)^{-1}[\,(P_B/P_A)_n \Delta f_j/\Delta f_{res}]^{½} \tag{5.23}$$

$$\Delta t'/T = (2\pi n)^{-1}[(P_c/P_A)_n \, \Delta f'_j \,/\Delta f_{res}]^{½} \tag{5.24}$$

where subscript f represents fundamental frequency, n is the harmonic order of the frequency component and T is the cavity round trip time. It is straightforward to show that the fluctuations of the pulse width are transformed into fluctuations of the energy of the second-harmonic pulses. However in our case, the contribution from pulse width fluctuations can be neglected due to the soliton nature of the pulses generated.

5.13 EXPERIMENTAL SETUP

To generate one or more pulses per round-trip, a combination of ring and linear Fabry–Perot can be used. Lasers in an unidirectional ring configuration with a slow absorber and lower threshold show self-starting easily whereas significantly more power (a factor of 10 to 100) is required for self-starting in a linear cavity [16,17]. Moreover, spatial hole burning which occurs in a linear cavity is a strong inhibitor of self-starting [9].

Figure.5.11 shows the experimental setup where a slow saturable absorber and additive mode locking with nonlinear polarization techniques are applied together to make passively mode locked EDFL. It should be noted that due to the usage of a slow absorber in our setup, self-starting mode locking is more easily achieved in the experiment.

Experimental results show that, self-starting is difficult to achieve in three kinds of setups: (i) those with shorter pulses (ii) those that have longer cavities and (iii) the setups which use fast or artificial saturable absorbers. Hence the cavity consists of a short piece of EDF, a WDM, a polarization controller with three fiber loops (fiber-

PC), a polarizing beam splitter (PBS), a saturable absorber, an isolator, a set of phase-retarder components (wave-plates) and an output coupler.

The SA specifications and typical fiber parameters are shown in Table 5.1. The laser oscillator consists of three different fibers namely a piece of 4 m long erbium doped fiber or a piece of 49 cm long Bi-EDF as a gain media and a 0.42 m long WDM fiber. The other sections of the ring cavity utilize a piece of corning single mode fiber (SMF28) used in coupler and PC. The SMF fiber section between the gain media and the SA is fixed to approximately 1.9 m in all configurations. All these fibers have different absorption coefficients and different nonlinear coefficients. Moreover, different EDFs also have different gain specifications.

For example, a highly doped EDF (DF1500L) from Fibercore Ltd. has a maximum peak absorption of around 11.8 dB/m. In another media, Bi-EDF from Asahi has a maximum peak absorption of 73 dB/m at 978 nm. The SA specifications and typical fiber parameters are listed in Table 5.1.

Considering the results presented in chapter 3, if the length of Bi-EDF is at least 1 m and pump power is below 150 mW, then it acts as an absorbing media instead of a gain media. The gain spectra for Bi-EDF show that the signal bandwidth (FWHM) strongly depends on the pump configuration rather than the total pump power. For high backward pump power, the gain and its bandwidth seem to be higher and wider than the forward pump power at an equivalent pump power. In addition note that EDFAs have two commonly-used pumping bands. The 980 nm band has a higher absorption cross-section and is generally used where low-noise performance is required. This absorption band is relatively narrow and thus wavelength stabilised laser sources are typically needed.

On the other hand, the 1480 nm band has a lower, yet broader, absorption cross-section. Hence in the case of Bi-EDF a piece of 49cm long fiber is backward pumped by a 1480 nm laser diode up to 150 mW through 1480/1550 nm WDM. The maximum launched power of 180 mW into the active media should be sufficient for generating mode locked pulses.

Table 5. 1: Specification of fibers and SA for the experimental setups.

Parameters	Value
Bi-EDF	49 cm
Erbium ions concentration	3250 wt. ppm
MFD@1550 nm/ cladding diameter	6.2/125 µm
La ion Co-dopants concentration	4.4 %
Peak absorption around 980 nm	73 dB/m
Peak absorption at 1480 /1560 nm	83/44.1 dB/m
Peak Absorption around 1530nm	133 dB/m
Absorption cross-section at 1532 nm	7.73×10^{-25} m^2
Emission cross-section at 1532 nm(Peak)	7.58×10^{-25} m^2
Fluorescence Lifetime $^4I_{13/2}$	2.84 ms
Background loss, signal $\alpha(\nu s)$	40 dB/km
Dispersion Bi-EDF at λ=1545 nm	+140±0.21 Ps^2/km
SA	Antiresonant
modulation depth of SA	15 %
relaxation time of SA	2 ps
non-saturable loss of SA	10 %
saturation fluence of SA	300 µj/cm^2
Absorbance of SA	25 %
Dispersion - Antiresonant SA	No influence
EDFA (DF1500L)	3 m
Mode field diameter(MFD)	5.9µm
Erbium absorption (975 nm)	12 dB/m
Erbium absorption cross section (σ_{ab})	(975nm)
Dispersion GVD	23.51 ±0.21 Ps^2/km
Background loss, signal	40 dB/km
Dispersion – Corning SMF28 (1545nm)	-22.75±0.91 Ps^2/km
Dispersion WDM(1548nm)	-9.94±0.18 Ps^2/km

The WDM is followed by the semiconductor saturable absorber (SA-1550-35 Batop, Germany) which is responsible for the initiation and stabilization of mode-locking for use at around 1550 nm.

The SA used is a transmission type of SA without a mirror and is therefore antiresonant without a significant dispersion influence. Our proposed SA has an absorbance (A_0) of 25%, a modulation depth of ΔR=15% , a saturation fluence ($\Phi_{sat.}$) of 300 μj/cm^2, a non-saturable loss (A_{ns}) of 10% and a relaxation time constant of 2 ps.

The SA chip for transmission applications is fiber butt-coupled inside a ceramic ferrule which is connected to monomode fiber patch cable.

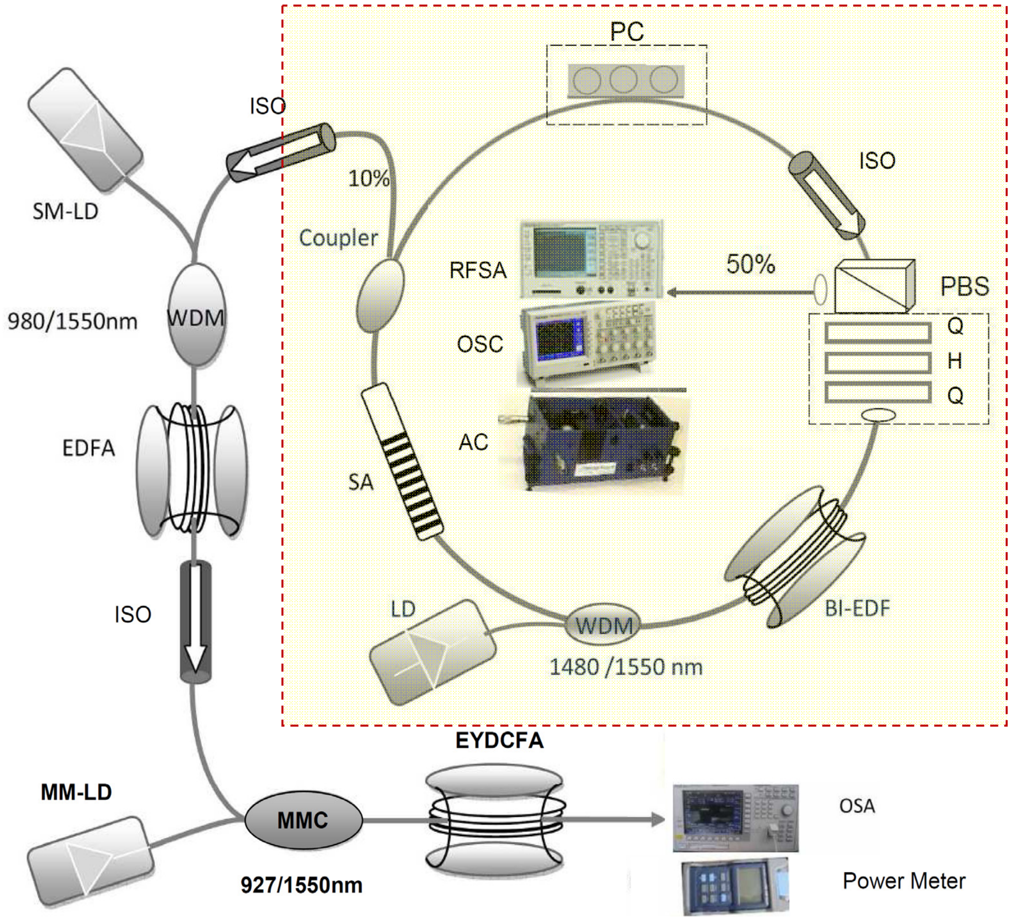

Figure 5. 11: Experimental setup of the Bi-EDFL. ”WDM: Wavelength Division Multiplexer; SA: Saturable Absorber; OSC: Oscilloscope; RFSA: RF Spectrum Analyzer; OSA: Optical Spectrum Analyzer; AC: Auto-correlator; PC: Polarization Controller; PBS-Isolator: Beam Polarizing Beam Splitter integrated with Isolator; H: (Zero order)1/2- wave retarder; Q: (Zero order) 1/4- wave retarder ;ISO:Isolator”.

Two output ports are utilized to measure and compare the autocorrelation traces, the microwave spectra, phase noises and the optical spectra. These investigations are necessary for choosing the optimal resonator output positions for the different applications. For generating bandwidth-limited pulses, the rejection port needs to be arranged at an appropriate location in the cavity [334]. However, it is not always convenient to place the rejection port at the optimal position. Alternatively, dechirping can be accomplished by utilizing an external dispersive delay-line or a external dispersive pulse compression [370].

A fiber-PC in conjunction with a set of retarder components including $\lambda/2$ and $\lambda/4$ wave plates (RC-PC) are used in the set-up to control the polarization state of light that travels inside the cavity. This approach allows continuous adjustment of the birefringence within the cavity to balance the gain and loss for generation of laser pulse. The stable pulse evolution in the cavity can be finely adjusted via fiber-PC and RC-PC. By removing either of Fiber-PC or RC-PC the desired mode-locked operation can not be initiated easily.

Spectral filtering via variation of the polarization state along the spectrum can be achieved by using a Polarizing beam splitter (PBS). This PBS is also utilized as a rejection port to provide a of 50% output power from cavity. To realize and enforce the unidirectional operation and polarization selectivity in the cavity, this PBS is integrated with an isolator (PBS-ISO). Based on the nonlinear polarization evolution (NPE) in the SMF section and the spectral broadening in the (Bi-)EDF, the fiber section length (2 m) between the SA and the PBS is critical in the pulse shaping mechanism [20].

The pulse characteristics for a large range of wavelength (1510 to 1590 nm) were compared at two output ports, a 90/10 splitter and the rejection port of a PBS placed at specific positions. As shown in Figure 5.11, a 40 MHz analogue oscilloscope combined with an autocorrelator (Femtochrome FR103XL), and a 400-MHz digital oscilloscope (Tektronix) together with a photodetector are used to simultaneously monitor the autocorrelation traces, the pulse width and pulse train.

A fast-response Si-photodiode with a bandwidth of 6 GHz and rise-time fall-time of 25 ps is used for monitoring the pulse train and also noise measurements. For a quantitative measurement of the noise, the signal from photodiode is analyzed using RFSA (Radio Frequency Spectrum Analyzer-ANRITSU MS2683A) with the resolution bandwidth of 300 Hz to 3 MHz and frequency ranges of 9 kHz to 7.8 GHz. The optical spectrum with a resolution of 0.07 nm is measured with an optical spectrum analyzer (ANRITSU-MS9710B). The output pulse average power is also measured by using a power meter.

5.14 EXPERIMENTAL RESULTS FOR MODE-LOCKED EDF LASER

The objective of this section is to measure the pulse characteristics and to observe the operating regimes in the aforementioned configuration when using a long silica-based EDF (DF1500L). Pulse dynamics are also investigated at two output ports of the ring cavity. At first, the net cavity GVD in the setup was set approximately to -0.04 ps^2 when the length of DF1500L was 4 m. In fact, the net dispersion in the cavity for a given repetition rate or a fixed total length, increases linearly by the length of DF1500L, as shown in Figure 5.12.

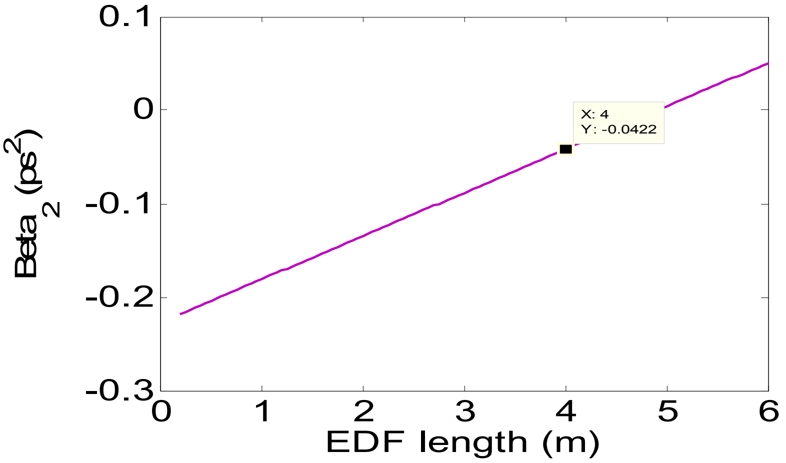

Figure 5. 12: Net cavity dispersion for various lengths of EDF in the cavity. The total length of cavity is fixed at 10.4 m.

Figure 5.13 compares the laser spectra, from the PBS output port and coupler port. The pump power is fixed at 100 mW in the figure. The polarization state along the spectrum is altered by polarization controllers.

The spectrum changes from a narrow to a relatively broad one and the variation of the polarization state leads to a strong spectral filtering by the PBS. These changes indicate transition from a CW to an initially Q-switching operation of the laser. The commencement of Q-switching is observed by an oscilloscope when it shows an unstable pulse train with periodic variation in pulse amplitude.

Further adjustment results in broader spectrum and stable mode locked pulse train. As the output characteristics are extremely sensitive to the settings of the PCs, we might deduce that the NLPR together with the PBS-ISO have crucial roles in the spectral and temporal filtering. In other words, the pulse shaping in is caused by the NPE in the setup.

As shown in Figure 5.13, FWHM optical bandwidth is observed to be approximately 5.64 nm with a resolution of 0.07 nm, implying 0.45 ps, Sech^2-shaped transform-limited pulse duration. The spectrum shows indication of Kelly sidebands [387] around the centre of the spectrum as they often arise in soliton lasers.

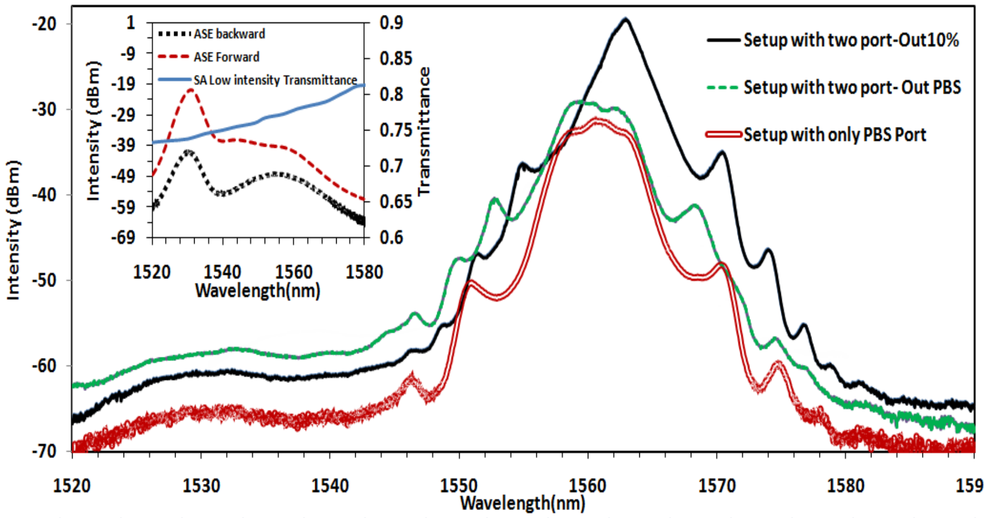

Figure 5. 13: Spectra measured at different output ports for a ring cavity with 4 m long EDF (DF1500L). Pump power is fixed at 100mW. Inset shows ASE spectra in forward and backward schemes and also transmittance spectrum (%) of SA.

The sidebands appeared as a pedestal under the pulse contain energy comparable to the pulse energy. It should be noted that the amount of continuum [334] that is generated and observed at a certain frequency is proportional to the spectral amplitude of the soliton at this frequency.

As the pulse width becomes shorter, sidebands would move closer to the center. Strong Kelly sidebands indicate that the pulse duration is near the minimum value possible. These sidebands can be useful in determining the net cavity GVD [388].

The pulse width was measured by considering conversion constants imposed by autocorrelator instrument. AC traces of the soliton pulses corresponding to the soliton spectra were also recorded to investigate the effect of the instability on the soliton pulses. A log-scale AC trace shows that Kelly sidebands in optical spectrum correspond to a spreading pulse background or a very strong pedestal in the temporal profile. However, the existence of the pedestal does not affect the average duration.

Figure 5.14 depicts the measured intensity autocorrelation of this setup. Digital data are also fitted by Matlab with a sech^2 profile. The inset of Figure 5.14, shows the pulse train from the output coupler. The oscilloscope trace and a RF spectrum verify that there is no multiple pulsing in the laser.

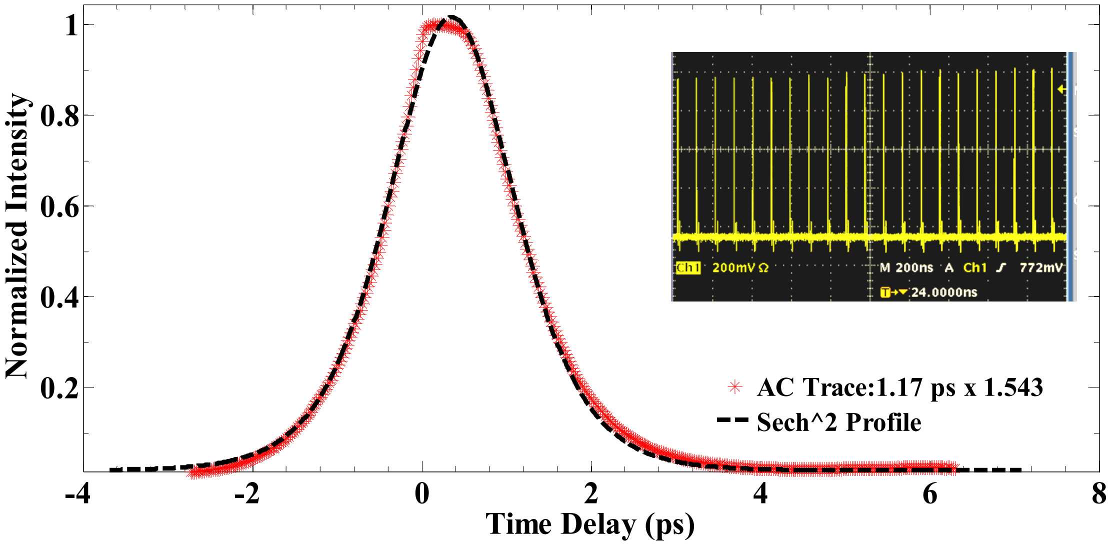

Figure 5. 14: Autocorrelation trace of 1.17 ps pulses. Dashed curve is sech^2 fit and inset shows pulse train with a repetition rate of 9.87 MHz.

It is possible to eliminate the associated energy background in the spectral sidebands by using a filter in the cavity [389]. As shown in the inset of figure 5.13, the peak of the ASE spectrum at 1530 nm is shifted to the peak of output spectra at 1560 nm due to the fact that the insertion loss and transmittance in EDF and SA naturally depend on the wavelength. It can be seen, that from coupler towards the PBS the spectral width increases.

The mode-locking in this setup shows a SA dominated self-starting at a repetition rate of 9.87 MHz. An output power of 4.9 mW from the seup with a slope efficiency of about 5%, translate to pulse energies of 0.5 nJ, pulse durations of 1.2 ps and pulse peak powers of 0.42 kW. The time-bandwidth product was measured to be 0.81 for this setting.

It is well known that a stable CW mode-locking with SA requires that the intracavity pulse energy per power to exceed a threshold energy per power. The pump power threshold was measured to be 11 mW for the laser oscillation while the measured threshold for mode-locking operation was 20 mW.

By removing the 10% coupler, a more practical resonator is obtained with a lower pedestals to pulse energy ratio, lower resonator loss and lower threshold for CW mode locking. The output spectrum of this configuration is also presented in Figure 5.13. The laser has similar characteristic compared to the laser configured with two output coupler. The difference is due to the shorter ring length resulting in a higher repetition rate (13.75 MHz) with weaker nonlinear polarization rotation.

The various lengths of SMF-28 in the cavity lead to changes in the sign and the value of net cavity GVD. Consequently, various types of pulses were observed at the PBS port such as stretched or parabolic pulses, fundamental soliton as well as the coexistence of a soliton with a tangible amount of continuum. By decreasing GVD to -0.30 ps^2, a noisy AC trace with strong coherence spikes was observed. This is a signature of leaving the regime of fundamental soliton generation. It is possible to cut an adjusted length of SMF from setup to obtain a near zero GVD of the cavity.

In order to obtain shorter and more stable pulses, the laser configuration is again upgraded. As illustrated in Figures 5.15(a) and 5.15(b) the effect of the sidebands can be avoided by decreasing the average dispersion of the cavity, allowing the FWHM of the spectrum to be increased to up to 9.8 nm. In this dispersion map a higher pump power threshold of 40 mW is required for mode locking operation.

From Equation 5.19 it is clear that the pulse duration decreases by increasing pump power and spectral width. This is the consequence of the higher gain and the higher nonlinearities present, which shortens the pulse. From the figure, after putting an extra pump power, the output power is increased, but no further improvement of pulse duration and FWHM of the spectrum are observed. However, optimizing the output coupling ratio and removing all FC/PC connectors in the setup allow us to decrease the pulse width and to enlarge the spectral width further. Since the Kelly sidebands are not too strong, we can ignore them and calculate the minimum pulse duration as the transform limit for the soliton spectrum (without the side bands).

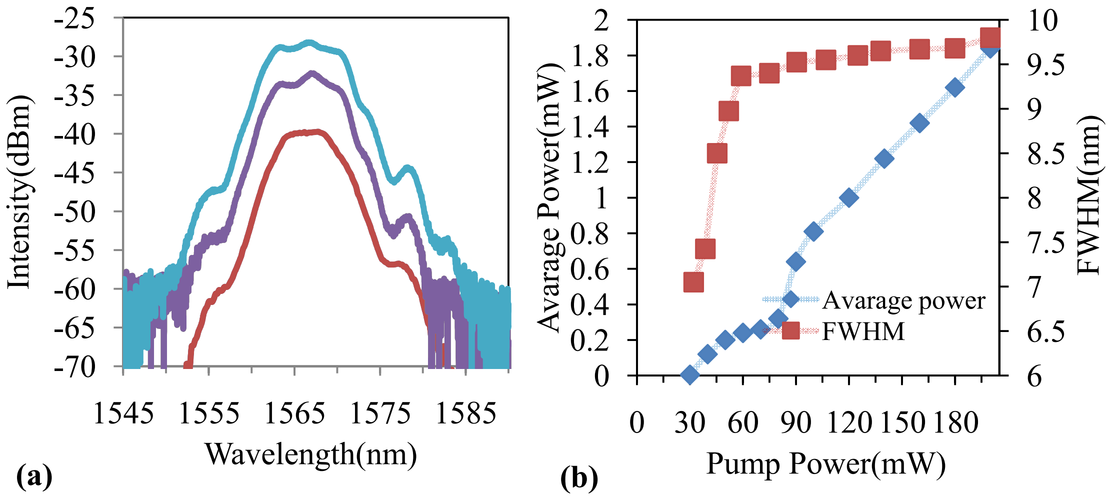

Figure 5. 15: (a) Spectra measured at PBS port, (b) The variation of the spectral width, and output power at the PBS port with the pump power.

The measured FWHM of the optical spectrum (9.8 nm) is in good agreement with the Fourier prediction of 260 fs for the pulse duration.

Figure 5.16 shows the RF spectrum in net negative GVD when we consider the first harmonic (fundamental pulse repetition rate) up to the highest order at 7 GHz.

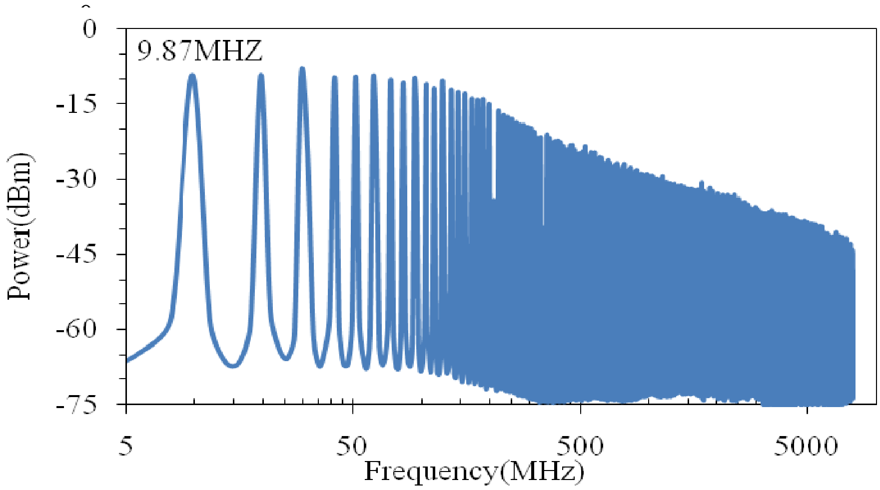

Figure 5. 16: RF spectrum of typical pulse train without multiple pulsing for net negative GVD. The frequency axis is logarithmic.

Figure 5.17 shows typical RF spectra of a 9.87 MHz sub-picosecond pulse train, up to the 33-th harmonic. A spectral resolution less than 3 kHz of the spectrum analyzer enabled us to detect all noise components accurately which is necessary to evaluate energy fluctuations and timing jitter at different output ports (see inset figure). The results are summarized below. Ratios of P_D/P_A, P_C/P_A and P_B/P_A at the 10% coupler port, were found to be 6.2×10^{-6}, 1.7×10^{-4} and 7.6×10^{-3} respectively. However, for PBS port, the minimum values for P_D/P_A and P_C/P_A were measured to be 2.4×10^{-5} and 3.4×10^{-4} respectively. Meanwhile, P_B/P_A remained constant. As a result, the pulse energy fluctuation at the coupler port is lower than the PBS port. Our experiments show similar results for Bi-EDF. It should be noted that, there was an increase in timing jitter to up to 14 ps when we were operating with a CW background.

For small timing-jitters, all the harmonics can be described by a Gaussian profile, whose widths increase proportional to the harmonic number. As the harmonic number increases, the deviation of the Gaussian tail increases as well. Note that the peak values of the different harmonics decay with a rate of 1/ω. The influence of longer time scale fluctuations on lower frequencies of the power spectrum modifies the shapes toward Lorentzians and makes their FWHM's smaller. This effect leads to higher-order dependence of the FWHM spectra on the harmonic number.

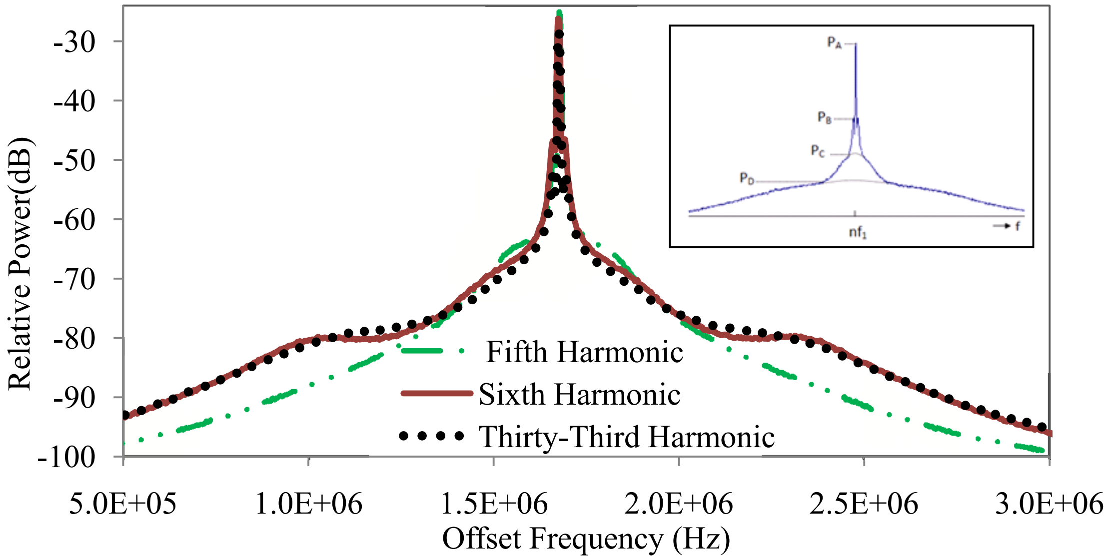

Figure 5. 17: Normalized spectra of different harmonics from PBS Port as a function of the scaled offset frequency in a sub-picoseconds pulse train. The RBW in RFSA is fixed at 3 kHz. Inset shows the noise structure and marks P_A, P_B, P_C and P_D.

A comparison of the energy fluctuations at the PBS port and the coupler port reveals that energy fluctuation from the coupler port to the PBS port is varied from 4.1% to 7.8%. For a fixed pump power of 92 mW, the low and high frequency jitter at the coupler port were measured to be 11.5 ps and 13.8 ps, correspondingly. Although, at the PBS port, these values can reach up to 17.5 ps and 40 ps, respectively. Note that, the true noise of the laser may be lower, since amplitude-to-phase conversion in the photo detection process is already limited the current measurements.

A low cavity loss would result in low phase noise and timing jitters because of the reduction of spontaneous emission. Hence the lowest timing jitter and the lowest pulse amplitude noise were achieved by optimizing the cavity loss and simply by removing the used connectors (four) from the setup. In the absence of a feedback loop for controlling the pump power and a temperature-sealed box for laser cavity, the jitters are larger than the corresponding pulse durations. This is due to limitations imposed by soliton lasers where large nonlinearities result in relatively high timing jitter [22]. It was discovered that when timing-jitter fluctuations between successive neighboring pulses are uncorrelated in time, different harmonics obtained a Lorentzian shaped spectra. The FWHM for each harmonic in the spectrum is proportional to the square of the harmonic number. Effects of correlations between the the timing fluctuations of neighboring pulses in the train, tend to produce spectra at different harmonics, which are both Gaussian in shape and have FWHM's that increase linearly with harmonic number.

5.15 EXPERIMENTAL RESULTS FOR MODE-LOCKED Bi-EDF LASER

For comparison purposes, the experiments are repeated for a similar setup using a 49 cm long Bi-EDF as a gain media. In the absence of SA, RC-PC and PBS in the setup, the total length of the cavity is 2.5 m.

A fraction of the 41.9 MHz pulse train which translates to a constant spacing of 24.2 ps operating at 1560 nm, can be extracted through the output coupler. However, using this configuration, the laser does not show self-starting mode-locking.

The high repetition rate pulse trains are produced and the multiple pulses circulate within the cavity because of the phenomenon of soliton energy quantization. It is observed that without a polarizer in cavity, soliton circulation in the cavity exhibit complicate polarization dynamics.

As shown in Figure 5.18, not only period-doubling of single vector soliton but also multiple vector solitons can be detected. By increasing the pump power, the number of vector solitons [390] circulating in the cavity is increased.

Employing the setup of Figure 5.11, the mode-locking at a repetition rate of 8.27 MHz again shows a self-starting which is SA dominated. However, when compared to the silica-based EDFA, Bi-EDF exhibits 30 % larger emission bandwidth which inevitably leads to a higher threshold pump power. The laser threshold was measured to be 26 mW for CW regime. Meanwhile, for mode-locking operation, the thresholds for setups with and without 10% coupler are respectively obtained at 70 mW and 55 mW.

Using one PC for both setups (with and without coupler), our measurements show an output spectrum with a FWHM less than 7.2 nm. Such pulses implies 341 fs (Sech^2 shaped) and 476 fs (Gaussian shaped) transform-limited durations.

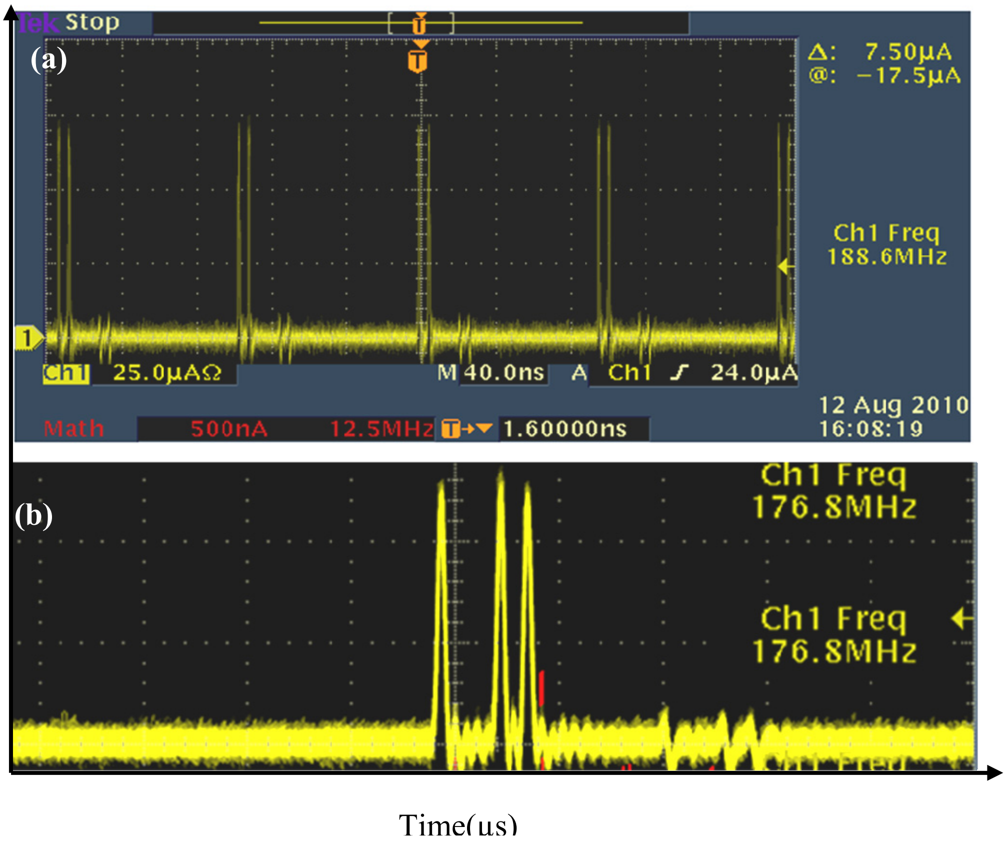

Figure 5. 18: Period-doubling of multiple vector solitons: (a) Two vector solitons, (b) three vector solitons.

Figure 5.19 shows the variation of the spectral width, TBWP and pulse duration as a function of the pump power. This figure implies that, as the pump power increases, the pulse duration and TBWP decrease to 580 fs and 0.51, respectively.

We observed that a SA with high modulation depth is desirable to achieve mode locking without dispersion compensation. It is important to note that with higher pulse energies, the spectral broadening caused by SPM can partially overcome the spectral limitations of the gain material [64].

This made pulses shorter, even though the absorber was already oversaturated. Consequently, the pulse duration decreased by increasing pulse energy and pump power.

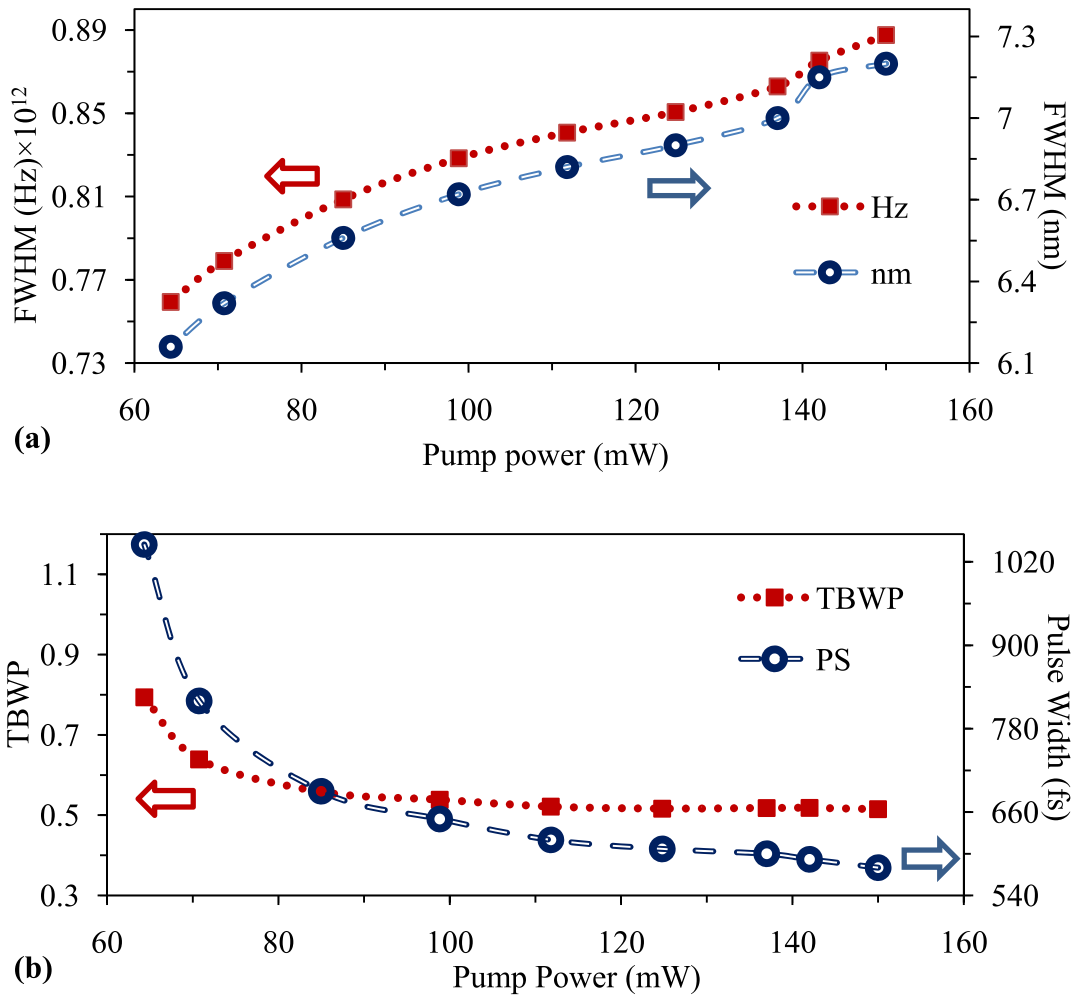

Figure 5. 19: Typical spectrum for an oscillator with a single polarization controller. Dependence of (a) output spectral width on the input power, (b) TBWP and pulse duration on the input power.

With pulse energy of 0.2 nJ and a peak power of 0.363 kW, the configuration with one PC exhibits a low average power, as shown in Figure 5.20(a).

To obtain shorter and more stable pulses, the laser configuration is upgraded by using RC-PC instead of PC. The spectrum shows Kelly sidebands as they arise in soliton lasers with a wider spectral width, (see Figure 20(b)). Under some circumstances, the spectral width can be further enlarged. Higher pulse energy can also be obtained by increasing the output coupling ratio, applying two polarization controllers before and after PBS and increasing the pump power.

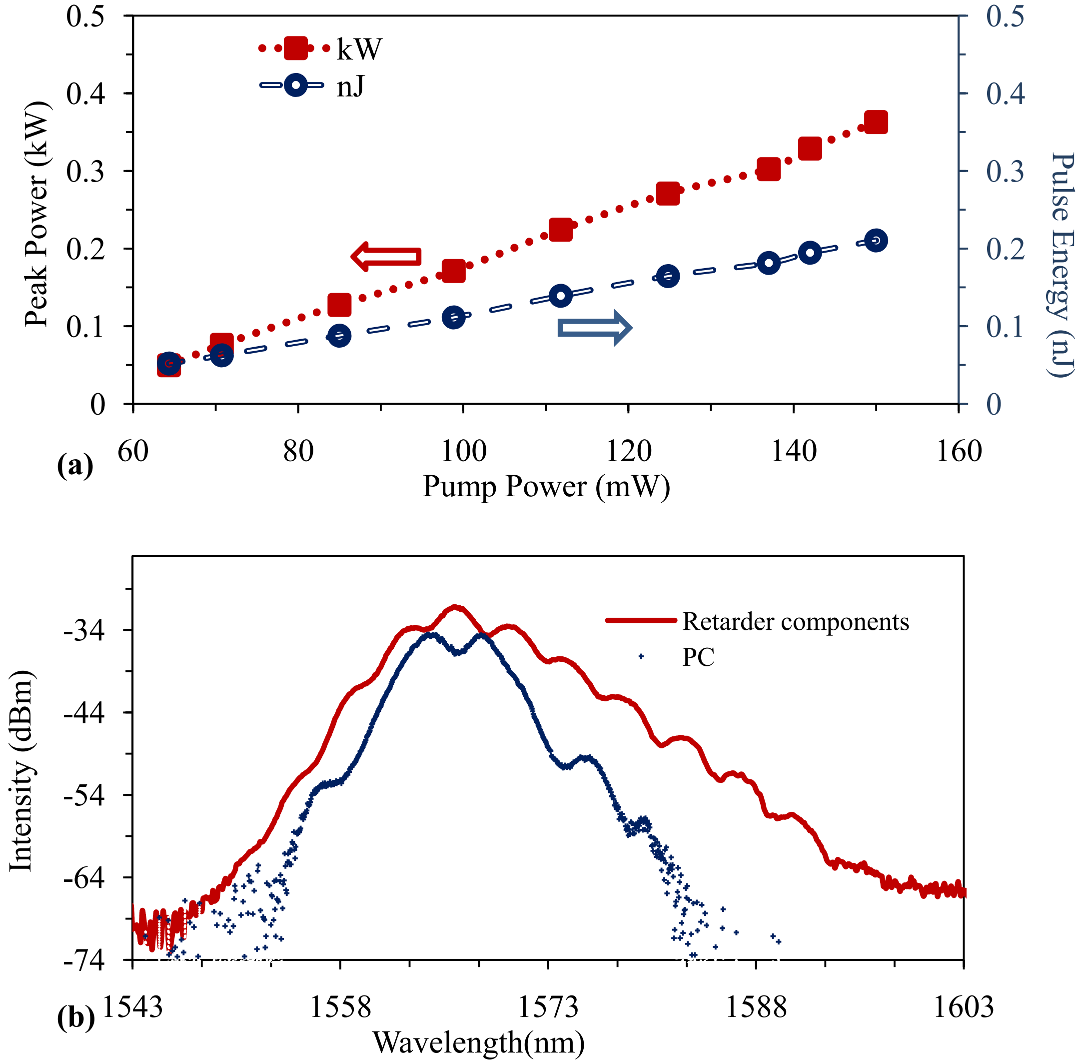

Figure 5. 20: Typical spectrum for an oscillator with a single polarization controller: (a) Peak power and pulse energy versus the input power (b) Comparison of output spectrum using PC and a set of retarder components.

For two polarization controller in the setup, the output spectra at different output ports are compared in Figure 5.21(a).

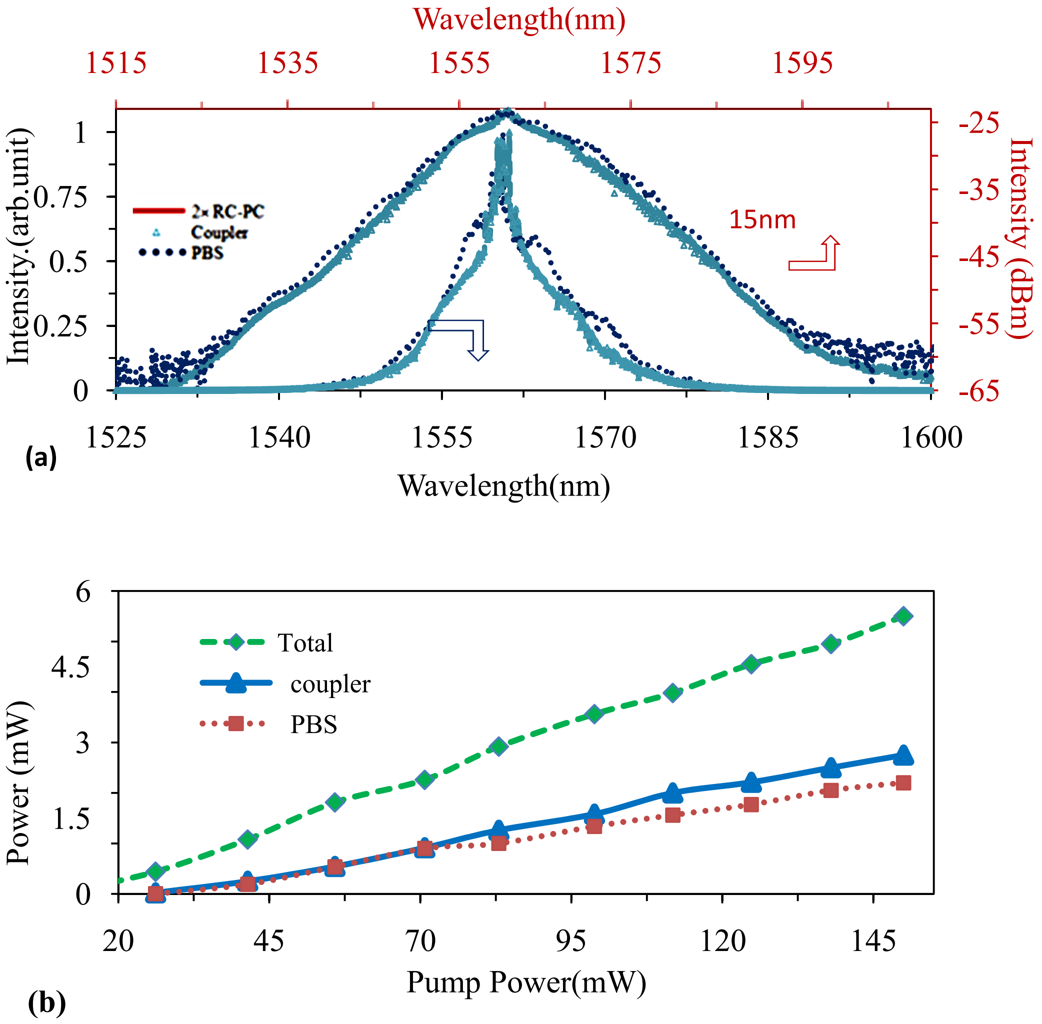

Figure 5. 21: (a) Optical spectrum of oscillator with two polarization controllers for 125 mW pump power, (b) The average power versus pump power for the various rejection ports.

Figure 5.21(b) shows the output power as a function of the pump power at the various output ports. Large emission bandwidth of Bi-EDF leads to a short radiative lifetime τ and a low attainable slope efficiency of 4.2% for total output powers.

It can be seen that for a given pump power, the spectral width increases (10%) and the pulses get narrower at PBS rejection port compared to output coupler. However, the spectrum at the output coupler depicts more symmetric shape.

The AC trace, pulse train (the inset) and sech^2 profile (dashed curve) at the PBS port are shown in Figure 5.22(a).

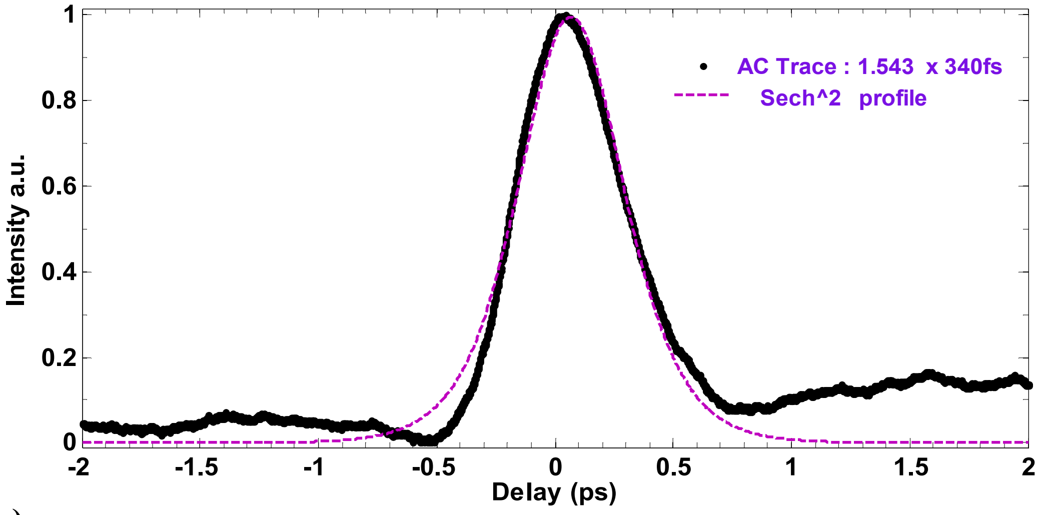

(a)

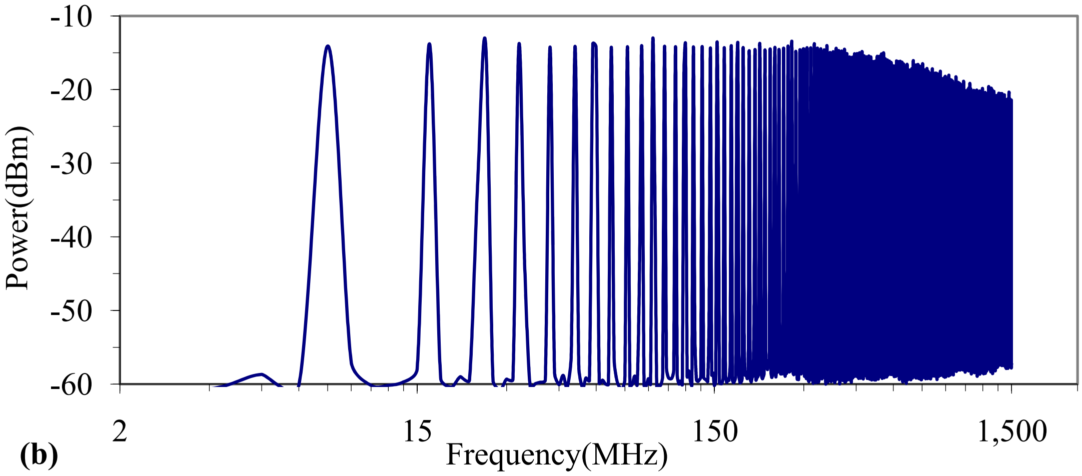

(b)

Figure 5. 22: (a) Autocorrelation trace and pulse train (inset) of the 340 fs pulses. Dashed curve: sech^2 fit, (b) The RF spectrum over a span of 1.5 GHz with a logarithmic axis.

Figure 5.22(b) shows the RF spectrum of Bi-EDF based mode locked laser over a span of 1.5 GHz. The first harmonic up to the 165-th harmonic is shown in this figure. It should be noted that the RF spectrum within a span of 100 kHz shows a narrow RF linewidth indicating that the width of the side bands are caused by the time scale on which the jitter takes place. We found that the noise arising via ASE and background radiation can be amplified. This in turn degrades the modulation depth of a SA.

Using two sets of retarders in both setups, a broader spectrum with a FWHM of 15 nm are achieved. Figure 5.23 shows a pulse spectrum in linear and dB scales which has a stretched pulse characteristic with a 3 dB-bandwidth of 17 nm at 125 mW of pump power.

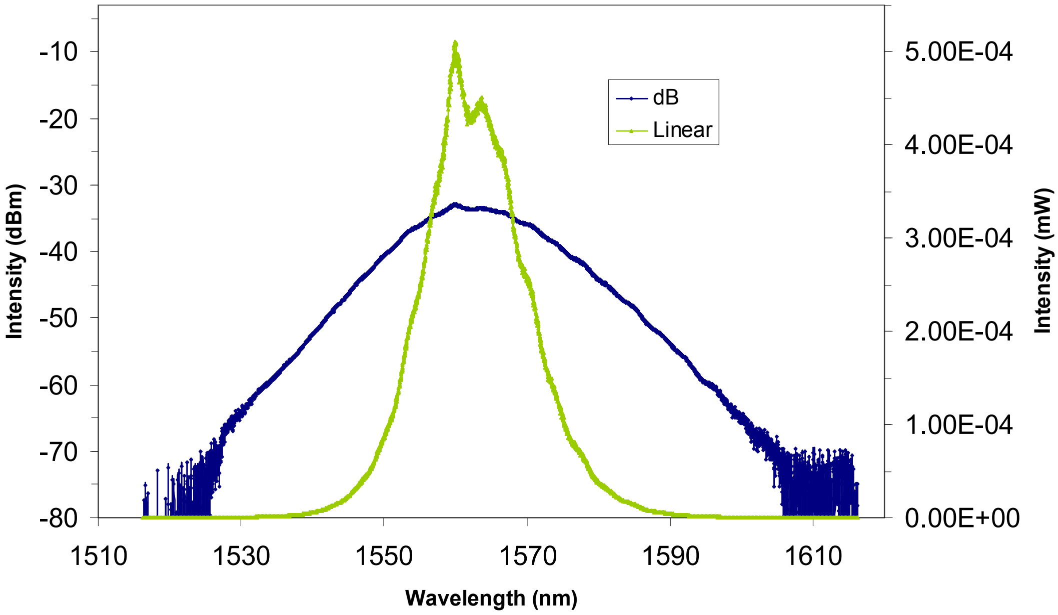

Figure 5. 23: Optical spectrum of mode locked laser in linear and dB scales. The pump power is fixed at 125 mW. Inset shows pulse train with a repetition rate of 8.27 MHz.

As shown in this figure the Kelly sidebands in the optical spectrum are not too strong, enabling us to ignore them and calculate the minimum pulse duration of 170 fs as the transform limit for the shown soliton spectrum.

For further temporal compression, we would need to have a higher pump power or to broaden the spectrum externally or internally by employing certain nonlinearities [334]. Reducing the pulse width to as short as ten femtoseconds by Bi-directional pumping could be subjects of future work.

By decreasing the lengths of single mode fibers having negative GVDs, the spectrum would be further narrowed and the nonlinear effects would become almost absent. Results show that with a high positive net GVD (ps^2), the system reaches mode locking fast.However the pulse width becomes broader because the SPM does not generate new frequencies in the leading and trailing edge of the spectrum.

It is possible to increase the nonlinear coefficient of the fiber (γ) so that a broader spectrum could be obtained. It is worth noting that, the Bi-EDF has a nonlinear coefficient (γ) of $\sim$60 $(W/km)^{-1}$ at 1550 nm and the nonlinear coefficient of SMF is much smaller than the γ for Bi-EDF in the setups.

Alternatively, by cutting off a piece of SMF and placing it in an appropriate position, it is feasible to change the peak intensities and nonlinearities within the cavity without changing the net dispersion of the cavity. A smaller dispersion to SPM ratio enabled us to achieve the pulses as short as 131 fs.

A comparison of the energy fluctuations at the PBS port and the coupler port reveals that energy fluctuations for PBS port are stronger. As shown in Figure 5.24(a), for a given configuration, energy fluctuations decrease by increasing pump power to a minimum lower bound which is limited by the available pump power.

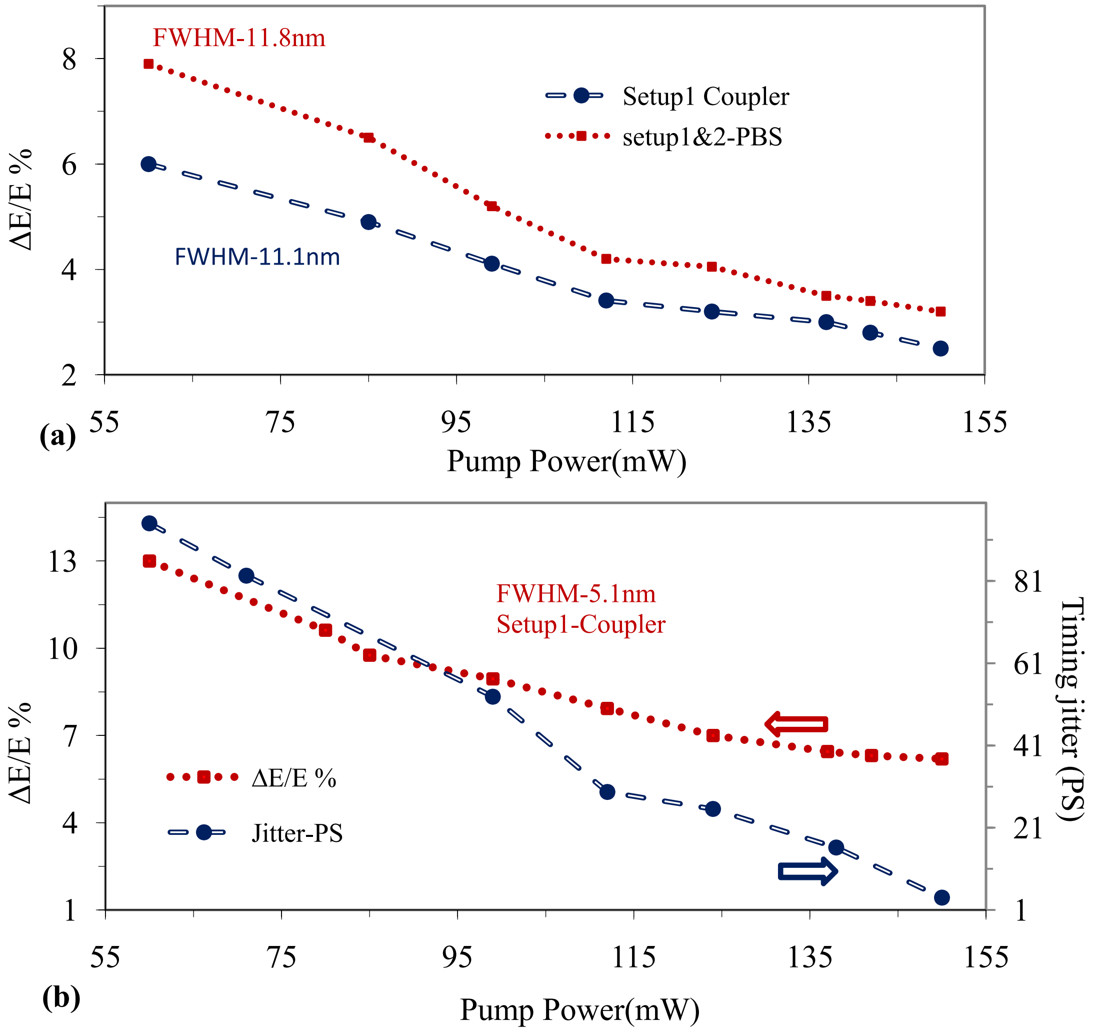

Figure 5. 24: (a) Energy fluctuations as a function of pump power for both rejection ports (b) The dependency of low frequency jitter noise and energy fluctuations on pump power and spectral width.

Figure 5.24(b) illustrates that, for a specific position for rejection port, energy fluctuations are related to FWHM of optical spectrum. As a result, a setup with narrower spectral bandwidth yields larger energy fluctuations.

Another important contributor to noise in the system is the low frequency jitter noise. Similar to contribution discussed previously, the low frequency jitter noise is inversely proportional to the pump power and spectral bandwidth. The low frequency jitter at a pump power of 150 mW and a 3 dB bandwidth of 5 nm was measured to be about 4 ps at the coupler port. Under the same condition, a larger amount of 6 ps was obtained at PBS port. By removing fiber adapters used in setup, the timing jitter was reduced by an order of magnitude. It seems that besides adjusting the net GVD in the ring, further experimental work is necessary to be done towards further reduction of fluctuations in the setup. For example, the timing jitter can also be reduced by using a filter in the ring cavity [23].

5.16 POWER SCALING

To increase the pulse energy, the oscillator has been used as a seed for a single mode Er doped pre–amplifier. The first stage is required to be well inverted such that a moderate amount of gain is obtained with minimal noise added. Then the pulse is amplified by DC-EYDFA. The NA of the second stage was chosen to be smaller than that of the first stage. In addition, the fiber end facets of the amplification stages are angle-polished to avoid any back-reflections in the core, which are known to reduce the performance of pulsed amplifiers by increasing ASE.

The details of amplifiers used in setup have been reported in the chapter 3 and chapter 4 [21]. A fundamental limit of operating a high peak power fiber laser arises from nonlinear effects in silica such as SPM, SRS, and SBS. A drop in the output power is a sign of stimulated Brillouin scattering. This process generates a backward propagating Stokes wave that can damage the laser diodes. Hence, the backward power continually was monitored during experiments.

It should be noted that the peaks of the ASE of the amplifiers were tuned to the laser operating wavelength to extract a reasonable amount of energy for pulses in train.

Figure 5.25(a) shows a) output spectrum without employing a double clad fiber (EDFA-EDFA) and b) the output spectrum when EYDCFA is used as the last stage amplifier (EDFA-EYDCFA).

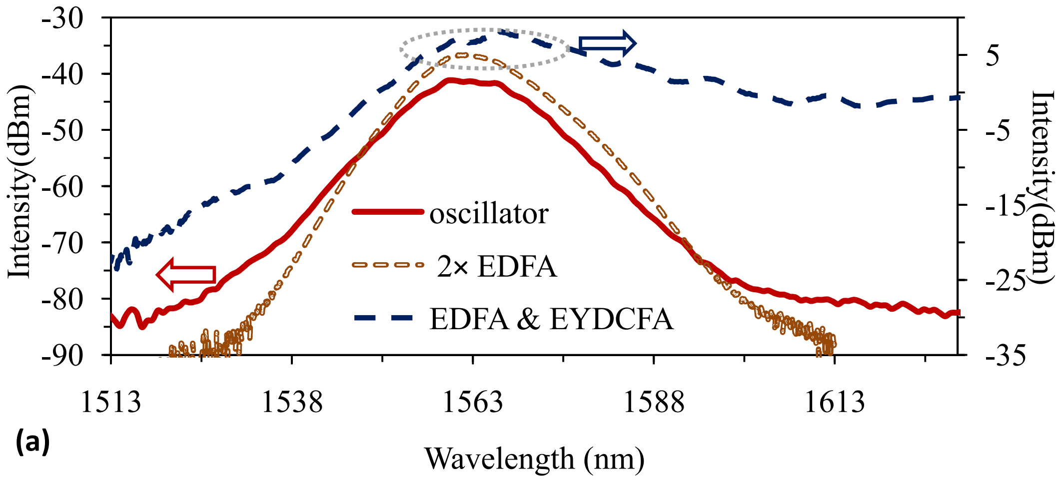

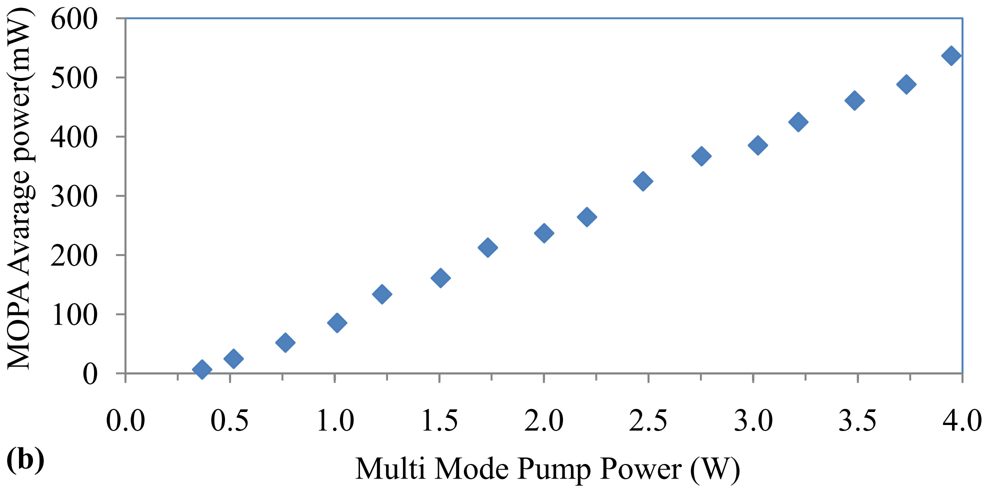

Figure 5. 25: (a) Pulse spectrum of amplified signals at maximum pump powers, (b) Output Power against multi mode laser diode after amplification.

The signal average power for EDFA is fixed at 3 mW while pumping power of EDFA and EYDFA are 120 mW and 4 W, respectively. No significant temporal degradation was observed after a short-length EDFA-EDFA configuration. The maximum average power of 75 mW corresponding to peak powers of 27.9 kW is obtained with a two stage EDFA. For the EDFA-EYDCFA configuration, the pulse train is amplified up to 500 mW, corresponding to peak powers of 177.3 kW, when a dispersive pulse compression has been used. This pulse is used as a source for supercontinuum generation in nonlinear fibers. Figure 5.25(b) shows no saturation in the output power and higher average powers would be possible with higher input signals and pump sources.

5.17 CONCLUSIONS

In summary we have demonstrated a Bi-EDF passively mode locked laser in which the pulse width can continuously vary from 1.2 ps to 131 fs with a minimum timing jitter of 4 ps and energy fluctuations of 2.5%. The laser can produce an average power of 5 mW at 1560 nm with a repetition rate of 8.27 MHz. Increasing pump power and broadening spectral width in the oscillator decrease time-bandwidth products (TBWP), pulse durations and output fluctuations. Despite large changes per round trip, the stretched pulse output has smaller amplitudes fluctuations, lower timing jitter, and asymmetric noise structures. This is due to the fact that, the two timing jitter noise sources i.e. GVD and filtering effects have smaller magnitudes in the proposed stretched pulse laser. Hence operating at a higher power and a smaller net GVD prevent frequency deviations to transform into timing jitter.

The pulse train was then amplified by a two-stage amplifier with an average power of up to 500 mW. In the next chapter, we will investigate a supercontinuum generation in different types of fibers when pumped by passively mode locked Bi-EDFL.

CHAPTER 6

SUPERCONTINUUM GENERATION WITH FEMTOSECOND PULSES

A Supercontinuum (SC) generation decribes an extreme spectral broadening induced by the coupling of a high peak power pulse laser in an adequately long nonlinear optical fiber. The SC spectrum in three different nonlinear fibers are presented and discussed in this chapter. As discussed in chapter two, nonlinear effects such as SRS, SPM, XPM and FWM contribute to SCG process. Pumping wavelength and its deviation from ZDW have significant effect on the shape of SC spectrum while depending on the dispersion characteristic of the fiber and the specification of the pump, some nonlinear effects are more significant for the amount of SC broadening.

6.1 EXPERIMENTAL SETUP

A pulse laser is generated by an earlier proposed mode locked Bismuth based Erbium-doped fiber laser oscillator. A fraction of mode locked pulses from 10% output coupler is extracted and amplified by a two-stage pre-amplifier. The first stage EDFA uses a 3 m long highly doped EDF which is pumped by single mode laser diode via a 980/1550 nm WDM coupler. The pulse train is then further amplified by a double-clad Er^{3+}/Yb^{3+} doped fiber amplifier (DC-EYDFA) before it would be launched into a piece of nonlinear fiber for SCG.

The unidirectional propagation between these stages is guaranteed by isolators. Depending on the pumping power, the amplifiers boost the signal to different levels of power and make it possible to investigate the evolution of SCG with the pulse peak powers. Maximum pumping power of EDFA at 980 nm is 120 mW and for DC-EYDFA is 4 W at 927 nm. The performance of the amplifiers used in the setup has been reported in chapter 3 and 4 [391, 392].

Amplification with EDFAs yields a maximum average power of 75 mW which translates to a peak power of 27.9 kW. The maximum average output power after DC-EYDFA configuration is measured to be around 500 mW, which again translates to a peak power of 177 kW for a 340 fs pulse train with the repetition rate of 8.27 MHz.

The experiment is carried out for different kinds of nonlinear fibers such as Photonic Crystal Fiber, Dispersion Flattened Highly Nonlinear Fiber (DF-HNLF, OFS) and Non-Zero Dispersion Shifted Fiber (NZ-DSF, OFS) [393, 394]. The nonlinear coefficient of all high nonlinear fibers is around 11 $(Wkm)^{-1}$.

Two different types of PCF; NL-1550-NEG-1 and SC-5.0-1040 are experimented in this chapter. These fibers are commercially available fiber from NKT Co. Ltd. The PCF (NL-1550-NEG-1) used has a total negative dispersion value in 750-1750 nm region while 20 m long SC-5.0-1040 has a ZDW at 1040 nm.

Two different lengths of PCF-NEG; 50 and 100 m are experimented in this chapter. The DF-HNLF used is also a commercially available fiber from OFS Co. Ltd. with a length of 100 m.

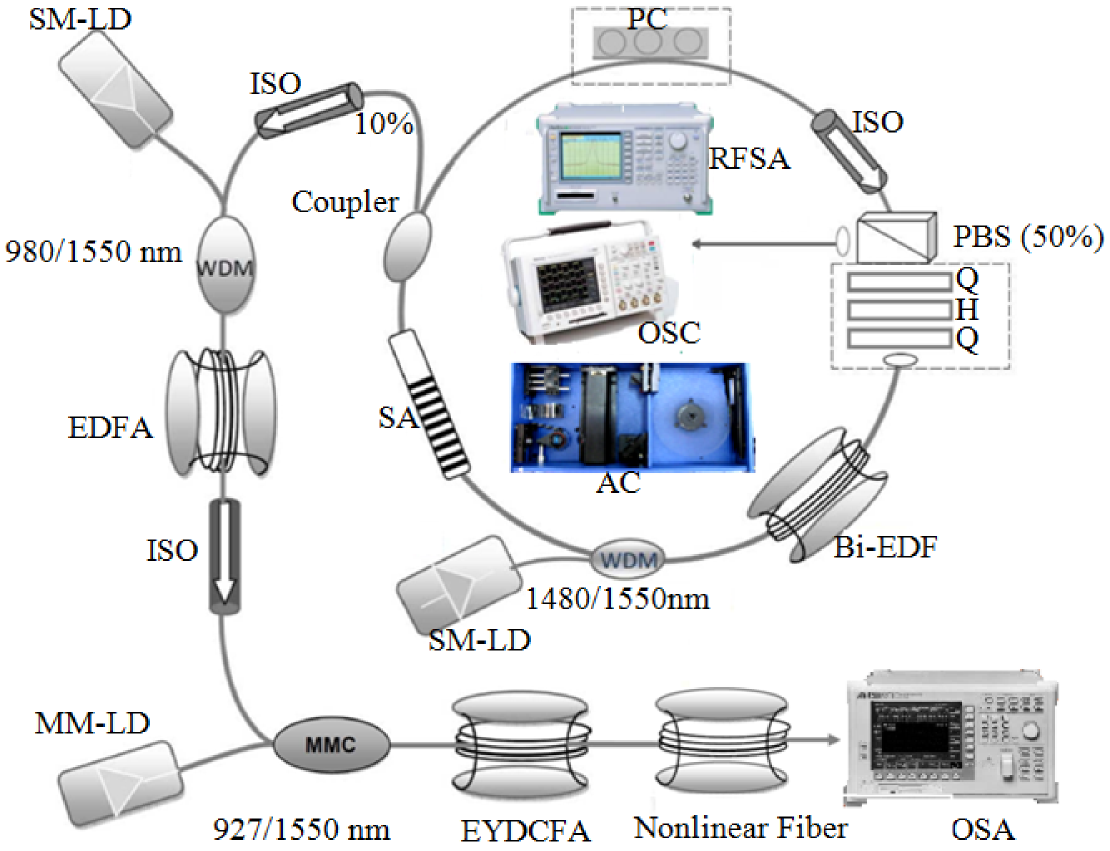

Figure 6. 1: Experimental setup of the Bi-EDFL: WDM: Wavelength Division Multiplexer; SA: Saturable Absorber; PC: Polarization Controller; PBS-Isolator: Beam Polarizing Beam Splitter integrated with Isolator; H: λ/2 retarder; Q: λ/4 retarder; ISO: Isolator; MMC: multimode combiner; MM-LD: multimode laser diode; OSC: Oscilloscope; RFSA: RF Spectrum Analyzer; OSA: Optical Spectrum Analyzer; AC: Auto-correlator.

The third type of fibers is a 10 km non-zero dispersion shifted fiber (NZ-DSF), which has low water absorption and is optimized for Raman amplification.The ZDW of this fiber is around 1405 nm such that the pump wavelength lies in the anomalous dispersion regime for it. Nonlinear coefficient of this fiber is quite low and therefore a long piece of NZ-DSF is employed in the experiment. Moreover this fiber exhibits a linear dispersion profile.

The dispersion profiles of high nonlinear fibers are plotted in the Figure 6.2 and specifications of fibers used are summarized in Table 6.1.

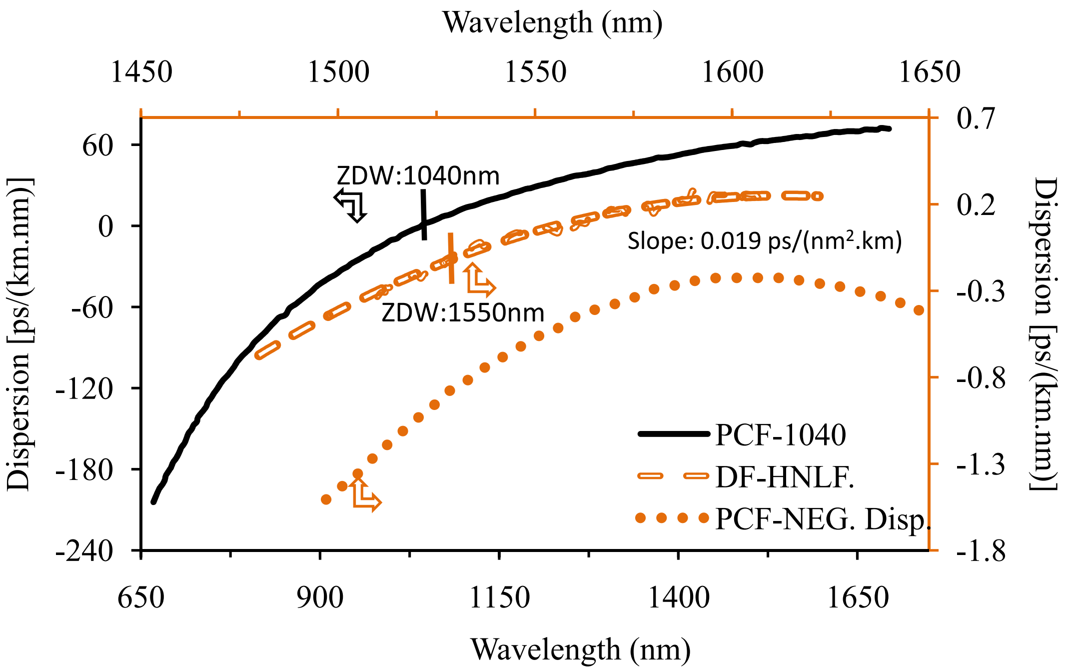

Figure 6. 2: Dispersion profile of different nonlinear fibers used in the experiments [394].

Table 6. 1: Parameters and specifications of nonlinear fibers used.

Parameters	**Value**
PCF-NEG(Pure Silica)	50&100m
Nonlinear coefficient(1550nm)	11(Wkm)$^{-1}$
MFD/ Cladding diameter	2.8 /128 µm
Minimum Attenuation	9 dB/km
DF- HNLF(GeO$_2$ doped Silica)	100m
Nonlinear coefficient (1550nm)	11.5(Wkm)$^{-1}$
MFD/ Cladding diameter	3.99/ 128 µm
Minimum Attenuation	0.9 dB/km
Zero Dispersion Wavelength	1550nm
PCF-1040(Pure Silica)	20m
Nonlinear coefficient (1060nm)	11(Wkm)$^{-1}$
MFD/ Cladding diameter	4.2/125 µm
Minimum Attenuation	2 dB/km
SMF(High purity synthetic Silica glass)	10km
Nonlinear coefficient (1550nm)	0.95(Wkm)$^{-1}$
MFD/ Cladding diameter	8.4 /125
Minimum Attenuation	0.2 dB/km
Dispersion Slope	0.045 ps/nm^2-km
Zero Dispersion Wavelength	1405nm

An optical spectrum analyzer (OSA, ANRITSU-MS9710B) with spectral measurement range limited to 1700 nm is used to measure the optical spectrum of the SC with resolution of 0.07 nm. To clearly illustrate the spectral evolution of the continuum, all attenuated SC spectra shown in following sections are offset vertically. The bandwidths of the spectra are measured in 20-dB scale which is limited by OSA spectral range. Hence a scanning monochromator with PBS detector is needed for wavelength beyond this limit.

6.2 RESULTS AND DISCUSSION

6.2.1 SCG Results in Photonic Crystal Fiber

SC generation experiments are performed for two different PCF lengths; 50 m and 100 m. Figure 6.3 shows the measured SC spectra generated in in a piece of 50 m PCF-NEG for different injected pulse peak power levels which is pumped by the 1564 nm femtosecond fiber laser. The dispersion is always negative for this fiber so that the SCG process can be explained with an argument that is similar to that of pumping in normal region. Since the pumping wavelength lies around the minimum of the dispersion profile, FWM effect plays an important role to generate SC components especially around pumping wavelength.

In fact at the initial stage of beam propagation in fiber, symmetrical sidebands are generated due to modulation instability and SPM. With further propagation, multiple sidebands grow from the phase matched FWM process, but only the spreading of continuum to longer wavelength side occurs due to overlap with Raman bandwidth and the SRS effect [144].

As shown in Figure 6.3, the SC lights, starts from1220 nm for pump peak powers of 5.1 kW while we observe an SC starting from 996 nm at maximum pump powers (177 kW). These spectra extend up to wavelength region of more than 1750 nm. The spectral broadening of 2 μm region has not been examined due to spectral sensitivity of the OSA.

The SC spectrum bandwidth increases from 420 nm to 660 nm as the peak power increases from 5.1 kW to 177 kW. The output spectra show residual peak at the pumping wavelength.

At the maximum pump power of 177 kW self-phase modulation effects are dominant over the other nonlinear processes. This leads to more extension of spectrum as well as a smoother and flatter emitted spectrum covering the wavelength range from 1150 to 1700 nm.

Note that a spectral component appears at around 1060 nm when the launched power exceeds 5.1 kW which is deemed to be second harmonic of red-shifted component of around 2.2 μm, see Figure 6.3.

The wavelength of this peak does not shift as the pump power increases. This component is boasted and broadened due to nonlinear effects interaction at higher powers which in turn becomes a major peak. The broadband light is also observed at visible green wavelength as shown in the Figure 5(b).

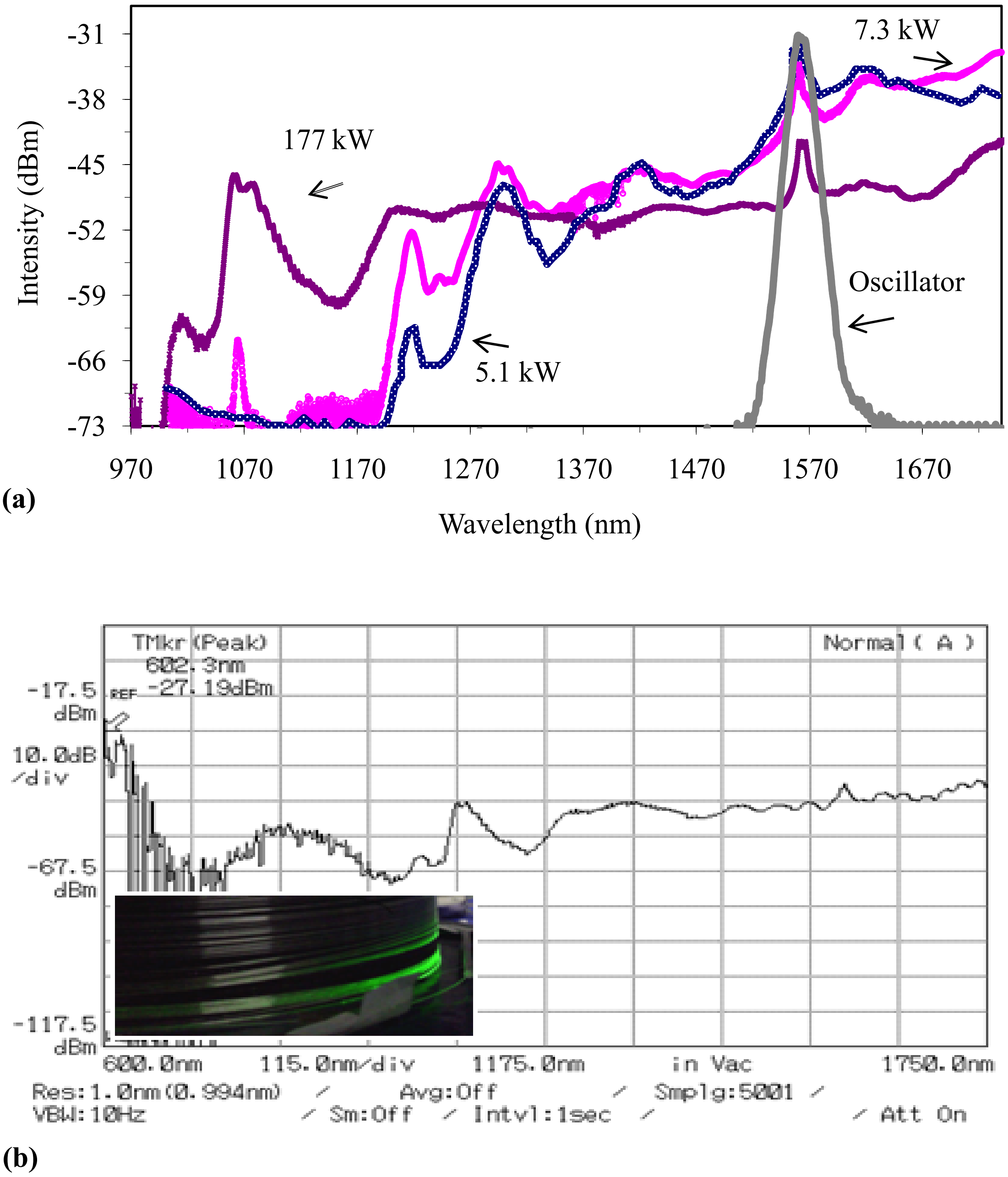

Figure 6. 3: (a) SCG with 50 m PCF at various pump powers. The narrow curve shows the spectrum of the initial 340 fs pulse, (b) SCG extending from 500 nm to 2.2 µm.

SC generation is also investigated in 100 m long PCF-NEG and the spectral evolution is shown in Figure 6.4. As shown in the figure the spectral component around 1060 nm does not appear for this case.

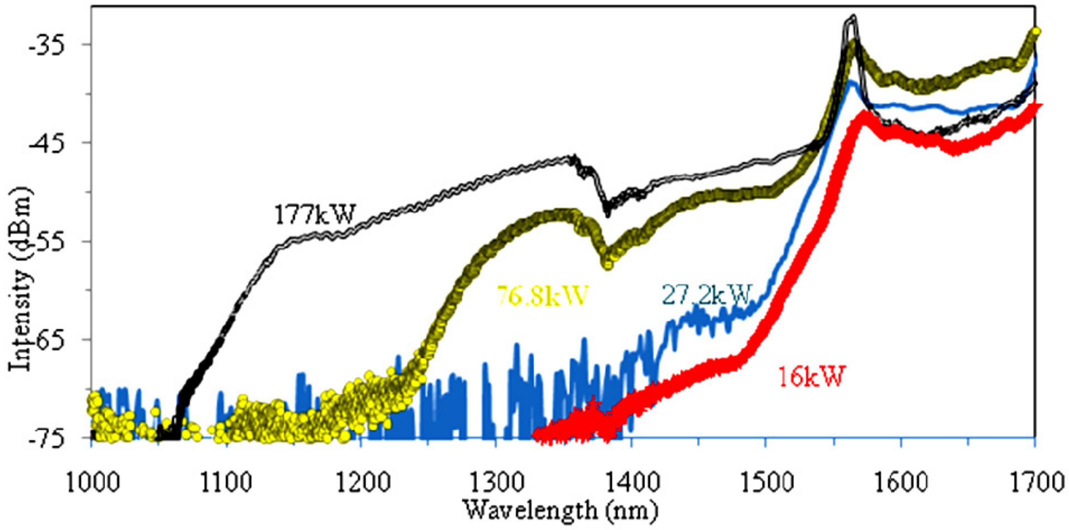

Figure 6. 4: Optical spectrum of the continuum generated in 100 m length of PCF-NEG as a function of coupled power.

Figure 6.5 compared the SCG with two different lengths of PCF at the maximum peak pump power of 177 kW. As shown in Figure 6.5, the power level of the SC at a longer wavelength region is higher with a longer PCF.

However, It is clearly shown that SC is less flat as the PCF length is changed from 50 m to 100 m. In fact using shorter lengths of PCF makes self-phase modulation effects dominant over the other nonlinear processes leading to a smoother emitted spectrum with an output power variation of less than 10 dB.

Note that the aforementioned component at 1060 nm is not observed in 100 m long PCF-NEG. In fact, this component is attributed to high birefringence in the small cores and it provides support for a phase-matched FWM process.

The conversion efficiency of this process can be changed by fiber length and enhanced via optimal phase matching conditions or by using novel fibers. Therefore, the birefringence property of the fiber must also be taken into account in the generation of a SC spectrum, particularly for a lower requirement of the pump power [165].

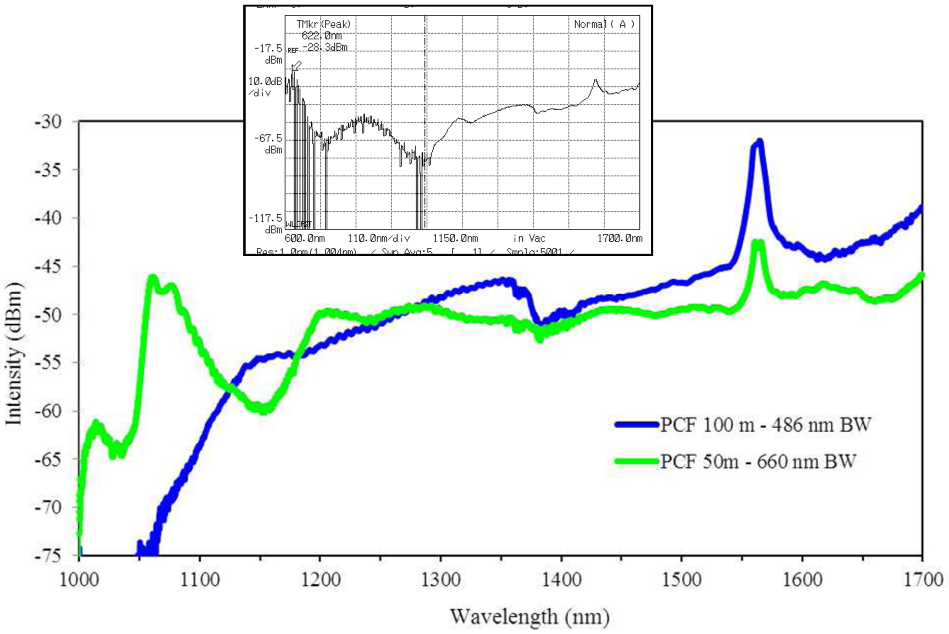

Figure 6. 5: The generated supercontinuum at different PCF lengths at fixed average pump power of 500 mW (peak power of 177 kW).

6.2.2 SCG Results in High Nonlinear Fiber (HNLF)

According to the dispersion profile of the DF-HNLF, the pumping wavelength is located in the anomalous region with a difference of 14 nm to ZDW of the fiber. Figure 6.6 shows the SCG in 100 m DF-HNLF at various injected pump peak powers.

Unlike the case of PCF-NEG, as the pump power increases, the SC bandwidth in DF-HNLF symmetrically increases around the pumping wavelength. The spectrum flatness also improves around ZDW as the pump power increases.

Considering the same value for nonlinearity coefficients of DF-HNLF and PCF, the main reason of having broader spectrum for DF-HNLF seems to be the pumping in anomalous region.

An increase in pumping power gives rise to nonlinear effects in the fiber [144]. The number of soliton waves and Raman induced shift (SSFS) are increased, which extends the spectrum to longer wavelength. On the other hand, the number of coupled spectral components at short wavelength side is increased due to NSR effect. From wavelength difference between ZDW and pumping wavelength, it is expected to have broader SC at the expense of more gaps around pumping wavelength, as can be seen in Figure 6.6(a) for low levels of power.

However, an increase in power not only fills these gaps around pumping wavelength but also makes the continuum much smooth. It is mainly due to more intense FWM and XPM effects around the pumping wavelength. As shown in the figure, the spectral density of the SC at highest peak power of 177 kW varies by less than 6 dB over a bandwidth of more than 680 nm. Hence the broadest and smoothest spectrum without gaps is obtained for DF-HNLF with 20-dB bandwidth of 750 nm (limited by OSA spectral range).

Figure 6.6(b) shows the SC spectrum in the 600-1750 nm wavelength range, as measured with OSA. However, the spectral broadening at 2 µm and UV regions was not recorded due to the limitation in sensitivity range of OSA.

We also observed the visible green spectral radiation from the fiber surface. This light is generated by a combination of Raman self-frequency shifting and third-harmonic generation. Further measurements with an IR monochromator indicated that the SC plateau extends to wavelengths longer than 2000 nm [395].

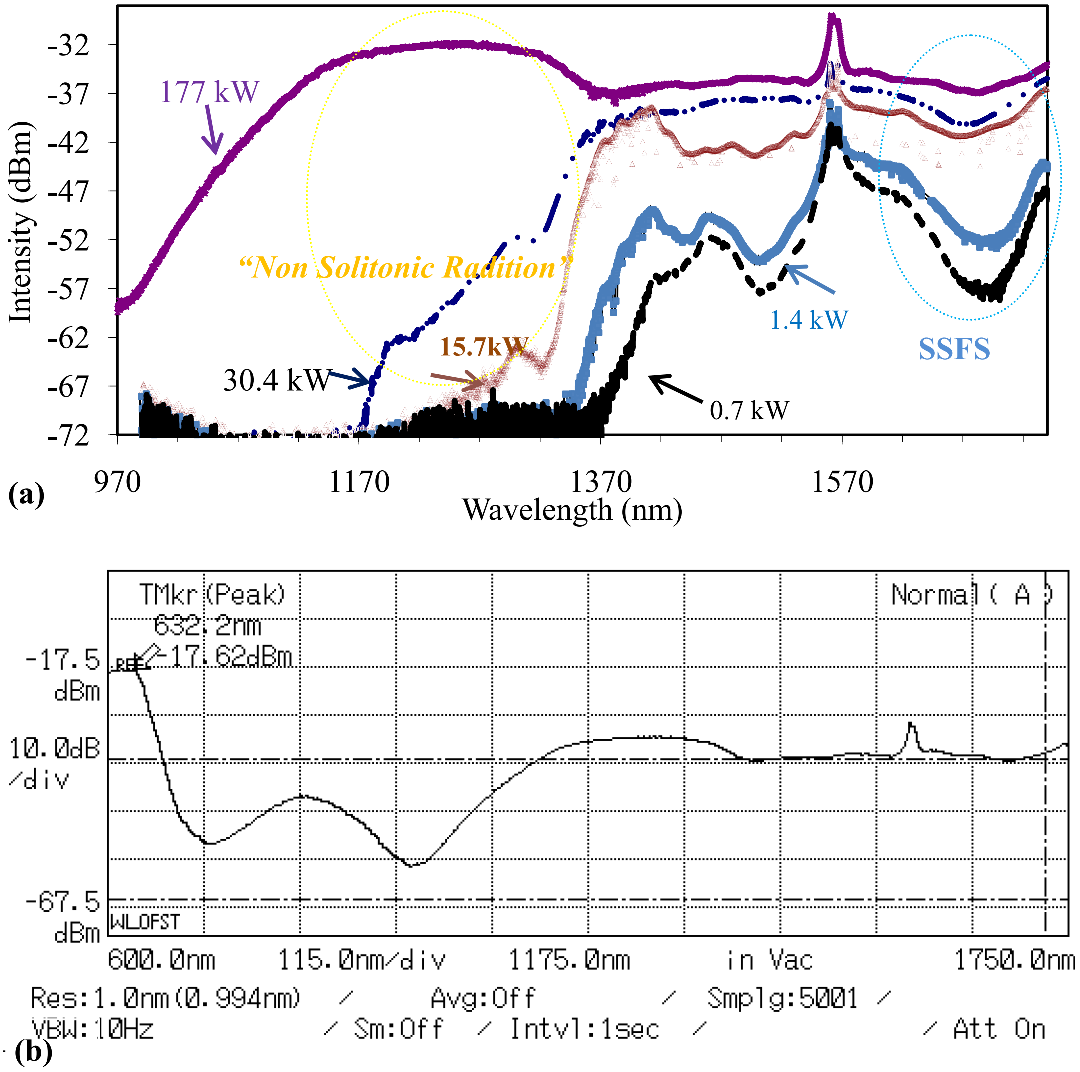

Figure 6. 6: (a) SC generation in 100 m HNLF at various pumping powers, (b) wide span measurement and disappearance of spectral peak at 1064nm.

6.2.3 SCG Results In Other Nonlinear Fibers

A comparison of SC spectra for five different fibers at the highest value of the launched peak power, i.e. 177 kW is shown in Figure 6.7. For the DF-HNLF, the spectrum obtained is broader compared to that of the PCF.

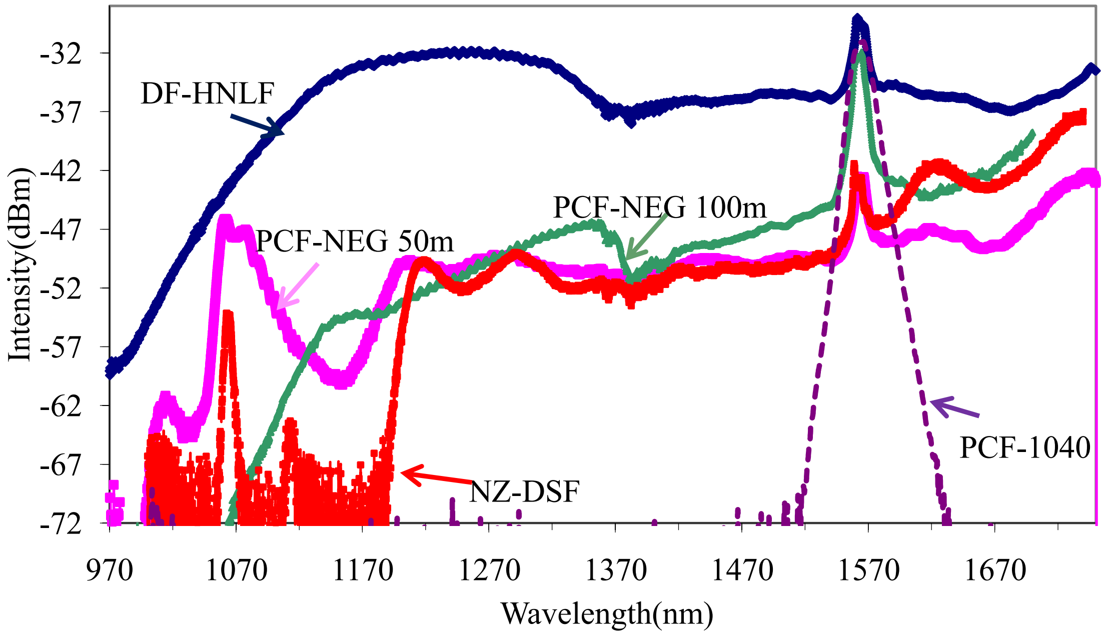

Figure 6. 7: SCG comparison in various fibers at highest level of power (177 kW peak power).

The narrow curve shows the spectrum of the continuum generated in a 20 m section of PCF-1040 which is pumped by a 1560 nm femtoseconds pulse. There is not any considerable spectral broadening, due to large detuning of pumping wavelength from ZDW and large amount of GVD at pump wavelength.

The SCG in 10 km length of NZ-DSF is also depicted. Similar to DF-HNLF, NZ-DSF exhibits positive dispersion at the pump wavelength and SCG in this fiber is expected to be mainly due to SRS effect and SSFS to long wavelength. Because of typical low nonlinearity of this fiber, which is about 0.95 $(W.km)^{-1}$, a considerable length of fiber (roughly 10 km) is required to generate the supercontinuum. SC is recorded only at highest level of peak power of 177 kW.

As shown in the figure, the power spectral density varies by less than 20 dB over a bandwidth of more than 505 nm from 1195 to 1700 nm. The spectrum is quite smooth without any dips around the pumping wavelength due to the considerable length of the fiber as well as the high launched power.

At the same time, the large wavelength difference between the zero dispersion and pumping wavelengths broadens the spectrum. The spectral component at 1064 nm appears again in the spectrum and is deemed to be a harmonic of red-shifted component at 2.2 µm.

However, given a 70 fs pulse train with center wavelength at 1570 nm and the peak power of 16 kW, SC has been reported as broad as 300 nm in a several-meter of similar NZ-DSF in [396].

Figure 6.8 shows 20-dB bandwidth of the SC as a function of launched power for PCF-NEG and DF-HNLF. Since SC wavelength range extends beyond the limit of OSA range, spectral bandwidths are actually broader than presented values.

In general, DF-HNLF spectrum is broader than PCF- NEG spectrum at the same length of the fiber. However at low powers, a 50 m long PCF-NEG exhibits the broadest spectrum.

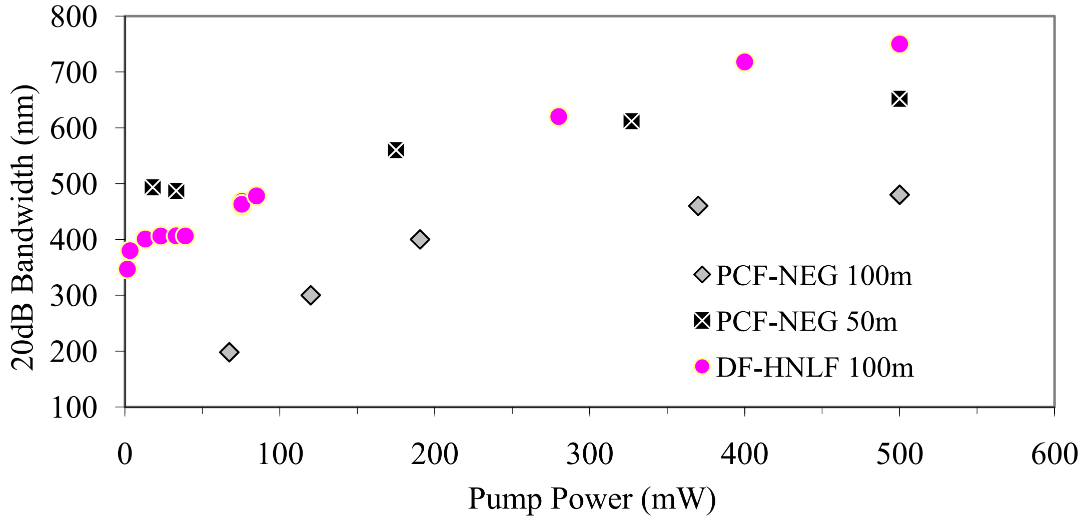

Figure 6. 8: Bandwidth evolution versus launched pump power.

In fact, SC spectrum in 50 m long PCF is broader than 100 m PCF spectrum for all powers mainly due to the appearance of spectral component at 1064 nm.

For DF-HNLF, the maximum bandwidth value is limited to the maximum available power. In contrast, the spectral band width for PCF-NEG does not continue increasing above 200 mW of the pump average power. At higher pump powers, SC reaches its saturation state. This is due to the more loss in the energy corresponding to SRS as well as the linear loss related to the propagation in optical fiber.

Additional increase in power does not necessarily lead to either larger bandwidth growth or higher SC output power. An alternative approach is to widen the pump pulse duration rather than to increase the pump peak power (which consequently increases the SC pulse energy). It can be done at the expense of lower expansion of SC through SSFS and lower energy solitons at red side of spectrum [397].

It should be noted that power measurements for the SC spectrum are not accurate due to the extension of the spectra more than bandwidth of our power meter. However for the narrowest spectrum obtained from 100 m long PCF, the supercontinuum power is about 210 mW at the maximum launched power.

6.2.4 Spectral Slicing of Supercontinuum Source

Throughout many years of development, many comb-filter configurations have been proposed in accomplishing multi-wavelength lasers such as Fabry-Perot interferometer [49], fiber Bragg gratings (FBGs) [50], Mach Zehnder interferometers [398] and fiber loop mirrors [53]. Among all, polarization maintaining fiber loop mirror is one of the promising configurations in terms of simple fabrication process, low fabrication cost, low insertion loss to the system cavity and capable of creating large number of lasing numbers [52, 53, 399, 400].

In the conventional temperature controlled scheme which relies on single PMF segment, the birefringence of the PMF descends with increasing temperature and thereby larger spectral spacing is observed in the transmission spectrum. The extension of this conventional scheme is restricted to the limited number control elements in the configuration. Besides, the conventional scheme also suffers from longer negative spectral spacing detuning time, due to the long temperature fall time in nature unless some expensive cooling system is incorporated in the configuration to hasten the process.

In addition, dynamic spacing tuneability is highly desirable in many applications. Discrete tuning in wavelength spacing allows limited number of selectable wavelength spacings within a wide tuning range [401-403] while continuous tuning scheme enables fine and continuous spacing tuning within in a small tuning range [401, 404, 405].

By exploiting the temperature-dependent birefringence of the PMF, the wavelength spacing of the fiber loop mirror can be finely and continuously increased or widely decreased by increasing the temperature of one of the segments .In this work a spectral sliced-tunable multi-wavelength source is demonstrated using a supercontinuum beam generated in nonlinear fibers and a proposed Sagnac fiber loop mirror [406].

6.2.4.1 Design of Temperature Sensitive Loop Mirror

Fig. 6.9 shows the proposed temperature sensitive loop mirror (TSLM) which will be used in spectral slicing experiment. It is constructed from a 3dB coupler and two segments of polarization maintaining fibers (PMF_1 and PMF_2). The segments are spliced at an offset rotation angle of 90^o while PMF_2 is set to be longer than PMF_1.

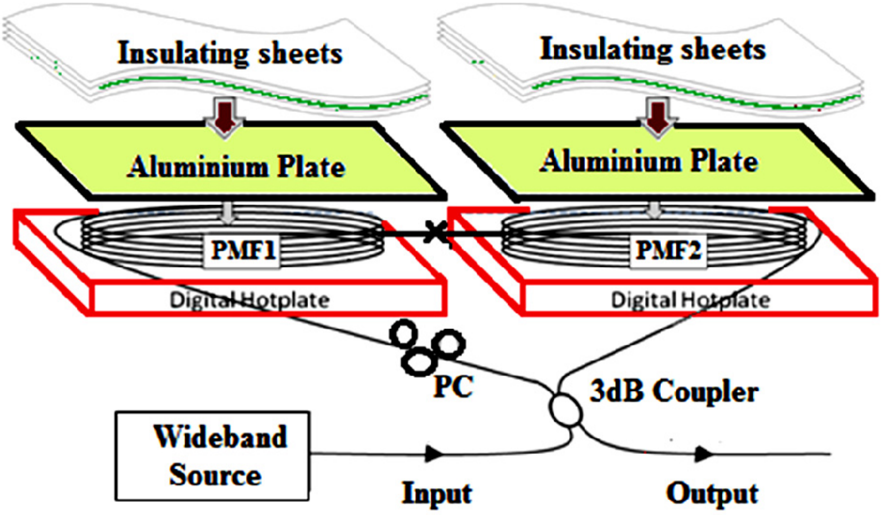

Figure 6. 9: Experimental Setup of the temperature-sensitive interferometer based on multisegment Polarization Maintaining Fiber Sagnac Loop Mirrors (PMF-FLM).

Temperature of each PMF segment is controlled and monitored by a digital hotplate. To ensure a consistent and uniform distribution of temperature, the fiber segment is sandwiched by a 5mm thick aluminium plate. Several pieces of paper sheets which act as insulators are placed on top of the aluminium plate to confine the heat generated by the hotplate and maintain the temperature in the fiber.The wavelength spacing can be increased (positive detuned) by increasing the temperature of the PMF_2 (T_2) while the other segment is maintained at room temperature:

Adversely, the wavelength spacing can be decreased (negative detuned) by increasing the temperature of PMF$_1$ (T_1) and maintain the temperature of the other segment, T_2 at room temperature. The temperature response of the positive detuning and negative detuning operations can be well characterized by the following two equations [62]:

Positive Detuning:

$$\Delta\lambda_+(T_2) \approx \Delta\lambda(T_0,T_0) + \frac{\Delta\lambda(T_0,T_0)^2}{\lambda^2}\left[b_1(T_2-T_0)+b_2(T_2-T_0)^2\right]L_2 \qquad (6.1)$$

Negative Detuning:

$$\Delta\lambda_-(T_1) \approx \Delta\lambda(T_0,T_0) - \frac{\Delta\lambda(T_0,T_0)^2}{\lambda^2}\left[b_1(T_1-T_0)+b_2(T_1-T_0)^2\right]L_1 \qquad (6.2)$$

where $\Delta\lambda(T_0,T_0)=\dfrac{\lambda^2}{\Delta n(T_0)(L_2-L_1)}$ is the wavelength spacing where both PMF segments are at room temperature T_0, b_1 and b_2 are the birefringence characterization curve coefficients, λ is the operating wavelength and L_1 and L_2 are the segment lengths of PMF1 and PMF2 respectively [402, 403].

Polarization controller PC can be also used to control the polarization state of the input wave to the loop mirror. In the experiment, the performances of two different PMF segment length combinations (2.5/1.0 m and 4.0/2.5 m) are observed. Both combinations were deliberately chosen in such a way that the same effective length ($L_{eff}=L_2-L_1$) of 1.5 m is acquired for the loop mirror and both combinations provide almost the same wavelength spacing of 1.74 nm at 1037 nm at room temperature.

The results of using this TSLM as a back mirror of a linear resonator in the vicinity of 1037 nm have been shown in Figures. 6.10 and 6.11 [406]. The forward amplified spontaneous emission (ASE) from the gain media is filtered by the loop mirror and the filtered spectrum oscillates in the ring cavity to generate a multi-wavelength laser comb.

In each figure, curves B-A and B-C represent the variation of wavelength spacing in the positive detuning and negative operations respectively in the temperature variation range of 30-150 ° C.

The three insets on the right hand side in the figures show output spectra of the laser at three different scenarios which are A): T_1 is room temperature and T_2 is 150 ° C, B): both T_1 and T_2 are room temperature and C): T_1 is 150 ° C and T_2 is room temperature, as stated in the respective inset. It is easy to observe that the wavelength spacing is in the descending order from inset A to C.

In the comparison of wavelength spacing tuning range between the two combinations, the experimental result shows that the combination with the longer segment lengths (L_1 and L_2) provides a larger tuning range. This proportionality can be easily determined from Equations (6.1) and (6.2) which spacing tuning span is linearly proportional to the total segments length $L_1 + L_2$:

$$\Delta\lambda_+(T) - \Delta\lambda_-(T) = \frac{\Delta\lambda(T_0,T_0)^2}{\lambda^2}\left[b_1(T-T_0) + b_2(T-T_0)^2\right](L_1+L_2) \quad (6.3)$$

Based on this relation, the tuning span can be further enhanced by using even longer PMF segments. In other words, the same tuning span can be achieved at lower temperature if longer PMF segments are used in the loop mirror. This approach provides a great flexibility in the design and capable of meeting many applications requirement.

The proposed configuration provides greater temperature sensitivity in the spectral spacing detuning compared to the conventional configuration. Besides, the proposed configuration also enables both efficient positive and negative spectral spacing detuning by rising the temperature of one of the PMF segments.

The experimental results as reported in [62], show the proposed configuration has achieved a great improvement in increasing spectral spacing variation range by 6.6 times and an increment of temperature sensitivity as much as 337.6% as compared to the conventional configuration.

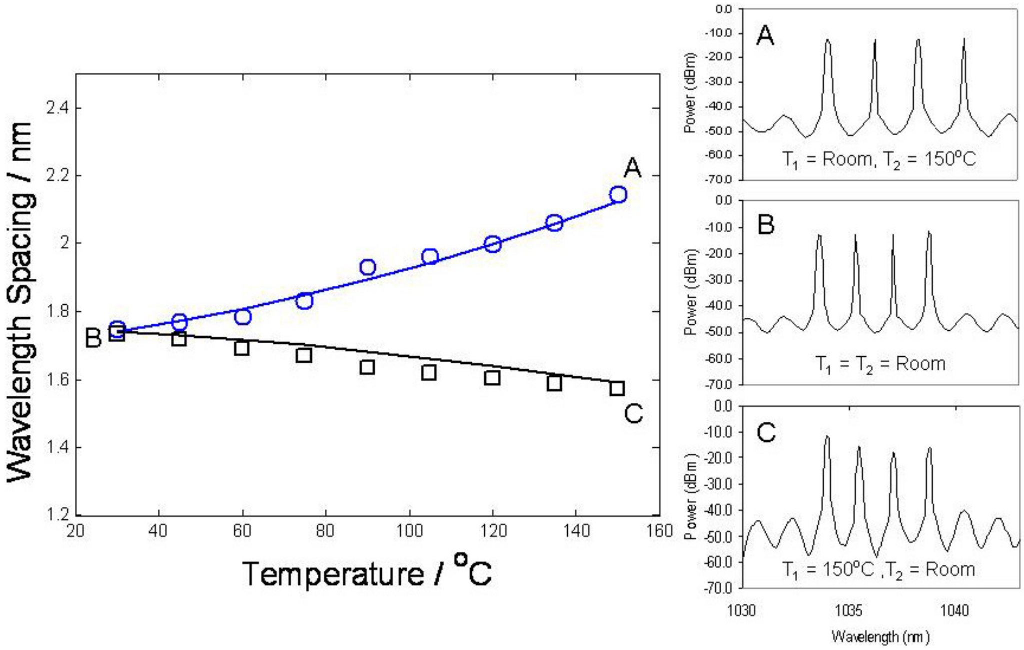

Figure 6. 10: L_2 =2.5 m, L_1 = 1.0 m, L_{eff} =1.5 m, λ = 1037 nm, T_0=28 °C (Estimated parameters $b_1 = 2.6\times10^{-7}$ °C^{-1}, $b_2 = 1.5\times10^{-9}$ °C^{-2}, $\Delta n(T_0)=4.07\times10^{-4}$).

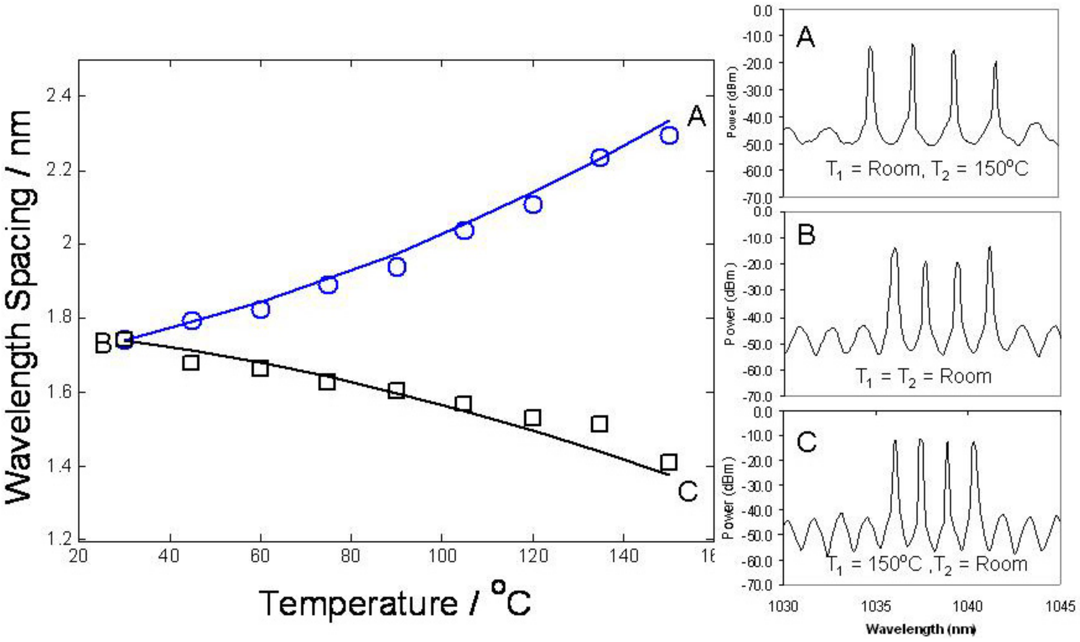

Figure 6. 11: $L_2 = 4.0$ m, $L_1 = 2.5$ m, $L_{eff} = 1.5$m, $\lambda = 1037$ nm, $T_0 = 28\,^\circ C$ (Estimated parameters $b_1 = 2.5\times10^{-7}\,^\circ C^{-1}$, $b_2 = 1.5\times10^{-9}\,^\circ C^{-2}$, $\Delta n(T_0) = 4.07\times10^{-4}$).

6.2.4.2 Multi-wavelength source by SC slicing technique

The TSLM is then used to generate a multi-wavelength laser source. This source is needed for wavelength division multiplexing (DWDM) optical networks which is a promising solution for future broadband access network. For a wideband multi-wavelength source a simple setup with the adjustable comb spacing covering 800 nm bandwidth is used in this thesis. It consists of a supercontinuum source and a thermal controlled fiber loop mirror with combination PMF lengths of 4.0 m and 2.5 m. By changing the temperature of the PMF segments, the spacing can be tuned from 1.69 nm to 4.35 nm. The multi-wavelength lasing with a flat output power and an average value for signal to noise ratio of more than 15 dB is obtained in the region of 1000 to1750 nm.

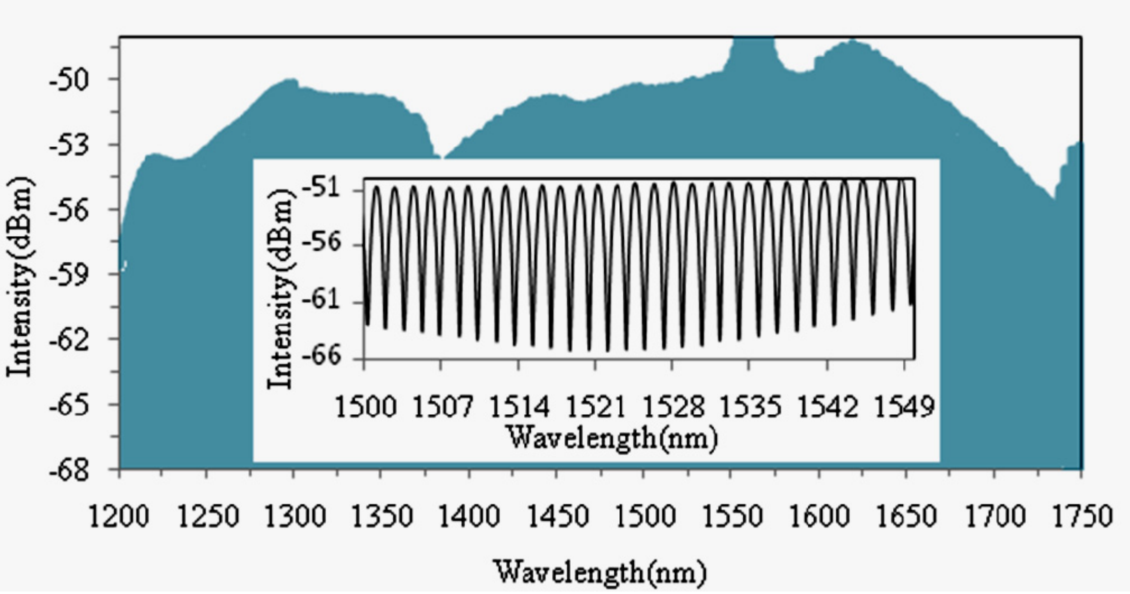

Figure 6. 12: The sliced spectra of all channels using proposed TSLM, inset shows a superposition of the spectra of 29 channels in the region of 1500 to 1549 nm with the maximum difference of 0.4 dB.

The higher number of lines is expected with the longer PMF. With realistic improvements in HNLF fabrication, further extensions in SC bandwidth and channel flatness should be possible [407].

A further reduction in optical power requirements or device lengths is also possible in this way.

At room temperature, the multi-wavelength output is observed to be stable with an output power variance as low as 0.4 dB and a maximum average output power of 20.7 dBm. Figure 6.12 shows a superposition of the spectra of all channels. Among all tested wavelengths, with an average value of 18 dB, the SNR (signal-to-noise ratio) for each of the channels was better than 10 dB. In order to obtain a broader and smoother comb profile, a pulse shaper can be used before HNLF [408].

6.3 CONCLUSIONS

The construction of a Bi-EDF mode locked laser, without using any intra- or extra -cavity pulse compressors has been successfully accomplished for the achievement of ultralow threshold and high efficiency in a relatively compact configuration. We demonstrated a mode locked oscillator using a slow SA which generated a 131 fs pulse train with a repetition rate of 8.27 MHz. The pulse train with a spectrum centred at 1560 nm was then amplified by a two-stage optical amplifier with an average power of up to 500 mW, corresponding to peak powers of 177 kW and a pulse durations of 340 fs.

Then, we presented experimental results of SCG in three kinds of nonlinear fibers with the same nonlinear coefficients: DF-HNLF, PCF-NEG and PCF-1040. We also repeated the same experiment for a conventional fiber (NZ-DSF).

In the -20 dB scale, spectral bandwidths of 750 nm and 652 nm were obtained for 100 m long DF-HNLF and 50 m long PCF-NEG, respectively. Meanwhile, SCG in NZ-DSF needs to be long. A flat spectrum with a bandwidth of 507 nm was yielded by a 10 km long NZ-DSF at the maximum pump power. For a PCF with a ZDW at 1040 nm the supercontinuum does not expand due to the large detuning of the pumping wavelength from the ZDW and due to a large amount of GVD at the pumping wavelength.

The broadest SC spectrum without dips was obtained for DF-HNLF. For this fiber bandwidth was limited only by the available pump power. The output spectra in this fiber exhibit a small transmitted peak at the pump wavelength and a symmetrical growth around this wavelength. At the maximum pump power, there exists an extremely flat spectrum covering the range from 500 nm to beyond 2.2 μm with a low spectral noise.

The fact that the fibers did not suffer any damage during the experiments indicates that higher power levels with broader bandwidths can be obtained at the output of the fibers.

Although high normal dispersion of the PCF-NEG imposes an upper limit on spectral broadening, it has been proven that pumping a PCF in the normal GVD regime is a trivial method to ensure coherent SC generation [28, 31].

We found that PCF-NEG exhibits broader spectrum at shorter lengths (e.g. 50 m). The new spectral component at 1064 nm seems to extend the spectrum to shorter wavelengths. This component does not shift with changes in power and is believed to be a second harmonic of red shifted component located around 2.2 μm.

However, the energy distribution in the SC spectra is higher in the longer wavelength region of a longer PCF. Similarly, deeper pumping in the anomalous dispersion regime (as shown in the case of DF-HNLF) leads to an enhanced power transfer to the longer wavelength components of the supercontinuum spectrum.

Finally, a temperature sensitive loop mirror (TSLM) was constructed from a 3 dB coupler and two segments of PMFs which are spliced at an offset rotation angle of 90° .

Using a proposed TSLM, a multi-wavelength source was experimentally demonstrated in the region of 1000 nm to 1750 nm by SC slicing. With an output power variance as low as 0.4 dB and a maximum average power of 20.7 dBm, the proposed TSLM enabled us to tune spectral spacing in either ways (both positively and negatively).

Compared to conventional schemes [62], experimental results suggest that by using TSLM one can potentially achieve a substantial improvement (6.6 times more) in increasing spectral spacing variation range and a considerable increment (337.6%) in temperature sensitivity.

CHAPTER 7

CONCLUSION AND FUTURE WORK

In this thesis, various configurations on the continuous-wave and pulsed fiber lasers were proposed and demonstrated using the Bi-EDF to generate various seed signals for optical amplifiers and nonlinear applications. Four topics were studied: : (a) Bismuth-based optical fibers as different glass hosts for rare-earth doped fiber lasers and amplifiers, (b) double clad amplifiers for high power amplification of both narrow lines as well as broadband signals, (c) saturable absorbers for ultra-short pulse generation and (d) nonlinear effects for SCG. In this chapter, we summarize all the presented works and offer some suggestions for future works.

7.1 CONCLUSION

7.1.1 Bismuth-Based Optical Fibres as Different Glass Hosts

In this thesis, the research began with a characterization of Bi-EDF. In chapter three, all the basic measurements needed for the performance evaluation of Bi-EDF were discussed. The FWM and SBS effects have been utilized for the generation of a multi-wavelength laser as well as estimating nonlinear and refractive index coefficients of the Bi-EDF [409]. To fully understand how the input signal power and wavelength affect the gain spectra and the noise figure, we did some experimental measurements for various pumping schemes.

A broadband FBG was used in a double-pass scheme to enhance the gain of Bi-EDFA. With an input signal power of -30 dBm, the peak gain of 38.8 dB was achieved at 1555 nm. Compared to the single-pass operation, the gain was increased by 12.6 dB at this small signal power (-30 dBm). A flat-gain of 14.8 dB with a gain variation of less than 1.1 dB was observed in the range of 1530-1565 nm at an input signal power of 0 dBm.

Using a double pass configuration and a low input signal power, the gain could be easily increased to more than 9 dB within the range of 1565 to 1600 nm.In another experiment, for various configurations and input signal powers, the noise figure spectra were measured as a function of pump power and input wavelength.

In all schemes the noise figure is reduced with an increase of the signal wavelength and reduction of the signal power. The minimum noise figure of 6.8 dB was achieved at 1555 nm for maximum pump power (160 mW).

Another feature of interest was the quantum conversion efficiency. The maximum QCE for 49 cm and 215 cm long of Bi-EDF were estimated to be approximately 17.0 % and 23.5% which was obtained at 1560 nm and 1605 nm respectively.

A tunable ring laser with a unidirectional pumping scheme was constructed based on a tunable band-pass filter (TBF) to generate narrow bandwidth signals with a tuning resolution of 0.05 nm [242]. By varying the pass-band of the TBF, the laser wavelength could be tuned from 1535 to 1575 nm (or 1540-1620 nm) for 49 cm (or 215 cm) long Bi-EDF. The tuning range can be easily extended to larger than 100 nm by using an optical switch to alter the length of Bi-EDF in the fiber ring laser cavity. The extinction ratio of better than 55 dB is achieved throughout the entire tuning range. The measured FWHM bandwidth of this multi-longitudinal mode laser is 0.09 nm, which is suitable for test and gain measurement in the chapter four.

The linewidth of the output signal had improved up to the order of kHz. Meanwhile the performance of a ring cavity BEFL based on the enhanced SBS phenomenon in the Bi-EDF was demonstrated [47]. To generate and amplify backward-propagating Brillouin Stokes, a signal power as a Brillouin pump (BP) from tuneable laser source was injected into the ring cavity via optical circulator. Using 215 cm of Bi-EDF a single stimulated Brilluoin scattering with a SMSR higher than 23 dB and an output spacing of about 0.08 nm is achieved when the wavelength of BP was at 1615.77 nm.

The spacing between the BP and the BFL was obtained at approximately 10-11 GHz. A piece of PCF approximately 20 m in length was employed to improve the FWM characteristics of the laser. Finally, at a BP power of 7 dBm and a 1480 nm pump power of 150 mW, signal wavelengths of 1559.1 nm and 1611.3 nm were injected into this new configuration. A single-wavelength stoke from BEFL was successfully achieved using only a 49 cm long Bi-EDF with a peak power of -11.84 dBm.

The beating between two CW optical carriers at frequencies of ω_1 and ω_2 through nonlinear Kerr effect modulates the refractive index of the fiber at their frequency difference. By employing this method, the nonlinear parameter γ and n_2 at 1600 nm region were estimated to be 59.16 $(\mathrm{W.km})^{-1}$ and 4.40×10^{-19} $(\mathrm{m}^2/\mathrm{W})$ respectively [54, 227].

7.1.2 Amplification of Narrow Linewidth and Broadband Signals

The performance of a high output power DC-EYDFA was also theoretically studied and experimentally investigated. The EYDFA in a double pass configuration provided a flat gain of 33.5 dB with a gain variation of less than 1 dB and an output power higher than 500 mW at the wavelength region of 1545 to 1566 nm.

To investigate the effect of the operating wavelength on the performance of the EYDFL, the slope efficiencies and the laser thresholds were listed for different wavelengths in chapter 4.

The laser slope efficiencies were measured to be about 33.7 %, 30.9 %, and 24.1% for the operating wavelengths of 1553.6, 1557.3, and 1562.8 nm, respectively. We observed that the efficiency is higher for shorter wavelengths due to the amplification characteristic of the EYDF which peaks at 1545 nm.

To achieve a highly efficient and narrow linewidth characteristic, BFL was constructed and amplified by DC-EYDFA. The linewidth of such tuneable source was experimentally measured by the heterodyne beat technique and compared to its Brillouin pump and tuneable Bi-EDFL. A maximum output power of 400 mW and an optical signal-to-noise ratio of more than 45 dB were obtained in narrow linewidth operation. The quantum conversion efficiency was improved from 8.7 to 12% with the increase of the input signal power from -10 to 5 dBm [410].

With a Brillouin pump linewidth of 5±0.001 MHz, the linewidth of the amplified BFL was measured to be around 10±1 kHz. However, with a coupling ratio of 50% and a Brillouin gain bandwidth of about 20 MHz, the laser linewidth of the local oscillator can be estimated to be less than 1 KHz. The results have been published by the author as regular papers in [255-257].

7.1.3 Ultra-Short Pulse Generation

In Chapter 5, the theory of mode locking was reviewed and the construction of a (Bi-)EDF mode locked laser without using any intra- or extra-cavity pulse compressors was successfully accomplished for the achievement of ultralow threshold and high efficiency in a relatively compact configuration.

The required ultra-short and high peak power pulses were generated and the proposed EYDFA was utilized for amplification of ultrashort pulses. The goal of that chapter was to develop a pulsed MOPA system seeded by a tunable passively mode-locked Bi-EDFL.

To that end, a laser oscillator with a net negative GVD was designed to generate 1560 nm pulses at a repetition rate of 8.27 MHz. Utilizing slow SA and NLPR technique, mode locking in ring geometry was demonstrated. The proposed (Bi-)EDFL demonstrated a very low threshold, and low jitter. The pump power threshold for laser oscillation was measured to be 11 mW while it was 20 mW for mode-locking operation. We found out the large emission bandwidth of Bi-EDF leads to a short radiative lifetime and a low attainable slope efficiency of 4.2% for total output powers.

The measurement and analysis of the jitter were also thoroughly discussed in the chapter five. At the same time, the output spectra and instabilities were compared at different output ports. To this end, the instability of mode locking was observed from sidebands around the fundamental and higher harmonics of frequency components in the RF spectrum.

The results show that for a given pump power, the spectral width increases by 10 % and pulses get narrower at the PBS rejection port, when compared to that of the output coupler. Moreover, the spectrum at the output coupler shows a more symmetric shape. The measured low frequency jitter at the maximum pump power was about 4 ps at the coupler port while it can be reached up to 6 ps at PBS port. We concluded that the energy fluctuations are related to bandwidth of optical spectrum such that a broader spectral bandwidth yields a smaller energy fluctuation in the system.

The low frequency jitter noise is inversely proportional to the pump power. By removing fiber adapters and controlling the environmental airflow in the setup, timing jitter was reduced by an order of magnitude, especially if a pump source with a fluctuation limit of less than 0.10% and a temperature controller with an accuracy of $\pm 0.01\ ^{o}C$ were used.

We have demonstrated a near transform limited passively mode locked laser in which the pulse width can be continuously tuned from 1.2 ps up to less than 131 fs. A smaller dispersion to SPM ratio enabled us to achieve the pulses as short as 131 fs with energy fluctuations of less than 2.5%. The Kelly sidebands in the optical spectrum were not too strong and hence negligible. Consequently, we could derive the minimum pulse duration as the transform limit for the presented soliton spectrum.

By increasing pump power and using a broader spectral width in the oscillator, one can further reduce the Time-Bandwidth products (TBWP), pulse duration and output fluctuations [59]. The pulse train with an average power of 5 mW was then amplified up to 447 mW corresponding to peak powers of 177.3 kW, before it was launched into a piece of nonlinear fiber for SCG.

The amplifiers boosted the signal to different power levels. Consequently, we could investigate the evolution of SC spectra as a function of pump peak powers in chapter six. The pulse train as a pump was launched into new classes of fibers with different engineered dispersion properties and nonlinearities.

7.1.4. Multi-wavelength comb and SCG with Femtosecond Pulses

In our work, the SCG was investigated in three types of fibers i.e. photonic crystal fiber (PCF), dispersion flattened highly nonlinear fiber (DF-HNLF) and non-zero dispersion shifted fiber (NZ-DSF).

Two different types of PCFs (PCF-NEG and PCF-1040) each having two different lengths were pumped by the pulse train. The PCF-NEG had a total negative dispersion value in the 750-1750 nm region while the PCF-1040 had a ZDW at 1040 nm. The order of SC expansion and its stability were found to depend upon both nonlinear fiber properties and the laser specifications. A comparison was made for these fibers and the evaluation of spectral bandwidth at high powers was probed.

For all of the high nonlinear fibers, the nonlinear coefficient was chosen to be 11 $(\mathrm{Wkm})^{-1}$. In a 100 m piece of DF-HNLF an extremely flat and low noise spectrum covering a wavelength range from 500 nm to about 2.2 μm was obtained. At a peak power of 177 kW, the -20 dB bandwidth was measured 750$\pm$0.01 nm in the region of 900-1700 nm**.** Since the SC wavelength range was extended beyond the limit of OSA range, spectral bandwidths in all experiments were actually broader than presented values.

At maximum pump power, a comparison between different dispersion profiles for two fibers at equal lengths showed that DF-HNLF spectrum was broader than

PCF-NEG spectrum. However, at low pump powers, the 50 m long PCF-NEG exhibits the broadest SC bandwidth.

The output spectra in 50 m and 100 m pieces of PCF exhibit a flat spectrum at maximum pump power extending over 660 nm and 486 nm respectively. Hence the SC spectrum in a 50 m long PCF is broader than its 100 m counterpart. The major difference between these spectra is the appearance of spectral component at 1064 nm in 50 m piece of PCF which contributes to more expansion of the SC spectrum to shorter wavelengths. It is deemed that this component is a harmonic of the long wavelength component around 2.2 μm. The spectral band width for PCF does not continue increasing above 200 mW of the pump average power.

In contrast, For DF- HNLF, the maximum bandwidth value is limited to the maximum available power. It should be noted that power measurements for the SC spectrum were not accurate due to the extension of the spectra to more than bandwidth of our power meter. However for the narrowest spectrum obtained from 100 m long PCF, the supercontinuum power was about 210 mW at the maximum launched power.

In a 10 km long NZ-DSF, the 20 dB bandwidth of 507 nm was observed for the SC spectrum in its anomalous pumping regime. In this case the spectral component appeared at 1064 nm does not play any role to expand SC spectrum towards shorter wavelengths.

Recently, dynamic spacing tuneability in multi-wavelength sources is highly desirable in many applications. The conventional schemes which rely on a single PMF segment do not have the potential to further improve due to limitation of of control elements.

In our work, nonlinear effects both through BEFL [57] and slicing of spectrum were used to generate multi-wavelength comb lines. Hence, a temperature sensitive loop mirror (TSLM) which consisted of a 3 dB coupler and two segments of PMFs was presented. In this setup, the segments were spliced at an offset rotation angle of 90°.

Compared to the conventional configurations, the proposed configuration provided greater temperature sensitivity in the spectral spacing detuning. It also conveniently allowed us to detune wavelengths in both positive and negative spectral spacing regimes. The details of this design have been reported in chapter six and the results of using TSLM as a back mirror of a resonator in the vicinity of 1037 nm have been published in [406].

The performance of two different combinations of the loop mirror, which were deliberately chosen in such a way that the same effective length was acquired, were observed and compared respectively. Hence, both combinations provided almost the same wavelength spacing of 1.74 nm at room temperature.

The experimental result shows that the combination with the longer segment lengths (L_1 and L_2) provides a larger spacing tuning range. In another word, the same tuning span can be achieved at lower temperature if longer PMF segments are used in the loop mirror. By changing the temperature of the PMF segments, the wavelength spacing with a combination of PMF lengths of 4.0 m and 2.5 m could be tuned from 1.69 nm to 4.35 nm.

Compared to the conventional schemes [62], the experimental results suggest that the TSLM can potentially achieve a substantial improvement (6.6 times more) in increasing spectral spacing variation range and a considerable increment (33.76%) in temperature sensitivity. Afterwards, by using proposed TSLM and SC slicing, a multi-wavelength source with a maximum average power of 20.7 dBm in the region of 1000-1750 nm was demonstrated. The output was observed stable at room temperature with an output power variance as low as 0.4 dB. An average value of more than 15 dB for signal to noise ratio of spectrum is obtained with this filter. The bigger number of lines is expected by further extension of SC bandwidth and longer PMF use in the experiment.

The more improvement in fabrication and reduction of device lengths, the further reduction in optical power requirements and improvement in channel flatness is feasible. In order to obtain a broader and smoother comb, a pulse shaper can be used before HNLF for smoothening the comb profile [408].

7.2 FUTURE WORKS

Current supercontinuum sources are typically based on PCFs or HNLF made of silica glass. However, the high losses of silica in the ultraviolet and mid-infrared ranges typically limit the bandwidth of the supercontinuum to visible and near-infrared wavelengths.

It has been observed that the UV intensity is enhanced when seed pulses are coupled into a higher-order transverse spatial mode of the Holey Fiber. A significant difference between the fundamental and higher order modes of the holey fiber is the dispersion property of higher mode. In particular, the higher order mode has a shorter ZDW. In order to make dispersion uniformly low across a broad range of wavelengths as well as trying to have a low total cumulative dispersion, the segments with different dispersion characteristics will need to be spliced together. We also hope to continue our research on developing supercontinuum with utilizing new tapered HNLFs with a ZDW decreasing along the fiber length, to extend the SC band towards the ultraviolet and mid-infrared regions.

For future work, the effect of polarization state of the pump on SC generation can be pursued. It can be done by defining the polarization state of pulse lasers at the front end of the fiber and altering the polarization state by means of wave plate polarizer. To this end, SCG with two orthogonal polarization states in a highly birefringent PCF will need to be also investigated, as it provides an extra degree of freedom to the tuning of the final spectral properties due to different spectral profiles and different dispersion characteristics of these states of polarization.

The SCG with enhanced unique properties such as better flatness, higher coherence, lower noise or fixed polarization can be generated for certain applications. Setting an objective as to design the best possible SC sources, each of aforementioned characteristics and properties can be compared in the PCF and highly-nonlinear fiber used in this thesis [411, 412].

Reports have also indicated that the FWM phase-matched by SPM as well as small anomalous dispersion in the presence of ASE are the causes for the loss of coherence in the fiber [413]. It is well known that coherence degradation in PCFs depends strongly on the input pulse wavelength. It is also believed that noise on ultra-short laser pulses injected into a HNLF behaves like a rogue optical wave. As a significant area of research in nonlinear optics, we can focus on systematic stimulation of these rogue optical waves by stimulated modulation instability.

On the other hands, it has been proven that the SC pulses generated with dispersion-flattened dispersion-decreasing fibers are more stable [414, 415]. It is also believed that shorter input pulses are required for generation of a broad SC with lower noise. Measurements in anomalous dispersion regime have also proven that the effect of modulation instability can be reduced by using much shorter pulses and shorter lengths [416, 417]. Therefore the study should also consider to reduce the length of the nonlinear fibers used or to replace them with other enhanced nonlinear fibers. On the other hand the nonlinearity can be enhanced with the use of a different class of fibers. Contrary to Bismuth based gain used in this thesis with a relatively low nonlinear coefficient of 58.3 $(W.km)^{-1}$, highly nonlinear bismuth-oxide fibers have been reported with a range of nonlinearity between 1100-5400 $(W.km)^{-1}$ in the normal dispersion regime. Given a non-tapered bismuth micro structured, the spectral broadening in a 2 cm length of these fibers is used to compress 150 fs pulses down to 25 fs [418].

The next step in this line of research would be continuum compression. Meanwhile the improvement of the coherence properties of supercontinuum will be analyzed using two-frequency cross-spectral density [28] and two-time mutual coherence functions [419]. To achieve pulse durations of less than 5 fs, a new compression technique based on continuum compression in hollow gas-filled fibers is suggested.

In addition to the peak power of the pump, the birefringence property of the fiber must also be taken into account in the generation of a SC spectrum with a lower requirement of the pump power. Moreover, the effect of difference between the pumping wavelength and the ZDW of the fiber on the amount of SC broadening should be investigated. It is believed that SCG provided by a visible pump near ZDW of fiber ensures more efficient SCG than conventional near IR pump. Hence mode locking in region of 1 μm can be offered by new class of bismuth doped fibers [420]. Therefore, a high brightness visible laser at region of 0.5 μm can be generated using SHG process to pump a HNLF.

Future developments will include full control over wavelength, temporal shape and phase of ultra-short pulses. This could include extending the tuning range of wavelengths based on the SSFS in an holey fiber amplifier seeded from our pulse width tunable oscillator [421]. We will continue to enhance our work in improving known techniques for pulse shortening and energy scaling [422]. There is quite a lot of interest in developing extremely stable and compact versions of the lasers without using any free space device. The efficiencies of the Bi-EDF laser can be improved by suppressing the up-conversion process through Lanthanum and Boron addition into the glass host. Furthermore, the slope efficiency and stability can be improved with the existence of advanced SA as both a dispersion compensator and an absorber element.

We did not seek to obtain shorter pulses from our cavity, but we believe that this is possible with further optimization of fiber length and overall dispersion compensation. In fact, the compensation of the third order dispersion (TOD) and higher order dispersions should be considered once the net GVD approached to zero and the pulse duration is desired to be further improved. The magnitude and the sign of the gain TOD may be suitable to perfectly or partially cancel the cavity TOD. To achieve anomalous dispersion, PCFs are produced with the small core sizes. This introduces a high nonlinear coefficient in PCFs and a challenge in the power scaling.The challenge in the power scaling resides in managing fiber nonlinearities to induce sufficient SPM for achieving efficient temporal compression. Hence, use of PCFs for intra-cavity dispersion compensation, imposes an upper limit on the achievable energy of the generated pulse.

However, photonic bandgap fibers (PBGs) provide a very low nonlinear coefficient. They can be spliced with low loss to standard fibers. As a consequence, the anomalous dispersion of the cavity can be managed simply by varying the length of the PBG. Dispersion in a PBG varies from highly normal (close to the short wavelength edge) to highly anomalous (near the long wavelength edge). At the same time, their spectral transmission bands can also be shifted by scaling the transverse dimensions of the fiber. In addition ZDW is possible at any wavelength in PBGs.

Further studies will also include the generation of short pulse using novel solid-core active microstructure media as both the gain medium and the dispersion compensator. Therefore, the possibility of solid-core photonic bandgap fibers for intracavity dispersion compensation, pulse stretching or external compression can be investigated.

We believe that with advancements in the fiber technology, further progress in the ultrafast fiber systems is expected. The use of PBGs is mostly desired to work with Bismuth doped fiber in wavelength region of 1 μm. It is hoped that, this thesis will make a contribution to the field of ultrafast optics.

APPENDIX

LIST OF PUBLICATIONS

A- ISI Journals

1. M. R. A. Moghaddam, S. Harun, S. Shahi, and H. Ahmad, "Broadband amplifier and high performance tunable laser with an extinction ratio of higher than 60 dB using bismuth oxide-based erbium-doped fiber," *Journal of Modern Optics* 59, 1106-1112 (2012).

2. M. R. A. Moghaddam, S. W. Harun, S. Shahi ,"Dual wavelength high power double-clad erbium/ytterbium-doped fiber laser," *Journal of Nonlinear Optical Physics and Materials* 20, 443-451 (2011).

3. M. R. A. Moghaddam, S. W. Harun, R. Parvizi, Z. Salleh, H. Arof, A. Lokman, and H. Ahmad, "Experimental and theoretical studies on ytterbium sensitized erbium-doped fiber amplifier," *Optik-International Journal for Light and Electron Optics* 122, 1783-1786 (2011).

4. M. R. A. Moghaddam, S. W. Harun, R. Akbari, and H. Ahmad, "Stable mode-locked fiber laser using 49 cm long bismuth oxide based erbium doped fiber and slow saturable absorber," *Laser physics* 21, 1-6 (2011).

5. M. R. A. Moghaddam, S. W. Harun, R. Akbari, and H. Ahmad, "Flatly broadened supercontinuum generation in nonlinear fibers using a mode locked bismuth oxide based erbium doped fiber laser," *Laser Physics Letters* 8, 369–375 (2011).

6. H. Ahmad, M. R. A Moghaddam, H. Arof, and S. W. Harun, "High output power, narrow linewidth Brillouin fibre laser master-oscillator/power-amplifier source," *Optoelectronics, IET* 5, 181-183 (2011).

7. K. S. LIM, M. R. A. Moghaddam, S. W. Harun, and H. AHMAD, "Tunable-Spacing Multi-wavelength Yb-Doped Fiber Laser (YDFL) Based on Temperature Sensitive Loop Mirror " *Lasers in Engineering* 20, 39-45 (2010).

8. S. Shahi, S. W. Harun, S. Norizan, M. R. A. Moghaddam, and H. Ahmad, "Brillouin-Raman Multi-Wavelength Laser Comb Generation Based on Bi-EDF by Using Dual-Wavelength in Dispersion Compensating Fiber," *Journal of Nonlinear Optical Physics and Materials* 19, 123-130 (2010).

9. M. R. A. Moghaddam, S. W. Harun, S. Shahi, K. Lim, and H. Ahmad, "Comparisons of multi-wavelength oscillations using Sagnac loop mirror and Mach-Zehnder interferometer for ytterbium doped fiber lasers," *Laser physics* 20, 516-521 (2010).

10. S. W. Harun, M. Paul, M. R. A. Moghaddam, S. Das, R. Sen, A. Dhar, M. Pal, S. Bhadra, and H. Ahmad, "Diode-pumped 1028 nm Ytterbium-doped fiber laser with near 90% slope efficiency," *Laser physics* 20, 656-660 (2010).

11. S. W. Harun, M. Paul, M. R. A. Moghaddam, S. Das, R. Sen, A. Dhar, M. Pal, S. Bhadra, and H. Ahmad, "Efficient diode pumped ytterbium-doped fibre laser," *Electronics Letters* 46, 68-69 (2010).

12. S. W. Harun, M. R. A. Moghaddam, and H. Ahmad, "High output power Erbium-Ytterbium doped cladding pumped fiber amplifier," *Laser physics* 20, 1899-1901 (2010).

13. S. W. Harun, M. R. A. Moghaddam, and H. Ahmad, "High output power Erbium-Ytterbium doped cladding pumped fiber amplifier," *Laser physics* 20, 1899-1901 (2010).

14. S. Shahi, M. R. A. Moghaddam, S. W. Harun, and H. Ahmad, "The Comparison Nonlinearity Behaviors of Photonic Crystal Fiber by Two Reduced Lengths of Bi-EDF in Ring Cavity," *Journal of Nonlinear Optical Physics and Materials* 18, 521-527 (2009).

15. M. Paul, S.W. Harun, M. R. A. Moghaddam, S. Das, R. Sen, A. Dhar, M. Pal, S. Bhadra, and H. Ahmad, "1028 nm single mode Ytterbium-doped fiber laser," *Laser physics* 19, 1021-1025 (2009).

16. M. R. A. Moghaddam, S. W. Harun, M. Tamjis, and H. Ahmad, "Double clad erbium/ytterbium doped fiber laser with a fiber Bragg grating," *Laser Physics Letters* 6, 586-589 (2009).

17. M. R. A. Moghaddam, S. W. Harun, M. Paul, M. Pal, A. Dhar, R. Sen, S. Das, S. Bhadra, and H. Ahmad, "Multiwavelength ytterbium doped fiber ring laser," *Microwave and Optical Technology Letters* 51, 2511-2512 (2009).

18. S. W. Harun, M. R. A. Moghaddam, K. Dimyati, and H. Ahmad, "The performance of double clad ytterbium doped fiber laser with different pumping wavelengths," *Laser Physics Letters* 6, 458-460 (2009).

B Conference Papers

1. M. R. A. Moghaddam, S. W. Harun, H. Ahmad, "Comparison between Analytical Solution and Experimental Setup of a Short Long Ytterbium Doped Fiber Laser," *Optics and Photonics Journal* 2, 65-72 (2012).

2. S. W.Harun, M. R. A. Moghaddam, H. Ahmad, " Supercontinuum generation using a mode locked picoseconds pulse laser," *Jurnal Fisika Dan Aplikasinya* 7, 110108-1 (2011).

3. M. R. A. Moghaddam, S. W. Harun, S. Shahi ,H. Ahmad, “Comparison between analytical solution and experimental setup of a short Yb doped fiber laser, “*5th Mathematics and Physical Sciences Graduate Congress, Faculty of Science* ,Chulalongkorn University, Bangkok, Thailand,7 – 9 December, (2009).

4. S. W. Harun, M. C. Paul, M. R. A. Moghaddam, S. Das, R. Sen , A. Dhar, M. Pal, S. K. Bhadra, H. Ahmad, “Diode-pumped ytterbium-doped fiber laser with near 90% slope efficiency, ”*18th International Laser Physics Workshop, LPHYS’09*, Barcelona, Spain, 13 – 17 July, (2009).

5. S. Shahi, S. W. Harun, K. S. Lim, R. Parvizi, M. R. A. Moghaddam and H. Ahmad, “Application Of Four-Wave Mixing For Determination Of Nonlinear Parameter Based On Bi-EDF, ” *5th Mathematics and Physical Sciences Graduate Congress, Faculty of Science* , Chulalongkorn University, Bangkok, Thailand, 7 – 9 December, (2009).

6. R. Parvizi, S. Shahi, X. S, Cheng , M. R. A. Moghaddam, S.W. Harun, H. Ahmad, E. Sadeghi , “ A blend of the sbs and four-wave mixing in bismuth based highly nonlinear fiber,” *5th Mathematics and Physical Sciences Graduate Congress, Faculty of Science,* Chulalongkorn University, Bangkok, Thailand, 7– 9 December ,(2009).

REFERENCES

1. L. Brillouin, "Diffusion de la lumière et des rayons X par un corps transparent homogène, influence de l'agitation thermique," *Ann. Phys* 17, 88-122 (1922).
2. M. N. Islam, Raman Amplifiers for Telecommunications: Sub-systems and systems (Springer, 2004).
3. M. Damzen, Stimulated brillouin scattering: fundamentals and applications (*Taylor & Francis, 2003*).
4. R. Mears, L. Reekie, I. Jauncey, and D. Payne, "Low-noise erbium-doped fibre amplifier operating at 1.54 m," *Electronics Letters* 23, 1026-1028 (1987).
5. M. P. Kalita, S. Yoo, and J. Sahu, "Bismuth doped fiber laser and study of unsaturable loss and pump induced absorption in laser performance," *Optics Express* 16, 21032-21038 (2008).
6. E. M. Dianov, "Bismuth-doped optical fibers: a challenging active medium for near-IR lasers and optical amplifiers," *Light: Science & Applications* 1, e12 (2012).
7. S. Harun, M. Paul, M. Moghaddam, S. Das, R. Sen, A. Dhar, M. Pal, S. Bhadra, and H. Ahmad, "Efficient diode pumped ytterbium-doped fibre laser," *Electronics Letters* 46, 68-69 (2010).
8. M. Paul, S. Harun, M. R. A. Moghaddam, S. Das, R. Sen, A. Dhar, M. Pal, S. Bhadra, and H. Ahmad, "1028 nm single mode Ytterbium-doped fiber laser," *Laser physics* 19, 1021-1025 (2009).
9. S. Harun, M. Paul, M. R. A. Moghaddam, S. Das, R. Sen, A. Dhar, M. Pal, S. Bhadra, and H. Ahmad, "Diode-pumped 1028 nm Ytterbium-doped fiber laser with near 90% slope efficiency," *Laser physics* 20, 656-660 (2010).
10. H. Po, J. Cao, B. Laliberte, R. Minns, R. Robinson, B. Rockney, R. Tricca, and Y. Zhang, "High power neodymium-doped single transverse mode fibre laser," *Electronics Letters* 29, 1500-1501 (1993).
11. L. Zenteno, "High-power double-clad fiber lasers," *Journal of Lightwave Technology,* 11, 1435-1446 (1993).
12. M. T. Asaki, C. P. Huang, D. Garvey, J. Zhou, H. C. Kapteyn, and M. M. Murnane, "Generation of 11-fs pulses from a self-mode-locked Ti: sapphire laser," *Optics letters* 18, 977-979 (1993).
13. M. Takahashi, R. Sugizaki, J. Hiroishi, M. Tadakuma, Y. Taniguchi, and T. Yagi, "Low-loss and low-dispersion-slope highly nonlinear fibers," *Journal of Lightwave Technology* 23, 3615 (2005).
14. R. Stolen, and C. Lin, "Self-phase-modulation in silica optical fibers," *Physical Review* A 17, 1448 (1978).
15. M. N. Islam, L. F. Mollenauer, R. H. Stolen, J. R. Simpson, and H. T. Shang, "Cross-phase modulation in optical fibers," *Optics letters* 12, 625-627 (1987).

16. A. Hasegawa, and F. Tappert, "Transmission of stationary nonlinear optical pulses in dispersive dielectric fibers. I. Anomalous dispersion," *Applied physics letters* 23, 142-144 (1973).

17. L. F. Mollenauer, R. H. Stolen, and J. P. Gordon, "Experimental observation of picosecond pulse narrowing and solitons in optical fibers," *Physical review letters* 45, 1095-1098 (1980).

18. L. Hargrove, R. Fork, and M. Pollack, "locking of he ne laser modes induced by synchronous intracavity modulation," *Applied physics letters* 5, 4-5 (1964).

19. K. Tamura, H. Haus, and E. Ippen, "Self-starting additive pulse mode-locked erbium fibre ring laser," *Electronics Letters* 28, 2226-2228 (1992).

20. Y. Sun, and A. Periasamy, "Fluorescence Microscopy Imaging in Biomedical Sciences," *Biomedical Optical Imaging Technologies*, 79-110 (2013).

21. A. Haboucha, W. Zhang, T. Li, M. Lours, A. Luiten, Y. L. Coq, and G. Santarelli, "An Optical Fibre Pulse Rate Multiplier for Ultra-low Phase-noise Signal Generation," *Arxiv preprint arXiv*:1106.5195 (2011).

22. R. R. Frontiera, and R. A. Mathies, "Femtosecond stimulated Raman spectroscopy," *Laser & Photonics Reviews* (2011).

23. D. J. Faber, and T. G. van Leeuwen, "Optical Coherence Tomography," Optical-Thermal Response of Laser-Irradiated Tissue, ISBN 978-90-481-8830-7. *Springer Science Business Media* BV, 2011, p. 713 1, 713 (2011).

24. S. Ishida, N. Nishizawa, T. Ohta, and K. Itoh, "Ultrahigh-Resolution Optical Coherence Tomography in 1.7 m Region with Fiber Laser Supercontinuum in Low-Water-Absorption Samples," *Applied Physics Express* 4, 052501 (2011).

25. C. Senel, F. O. Ilday, O. Kara, C. Birlikseven, C. Erdogan, and R. Hamid, "All-normal-dispersion fiber lasers for frequency metrology," *in CLEO:2011 - Laser Applications to Photonic Applications, OSA Technical Digest,* paper CFM2(Optical Society of America, 2011).

26. A. Arai, J. Xu, J. Sohn, and G. C. Cho, "Applications of Femtosecond Fiber Lasers in Material Processing," *in CLEO/Europe and EQEC 2011 Conference Digest,* paper TF1_1 (Optical Society of America, 2011).

27. R. Alfano, and S. Shapiro, "Emission in the region 4000 to 7000 Å via four-photon coupling in glass," *Physical review letters* 24, 584-587 (1970).

28. J. M. Dudley, G. Genty, and S. Coen, "Supercontinuum generation in photonic crystal fiber," *Reviews of modern physics* 78, 1135 (2006).

29. C. Lin, and R. Stolen, "New nanosecond continuum for excited state spectroscopy," *Applied physics letters* 28, 216-218 (1976).

30. L. Thevenaz, Advanced Fiber Optics Concepts And Technology (*EPFL Press, 2011*).

31. S. Roy, S. K. Bhadra, and G. P. Agrawal, "Dispersive wave generation in supercontinuum process inside nonlinear microstructured fibre," *Current science* 100, 321 (2011).

32. W. Reeves, D. Skryabin, F. Biancalana, J. Knight, P. S. J. Russell, F. Omenetto, A. Efimov, and A. Taylor, "Transformation and control of ultra-short pulses in dispersion-engineered photonic crystal fibres," *Nature* 424, 511-515 (2003).

33. O. Graydon, "Supercontinua: Broader than ever," *Nature Photonics* 6, 413-413 (2012).

34. S. Kaasalainen, T. Lindroos, and J. Hyyppa, "Toward hyperspectral lidar: Measurement of spectral backscatter intensity with a supercontinuum laser source," *Geoscience and Remote Sensing Letters,* IEEE 4, 211-215 (2007).

35. K. Kurokawa, T. Yamamoto, K. Tajima, A. Aratake, K. Suzuki, and T. Kurashima, "WDM transmission in 1.0µm band over PCF using supercontinuum source," *IEICE Electronics Express* 5, 395-399 (2008).

36. J. T. Gopinath, H. M. Shen, H. Sotobayashi, E. P. Ippen, T. Hasegawa, T. Nagashima, and N. Sugimoto, "Highly nonlinear bismuth-oxide fiber for supercontinuum generation and femtosecond pulse compression," *Journal of Lightwave Technology* 23, 3591 (2005).

37. T. Yasui, S. Yokoyama, H. Inaba, K. Minoshima, T. Nagatsuma, and T. Araki, "Terahertz frequency metrology based on frequency comb," *Selected Topics in Quantum Electronics*, IEEE Journal of, 1-11 (2011).

38. Y. G. Han, T. Tran, S. H. Kim, and S. B. Lee, "Multiwavelength Raman-fiber-laser-based long-distance remote sensor for simultaneous measurement of strain and temperature," *Optics letters* 30, 1282-1284 (2005).

39. A. During, C. Fossati, and M. Commandré, "Multiwavelength imaging of defects in ultraviolet optical materials," *Applied optics* 41, 3118-3126 (2002).

40. N. Awang, M. Zulkifli, A. Latif, S. Harun, and H. Ahmad, "Stable power multi-wavelength fibre laser based on four-wave mixing in a short length of highly non-linear fibre," *Journal of Optics* 13, 075401 (2011).

41. J. Zyskind, and A. Srivastava, Optically Amplified WDM Networks (*Academic Press, 2009*).

42. S. Yamashita, and K. Hotate, "Multiwavelength erbium-doped fibre laser using intracavity etalon and cooled by liquid nitrogen," *Electronics Letters* 32, 1298-1299 (1996).

43. O. Graydon, W. Loh, R. Laming, and L. Dong, "Triple-frequency operation of an Er-doped twincore fiber loop laser," *Photonics Technology Letters*, IEEE 8, 63-65 (1996).

44. R. Nagarajan, "Distributed Feedback Lasers," *Wiley Encyclopedia of Electrical and Electronics Engineering* (1999).

45. M. J. Connelly, Semiconductor optical amplifiers (*Springer Netherlands*, 2002).

46. N. Pleros, T. Houbavlis, G. Theophilopoulos, K. Vlachos, C. Bintjas, and H. Avramopoulos, "SOA-based multi-wavelength laser sources," *Fiber and integrated optics* 23, 263-274 (2004).

47. S. Shahi, S. Harun , S. Norizan, M. R. A. Moghaddam, and H. Ahmad, "Brillouin-Raman Multi-Wavelength Laser Comb Generation Based on Bi-EDF by Using Dual-Wavelength in Dispersion Compensating Fiber," *Journal of Nonlinear Optical Physics and Materials* 19, 123-130 (2010).

48. S. W. Harun S.Shahi, S.F.Norizan, M.R.A.Moghaddam and H.Ahmad, , "Brillouin/Raman Multi-Wavelength laser comb generation based on Bi-EDF by using dual-wavelength in dispersion compensating fiber," *Nonlinear optics and material journal (JNOPM)* 9, 123-130 (2010).

49. C. Yeh, C. Chow, Y. Wu, F. Shih, C. Wang, and S. Chi, "Multiwavelength erbium-doped fiber ring laser employing Fabry-Perot etalon inside cavity operating in room temperature," *Optical Fiber Technology* 15, 344-347 (2009).

50. D. Chen, S. Qin, and S. He, "Channel-spacing-tunable multi-wavelength fiber ring laser with hybrid Raman and Erbium-doped fiber gains," *Optics Express* 15, 930-935 (2007).

51. M. R. A. Moghaddam, S. Harun, S. Shahi, K. Lim, and H. Ahmad, "Comparisons of multi-wavelength oscillations using Sagnac loop mirror and Mach-Zehnder interferometer for ytterbium doped fiber lasers," *Laser physics* 20, 516-521 (2010).

52. D. M. Liang, X. F. Xu, Y. Li, J. H. Pei, Y. Jiang, Z. H. Kang, and J. Y. Gao, "Multiwavelength fiber laser based on a high birefringence fiber loop mirror," *Laser Physics Letters* 4, 57-60 (2007).

53. Y. Zhao, T. T. Song, and Q. Wang, "Recent Developments and Applications of Polarization-Maintaining Fiber Loop Mirrors,"*Instrumentation Science & Technology* 40, 239-261 (2012).

54. S. W. Harun. S. Shahi, K. S. Lim, R.Parvizi, M. R. A. Moghaddam and H. Ahmad,, "Application of four-wave mixing for determination of nonlinear parameter based on Bi-EDF," *in 5th Mathematics and Physical Sciences Graduate Congress* (Faculty of Science, Chulalongkorn University, Bangkok, Thailand 7–9 December ,2009).

55. K.S. Lim, M. R. A. Moghaddam,.S. W. Harun and H. Ahmad, "Tunable-spacing multi-wavelength Yb-doped fiber laser (YDFL) based on temperature sensitive loop mirror " *Lasers in Engineering* 20, 39-45 (2010).

56. M. R. A. Moghaddam,. S. Shahi, S. W. Harun and H. Ahmad " The comparison nonlinearity behaviors of photonic crystal fiber by two reduced lengths of Bi-EDF in ring cavity," *Journal of Nonlinear Optical Physics & Materials*, 18, 521-527 (2009.).

57. S. Shahi, S. W. Harun, S. Norizan, M. R. A. Moghaddam, and H. Ahmad, "Brillouin-Raman Multi-Wavelength Laser Comb Generation Based on Bi-EDF by Using Dual-Wavelength in Dispersion Compensating Fiber," *Journal of Nonlinear Optical Physics and Materials* 19, 123-130 (2010).

58. S. S. R. Parvizi, X.S, Cheng , M. R. A. Moghaddam, S.W. Harun, H.Ahmad, E .Sadeghi, "A blend of the SBS and four-wave mixing in bismuth based highly nonlinear fiber, "*in 5th Mathematics and Physical Sciences Graduate* Congress

(Faculty of Science ,Chulalongkorn University, Bangkok, Thailand 7 – 9 December ,2009).

59. M. R. A. Moghaddam, S. Harun, R. Akbari, and H. Ahmad, "Stable mode-locked fiber laser using 49 cm long bismuth oxide based erbium doped fiber and slow saturable absorber," *Laser physics* 21, 1-6 (2011).
60. M. Moghaddam, S. Harun, R. Akbari, and H. Ahmad, "Flatly broadened supercontinuum generation in nonlinear fibers using a mode locked bismuth oxide based erbium doped fiber laser," *Laser Physics Letters* (2011).
61. E. Desurvire, Erbium-doped fiber amplifiers: principles and applications (*Wiley New York,* 1994).
62. K. Lim, C. Pua, S. Harun, and H. Ahmad, "Temperature-sensitive dual-segment polarization maintaining fiber Sagnac loop mirror," *Optics & Laser Technology* 42, 377-381 (2010).
63. F. Träger, Springer handbook of lasers and optics (*Springer Verlag*, 2007).
64. G. P. Agrawal, Applications of nonlinear fiber optics (*Academic Press*, 2008).
65. M. Morin, and F. Trépanier, "Dispersion control for ultrafast optics," (*TeraXion Inc,* 2009),.
66. Y. R. Shen, "The principles of nonlinear optics," *New York, Wiley-Interscience,* 1984, 575 p. 1 (1984).
67. R. Stolen, J. Bjorkholm, and A. Ashkin, "Phase matched three wave mixing in silica fiber optical waveguides," *Applied physics letters* 24, 308-310 (1974).
68. R. Stolen, and J. Bjorkholm, "Parametric amplification and frequency conversion in optical fibers," *IEEE Journal of Quantum Electronics,* 18, 1062-1072 (1982).
69. R. Stolen, "Phase-matched-stimulated four-photon mixing in silica-fiber waveguides," *IEEE Journal of Quantum Electronics,* 11, 100-103 (1975).
70. R. W. Boyd, Nonlinear optics (Academic Pr, 2003).
71. Y. Jaouën, G. Canat, Y. Sikali Mamdem, R. Gabet, L. Lombard, and E. Burov, "Stimulated Brillouin scattering in specialty optical fibers: importance of material, structure and manufacturing parameters," *in CLEO: Science and Innovations CF3N*,Page CF3N.1 (Optical Society of America, 2012).
72. G. Agrawal, "Nonlinear fiber optics 4th Ed," *in Nonlinear Science at the Dawn of the 21st Century*(2007), pp. 195-211.
73. E. Ippen, and R. Stolen, "Stimulated Brillouin scattering in optical fibers," *Applied physics letters* 21, 539-541 (1972).
74. B. E. A. Saleh, and M. C. Teich, Fundamentals of photonics (*John Wiley & Sons,* 2007).
75. R. Ell, U. Morgner, F. KÃÂrtner, J. Fujimoto, E. Ippen, V. Scheuer, G. Angelow, T. Tschudi, M. Lederer, and A. Boiko, "Generation of 5-fs pulses and

octave-spanning spectra directly from a Ti: sapphire laser," *Optics letters* 26, 373-375 (2001).

76. D. Sutter, G. Steinmeyer, L. Gallmann, N. Matuschek, F. Morier-Genoud, U. Keller, V. Scheuer, G. Angelow, and T. Tschudi, "Semiconductor saturable-absorber mirror assisted Kerr-lens mode-locked Ti: sapphire laser producing pulses in the two-cycle regime," *Optics letters* 24, 631-633 (1999).

77. O. Pronin, J. Brons, C. Grasse, V. Pervak, G. Boehm, M. C. Amann, A. Apolonski, V. Kalashnikov, and F. Krausz, "High-power Kerr-lens mode-locked Yb: YAG thin-disk oscillator in the positive dispersion regime," *Optics letters* 37, 3543-3545 (2012).

78. G. Cerullo, S. D. Silvestri, and V. Magni, "Self-starting Kerr-lens mode locking of a Ti: sapphire laser," *Optics letters* 19, 1040-1042 (1994).

79. D. Richardson, R. Laming, D. Payne, M. Phillips, and V. Matsas, "320 fs soliton generation with passively mode-locked erbium fibre laser," *Electronics Letters* 27, 730-732 (1991).

80. M. Bass, and E. W. Van Stryland, Fiber Optics Handbook: fiber, devices, and systems for optical communications (*McGraw-Hill Professional,* 2002).

81. L. Mollenauer, J. Gordon, and P. Mamyshev, "Solitons in high bit-rate, long-distance transmission," *Optical Fiber Telecommunications IIIA*, 373–460 (1997).

82. C. McKinstrie, C. Xie, and C. Xu, "Effects of cross-phase modulation on phase jitter in soliton systems with constant dispersion," *Optics letters* 28, 604-606 (2003).

83. A. Zheltikov, A. L'Huillier, and F. Krausz, "Nonlinear Optics," *Springer Handbook of Lasers and Optics*, 161-251 (2012).

84. J. Yu, X. Zheng, C. Peucheret, A. T. Clausen, H. N. Poulsen, and P. Jeppesen, "40-Gb/s all-optical wavelength conversion based on a nonlinear optical loop mirror," *Journal of Lightwave Technology* 18, 1001 (2000).

85. A. Lamminpää, "Measurement of nonlinearity of optical fiber," Helsinki university of technology, *Master thesis*, 17th of July (2003).

86. M. Asobe, T. Kanamori, and K. Kubodera, "Applications of highly nonlinear chalcogenide glass fibers in ultrafast all-optical switches," *IEEE Journal of Quantum Electronics,* 29, 2325-2333 (1993).

87. R. Billington, "A Report of Four-Wave Mixing in Optical Fibre and its Metrological Applications," *NPL Report COEM* 24 (1999).

88. J. Armstrong, N. Bloembergen, J. Ducuing, and P. Pershan, "Interactions between light waves in a nonlinear dielectric," *Physical Review* 127, 1918 (1962).

89. M. Schubert, and B. Wilhelmi, "Nonlinear optics and quantum electronics," (1986).

90. P. N. Butcher, and D. Cotter, The elements of nonlinear optics (*Cambridge Univ Pr, 1991).*

91. S. P. Singh, and N. Singh, "Nonlinear effects in optical fibers: Origin, management and applications," *Progress In Electromagnetics Research* 73, 249-275 (2007).

92. C. Wei, M. Zhou, Z. Hui-Juan, and L. Hong, "Numerical simulation of four-wave mixing efficiency and its induced relative intensity noise," *Chinese Physics B* 21, 067802 (2012).

93. J. E. Sharping, M. Fiorentino, A. Coker, P. Kumar, and R. S. Windeler, "Four-wave mixing in microstructure fiber," *Optics letters* 26, 1048-1050 (2001).

94. R. Tkach, A. Chraplyvy, F. Forghieri, A. Gnauck, and R. Derosier, "Four-photon mixing and high-speed WDM systems," *Journal of* Lightwave *Technology,* 13, 841-849 (1995).

95. T. Hasegawa, T. Nagashima, and N. Sugimoto, "Determination of nonlinear coefficient and group-velocity-dispersion of bismuth-based high nonlinear optical fiber by four-wave-mixing," *Optics Communications* 281, 782-787 (2008).

96. M. P. Nikodem, W. Zurawski, and K. M. Abramski, "Four-wave mixing in non-zero dispersion shifted fibers," *in Transparent Optical Networks, 10th Anniversary International Conference on* (*IEEE*), 342-345 (2008).

97. D. K. Mynbaev, and L. L. Scheiner, Fiber-optic communications technology (*Prentice Hall Upper Saddle River,* NJ, 2001).

98. M. P. Nikodem, W. Zurawski, and K. M. Abramski, "Four-wave mixing in non-zero dispersion shifted fibers," (IEEE), pp. 342-345.

99. O. Aso, M. Tadakuma, and S. Namiki, "Four-wave mixing in optical fibers and its applications," *Furukawa Review,* 19, dEp 1, 2 (2000).

100. J. E. Sharping, M. Fiorentino, P. Kumar, and R. S. Windeler, "Optical parametric oscillator based on four-wave mixing in microstructure fiber," *Optics letters* 27, 1675-1677 (2002).

101. M. Shirazi, N. Shahabuddin, S. Aziz, K. Thambiratnam, S. Harun, and H. Ahmad, "A linear cavity Brillouin fiber laser with multiple wavelengths output," *Laser Physics Letters* 5, 361-363 (2008).

102. K. Inoue, and H. Toba, "Wavelength conversion experiment using fiber four-wave mixing," *Photonics Technology Letters, IEEE* 4, 69-72 (1992).

103. C. Dorman, I. Kucukkara, and J. Marangos, "Measurement of high conversion efficiency to 123.6-nm radiation in a four-wave-mixing scheme enhanced by electromagnetically induced transparency," *Physical Review A* 61, 013802 *(1999).*

104. J. E. Sharping, M. Fiorentino, P. Kumar, and R. S. Windeler, "Optical parametric oscillator based on four-wave mixing in microstructure fiber," *Optics letters* 27, 1675-1677 (2002).

105. W. Belardi, J. Lee, K. Furusawa, Z. Yusoff, P. Petropoulos, M. Ibsen, T. Monro, and D. Richardson, “A 10 Gbit/s tunable wavelength converter based on four-wave mixing in highly nonlinear holey fiber,” *ECOC, PD1.2, Copenhagen, Denmark* (2002).

106. O. Aso, S. Arai, T. Yagi, M. Tadakuma, Y. Suzuki, and S. Namiki, "Broadband four-wave mixing generation in short optical fibres," *Electronics Letters* 36, 709-711 (2000).

107. R. Smith, "Optical power handling capacity of low loss optical fibers as determined by stimulated Raman and Brillouin scattering," *Applied optics* 11, 2489-2494 (1972).

108. C. Headley, Raman amplification in fiber optical communication systems (*Academic press,* 2005).

109. F. Galeener, A. Leadbetter, and M. Stringfellow, "Comparison of the neutron, Raman, and infrared vibrational spectra of vitreous SiO_2, GeO_2, and BeF_2," *Physical Review B* 27, 1052 (1983).

110. K. J. Blow, and D. Wood, "Theoretical description of transient stimulated Raman scattering in optical fibers," *IEEE Journal of Quantum Electronics,* 25, 2665-2673 (1989).

111. R. H. Stolen, J. P. Gordon, W. Tomlinson, and H. A. Haus, "Raman response function of silica-core fibers," *JOSA B 6,* 1159-1166 (1989).

112. M. F. S. Ferreira, Nonlinear effects in optical fibers (Wiley-OSA, 2011).

113. S. Namiki, and Y. Emori, "Ultrabroad-band Raman amplifiers pumped and gain-equalized by wavelength-division-multiplexed high-power laser diodes," *IEEE Journal of Selected Topics in Quantum Electronics*, 7, 3-16 (2001).

114. R. G. Smith, "Optical power handling capacity of low loss optical fibers as determined by stimulated Raman and Brillouin scattering," *Applied Optics* 11, 2489 (1972).

115. C. De Matos, K. Hansen, and J. Taylor, "Experimental characterisation of Raman gain efficiency of holey fibre," Electronics Letters 39, 424-425 (2003).

116. J. P. Gordon, "Theory of the soliton self-frequency shift," *Optics letters* 11, 662-664 (1986).

117. M. Nikles, L. Thevenaz, and P. A. Robert, "Brillouin gain spectrum characterization in single-mode optical fibers," *Journal of Lightwave Technology,* 15, 1842-1851 (1997).

118. D. Cotter, "Stimulated Brillouin scattering in monomode optical fiber," *Journal of Optical Communications* 4, 10-19 (1983).

119. M. Suzuki, and N. Edagawa, "Dispersion-managed high-capacity ultra-long-haul transmission," *Journal of Lightwave Technology* 21, 916 (2003).

120. G. P. Agrawal, "Signal propagation in fibers," *Light wave technology telecommunication systems, A JOHN WILEY & SONS, Inc,* 66-*104* (2005).

121. Z. Fang, K. Chin, R. Qu, and H. Cai, Fundamentals of Optical Fiber Sensors (*Wiley,* 2012).

122. J. C. Palais, Fiber optic communications (*Prentice Hall,* 1988).

123. A. Debut, S. Randoux, and J. Zemmouri, "Linewidth narrowing in Brillouin lasers: Theoretical analysis," *Physical Review A* 62, 023803 (2000).

124. Y. Aoki, K. Tajima, and I. Mito, "Input power limits of single-mode optical fibers due to stimulated Brillouin scattering in optical communication systems," *Journal of Light wave Technology,* 6, 710-719 (1988).

125. S. Le Floch, and P. Cambon, "Theoretical evaluation of the Brillouin threshold and the steady-state Brillouin equations in standard single-mode optical fibers," *JOSA A* 20, 1132-1137 (2003).

126. F. Zarinetchi, S. Smith, and S. Ezekiel, "Stimulated Brillouin fiber-optic laser gyroscope," *Optics letters* 16, 229-231 (1991).

127. P. Bayvel, and I. Giles, "Evaluation of performance parameters of single-mode all-fiber Brillouin ring lasers," *Optics letters* 14, 581-583 (1989).

128. S. Smith, F. Zarinetchi, and S. Ezekiel, "Narrow-linewidth stimulated Brillouin fiber laser and applications," *Optics letters* 16, 393-395 (1991).

129. M. Shirazi, S. Harun, M. Biglary, and H. Ahmad, "Linear cavity Brillouin fiber laser with improved characteristics," *Optics letters* 33, 770-772 (2008).

130. D. Culverhouse, F. Farahi, C. Pannell, and D. Jackson, "Potential of stimulated Brillouin scattering as sensing mechanism for distributed temperature sensors," *Electronics Letters* 25, 913-915 (1989).

131. J. Satsuma, and N. Yajima, "B. Initial Value Problems of One-Dimensional Self-Modulation of Nonlinear Waves in Dispersive Media," *Progress of Theoretical Physics Supplement* 55, 284-306 (1974).

132. K. Tajima, "Compensation of soliton broadening in nonlinear optical fibers with loss," Optics letters 12, 54-56 (1987).

133. J. P. Gordon, and L. F. Mollenauer, "Effects of fiber nonlinearities and amplifier spacing on ultra-long distance transmission," *Lightwave Technology, Journal of* 9, 170-173 (1991).

134. J. P. Gordon, "Dispersive perturbations of solitons of the nonlinear Schrödinger equation," *JOSA B* 9, 91-97 (1992).

135. W. Hodel, and H. P. Weber, "Decay of femtosecond higher-order solitons in an optical fiber induced by Raman self-pumping," *Optics letters* 12, 924-926 (1987).

136. J. Lucek, and K. Blow, "Soliton-self-frequency shift in telecommunications fiber," *Physical review. A* 45, 6666-6674 (1992).

137. K. Porsezian, and K. Nakkeeran, "Optical solitons in presence of Kerr dispersion and self-frequency shift," *Physical review letters* 76, 3955-3958 (1996).

138. J. P. Gordon, and H. A. Haus, "Random walk of coherently amplified solitons in optical fiber transmission," *Optics letters* 11, 665-667 (1986).

139. J. Bromage, K. Rottwitt, and M. Lines, "A method to predict the Raman gain spectra of germanosilicate fibers with arbitrary index profiles," *Photonics Technology Letters, IEEE* 14, 24-26 (2002).

140. D. Hollenbeck, and C. D. Cantrell, "Multiple-vibrational-mode model for fiber-optic Raman gain spectrum and response function," *JOSA B* 19, 2886-2892 (2002).

141. Q. Lin, "Polarization and fiber nonlinearities," *Doctoral dissertation, University of Rochester*(2006).

142. R. Sinha, and S. K. Varshney, "Dispersion properties of photonic crystal fibers," *Microwave and Optical Technology Letters* 37, 129-132 (2003).

143. T. Birks, J. Knight, and P. S. J. Russell, "Endlessly single-mode photonic crystal fiber," *Optics letters* 22, 961-963 (1997).

144. G. Genty, M. Lehtonen, H. Ludvigsen, J. Broeng, and M. Kaivola, "Spectral broadening of femtosecond pulses into continuum radiation in microstructured fibers," *Optics Express* 10, 1083-1098 (2002).

145. M. Nielsen, C. Jacobsen, N. Mortensen, J. Folkenberg, and H. Simonsen, "Low-loss photonic crystal fibers for transmission systems and their dispersion properties," *Optics Express* 12, 1372-1376 (2004).

146. P. Russell, "Photonic crystal fibers," Science 299, 358 (2003).

147. S. Fang, K. Yamane, J. Zhu, C. Zhou, Z. Zhang, and M. Yamashita, "Generation of Sub-900uJ Supercontinuum with A Two-Octave Bandwidth Based on Induced Phase Modulation in Argon-Filled Hollow Fiber," *Photonics Technology Letters, IEEE,* 1-1 (2011).

148. J. Knight, J. Broeng, T. Birks, and P. S. J. Russell, "Photonic band gap guidance in optical fibers," *Science* 282, 1476 (1998).

149. P. S. J. Russell, "Photonic-crystal fibers," *Journal of Lightwave Technology,* 24, 4729-4749 (2006).

150. J. C. Baggett, T. M. Monro, K. Furusawa, and D. J. Richardson, "Comparative study of large-mode holey and conventional fibers," *Optics letters* 26, 1045-1047 (2001).

151. V. Finazzi, T. M. Monro, and D. J. Richardson, "Small-core silica holey fibers: nonlinearity and confinement loss trade-offs," *JOSA B* 20, 1427-1436 (2003).

152. Z. De-Sheng, S. Qiu-Qin, and D. Xiao-Yi, "Properties of Zero Dispersion Wavelengths in Silica Strands and Photonic Crystal Fibres," *Chinese Physics Letters* 25, 993 (2008).

153. J. Knight, J. Arriaga, T. Birks, A. Ortigosa-Blanch, W. Wadsworth, and P. S. J. Russell, "Anomalous dispersion in photonic crystal fiber," *Photonics Technology Letters, IEEE* 12, 807-809 (2000).

154. Y. S. Kivshar, and G. P. Agrawal, Optical solitons: from fibers to photonic crystals (*Academic Pr,* 2003).

155. T. Okuno, M. Onishi, T. Kashiwada, S. Ishikawa, and M. Nishimura, "Silica-based functional fibers with enhanced nonlinearity and their applications," *IEEE Journal of Selected Topics in Quantum Electronics,* 5, 1385-1391 (1999).

156. R. Buczynski, D. Pysz, T. Martynkien, D. Lorenc, I. Kujawa, T. Nasilowski, F. Berghmans, H. Thienpont, and R. Stepien, "Ultra flat supercontinuum generation in silicate dual core microstructured fiber," *Laser Physics Letters* 6, 575-581 (2009).

157. Y. Peiguang, W. Huifeng, R. Shuangchen, Z. Junqing, Z. Jian, S. Jie, and L. Jie, "Fabrication of a 145-m long microstructured optical fiber taper and its supercontinuum generation," *Optical Engineering* 50, 105003 (2011).

158. A. Husakou, and J. Herrmann, "Supercontinuum generation of higher-order solitons by fission in photonic crystal fibers," *Physical review letters* 87, 203901 (2001).

159. G. Genty, M. Lehtonen, and H. Ludvigsen, "Effect of cross-phase modulation on supercontinuum generated in microstructured fibers with sub-30 fs pulses," *Optics Express* 12, 4614-4624 (2004).

160. X. Liu, C. Xu, W. Knox, J. Chandalia, B. Eggleton, S. Kosinski, and R. Windeler, "Soliton self-frequency shift in a short tapered air–silica microstructure fiber," *Optics letters* 26, 358-360 (2001).

161. J. M. Dudley, and S. Coen, "Numerical simulations and coherence properties of supercontinuum generation in photonic crystal and tapered optical fibers," *IEEE Journal of Selected Topics in Quantum Electronics,* 8, 651-659 (2002).

162. J. M. Dudley, L. Provino, N. Grossard, H. Maillotte, R. S. Windeler, B. J. Eggleton, and S. Coen, "Supercontinuum generation in air–silica microstructured fibers with nanosecond and femtosecond pulse pumping," *JOSA B* 19, 765-771 (2002).

163. N. Nishizawa, Y. Ito, and T. Goto, "0.78-0.90- m wavelength-tunable femtosecond soliton pulse generation using photonic crystal fiber," *Photonics Technology Letters, IEEE* 14, 986-988 (2002).

164. K. Sakamaki, M. Nakao, M. Naganuma, and M. Izutsu, "Soliton induced supercontinuum generation in photonic crystal fiber," *IEEE Journal of Selected Topics in Quantum Electronics,* 10, 876-884 (2004).

165. M. Lehtonen, G. Genty, H. Ludvigsen, and M. Kaivola, "Supercontinuum generation in a highly birefringent microstructured fiber," *Applied physics letters* 82, 2197 (2003).

166. K. P. Hansen, J. J. Larsen, J. R. Jensen, S. Keiding, J. Broeng, H. R. Simonsen, and A. Bjarklev, "Super continuum generation at 800 nm in highly nonlinear photonic crystal fibers with normal dispersion," *in Lasers and Electro-Optics Society, 2001. LEOS 2001. The 14th Annual Meeting of the IEEE* (*IEEE, 2001), pp. 703-704.*

167. Y. Takushima, F. Futami, and K. Kikuchi, "Generation of over 140-nm-wide super-continuum from a normal dispersion fiber by using a mode-locked semiconductor laser source," *Photonics Technology Letters, IEEE* 10, 1560-1562 (1998).

168. A. V. Husakou, and J. Herrmann, "Supercontinuum generation, four-wave mixing, and fission of higher-order solitons in photonic-crystal fibers," *JOSA B* 19, 2171-2182 (2002).

169. K. P. Hansen,"Pumping wavelength dependence of super continuum generation in photonic crystal fibers," in Optical Fiber Communication Conference and Exhibit, 2002. OFC 2002(IEEE, 2002), pp. 622-624.

170. S. Coen, A. H. L. Chau, R. Leonhardt, J. D. Harvey, J. C. Knight, W. J. Wadsworth, and P. S. J. Russell, "Supercontinuum generation by stimulated Raman scattering and parametric four-wave mixing in photonic crystal fibers," JOSA *B* 19, 753-764 (2002).

171. P. Horak, K. K. Chen, S. Alam, S. Dasgupta, and D. J. Richardson, "High-Power Supercontinuum generation with picosecond pulses," *in Transparent Optical Networks (ICTON), 2010 12th International Conference on* (*IEEE*, 2010), pp. 1-4.

172. S. Chernikov, Y. Zhu, J. Taylor, and V. Gapontsev, "Supercontinuum self-Q-switched ytterbium fiber laser," *Optics letters* 22, 298-300 (1997).

173. M. Yamada, "Overview of Wideband Optical Fiber Amplification Technologies," *NTT Technical Review* 2, 34 (2004).

174. C. J. Koester, and E. Snitzer, "Amplification in a fiber laser," *Applied optics* 3, 1182-1186 (1964).

175. J. Zhang, Y. Luo, Z. M. Sathi, N. Azadpeyma, and G. D. Peng, "Test of spectral emission and absorption characteristics of active optical fibers by direct side pumping," *Optics Express* 20, 20623-20628 (2012).

176. A. Kenyon, "Erbium in silicon," *Semiconductor science and technology* 20, R65 (2005).

177. H. Shalibeik, Rare-Earth-Doped Fiber Lasers and Amplifiers (*Cuvillier Verlag,* 2007).

178. R. Hui, and M. S. O'Sullivan, Fiber optic measurement techniques (*Academic Press,* 2009).

179. K. Rottwitt, "Fibre Amplifiers," *Fibre Optic Communication* 161, 473-509 (2012).

180. E. Desurvire, M. Zirngibl, H. Presby, and D. DiGiovanni, "Characterization and modeling of amplified spontaneous emission in unsaturated erbium-doped fiber amplifiers," *Photonics Technology Letters, IEEE* 3, 127-129 (1991).

181. D. Derickson, "Fiber optic test and measurement," (*Prentice Hall PTR,* 1998), p. 642.

182. C. R. Giles, and E. Desurvire, "Modeling erbium-doped fiber amplifiers," *Journal of Lightwave Technology* 9, 271-283 (1991).

183. E. B. Desurvire, "Capacity demand and technology challenges for lightwave systems in the next two decades," *Journal of Lightwave Technology* 24, 4697-4710 (2006).

184. A. Bjarklev, Optical fiber amplifiers: design and system applications (*Artech House,* 1993).

185. D. McCumber, "Theory of phonon-terminated optical masers," *Phys. Rev* 134, A299-A306 (1964).

186. N. Sugimoto, "Optical amplifier materials," *Current Opinion in Solid State and Materials Science*, 5, 471-473 (2001).

187. P. Myslinski, D. Nguyen, and J. Chrostowski, "Effects of concentration on the performance of erbium-doped fiber amplifiers," *Lightwave Technology, Journal of* 15, 112-120 (1997).

188. P. Myslinski, C. Szubert, A. J. Bruce, D. J. DiGiovanni, and B. Palsdottir, "Performance of high-concentration erbium-doped fiber amplifiers," *Photonics Technology Letters, IEEE* 11, 973-975 (1999).

189. Y. Kondo, T. Nagashima, S. Takenobu, N. Sugimoto, S. Ito, S. Tanabe, and T. Hanada, "Fabrication of Bi_2O_3-based Er-doped waveguide for integrated optical amplifiers," i*n Optical Fiber Communication Confe. and Exhibit. (OFC)* (*Optical Society of America,* 2002), p. 17.

190. E. Desurvire, J. L. Zyskind, and C. R. Giles, "Design optimization for efficient erbium-doped fiber amplifiers," *Journal of Lightwave Technology,* 8, 1730-1741 (1990).

191. P. Myslinski, J. Fraser, and J. Chrostowski, "Nanosecond kinetics of upconversion process in EDF and its effect on EDFA performance," *Technical Digest Series-Optical Society of America* 18, 100-100 (1995).

192. Y. Fu, K. Zheng, W. Jian, and S. Jian, "Performance of optical amplifier employing silica host magnesium-aluminum-germanium co-doped erbium-doped fiber," *Chinese Optics Letters* 3, 187-189 (2005).

193. B. J. Ainslie, "A review of the fabrication and properties of erbium-doped fibers for optical amplifiers," *Lightwave Technology, Journal of* 9, 220-227 (1991).

194. S. Tammela, "Direct nanoparticle deposition process for manufacturing very short high gain Er-doped silica glass fibers," *in Optical Communication, 2002. ECOC 2002. 28th European Conference on*(IEEE, 2002), pp. 1-2.

195. S. Tammela, "The potential of direct nanoparticle deposition for the next generation of optical fibers," *in Proceedings of SPIE Photonics West* (2006), p. 16.

196. H. Ahmad, S. Shahi, and S. Harun, "Bismuth-based erbium-doped fiber as a gain medium for L-band amplification and Brillouin fiber laser," *Laser physics* 20, 716-719 (2010).

197. C. Jiang, W. Hu, and Q. Zeng, "Improved gain characteristics of high concentration erbium-doped phosphate fiber amplifier," *Photonics Technology Letters, IEEE* 16, 774-776 (2004).

198. D. Shi-Xun, X. Tie-Feng, N. Qiu-Hua, S. Xiang, and W. Xun-Si, "Concentration Quenching in Erbium Doped Bismuth Silicate Glasses," *Chinese Physics Letters* 23, 1923 (2006).

199. Y. Ohishi, A. Mori, M. Yamada, H. Ono, Y. Nishida, and K. Oikawa, "Gain characteristics of tellurite-based erbium-doped fiber amplifiers for 1.5-μm broadband amplification," *Optics letters* 23, 274-276 (1998).

200. L. Zhang, N. K. Chen, and L. Hu, "High Er^{3+} concentration low refractive index fluorophosphate glass for evanescent wave optical amplifiers," *Physica B: Condensed Matter* 403, 3470-3472 (2008).

201. S. Shahi, S. Harun, and H. Ahmad, "Multi wavelength Brillouin fiber laser using a holey fiber and a bismuth oxide based erbium doped fiber," *Laser Physics Letters* 6, 454-457 (2009).

202. S. Harun, S. Shahi, and H. Ahmad, "Brillouin fiber laser with a 49 cm long Bismuth based erbium doped fiber," *Laser Physics Letters* 7, 60-62 (2010).

203. H. Ahmad, R. Parvizi, K. Dimyati, M. Tamjis, and S. Harun, "FWM-based multi-wavelength erbium-doped fiber laser using Bi-EDF," *Laser physics* 20, 1414-1417 (2010).

204. P. Becker, "Thermal and optical properties of glasses of the system Bi_2O_3–B_2O_3," *Crystal Research and Technology* 38, 74-82 (2003).

205. E. M. Dianov, "Bismuth-doped optical fibers: a challenging active medium for near-IR lasers and optical amplifiers," *Light: Science & Applications* 1, e12 (2012).

206. H. Yang, H. Lin, L. Lin, Y. Zhang, B. Zhai, and E. Pun, "Powerful visible upconversion fluorescence of Er^{3+} in novel bismuth gallate glasses compared with in common tellurite glasses," *Journal of Alloys and Compounds* 453, 493-498 (2008).

207. G. Jose, P. Nandi, S. Shen, J. Zhang, and A. Jha, "Novel Glass Hosts for Integrated Planar Amplifiers in the Optical Communication Window (1200-1700 nm)," *in International Conference on Transparent optical Networks*(*ICTON*)(*IEEE,* 2007), pp. 284-287.

208. Y. Kondo, T. Nagashima, S. Takenobu, N. Sugimoto, and S. Ito, "Fabrication of Bi_2O_3-based Er-doped waveguide for integrated optical amplifiers," *in Optical Fiber Communication Confe. And Exhibit.* (*IEEE,* 2002), pp. 11-12.

209. S. Firstov, I. Bufetov, V. Khopin, A. Shubin, A. Smirnov, L. Iskhakova, N. Vechkanov, A. Guryanov, and E. Dianov, "2 W bismuth doped fiber lasers in the wavelength range 1300–1500 nm and variation of Bi doped fiber parameters with core composition," *Laser Physics Letters* 6, 665-670 (2009).

210. S. Xu, Z. Yang, S. Dai, J. Yang, L. Hu, and Z. Jiang, "Spectral properties and thermal stability of Er^{3+}-doped oxyfluoride silicate glasses for broadband optical amplifier," *Journal of Alloys and Compounds* 361, 313-319 (2003).

211. S. Xu, Z. Yang, S. Dai, G. Wang, L. Hu, and Z. Jiang, "Effect of Bi_2O_3 on spectroscopic properties of Er^{3+}-doped lead oxyfluorosilicate glasses for broadband optical amplifiers," *Journal of non-crystalline solids* 347, 197-203 (2004).

212. H. Hayashi, S. Ohara, N. Sugimoto, and S. Tanabe, "Effects of lanthanum and boron addition on suppression of cooperative upconversion in bismuth oxide-based erbium-doped fibers," *Japanese journal of applied physics* 46, 3452-3454 (2007).

213. N. Sugimoto, "Erbium doped fiber and highly non-linear fiber based on bismuth oxide glasses," *Journal of non-crystalline solids* 354, 1205-1210 (2008).

214. J. Yang, S. Dai, N. Dai, S. Xu, L. Wen, L. Hu, and Z. Jiang, "Effect of Bi_2O_3 on the spectroscopic properties of Erbium-Doped Bismuth Silicate Glasses," *JOSA B* 20, 810-815 (2003).

215. K. Taira, K. Kikuchi, N. Sugimoto, "Dispersion and pulse amplification characteristics of Bismuth oxide-based Erbium doped fiber amplifiers'," *in Proc. Optical Amplifiers and Applications Conference* (*OAA* 2002) (*Vancouver*, July 2002), p. Paper OTuC2

216. M. W. Jung, J. H. Shin, Y. M. Jhon, and J. H. Lee, "A Theoretical and Experimental Investigation into Pair-induced Quenching in Bismuth Oxide-based Erbium-doped Fiber Amplifiers," *Journal of the Optical Society of Korea* 14, 298-304 (2010).

217. K. Aiso, Y. Tashiro, T. Suzuki, and T. Yagi, "Erbium Lanthanum co-doped fiber for L-band amplifier with high efficiency, low non-linearity and low NF," *in Optical Fibre Communication Conference and Exhibition*(*OFC* 2001)(*IEEE,* 2001), pp. TuA6-1-TuA6-3

218. N. Sugimoto, T. Nagashima, T. Hasegawa, S. Ohara, K. Taira, and K. Kikuchi, "Bismuth-based optical fiber with nonlinear coefficient of 1360 W-1km-1," *in Optical Fiber Communication Conference* (*OFC*)(*Optical Society of America*, Los Angeles, California , USA, 2004).

219. J. C. G. Bünzli, and V. K. Pecharsky, Handbook on the Physics and Chemistry of Rare Earths (*Elsevier Science*, 2012).

220. J. Yang, S. Dai, Y. Zhou, L. Wen, L. Hu, and Z. Jiang, "Spectroscopic properties and thermal stability of erbium-doped bismuth-based glass for optical amplifier," *Journal of applied physics* 93, 977-983 (2003).

221. N. Sugimoto, T. Hasegawa, T. Nagashima, and S. Ohara, "Bi-based fibers for amplifiers and nonlinear applications," *in LEOS Summer Topical Meetings*(*IEEE, Quebec City, Que.* , 2006), pp. 46-47.

222. H. Sotobayashi, J. T. Gopinath, Y. Takushima, K. Hsu, and E. P. Ippen, "Broad-band wavelength-tunable, single frequency, and single polarization

bismuth oxide-based erbium-doped fiber laser," *Photonics Technology Letters*, IEEE 16, 1628-1630 (2004).

223. K. Kikuchi, and K. Taira, "Highly nonlinear bismuth oxide-based glass fibres for all-optical signal processing," *Electronics Letters* 38, 166-167 (2002).

224. N. Sugimoto, "Recent progress in Bi-EDF technologies," *in Optical Fiber Communication Conference* (Anaheim, California, March 6, 2005), p. OWF6.

225. S. Ohara, N. Sugimoto, K. Ochiai, H. Hayashi, Y. Fukasawa, T. Hirose, T. Nagashima, and M. Reyes, "Ultra-wideband amplifiers based on Bi_2O_3-EDFAs," *Optical Fiber Technology* 10, 283-295 (2004).

226. H. Kitano, A. Tokuhisa, M. Doi, and S. Owa, "Measurements of the Nonlinear Refractive Index of an Er^{3+}-Doped B_2O_3-Based Glass Fiber," *Japanese Journal Of Applied Physics Part 2* Letters 40, 955-957 (2001).

227. S. W. Haurn. S. Shahi, K.S. Lim, R.Parvizi, M.R.A.Moghaddam and H. Ahmad,, "Application of Four-Wave Mixing for Determination of Nonlinear Parameter Based On Bi-EDF," *in 5th Mathematics and Physical Sciences Graduate Congress* (Chulalongkorn University, Bangkok, Thailand, 7–9 December ,2009).

228. O. Lumholt, J. H. Povlsen, K. Schusler, A. Bjarklev, S. Dahl-Petersen, T. Rasmussen, and K. Rottwitt, "Quantum limited noise figure operation of high gain Erbium doped fiber amplifiers," *Journal of Lightwave Technology*, 11, 1344-1352 (1993).

229. M. Bolshtyansky, I. Mandelbaum, and F. Pan, "Signal excited-state absorption in the L-band EDFA: Simulation and measurements," *Journal of Lightwave Technology* 23, 2796 (2005).

230. D. Khoptyar, S. Sergeyev, and B. Jaskorzynska, "Homogeneous upconversion in Er-doped fibers under steady state excitation: analytical model and its Monte Carlo verification," JOSA B 22, 582-590 (2005).

231. D. McCumber, "Einstein relations connecting broadband emission and absorption spectra," *Phys. Rev* 136, A954-A957 (1964).

232. F. Auzel, D. Meichenin, A. Mendorioz, R. Balda, and J. Fernandez, "Determination of the quantum efficiency of Er3+ in glasses: indirect and direct methods," *Journal of Luminescence* 72, 152-154 (1997).

233. Y. Jian-Hu, D. Shi-Xun, W. Lei, L. Zhu-Ping, H. Li-Li, and J. Zhong-Hong, "Mixed former effect: A kind of composition adjusting method of Er-doped glass for broadband amplification," *Chinese Physics Letters* 19, 1516 (2002).

234. H. Hayashi, S. Tanabe, and N. Sugimoto, "Quantitative analysis of optical power budget of bismuth oxide-based erbium-doped fiber," *Journal of Luminescence* 128, 333-340 (2008).

235. H. Ono, M. Yamada, M. Shimizu, and Y. Ohishi, "Signal output characteristics of 1.58 m band gain-flattened Er 3+-doped fibre amplifiers for WDM systems," *Electronics Letters* 34, 1513-1514 (1998).

236. K. Rottwitt, J. H. Povlsen, A. Bjarklev, O. Lumholt, B. Pedersen, and T. Rasmussen, "Optimum signal wavelength for a distributed erbium-doped fiber amplifier," *Photonics Technology Letters, IEEE* 4, 714-717 (1992).

237. D. M. Baney, P. Gallion, and R. S. Tucker, "Theory and measurement techniques for the noise figure of optical amplifiers," *Optical Fiber Technology* 6, 122-154 (2000).

238. E. Desurvire, "Analysis of gain difference between forward-and backward-pumped erbium-doped fiber amplifiers in the saturation regime," *Photonics Technology Letters, IEEE* 4, 711-714 (1992).

239. R. Laming, J. Townsend, D. Payne, F. Meli, G. Grasso, and E. Tarbox, "High-power erbium-doped-fiber amplifiers operating in the saturated regime," *Photonics Technology Letters, IEEE* 3, 253-255 (1991).

240. F. A. Flood, "Gain saturation behavior in L-band EDFAs," *Photonics Technology Letters, IEEE* 12, 1156-1158 (2000).

241. Y. Kimura, K. Suzuki, and M. Nakazawa, "Noise figure characteristics of Er3+-doped fibre amplifier pumped in 0.8 mu m band," *Electronics Letters* 27, 146-148 (1991).

242. H. Liu, H. Tam, W. Chung, P. Wai, and N. Sugimoto, "La-codoped bismuth-based erbium-doped fiber ring laser with 106-nm tuning range," *Photonics Technology Letters, IEEE* 17, 297-299 (2005).

243. N. Sugimoto, "Ultrafast optical switches and wavelength division multiplexing (WDM) amplifiers based on Bismuth oxide glasses," *Journal of the American Ceramic Society* 85, 1083-1088 (2002).

244. W. M. Steen, and J. Mazumder, "Biomedical Laser Processes and Equipment," *Laser Material Processing*, 441-484 (2010).

245. A. Tünnermann, T. Schreiber, and J. Limpert, "Fiber lasers and amplifiers: an ultrafast performance evolution," *Applied optics* 49, F71-F78 (2010).

246. D. Richardson, J. Nilsson, and W. Clarkson, "High power fiber lasers: current status and future perspectives [Invited]," *JOSA B* 27, B63-B92 (2010).

247. R. Poprawe, Tailored “Light 2: Laser Application Technology” (*Springer Verlag,* 2009).

248. M. Baba, T. Fujishiro, S. Yamaguchi, K. Tei, M. Yoshida, T. Sakurai, and K. Tanaka, "Linearly polarized 100-kW-Peak-power pulsed fiber laser with a novel master oscillator," *Optical review* 17, 50-53 (2010).

249. P. Jiang, D. Yang, Y. Wang, T. Chen, B. Wu, and Y. Shen, "All fiberized MOPA structured single mode pulse Yb fiber laser with a linearly polarized output power of 30 W," *Laser Physics Letters* 6, 384-387 (2009).

250. P. A. Nicati, K. Toyama, S. Huang, and H. J. Shaw, "Temperature effects in a Brillouin fiber ring laser," *Optics letters* 18, 2123-2125 (1993).

251. P. V. Mamyshev, S. V. Chernikov, and E. Dianov, "Generation of fundamental soliton trains for high-bit-rate optical fiber communication lines," *Quantum Electronics, IEEE Journal of* 27, 2347-2355 (1991).

252. W. Jindong, C. D. L. W. Z. Liyong, and W. X. Q. Jianrong, "Fabrication of Bi-Doped Silica Fibers with Near Infrared Broadband Emission," *Acta Optica Sinica,* 04 (2011).

253. M. Karasek, "Optimum design of Er^{3+}-Y^{b3+} codoped fibers for large-signal high-pump-power applications," *Quantum Electronics, IEEE Journal of* 33, 1699-1705 (1997).

254. B. Peng, H. Zhang, M. Gong, and P. Yan, "All-fiber eye-safe pulsed laser with Er-Yb Co-doped multi-stage amplifier," *Laser physics* 19, 2019-2022 (2009).

255. M. Moghaddam, S. Harun, M. Tamjis, and H. Ahmad, "Double clad erbium/ytterbium doped fiber laser with a fiber Bragg grating," *Laser Physics Letters* 6, 586-589 (2009).

256. S. Harun, M. R. A. Moghaddam, and H. Ahmad, "High output power Erbium-Ytterbium doped cladding pumped fiber amplifier," *Laser physics,* 1-3 (2010).

257. M. R. A. Moghaddam, S. Harun, R. Parvizi, Z. Salleh, H. Arof, A. Lokman, and H. Ahmad, "Experimental and theoretical studies on ytterbium sensitized erbium-doped fiber amplifier," *Optik-International Journal for Light and Electron Optics* 122, 1783-1786 (2011).

258. J. Sahu, C. Renaud, K. Furusawa, R. Selvas, J. Alvarez-Chavez, D. Richardson, and J. Nilsson, "Jacketed air-clad cladding pumped ytterbium-doped fibre laser with wide tuning range," *Electronics Letters* 37, 1116-1117 (2001).

259. T. Birks, "Reducing losses in photonic crystal fibres," (*Optical Society of America*, 2006).

260. K. Oh, S. Yoo, U. C. Ryu, S. Kim, U. C. Paek, D. Soh, J. K. Sahu, and J. Nilsson, "Spectral control of optical gain in a rare earth-doped optical fiber using novel triple layered structures," *Optical Fiber Technology* 12, 297-304 (2006).

261. G. G. Vienne, J. E. Caplen, L. Dong, J. D. Minelly, J. Nilsson, and D. N. Payne, "Fabrication and characterization of Yb^{3+}: Er^{3+} phosphosilicate fibers for lasers," *Journal of Lightwave Technology,* 16, 1990-2001 (1998).

262. S. Harun, H. Abdul-Rashid, S. Muhd-Yassin, M. Abd-Rahman, K. Jayapalan, and H. Ahmad, "37.2 dB small-signal gain from Er/Yb Co-doped fiber amplifier with 20ámW pump power," *Optics & Laser Technology* 40, 88-91 (2008).

263. M. Federighi, and F. Di Pasquale, "The effect of pair-induced energy transfer on the performance of silica waveguide amplifiers with high Er3+/Yb3+ concentrations," *Photonics Technology Letters, IEEE* 7, 303-305 (1995).

264. V. Doya, O. Legrand, and F. Mortessagne, "Optimized absorption in a chaotic double-clad fiber amplifier," *Optics letters* 26, 872-874 (2001).

265. D. J. Digiovanni, and A. J. Stentz, "Tapered fiber bundles for coupling light into and out of cladding-pumped fiber devices," (*US Patent* 5,864,644, 1999).

266. S. Tammela, and K. Ylä-jarkko, "Optical fibre bundle," (*EP Patent* 2,259,106, 2012).

267. L. Jin, Y. Zou, X. Ma, Z. Yang, Z. Xue, Y. Jin, L. Xu, Q. Sui, W. Zhao, and Z. Zhang, "Simulation and optimization of pump technology on high-power fiber laser," *International Conference of Optoelectronics and Microelectronics* (*ICOM, IEEE*) pp.77-80 (2012),.

268. A. B. Grudinin, D. N. Payne, P. W. Turner, L. J. A. Nilsson, M. N. Zervas, M. Ibsen, and M. K. Durkin, "Multi-fibre arrangements for high power fibre lasers and amplifiers," (*US Patent* 6,826,335, 2004).

269. G. P. Valentin, and S. Igor, "Coupling arrangement between a multi-mode light source and an optical fiber through an intermediate optical fiber length," (*US Patent* 5,999,673, 1999).

270. W. Fan, L. Htein, B. H. Kim, and W. T. Han, "Broad upconversion luminescence at 800-1000 nm in Bi-doped germano-silicate glass fiber," *in Opto-Electronics and Communications Conference* (*OECC*), 2012 *17th* (*IEEE,* 2012), pp. 208-209.

271. I. I. Oprea, H. Hesse, and K. Betzler, "Luminescence of erbium-doped bismuth-borate glasses," Optical Materials 28, 1136-1142 (2006).

272. D. R. Zimmerman, and L. H. Spiekman, "Amplifiers for the masses: EDFA, EDWA, and SOA amplets for metro and access applications," *Journal of Lightwave Technology* 22, 63 (2004).

273. G. Sobon, P. Kaczmarek, A. Antonczak, J. Sotor, and K. M. Abramski, "Controlling the 1 m spontaneous emission in Er^{3+}/Yb^{3+} co-doped fiber amplifiers," *Optics Express* 19, 19104-19113 (2011).

274. Y. Jeong, J. Sahu, D. Soh, C. Codemard, and J. Nilsson, "High-power tunable single-frequency single-mode erbium: ytterbium codoped large-core fiber master-oscillator power amplifier source," *Optics letters* 30, 2997-2999 (2005).

275. C. Berkdemir, and S. Özsoy, "Numerical analysis of the signal gain and noise figure of Yb^{3+}-sensitized Er^{3+}-doped fiber amplifiers at different pumping power configurations," *Optical Materials* 31, 229-232 (2008).

276. E. Snoeks, G. N. Hoven, A. Polman, B. Hendriksen, M. Diemeer, and F. Priolo, "Cooperative upconversion in erbium-implanted soda-lime silicate glass optical waveguides," *JOSA B* 12, 1468-1474 (1995).

277. W. J. Miniscalco, and R. S. Quimby, "General procedure for the analysis of Er^{3+} cross sections," *Opt. Lett* 16, 258-260 (1991).

278. E. Desurvire, C. R. Giles, and J. R. Simpson, "Gain saturation effects in high-speed, multichannel erbium-doped fiber amplifiers at = 1.53 m," *Journal of Lightwave Technology*, 7, 2095-2104 (1989).

279. Y. Jaouen, J. P. Bouzinac, J. M. P. Delavaux, C. Chabran, and M. Le Flohic, "Generation of four-wave mixing products inside WDM c-band 1 W Er $^{3+}$/Yb^{3+} amplifier," *Electronics Letters* 36, 233-235 (2000).

280. G. Kulcsar, Y. Jaouen, E. Olmedo, and G. Canat, "Maximizing energy extraction from Er^{3+}/Yb^{3+} doped fiber amplifier in shaped microsecond pulses," *in Conference on Lasers and Electro-Optics* (*IEEE,* 2003), p. 2 pp.

281. R. Wu "Fluorescence lifetime and 980 nm pump energy transfer dynamics in erbium and ytterbium co-doped phosphate laser glasses," *in Proceedings of SPIE*(2003), pp. 11-17.

282. Y. Jaouen, "35 kW subpicosecond pulse generation at 1.55 m using Er^{3+}/Yb^{3+} fiber amplifier," *in Lasers and Electro-Optics, 2001. CLEO'01. Technical Digest.* (*IEEE,* 2001), pp. 217-218.

283. U. S. Inan, and R. A. Marshall, Numerical Electromagnetics: The FDTD Method (*Cambridge Univ* Pr, 2011).

284. S. Y. Park, and H. K. Kim, "Efficient and low-noise operation in a gain-flattened 1580 nm band EDFA," *in OFC/IOOC 1999 Technical Digest* (*IEEE*, 1999), pp. 123-125 vol. 122.

285. E. Desurvire, "Analysis of distributed erbium-doped fiber amplifiers with fiber background loss," *Photonics Technology Letters, IEEE* 3, 625-628 (1991).

286. F. Willems, and J. Van der Plaats, "Experimental demonstration of noise figure reduction caused by nonlinear photon statistics of saturated EDFA's," *Photonics Technology Letters, IEEE* 7, 488-490 (1995).

287. K. Thyagarajan, and A. Ghatak, Lasers: Fundamentals and Applications (*Springer Verlag,* 2010).

288. J. Geng, C. Spiegelberg, and S. Jiang, "Narrow linewidth fiber laser for 100-km optical frequency domain reflectometry," *Photonics Technology Letters, IEEE* 17, 1827-1829 (2005).

289. Y. Cheng, J. Kringlebotn, W. Loh, R. Laming, and D. Payne, "Stable single-frequency traveling-wave fiber loop laser with integral saturable-absorber-based tracking narrow-band filter," *Optics letters* 20, 875-877 (1995).

290. D. Chang, M. Guy, S. Chernikov, J. Taylor, and H. Kong, "Single-frequency erbium fibre laser using the twisted-mode technique," *Electronics Letters* 32, 1786-1787 (1996).

291. V. Lecoeuche, P. Niay, M. Douay, P. Bernage, S. Randoux, and J. Zemmouri, "Bragg grating based Brillouin fibre laser," *Optics Communications* 177, 303-306 (2000).

292. M. R. Phillips, "Amplified 1550-nm CATV lightwave system," *in Proc.Optical Fiber Communication Conf., ser. OSA Tech. Dig. Washington, DC: Opt. Soc.Amer* (1998), pp. 85–86.

293. H. Heffner, "The fundamental noise limit of linear amplifiers," *Proceedings of the IRE* 50, 1604-1608 (1962).

294. G. Cowle, P. Morkel, R. Loming, and D. Payne, "Spectral broadening due to fibre amplifier phase noise," *Electronics Letters* 26, 424-425 (1990).

295. L. Moller, "Novel aspects of spectral broadening due to fiber amplifier phase noise," *IEEE Journal of Quantum Electronics,* 34, 1554-1558 (1998).

296. G. J. Cowle, "Narrow-linewidth erbium-doped fibre lasers," (*University of Southampton,* 1991).

297. M. Horowitz, R. Daisy, B. Fischer, and J. Zyskind, "Narrow-linewidth, singlemode erbium-doped fibre laser with intracavity wave mixing in saturable absorber," *Electronics Letters* 30, 648-649 (1994).

298. H. Pask, R. J. Carman, D. C. Hanna, A. C. Tropper, C. J. Mackechnie, P. R. Barber, and J. M. Dawes, "Ytterbium-doped silica fiber lasers: versatile sources for the 1-1.2 m region," *IEEE Journal of Selected Topics in Quantum Electronics,* 1, 2-13 (1995).

299. R. Paschotta, J. Nilsson, A. C. Tropper, and D. C. Hanna, "Ytterbium-doped fiber amplifiers," *Quantum Electronics, IEEE Journal of* 33, 1049-1056 (1997).

300. G. Cowle, D. Payne, and D. Reid, "Single-frequency travelling-wave erbium-doped fibre loop laser," *Electronics Letters* 27, 229-230 (1991).

301. R. Loudon, The quantum theory of light (Oxford University Press, USA, 2000).

302. M. Shirazi, M. Biglary, S. Harun, K. Thambiratnam, and H. Ahmad, "Bidirectional multiwavelength Brillouin fiber laser generation in a ring cavity," *Journal of Optics A: Pure and Applied Optics* 10, 055101 (2008).

303. T. Okoshi, K. Kikuchi, and A. Nakayama, "Novel method for high resolution measurement of laser output spectrum," *Electronics Letters* 16, 630-631 (1980).

304. A. L. Gaeta, and R. W. Boyd, "Stochastic dynamics of stimulated Brillouin scattering in an optical fiber," *Physical Review A* 44, 3205-3209 (1991).

305. P. Callahan, M. Gross, and M. Dennis, "Frequency-Independent Phase Noise in a Dual-Wavelength Brillouin Fiber Laser," *IEEE Journal of Quantum Electronics, ,* 1-1 (2011).

306. S. Harris, and R. Targ, "FM Oscillation of the He Ne Laser," *Applied physics letters* 5, 202-204 (1964).

307. E. Ippen, C. Shank, and A. Dienes, "Passive mode locking of the cw dye laser," *Applied physics letters* 21, 348-350 (1972).

308. M. Dzhibladze, Z. Esiashvili, É. S. Teplitski , S. Isaev, and V. Sagaradze, "Mode locking in a fiber laser," *Soviet Journal of Quantum Electronics* 13, 245 (1983).

309. L. F. Mollenauer, and R. H. Stolen, "The soliton laser," *Optics letters* 9, 13-15 (1984).

310. G. Geister, and R. Ulrich, "Neodymium-fibre laser with integrated-optic mode locker," *Optics Communications* 68, 187-189 (1988).

311. J. Kafka, T. Baer, and D. W. Hall, "Mode-locked erbium-doped fiber laser with soliton pulse shaping," *Optics letters* 14, 1269-1271 (1989).

312. M. Hofer, M. Ober, F. Haberl, and M. Fermann, "Characterization of ultrashort pulse formation in passively mode-locked fiber lasers," *Quantum Electronics, IEEE Journal of* 28, 720-728 (1992).

313. U. Keller, D. Miller, G. Boyd, T. Chiu, J. Ferguson, and M. Asom, "Solid-state low-loss intracavity saturable absorber for Nd: YLF lasers: an antiresonant semiconductor Fabry–Perot saturable absorber," *Optics letters* 17, 505-507 (1992).

314. J. NEEV, "Handbook of ultra-short pulse lasers for biomedical and medical applications," (*McGraw-Hill New York*, 2012).

315. S. O. Konorov, V. P. Mitrokhin, A. B. Fedotov, D. A. Sidorov-Biryukov, V. I. Beloglazov, N. B. Skibina, A. V. Shcherbakov, E. Wintner, M. Scalora, and A. M. Zheltikov, "Laser ablation of dental tissues with picosecond pulses of 1.06-μm radiation transmitted through a hollow-core photonic-crystal fiber," *Applied Optics* 43, 2251-2256 (2004).

316. V. N. Serkin, and A. Hasegawa, "Soliton Management for Ultra-high Speed Telecommunications," *Telecommunication Systems* 12, 17 (2012).

317. M. Attygalle, C. Lim, and A. Nirmalathas, "Dispersion-tolerant multiple WDM channel millimeter-wave signal generation using a single monolithic mode-locked semiconductor laser," *Journal of Lightwave Technology* 23, 295 (2005).

318. H. Yokoyama, A. Sato, H. C. Guo, K. Sato, M. Mure, and H. Tsubokawa, "Nonlinear-microscopy optical-pulse sources based on mode-locked semiconductor lasers," *Optics Express* 16, 17752-17758 (2008).

319. M. Kuramoto, N. Kitajima, H. Guo, Y. Furushima, M. Ikeda, and H. Yokoyama, "Two-photon fluorescence bioimaging with an all-semiconductor laser picosecond pulse source," *Optics letters* 32, 2726-2728 (2007).

320. P. Giaccari, J. D. Deschênes, P. Saucier, J. Genest, and P. Tremblay, "Active Fourier-transform spectroscopy combining the direct RF beating of two fiber-based mode-locked lasers with a novel referencing method," *Optics Express* 16, 4347-4365 (2008).

321. T. Klein, W. Wieser, B. R. Biedermann, C. M. Eigenwillig, G. Palte, and R. Huber, "Raman-pumped Fourier-domain mode-locked laser: analysis of operation and application for optical coherence tomography," *Optics letters* 33, 2815-2817 (2008).

322. S. Schilt, "Optical frequency comb with sub-radian CEO phase noise from a SESAM-modelocked 1.5-μ m solid-state laser," *in CLEO: Science and Innovations*(2011).

323. T. Mizunami, "Femtosecond-pulsed laser micromachining and optical damage by an erbium-doped fiber-laser system," *Microelectronic Engineering* 88, 2334-2337 (2011).

324. J. Russell and R. Cohn, Mode-locking (*Book on Demand Ltd.,* May 3, 2012).

325. U. Kellers, "Laser physics and applications," *in Sub-volume B, part 1*(*Springer-Verlag, Berlin,* 2007).

326. H. Haus, "A theory of forced mode locking," *IEEE Journal of Quantum Electronics,* 11, 323-330 (1975).

327. H. A. Haus, "Mode-locking of lasers," *Journal of Selected Topics in Quantum Electronics, IEEE* 6, 1173-1185 (2000).

328. G. T. Harvey, and L. F. Mollenauer, "Harmonically mode-locked fiber ring laser with an internal Fabry-Perot stabilizer for soliton transmission," *Optics letters* 18, 107-109 (1993).

329. L. Yun, and X. Liu, "Generation and propagation of bound-state pulses in a passively mode-locked figure-eight laser," *Photonics Journal, IEEE* 4, 512-519 (2012).

330. U. Keller, K. J. Weingarten, F. X. Kartner, D. Kopf, B. Braun, I. D. Jung, R. Fluck, C. Honninger, N. Matuschek, and J. Aus der Au, "Semiconductor saturable absorber mirrors (SESAM's) for femtosecond to nanosecond pulse generation in solid-state lasers," *Selected Topics in Quantum Electronics, IEEE Journal of* 2, 435-453 (1996).

331. E. Ippen, "Femtosecond Pulse Generation: Principles and Fiber Applications," *Ultrafast Dynamics of Quantum Systems,* 213-231 (2002).

332. W. Knox, "Dispersion measurements for femtosecond-pulse generation and applications," *Applied Physics B: Lasers and Optics* 58, 225-235 (2004).

333. H. A. Haus, Waves and fields in optoelectronics (*Prentice-Hall New Jersey*, 1984).

334. R. Paschotta, Encyclopedia of laser physics and technology (*Wiley-VCH,* 2008).

335. H. A. Haus, "Theory of mode locking with a fast saturable absorber," *Journal of applied physics* 46, 3049-3058 (1975).

336. J. N. Kutz, B. C. Collings, K. Bergman, S. Tsuda, S. T. Cundiff, W. H. Knox, P. Holmes, and M. Weinstein, "Mode-locking pulse dynamics in a fiber laser with a saturable Bragg reflector," *JOSA B* 14, 2681-2690 (1997).

337. I. Walmsley, L. Waxer, and C. Dorrer, "The role of dispersion in ultrafast optics," *Review of Scientific Instruments* 72, 1 (2001).

338. F. Ilday, J. Buckley, W. Clark, and F. Wise, "Self-similar evolution of parabolic pulses in a laser," *Physical review letters* 92, 213902 (2004).

339. S. Naumov, A. Fernandez, R. Graf, P. Dombi, F. Krausz, and A. Apolonski, "Approaching the microjoule frontier with femtosecond laser oscillators," *New Journal of Physics* 7, 216 (2005).

340. V. Kalashnikov, E. Podivilov, A. Chernykh, and A. Apolonski, "Chirped-pulse oscillators: theory and experiment," *Applied Physics B: Lasers and Optics* 83, 503-510 (2006).

341. J. Buckley, F. Wise, F. Ö. Ilday, and T. Sosnowski, "Femtosecond fiber lasers with pulse energies above 10 nJ," *Optics letters* 30, 1888-1890 (2005).

342. J. Buckley, A. Chong, S. Zhou, W. Renninger, and F. W. Wise, "Stabilization of high-energy femtosecond ytterbium fiber lasers by use of a frequency filter," *JOSA B* 24, 1803-1806 (2007).

343. A. Chong, W. H. Renninger, and F. W. Wise, "Properties of normal-dispersion femtosecond fiber lasers," *JOSA B* 25, 140-148 (2008).

344. W. Renninger, A. Chong, and F. Wise, "Dissipative solitons in normal-dispersion fiber lasers," *Physical Review A* 77, 023814 (2008).

345. H. A. Haus, J. G. Fujimoto, and E. P. Ippen, "Analytic theory of additive pulse and Kerr lens mode locking," *Quantum Electronics, IEEE Journal of* 28, 2086-2096 (1992).

346. A. Owyoung, R. Hellwarth, and N. George, "Intensity-induced changes in optical polarizations in glasses," *Physical Review B* 5, 628 (1972).

347. E. Ippen, "Principles of passive mode locking," *Applied Physics B* 58, 159-170 (1994).

348. L. Nelson, D. Jones, K. Tamura, H. Haus, and E. Ippen, "Ultrashort-pulse fiber ring lasers," *Applied Physics B* 65, 277-294 (1997).

349. T. D. Yuan, and L. Zhao, "Deterministic Dynamics of Solitons in Passive Mode-Locked Fiber Lasers," *Nonlinear Optical Systems: Principles, Phenomena, and Advanced Signal Processing* 6, 203 (2012).

350. P. Gourley, and T. Drummond, "Resonant, dispersive optical tuning in an epitaxial (Al, Ga) As Fabry–Perot étalon," *Applied physics letters* 52, 7-9 (1988).

351. M. Moenster, U. Griebner, W. Richter, and G. Steinmeyer, "Resonant saturable absorber mirrors for dispersion control in ultrafast lasers," *Quantum Electronics, IEEE Journal of* 43, 174-181 (2007).

352. M. Lumb, "Dispersionless saturable absorber mirrors with large modulation depths and low saturation fluences," *Applied Physics B: Lasers and Optics* 97, 53-60 (2009).

353. D. Kopf, G. Zhang, R. Fluck, M. Moser, and U. Keller, "All-in-one dispersion-compensating saturable absorber mirror for compact femtosecond laser sources," *Optics letters* 21, 486-488 (1996).

354. I. Jung, L. Brovelli, M. Kamp, U. Keller, and M. Moser, "Scaling of the antiresonant Fabry–Perot saturable absorber design toward a thin saturable absorber," Optics letters 20, 1559-1561 (1995).

355. G. Spühler, K. Weingarten, R. Grange, L. Krainer, M. Haiml, V. Liverini, M. Golling, S. Schön, and U. Keller, "Semiconductor saturable absorber mirror structures with low saturation fluence," *Applied Physics B: Lasers and Optics* 81, 27-32 (2005).

356. R. Herda, and O. G. Okhotnikov, "Effect of amplified spontaneous emission and absorber mirror recovery time on the dynamics of mode-locked fiber lasers," *Applied physics letters* 86, 011113-011113 (2005).

357. M.sheikbahae, "Semiconductor Saturable Absorber Mirror," *Phys/EECE* 555 (University of New Mexico Spring 2005)

358. L. Krainer, R. Paschotta, S. Lecomte, M. Moser, K. J. Weingarten, and U. Keller, "Compact Nd: YVO4 lasers with pulse repetition rates up to 160 GHz," *Quantum Electronics, IEEE Journal of* 38, 1331-1338 (2002).

359. S. C. Zeller, L. Krainer, G. Spuhler, R. Paschotta, M. Golling, D. Ebling, K. Weingarten, and U. Keller, "Passively modelocked 50 GHz Er: Yb: glass laser," *Electronics Letters* 40, 875-877 (2004).

360. R. Paschotta, L. Krainer, S. Lecomte, G. Spühler, S. Zeller, A. Aschwanden, D. Lorenser, H. Unold, K. Weingarten, and U. Keller, "Picosecond pulse sources with multi-GHz repetition rates and high output power," *New Journal of Physics* 6, 174 (2004).

361. C. Hönninger, R. Paschotta, F. Morier-Genoud, M. Moser, and U. Keller, "Q--switching stability limits of continuous-wave passive mode locking," *JOSA B* 16, 46-56 (1999).

362. F. Kartner, I. Jung, and U. Keller, "Soliton mode-locking with saturable absorbers," *Selected Topics in Quantum Electronics, IEEE Journal of* 2, 540-556 (1996).

363. R. Paschotta, and U. Keller, "Passive mode locking with slow saturable absorbers," *Applied Physics B: Lasers and Optics* 73, 653-662 (2001).

364. M. Bass, Handbook of optics (*McGraw-Hill*, 2001).

365. T. Hakulinen, R. Herda, and O. G. Okhotnikov, "Nonlinear response of saturable absorber mirrors for different operation regimes," *IEEE Photonics Technology Letters* 19, 333 (2007).

366. H. A. Haus, J. G. Fujimoto, and E. P. Ippen, "Structures for additive pulse mode locking," *JOSA B* 8, 2068-2076 (1991).

367. V. Chauhan, P. Bowlan, J. Cohen, and R. Trebino, "Single-diffraction-grating and grism pulse compressors," *JOSA B* 27, 619-624 (2010).

368. D. Anderson, M. Desaix, M. Lisak, and M. L. Quiroga–Teixeiro, "Wave breaking in nonlinear-optical fibers," *JOSA B* 9, 1358-1361 (1992).

369. M. Rusu, "Frequency conversion using ultrafast fiber lasers," (*Tampere University of Technology, Tampere, Finland,* 2006).

370. K. Tamura, E. Ippen, H. Haus, and L. Nelson, "77-fs pulse generation from a stretched-pulse mode-locked all-fiber ring laser," *Optics letters* 18, 1080-1082 (1993).

371. C. X. Yu, S. Namiki, and H. A. Haus, "Noise of the stretched pulse fiber laser. II. Experiments," *IEEE Journal of Quantum Electronics,* 33, 660-668 (1997).

372. K. Tamura, E. Ippen, and H. Haus, "Pulse dynamics in stretched pulse fiber lasers," *Applied physics letters* 67, 158-160 (1995).

373. H. Haus, K. Tamura, L. Nelson, and E. Ippen, "Stretched-pulse additive pulse mode-locking in fiber ring lasers: theory and experiment," *Quantum Electronics, IEEE Journal of* 31, 591-598 (1995).

374. M. Tiihonen, "Stretched Pulse Generation in Erbium-doped Fibre Ring Laser," (*Royal Institute of Technology, Sweden,* January 2002).

375. F. Ö. Ilday, J. Buckley, H. Lim, F. Wise, and W. Clark, "Generation of 50-fs, 5-nJ pulses at 1.03 m from a wave-breaking-free fiber laser," *Optics letters* 28, 1365-1367 (2003).

376. P. A. Bélanger, "On the profile of pulses generated by fiber lasers," *Optics Express* 13, 8089-8096 (2005).

377. M. Guina, N. Xiang, A. Vainionpää, O. Okhotnikov, T. Sajavaara, and J. Keinonen, "Self-starting stretched-pulse fiber laser mode locked and stabilized with slow and fast semiconductor saturable absorbers," *Optics letters* 26, 1809-1811 (2001).

378. M. E. Fermann, and I. Hartl, "Ultrafast fiber laser technology," *Selected Topics in Quantum Electronics, IEEE Journal of* 15, 191-206 (2009).

379. K. Tamura, C. Doerr, L. Nelson, H. Haus, and E. Ippen, "Technique for obtaining high-energy ultrashort pulses from an additive-pulse mode-locked erbium-doped fiber ring laser," *Optics letters* 19, 46-48 (1994).

380. V. Matsas, T. Newson, D. Richardson, and D. Payne, "Selfstarting passively mode-locked fibre ring soliton laser exploiting nonlinear polarisation rotation," *Electronics Letters* 28, 1391-1393 (1992).

381. G. Lenz, K. Tamura, H. Haus, and E. Ippen, "All-solid-state femtosecond source at 1.55 μm," *Optics letters* 20, 1289-1291 (1995).

382. J. Fekete, A. Cserteg, and R. Szip ocs, "All fiber, all normal dispersion ytterbium ring oscillator," *Laser Physics Letters* 6, 49-53 (2009).

383. J. Kim, K. Jung, C. Kim, H. Kim, T. Kim, S. Park, Y. Song, and H. Yang, "Progress in ultrafast fiber lasers for ultralow-jitter signal sources," *in Proc. of SPIE* Vol (2012), pp. 823715-823711.

384. H. Haus, "Parameter ranges for CW passive mode locking," *Quantum Electronics, IEEE Journal of* 12, 169-176 (1976).

385. S. Namiki, C. Yu, and H. Haus, "Observation of nearly quantum-limited timing jitter in an all-fiber ring laser," *JOSA B* 13, 2817-2823 (1996).

386. H. A. Haus, and A. Mecozzi, "Noise of mode-locked lasers," *Quantum Electronics, IEEE Journal of* 29, 983-996 (1993).

387. R. Paschotta, "Mode-locked Fiber Lasers," *http://www.rp-photonics.com/mode_locked_fiber_lasers.html.*

388. M. L. Dennis, and I. N. Duling III, "Experimental study of sideband generation in femtosecond fiber lasers," *Quantum Electronics, IEEE Journal of* 30, 1469-1477 (1994).

389. K. Tamura, C. Doerr, H. Haus, and E. Ippen, "Soliton fiber ring laser stabilization and tuning with a broad intracavity filter," *Photonics Technology Letters, IEEE* 6, 697-699 (1994).

390. H. Zhang, "Vector Soliton Fiber Lasers," *Arxiv preprint arXiv*:1111.4502 (2011).

391. M. Moghaddam, S. Harun, R. Parvizi, Z. Salleh, H. Arof, A. Lokman, and H. Ahmad, "Experimental and theoretical studies on ytterbium sensitized erbium-doped fiber amplifier," *Optik-International Journal for Light and Electron Optics* (2011).

392. S. Harun, M. R. A. Moghaddam, and H. Ahmad, "High output power Erbium-Ytterbium doped cladding pumped fiber amplifier," *Laser physics* 20, 1899-1901 (2010).

393. T. Hori, J. Takayanagi, N. Nishizawa, and T. Goto, "Flatly broadened, wideband and low noise supercontinuum generation in highly nonlinear hybrid fiber," *Optics Express* 12, 317-324 (2004).

394. "Nonlinear Photonic Crystal Fiber , NL-1050-NEG-1 - NKT Photonics," *http://www.nktphotonics.com/files/files/NL-1050-NEG-1-100409.pdf.*

395. N. Shahabuddin, N. Awang, H. Ahmad, H. Arof, K. Dimyati, Z. Yusoff, and S. Harun, "Supercontinuum generation using a passive mode-locked stretched-pulse bismuth-based erbium-doped fiber laser," *Optics & Laser Technology* (2011).

396. Y. Gu, L. Zhan, D. D. Deng, Y. X. Wang, and Y. X. Xia, "Supercontinuum generation in short dispersion-shifted fiber by a femtosecond fiber laser," *Laser physics* 20, 1459-1462 (2010).

397. S. Kobtsev, S. Kukarin, and S. Smirnov, "All-fiber high-energy supercontinuum pulse generator," *Laser physics* 20, 375-378 (2010).

398. Z. C. Luo, W. J. Cao, A. P. Luo, and W. C. Xu, "Polarization-Independent, Multifunctional All-Fiber Comb Filter Using Variable Ratio Coupler-Based Mach–Zehnder Interferometer," *Journal of Lightwave Technology* 30, 1857-1862 (2012).

399. Z. Wang, Z. Hu, C. Ge, X. Jiang, H. Bao, D. Jia, and S. Li, "Tunable multi-wavelength fiber ring laser based on a Hi-Bi fiber loop mirror," *Chinese Optics Letters* 2, 531-533 (2005).

400. R. Álvarez-Tamayo, M. Durán-Sánchez, O. Pottiez, E. Kuzin, B. Ibarra-Escamilla, and A. Flores-Rosas, "Theoretical and experimental analysis of tunable Sagnac high-birefringence loop filter for dual-wavelength laser application," *Applied optics* 50, 253-260 (2011).

401. J. E. Antonio-Lopez, D. A. May-Arrioja, P. LiKamWa, and J. J. Sanchez-Mondragon, "Tunable Dual-Wavelength Erbium-Doped Fiber Ring Laser," *in Frontiers in Optics*(*Optical Society of America*, 2012).

402. Q. Zhang, X. Zeng, F. Pang, M. Wang, and T. Wang, "Switchable multiwavelength fiber laser by using a compact in-fiber Mach–Zehnder interferometer," *Journal of Optics* 14, 045403 (2012).

403. T. Wang, X. Miao, X. Zhou, and S. Qian, "Tunable multiwavelength fiber laser based on a double Sagnac HiBi fiber loop," *Applied optics* 51, 111-116 (2012).

404. W. Wang, H. Meng, X. Wu, H. Xue, C. Tan, and X. Huang, "Three Channel-Spacing Switchable Multiwavelength Fiber Laser With Two Segments of Polarization-Maintaining Fiber," *Photonics Technology Letters, IEEE* 24, 470-472 (2012).

405. M. P. Fok, C. Shu, and W. W. Tang, "A cascadable approach to produce widely selectable spectral spacing in birefringent comb filters," *Photonics Technology Letters, IEEE* 18, 1937-1939 (2006).

406. K. S. LIM, M. R. A. Moghaddam, S. W. Harun , and H. AHMAD, "Tunable-Spacing Multi-wavelength Yb-Doped Fiber Laser (YDFL) Based on Temperature Sensitive Loop Mirror " *Lasers in Engineering* 20, 39-45 (2010).

407. J. W. Nicholson, and P. S. Westbrook, "Stabilized optical fiber continuum frequency combs using post-processed highly nonlinear fibers," (*Google Patents,* 2011).

408. C. B. Huang, "Control and characterization of phase-modulated continuous-wave laser frequency combs," (*Purdue University*, 2009).

409. S. Shahi, M. Moghaddam, S. Harun, and H. Ahmad, "The Comparison Nonlinearity Behaviors of Photonic Crystal Fiber by Two Reduced Lengths of Bi-Edf in Ring Cavity," *Journal of Nonlinear Optical Physics and Materials* 18, 521-527 (2009).

410. H. Ahmad, M. Moghaddam, H. Arof, and S. Harun, "High output power, narrow linewidth Brillouin fibre laser master-oscillatorpower-amplifier source," *Optoelectronics, IET* 5, 181-183 (2011).

411. B. Washburn, and N. Newbury, "Phase, timing, and amplitude noise on supercontinua generated in microstructure fiber," *Optics Express* 12, 2166-2175 (2004).

412. X. Gu, M. Kimmel, A. Shreenath, R. Trebino, J. Dudley, S. Coen, and R. Windeler, "Experimental studies of the coherence of microstructure-fiber supercontinuum," *Optics Express* 11, 2697-2703 (2003).

413. V. V. Alexander, O. P. Kulkarni, M. Kumar, C. Xia, M. N. Islam, F. L. Terry Jr, M. J. Welsh, K. Ke, M. J. Freeman, and M. Neelakandan, "Modulation instability initiated high power all-fiber supercontinuum lasers and their applications," *Optical Fiber Technology* 18, 349–374 (2012).

414. O. Vanvincq, B. Barviau, A. Mussot, G. Bouwmans, Y. Quiquempois, and A. Kudlinski, "Supercontinuum pulse-to-pulse fluctuations in a photonic bandgap fiber," (*Optical Society of America,* 2011).

415. N. Nishizawa, "Generation and application of high-quality supercontinuum sources," *Optical Fiber Technology* 18, 394–402 (2012).

416. J. M. Dudley, and S. Coen, "Coherence properties of supercontinuum spectra generated in photonic crystal and tapered optical fibers," *Optics letters* 27, 1180-1182 (2002).

417. K. Corwin, N. Newbury, J. M. Dudley, S. Coen, S. Diddams, K. Weber, and R. Windeler, "Fundamental noise limitations to supercontinuum generation in microstructure fiber," *Physical review letters* 90, 113904 (2003).

418. J. H. V. Price, X. Feng, A. M. Heidt, G. Brambilla, P. Horak, F. Poletti, G. Ponzo, P. Petropoulos, M. Petrovich, and J. Shi, "Supercontinuum generation in non-silica fibers," *Optical Fiber Technology* 18, 327–344 (2012).

419. M. Erkintalo, M. Surakka, J. Turunen, A. T. Friberg, and G. Genty, "Coherent-mode representation of supercontinuum," *Optics letters* 37, 169-171 (2012).

420. M. Nakatsuka, Y. Fujimoto, Y. Seo, T. Sano, and K. Kuwada, "New bismuth-doped silica glass for LD-pumpedultra-short –pulse laser at 1.2-micron wavelength," in International Workshop on High Energy Class Diode Pumped Solid State Lasers(*presented at HEC-DPSSL meeting at LLNL, Livermore, California, U.S.A., USA,* May 17-19,2006).

421. K. Wang, and C. Xu, "Tunable high-energy soliton pulse generation from a large-mode-area fiber and its application to third harmonic generation microscopy," *Applied physics letters* 99, 071112 (2011).

422. S. Boscolo, and S. K. Turitsyn, "Pulse Shaping in Mode-Locked Ring-Cavity Fibre Lasers," (Optical Society of America, 2011).